



Norwegian University of  
Science and Technology

# Experimental and Numerical Study of Sandwich Panels Exposed to Blast Loading

**Olaf Moriggi Kielland**  
**Sigurd Løvstad Lekve**

Mechanical Engineering

Submission date: June 2018

Supervisor: Tore Børvik, KT

Co-supervisor: Aase Reyes, KT

Norwegian University of Science and Technology  
Department of Structural Engineering





## MASTER THESIS 2018

|  |                                     |                                |
|--|-------------------------------------|--------------------------------|
| SUBJECT AREA:<br>Computational Mechanics | DATE:<br>June 11 <sup>th</sup> 2018 | NO. OF PAGES:<br>12 + 132 + 35 |
|--|-------------------------------------|--------------------------------|

TITLE:

### **Experimental and Numerical Study of Sandwich Panels Exposed to Blast Loading**

Eksperimentelt og numerisk studie av sandwich paneler utsatt for eksplosjonslast

BY:

Olaf Kielland

Sigurd Lekve



SUMMARY:

The main objective of this thesis is to investigate, both experimentally and numerically, the mechanical response of various sandwich components with foam cores subjected to a range of blast load scenarios.

Experiments were performed in a shock tube facility at Structural Impact Laboratory (SIMLab), Norwegian University of Science and Technology (NTNU). Multiple sandwich configurations consisting of AA1050-H14 aluminum and DOCOL 600DL steel skins with a variation of XPS-foam cores were investigated. The components were exposed to nominal firing pressures in the range \$10\$ to \$35\sim\{\text{bar}\}\$. Three-dimensional digital image correlation (3D-DIC) was used to obtain deformation profiles and midpoint displacements of the back skins.

Experimental results indicate that foam core activation is increased using a low-density XPS-250 foam, compared to higher density XPS-foams. The use of a ROMER Absolute Arm in a scanning procedure post-experiment provided supplementary deformation data, which was included in a qualitative deformation analysis. Material tests were performed on the AA1050-H14 aluminum skins used in this study. Compression test data for the XPS-foams were taken from a previous study and was used for further investigation of the densification initiation strain and to introduce a density-dependent model.

A reference model was validated through a comparison of experimental and numerical results, which showed a slight overestimation of midpoint displacement by numerical simulations. However, general agreement in deformation history was found. A parametric study was conducted to identify trends in the structural behavior, concerning protective capabilities, by varying parameters such as foam density and core thickness. An optimal foam core configuration was found, regarding minimization of displacement and percent of energy absorbed in the back skin, while maximizing foam core activation. The optimal configuration was also found to vary with blast intensity.

RESPONSIBLE TEACHER: Professor Tore Børvik

SUPERVISORS: Professor Tore Børvik, Professor Aase Reyes and PhDc Christoffer Aune Brekken

CARRIED OUT AT: Department of Structural Engineering





## MASTEROPPGAVE 2018

|                                  |                        |                                |
|----------------------------------|------------------------|--------------------------------|
| FAGOMRÅDE:<br>Beregningsmekanikk | DATO:<br>11. juni 2018 | ANTALL SIDER:<br>12 + 132 + 35 |
|----------------------------------|------------------------|--------------------------------|

TITTEL:

**Eksperimentelt og numerisk studie av sandwich-paneler utsatt for eksplosjonslast**

Experimental and Numerical Study of Sandwich Panels Exposed to Blast Loading

UTFØRT AV:

Olaf Kielland

Sigurd Lekve



SAMMENDRAG:

Formålet med denne avhandlingen er å undersøke, både eksperimentelt og numerisk, den mekaniske responsen til ulike sandwich-komponenter med skumkjerner utsatt for eksplosjonslaster.

Eksperimenter ble utført i shocktuben ved Structural Impact Laboratory (SIMLab), Norges teknisk-naturvitenskapelige universitet (NTNU). Flere sandwich-paneler med hudkonfigurasjoner av AA1050-H14 aluminium og DOCOL 600DL stål og skumkjerner av forskjellige XPS-variasjoner ble undersøkt. Komponentene ble utsatt for nominelle avfyringstrykk fra 10 til 35 bar. Tredimensjonal digital bildekorrelasjon (3D-DIC) ga deformasjonsprofiler og midtpunktsdeformasjon av bakre hud.

De eksperimentelle resultatene viste at skumaktiveringen økte ved bruk av lavtetthetsskummet XPS-250, sammenlignet med XPS-skum med høyere tetthet. Bruken av ROMER Absolute Arm for skanning av plater ga supplementerende deformasjonsdata, som ble inkludert i en kvalitativ deformasjonsanalyse. Materialtester ble utført på hudene av aluminium brukt i studiet. Data fra trykktester på XPS-skum ble hentet fra en tidligere avhandling og ble brukt til å gjøre ytterligere undersøkelser av fortettingstøyning og til å innføre en tetthetsavhengig modell.

En referansemodell ble validert gjennom en sammenligning av eksperimentelle og numeriske resultater, som ga en liten overestimert midtpunktsforskyvning i de numeriske resultatene. Generell overenstemmelse ble funnet for deformasjonsforløpet. En parameterstudie ble gjennomført for å undersøke trender i den mekaniske responsen, med tanke på beskyttelsesevne, ved å variere parametere som skumtetthet og skumtykkelse. En optimal skumkonfigurasjon ble funnet for vektlegging av minimering av deformasjon og prosentvist energioptak i bakre hud og maksimering av skumaktivering. Den optimale konfigurasjonen ble også funnet til å være trykkavhengig.

FAGLÆRER: Professor Tore Børvik

VEILEDERE: Professor Tore Børvik, Professor Aase Reyes og PhdC Christoffer Aune Brekken

UTFØRT VED: Institutt for konstruksjonsteknikk



## **MASTER'S THESIS 2018**

for

*Olaf Kielland and Sigurd Lekve*

### **Experimental and Numerical Study on Sandwich Panels Exposed to Blast Loading**

#### **1. INTRODUCTION**

In the event of high-energy accidents and targeted attacks, it is important to reduce the consequences to human lives and critical infrastructure. Sandwich panels, which traditionally take the form of a plated structure with a core layer encapsulated by face sheets on either side, are found to be efficient energy absorbers. As the sandwich structure deforms, energy is dissipated within the layers – reducing the forces transferred to other more critical components. Such panels may be used as sacrificial claddings on structures or as part of the structure itself. It is important to understand the fundamental mechanisms and mechanical properties of the different panel layers, when exposed to various blast scenarios in order to investigate the energy absorption capabilities of the sandwich configurations in question.

#### **2. OBJECTIVES**

The primary objective of the research project is to investigate, both experimentally and numerically, the mechanical response of various sandwich panel configurations with core layer made of polymeric foam materials exposed to blast loading.

#### **3. A SHORT DESCRIPTION OF THE RESEARCH PROJECT**

The main topics in the research project will be as follows:

1. The candidates shall conduct a study of relevant literature concerning sandwich panels, the constitutive modeling of cellular and metallic materials, and retrieve experimental data of relevant materials and components.
2. Establish robust numerical models for sandwich panels subjected to blast loading in the finite element code LS-DYNA in order to establish an experimental program and to get an initial understanding of which key parameters influence the mechanical response of such designs.
3. Conduct necessary experimental material tests on core and skin materials, and to calibrate these to constitutive material models available in LS-DYNA.
4. A series of experimental component tests with various sandwich configurations shall be carried out in the SIMLab Shock Tube Facility (SSTF) for further understanding of the underlying physical mechanisms in design characteristics. 3D-DIC shall be used to measure the deflection of the sandwich panels as a function of the applied loading.
5. The candidates shall compare the established numerical models to the experimental results and validate the numerical simulations of the various experimental sandwich configurations.
6. Numerical parametric studies should be conducted on the sandwich panels to investigate the geometrical and material effects on energy absorption, force transfer and panel deflection.

*Supervisors:* Tore Børvik, Kristoffer Aune Brekken and Aase Reyes

The candidates may agree with the supervisors to pay special attention to specific parts of the investigation, or to include other aspects than those already mentioned. The thesis must be written according to current requirements and submitted to Department of Structural Engineering, NTNU, no later than June 11<sup>th</sup>, 2018.

NTNU, January 15<sup>th</sup>, 2018



Tore Børvik  
Professor

# Abstract

The main objective of this thesis is to investigate, both experimentally and numerically, the mechanical response of various sandwich components with foam cores subjected to a range of blast load scenarios.

Experiments were performed in a shock tube facility at Structural Impact Laboratory (SIM-Lab), Norwegian University of Science and Technology (NTNU). Multiple sandwich configurations consisting of AA1050-H14 aluminum and DOCOL 600DL steel skins with a variation of XPS-foam cores were investigated. The components were exposed to nominal firing pressures in the range 10 to 35 *bar*. Three-dimensional digital image correlation (3D-DIC) was used to obtain deformation profiles and midpoint displacements of the back skins.

Experimental results indicate that foam core activation is increased using a low-density XPS-250 foam, compared to higher density XPS-foams. The use of a ROMER Absolute Arm in a scanning procedure post-experiment provided supplementary deformation data, which was included in a qualitative deformation analysis. Material tests were performed on the AA1050-H14 aluminum skins used in this study. Compression test data for the XPS-foams were taken from a previous study and was used for further investigation of the densification initiation strain and to introduce a density-dependent model.

A reference model was validated through a comparison of experimental and numerical results, which showed a slight overestimation of midpoint displacement by numerical simulations. However, general agreement in deformation history was found. A parametric study was conducted to identify trends in the structural behavior, concerning protective capabilities, by varying parameters such as foam density and core thickness. An optimal foam core configuration was found, regarding minimization of displacement and percent of energy absorbed in the back skin, while maximizing foam core activation. The optimal configuration was also found to vary with blast intensity.





# Acknowledgements

This thesis is written for Centre for Advanced Structural Analysis (CASA) at Norwegian University of Science and Technology (NTNU). The centre aims to build an attractive scientific working environment where fundamental knowledge is created through multidisciplinary theoretical, numerical and experimental research on different scales. The vision of the project is to establish a world-leading center for multi-scale testing, modeling, and simulation of materials and structures for industrial applications.

The authors would like to express our sincere gratitude to our supervisors Professor Tore Børvik and Professor Aase Reyes for excellent guidance and engaging discussions during weekly progress meetings. We are also very grateful for the dedicated assistance provided by our supervisor Ph.D. candidate Kristoffer Aune Brekken throughout the work done on this thesis.

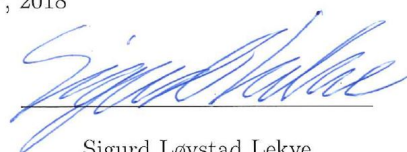
We would also like to thank Technical Engineer Trond Austad for the assistance provided throughout the experimental work, Dr. Egil Fagerholt for valuable guidance regarding the 3D-DIC analysis and Dr. Torodd Berstad for advising us on the use of LS-DYNA and the computational cluster "Snurre".

Lastly, we would also like to thank our fellow students Benjamin Stavnar Elveli, Mads Bakken Iddberg, Vegard Haraldseid, Christoffer Martinsen, Nikolai Korvald Skaare, Håkon Normann and Morten Lynnebakken for providing a great working environment through inspiring discussions, feedback, and support.

Trondheim, June 11<sup>th</sup>, 2018



Olaf Moriggi Kielland



Sigurd Løvstad Lekve



# Nomenclature

## Abbreviations

|                 |  |
|-----------------|--|
| <i>2D – DIC</i> | Two-Dimensional Digital Image Correlation      |
| <i>3D – DIC</i> | Three-Dimensional Digital Image Correlation    |
| <i>CASA</i>     | Centre for Advanced Structural Analysis        |
| <i>DIS</i>      | Densification Initiation Strain                |
| <i>FSI</i>      | Fluid-Structure Interaction                    |
| <i>IED</i>      | Improvised Explosive Device                    |
| <i>LSTC</i>     | Livermore Software Technology Corporation      |
| <i>NTNU</i>     | Norwegian University of Science and Technology |
| <i>SIMLab</i>   | Structural Impact Laboratory                   |
| <i>SSAB</i>     | Swedish Steel Ltd.                             |
| <i>SSTF</i>     | SIMLab Shock Tube Facility                     |
| <i>TNT</i>      | Trinitrotoluene                                |
| <i>XPS</i>      | Extruded Polystyrene                           |

## Experimental and Numerical Abbreviations

|            |   |
|------------|---|
| <i>S</i>   | Skin component                          |
| <i>SW</i>  | Sandwich component                      |
| <i>Al</i>  | Aluminum front and back skin            |
| <i>AlS</i> | Aluminum front skin and steel back skin |
| 250        | XPS-250 foam core                       |
| 400        | XPS-400 foam core                       |
| 700        | XPS-700 foam core                       |
| <i>P10</i> | 10 <i>bar</i> firing pressure           |
| <i>P15</i> | 15 <i>bar</i> firing pressure           |
| <i>P25</i> | 25 <i>bar</i> firing pressure           |
| <i>P35</i> | 35 <i>bar</i> firing pressure           |
| <i>RM</i>  | Reference Model                         |

|                           |  |
|---------------------------|--|
| $DP$                      | Distance Piece                           |
| $PS$                      | Pre-stress                               |
| $DD$                      | Density-dependent                        |
| <b>Greek Symbols</b>      |  |
| $\alpha$                  | Foam shape factor                        |
| $\alpha_2, \beta, \gamma$ | Deshpande-Fleck model parameters         |
| $\chi$                    | Taylor-Quinney coefficient               |
| $\eta$                    | Energy absorption efficiency             |
| $\hat{\sigma}$            | Equivalent stress                        |
| $\hat{\varepsilon}$       | Equivalent strain                        |
| $\kappa$                  | Thread geometry and friction coefficient |
| $\Lambda$                 | Hopkinson-Cranz scale factor             |
| $\nu$                     | Poisson's ratio                          |
| $\omega$                  | Damage parameter                         |
| $\rho$                    | Density                                  |
| $\rho_f$                  | Foam density                             |
| $\rho_{f0}$               | Foam base material density               |
| $\sigma$                  | Cauchy stress tensor                     |
| $\sigma'$                 | Deviatoric stress                        |
| $\sigma_0$                | Yield stress                             |
| $\sigma_e$                | Engineering stress                       |
| $\sigma_m$                | Mean stress                              |
| $\sigma_p$                | Plateau stress                           |
| $\sigma_t$                | True stress                              |
| $\sigma_{c0}$             | Collapse initiation stress               |
| $\sigma_{d0}$             | Densification initiation stress          |
| $\sigma_{eq}$             | Equivalent von Mises stress              |
| $\sigma_{kk}$             | Sum of principal stresses                |
| $\varepsilon$             | Strain                                   |
| $\varepsilon_e$           | Engineering strain                       |
| $\varepsilon_t$           | True strain                              |
| $\varepsilon_{c0}$        | Collapse initiation strain               |
| $\varepsilon_{d0}$        | Densification initiation strain          |

|                            |                                   |
|----------------------------|-----------------------------------|
| $\varepsilon_d$            | Densification strain              |
| $\varepsilon_{el}$         | Elastic strain                    |
| $\varepsilon_{pl}$         | Plastic strain                    |
| $\varphi$                  | Bolt diameter                     |
| <b>Latin Symbols</b>       |                                   |
| $\dot{p}$                  | Equivalent plastic strain rate    |
| $\dot{p}^*$                | Dimensionless plastic strain rate |
| $A_0$                      | Initial area                      |
| $A_c$                      | Contact area                      |
| $b$                        | Exponential decay coefficient     |
| $C_0, C_1, n$              | Power law constants               |
| $C_1, Q_1, C_2, Q_2, c, m$ | Johnson-Cook model constants      |
| $C_p$                      | Specific heat                     |
| $E$                        | Young's modulus                   |
| $E_{int}^0$                | Initial internal energy           |
| $E_{kin}^0$                | Initial kinetic energy            |
| $E_{damp}$                 | Damping energy                    |
| $E_{EXP}$                  | Energy released by an explosive   |
| $E_{hg}$                   | Hourglass energy                  |
| $E_{int}$                  | Internal energy                   |
| $E_{kin}$                  | Kinetic energy                    |
| $E_{rw}$                   | Rigid wall energy                 |
| $E_{si}$                   | Sliding energy                    |
| $E_{TNT}$                  | Energy released by TNT            |
| $E_{total}$                | Total energy                      |
| $F$                        | Normal force                      |
| $f$                        | Yield function                    |
| $F_p$                      | Pre-tensioning force              |
| $i_{r+}$                   | Positive specific impulse         |
| $L$                        | Length                            |
| $L_0$                      | Initial length                    |
| $M$                        | Bending moment                    |
| $M_t$                      | Initial torque                    |

|                        |                                    |
|------------------------|------------------------------------|
| $N$                    | Normal force                       |
| $P$                    | Pressure                           |
| $p$                    | Equivalent plastic strain          |
| $P_a$                  | Atmospheric pressure               |
| $P_r$                  | Reflected pressure                 |
| $P_{so}$               | Incident pressure                  |
| $R$                    | Stand-off distance                 |
| $R(\hat{\varepsilon})$ | Strain hardening                   |
| $R(p)$                 | Isotropic hardening                |
| $T$                    | Temperature                        |
| $t$                    | Time                               |
| $T^*$                  | Normalized temperature             |
| $t_+$                  | Positive duration of pressure      |
| $t_-$                  | Negative duration of pressure      |
| $T_0$                  | Reference temperature              |
| $t_a$                  | Time after explosion               |
| $T_m$                  | Melting temperature                |
| $T_r$                  | Room temperature                   |
| $u$                    | Material point displacement        |
| $v_p$                  | Plastic coefficient of contraction |
| $W_c$                  | Fracture parameter                 |
| $W_{EXP}$              | Weight of explosive                |
| $W_{ext}$              | External work                      |
| $W_{TNT}$              | Equivalent TNT weight              |
| $Y$                    | Yield stress                       |
| $Z$                    | Scaled distance                    |

# Contents

|  |            |
|--|------------|
| <b>Abstract</b>                                  | <b>i</b>   |
| <b>Acknowledgements</b>                          | <b>iii</b> |
| <b>Nomenclature</b>                              | <b>v</b>   |
| <b>1 Introduction</b>                            | <b>1</b>   |
| 1.1 Motivation . . . . .                         | 1          |
| 1.2 Scope . . . . .                              | 2          |
| <b>2 Theory</b>                                  | <b>3</b>   |
| 2.1 Blast Phenomenon . . . . .                   | 3          |
| 2.1.1 Explosions . . . . .                       | 3          |
| 2.1.2 Blast Loading . . . . .                    | 6          |
| 2.1.3 Blast Loads in Structural Design . . . . . | 7          |
| 2.1.4 Structural Response . . . . .              | 10         |
| 2.1.5 Fluid-structure Interaction . . . . .      | 11         |
| 2.2 SIMLab Shock Tube Facility . . . . .         | 12         |
| 2.2.1 Design . . . . .                           | 12         |
| 2.2.2 Shock Wave . . . . .                       | 14         |
| 2.3 Digital Image Correlation . . . . .          | 17         |
| 2.4 Foam . . . . .                               | 18         |
| 2.4.1 Mechanical Properties . . . . .            | 18         |
| 2.5 Constitutive Models . . . . .                | 20         |
| 2.5.1 Foam . . . . .                             | 20         |
| 2.5.2 Aluminum and Steel . . . . .               | 21         |
| 2.6 State-of-the-Art . . . . .                   | 23         |
| 2.6.1 Sandwich Structures . . . . .              | 23         |
| 2.6.2 Foam Materials . . . . .                   | 25         |
| <b>3 Preliminary Numerical Work</b>              | <b>27</b>  |
| 3.1 LS-DYNA . . . . .                            | 27         |
| 3.2 Reference Model . . . . .                    | 28         |
| 3.3 Experimental Firing Pressure . . . . .       | 31         |
| 3.3.1 Aluminum Skins . . . . .                   | 32         |
| 3.3.2 Aluminum and Steel Skins . . . . .         | 33         |
| 3.4 Boundary Conditions . . . . .                | 34         |
| 3.5 Pre-stress . . . . .                         | 36         |
| 3.6 Friction . . . . .                           | 37         |
| 3.7 Mesh Sensitivity . . . . .                   | 38         |
| 3.8 Main Findings . . . . .                      | 40         |



|          |  |           |
|----------|--|-----------|
| <b>4</b> | <b>Material Study</b>                                      | <b>41</b> |
| 4.1      | Aluminum . . . . .   | 41        |
| 4.1.1    | Digital Image Correlation . . . . .                        | 42        |
| 4.1.2    | Material Model . . . . .                                   | 42        |
| 4.1.3    | Elastic Properties . . . . .                               | 43        |
| 4.1.4    | Plastic Properties . . . . .                               | 45        |
| 4.1.5    | Numerical Validation . . . . .                             | 46        |
| 4.2      | Steel . . . . .  | 48        |
| 4.3      | Foam . . . . .   | 49        |
| 4.3.1    | Material Parameters . . . . .                              | 49        |
| 4.3.2    | Numerical Validation . . . . .                             | 49        |
| 4.3.3    | Plastic Properties . . . . .                               | 51        |
| 4.3.4    | Density-Dependent Model . . . . .                          | 52        |
| 4.4      | Main Findings . . . . .                                    | 56        |
| <b>5</b> | <b>Experimental Work</b>                                   | <b>57</b> |
| 5.1      | Experimental Setup and Program . . . . .                   | 57        |
| 5.2      | Three-Dimensional Digital Image Correlation . . . . .      | 60        |
| 5.3      | Results . . . . .  | 62        |
| 5.3.1    | Skins - Aluminum . . . . .                                 | 63        |
| 5.3.2    | Sandwich Panels - Aluminum Skins . . . . .                 | 64        |
| 5.3.3    | Skins - Aluminum and Steel . . . . .                       | 66        |
| 5.3.4    | Sandwich Panels - Aluminum and Steel Skins . . . . .       | 67        |
| 5.3.5    | Pressure Load - Aluminum Skins . . . . .                   | 68        |
| 5.3.6    | Pressure Load - Aluminum and Steel Skins . . . . .         | 69        |
| 5.3.7    | Midpoint Displacement - Aluminum Skins . . . . .           | 71        |
| 5.3.8    | Midpoint Displacement - Aluminum and Steel Skins . . . . . | 73        |
| 5.3.9    | Scanned Deformation Profiles . . . . .                     | 75        |
| 5.4      | Previous Study . . . . .                                   | 77        |
| 5.4.1    | Results . . . . .  | 78        |
| 5.5      | Main Findings . . . . .                                    | 82        |
| <b>6</b> | <b>Numerical Work</b>                                      | <b>83</b> |
| 6.1      | Updated Material Parameters for Aluminum . . . . .         | 83        |
| 6.2      | Validation of Reference Model . . . . .                    | 85        |
| 6.2.1    | Pressure Load . . . . .                                    | 85        |
| 6.2.2    | Midpoint Displacement - Aluminum Skins . . . . .           | 87        |
| 6.2.3    | Midpoint Displacement - Aluminum and Steel Skins . . . . . | 89        |
| 6.2.4    | Deformation Profiles - Aluminum Skins . . . . .            | 90        |
| 6.2.5    | Deformation Profiles - Aluminum and Steel Skins . . . . .  | 92        |
| 6.3      | Further Numerical Results . . . . .                        | 93        |
| 6.3.1    | Foam Compression . . . . .                                 | 93        |
| 6.3.2    | Strain . . . . .   | 97        |
| 6.3.3    | Energy Absorption . . . . .                                | 100       |
| 6.3.4    | Specific Energy Absorption . . . . .                       | 102       |
| 6.3.5    | Reaction Force . . . . .                                   | 104       |
| 6.4      | Parameter Study . . . . .                                  | 106       |
| 6.4.1    | Density . . . . .  | 106       |
| 6.4.2    | Thickness . . . . .  | 111       |
| 6.4.3    | Constant Mass . . . . .                                    | 114       |

|          |  |            |
|----------|--|------------|
| 6.5      | Main Findings . . . . .                        | 117        |
| 6.5.1    | Validation of Reference Model . . . . .        | 117        |
| 6.5.2    | Further Numerical Results . . . . .            | 117        |
| 6.5.3    | Parameter Study . . . . .                      | 118        |
| <b>7</b> | <b>Summary and Discussion</b>                  | <b>119</b> |
| 7.1      | Preliminary Study . . . . .                    | 119        |
| 7.2      | Material Tests . . . . .                       | 120        |
| 7.3      | Component Tests . . . . .                      | 121        |
| 7.4      | Numerical Work . . . . .                       | 123        |
| <b>8</b> | <b>Conclusion</b>                              | <b>125</b> |
| <b>9</b> | <b>Further Work</b>                            | <b>127</b> |
| <b>A</b> | <b>Measurements of Foam Density</b>            | <b>133</b> |
| <b>B</b> | <b>Component Test</b>                          | <b>135</b> |
| <b>C</b> | <b>Parameter Study</b>                         | <b>147</b> |
| C.1      | Foam Density . . . . .                         | 148        |
| C.2      | Thickness . . . . .                            | 153        |
| C.3      | Thickness - Alternative Presentation . . . . . | 158        |
| C.4      | Constant Mass . . . . .                        | 163        |



# Chapter 1

## Introduction

### 1.1 Motivation

Explosions are a complex phenomenon that can be caused by natural reactions, by accidents or by attacks. For either case, it is desired to protect both human lives and critical infrastructure during the accidental or intentional explosive detonation. Many precautionary measures can contribute to protective solutions, one of these are a reinforcement, enhancement or structural design to protect the building mass exposed to an explosion. Conventionally structures meant to protect against explosives have been constructed with massive concrete or steel elements, which tend to become large, heavy and immobile. To reduce the size, weight and increase the mobility of protective structures, smarter designs incorporating more lightweight materials must be utilized to obtain the same protective capabilities. A proposed solution is the use of sandwich components, which combines the high strength and ductility of materials such as aluminum and steel with the excellent energy absorption properties of foam materials. A well-designed sandwich panel absorbs significant quantities of energy and transfers little force to the boundaries of the panel, and keeps the deformation of the back skin of the component low. This results in an efficient energy absorbent and a versatile protective structure.

Knowledge of the structural behavior of different sandwich configurations under a variation of blast loading scenarios is vital for a meaningful and efficient choice of protective structures. This knowledge can be obtained through experimental programs focusing on the mechanical behavior of sandwich panels. However, it is also valuable in terms of saving time and cost to be able to accurately investigate and document the structural response of the panels numerically.

## 1.2 Scope

The scope of this thesis is the experimental and numerical investigation and documentation of the mechanical response of sandwich configurations exposed to various blast load intensities. A brief introduction to the theory behind foam materials, aluminum and steel, the blast phenomenon, digital image correlation, the shock tube facility, and the state-of-the-art of blast loading on sandwich components are presented. A preliminary study was conducted with the aim to establish and evaluate a reference model for further numerical work, establish a meaningful firing pressure range for the experimental program and to evaluate and compare different boundary conditions for the sandwich components in question.

The materials of interest in this thesis are the aluminum alloy AA1050-H14, DOCOL 600DL steel, and XPS foam, with an extra focus on XPS-250, XPS-400, and XPS-700. Material tests for the aluminum alloy AA1050-H14 were conducted to accurately determine the material parameters for the aluminum material model. Nine uniaxial tension tests were performed on dog bone specimens, with three tests in 0-degree, 45-degree and 90-degree loading direction relative to the rolling direction of the aluminum. Material parameters for DOCOL 600DL steel has been thoroughly studied in previous work [1, 2] and necessary material parameters were obtained from a study by Holmen et al. [1]. Data from compression tests of the XPS-250, XPS-400, and XPS-700 were obtained from a study performed by Sigurdsson [3] to validate numerical compression models, investigate the densification initiation strain and construct a density-dependent material model.

Experiments were performed in the shock tube facility at Structural Impact Laboratory (SIM-Lab), Norwegian University of Science and Technology (NTNU), ensuring a controlled and repeatable environment of blast load scenarios. Multiple sandwich configurations were tested, where the blast-exposed area of the sandwich panels were  $300 \times 300 \text{ mm}^2$ . The sandwich panels were composed of a front skin, a foam core, and a back skin with nominal thicknesses of 0.8, 50.0 and 0.8  $\text{mm}$ , respectively. Two skin configurations were used in the tests; one with a front and back skin of AA1050-H14 aluminum, and another with a front skin of AA1050-H14 aluminum and a back skin of DOCOL 600DL steel. Both skin configurations were tested with foam cores of XPS-250, XPS-400, and XPS-700, with nominal densities of 33, 37 and 50  $\text{kg/m}^3$ , respectively. The aluminum skin configuration was exposed to a nominal firing pressure of 10 and 15  $\text{bar}$ , and the aluminum and steel configuration was exposed to a nominal firing pressure of 35  $\text{bar}$ . As a reference, both skin configurations were tested without a foam core at various firing pressures. Three-dimensional digital image correlation (3D-DIC) was used to obtain deformation profiles and midpoint displacements for the back skins.

Further numerical work was conducted in the finite element software LS-DYNA, where a reference model was validated through a comparison of experimental and numerical results for pressure histories, midpoint displacement curves, and deformation profiles. To identify trends in the structural behavior and the importance of parameters such as foam density and foam thickness concerning the protective capability, a parametric study was conducted.

# Chapter 2

## Theory

The objective of this thesis spans a vast amount of theoretical concepts and research fields. In this chapter, the essential background theory for this study is introduced, followed by a summary of the state-of-the-art on topics such as the energy absorption capabilities of sandwich structures and the mechanical properties of foam materials.

### 2.1 Blast Phenomenon

The main topic of this thesis is the dynamic response of structures exposed to blast loading, and not the blast phenomenon itself. Regardless, an understanding of the basic concepts related is necessary. This section will give a brief overview of explosions, blast loading and some commonly used methods in structural design with regards to blast loading. This section is mainly an adaptation from parts of work done by Aune [2]. For a more in-depth presentation, the reader is referred to [2].

#### 2.1.1 Explosions

An explosion is defined as a rapid release of energy and categorized based on the way the energy propagates, i.e., if it deflagrates or detonates [4]. Deflagrations are created by low explosives through a slower burning process, while detonations are a rapid and stable chemical reaction created by high explosives where the shock wave travel at supersonic speed. Figure 2.1 shows the pressure-time history of a typical deflagration and detonation wave.

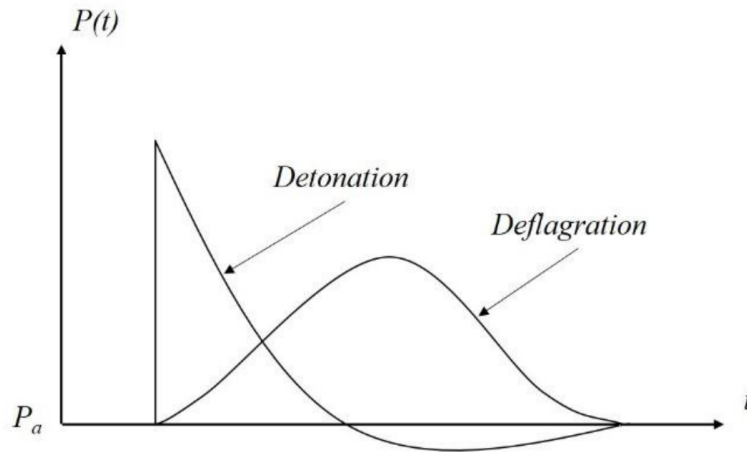


Figure 2.1: Pressure-time history of a typical deflagration and detonation wave [5].

Chemical explosions are the most common source of both accidental and intentional blast loading, which makes chemical explosions the main concern in protective design. However, to study the structural response to chemical explosions, a load of similar magnitude can be generated in a controlled environment where the source of the explosion can be, for example, mechanical. Different types of explosions are listed in Table 2.1.

Table 2.1: Categorization of explosions with corresponding examples.

| Category     | Example                       |
|--------------|-------------------------------|
| Natural      | Volcano                       |
| Astronomical | Supernova                     |
| Chemical     | Dynamite                      |
| Electrical   | High current electrical fault |
| Mechanical   | High pressure container       |
| Nuclear      | Fission/fusion                |

During a detonation in open air, there are three primary blast environments depending on the location of the charge relative to the target. In Figure 2.2 (left) a free air burst blast is shown, where the height above ground of the explosive charge is greater than the projected distance to the target, causing the shock wave to interact with the target before encountering the ground. Figure 2.2 (center) illustrates an air burst blast, where the height is smaller than the projected distance, and the shock wave is reflected by the ground before interacting with the target. The third blast environment is a surface blast where the explosive is located at ground level, as seen in Figure 2.2 (right). In a surface blast the shock wave is immediately reflected from the ground, and typically causes higher pressures than the air burst detonations.

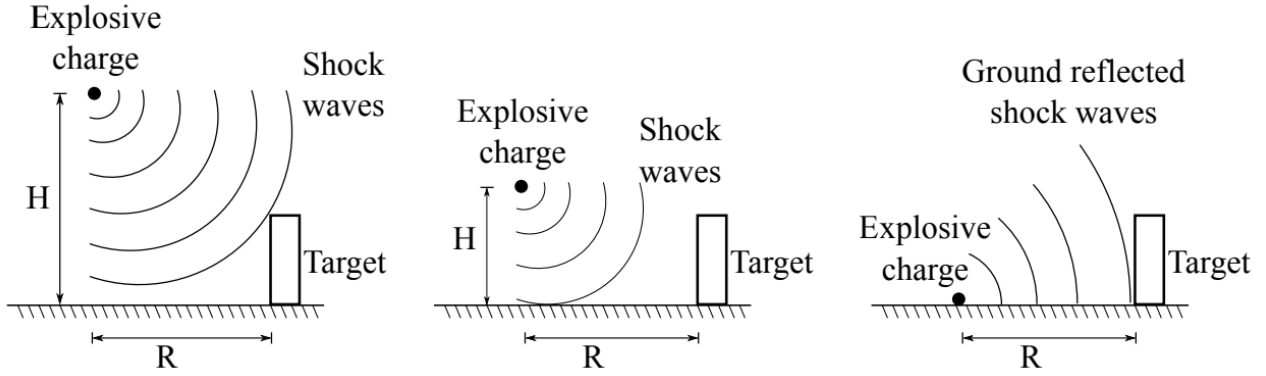


Figure 2.2: Free air burst blast:  $H > R$  (left), air burst blast:  $H < R$  (center) and surface blast:  $H = 0$  (right) [2].

The energy released by a detonation is commonly compared to trinitrotoluene (TNT), known as the TNT equivalent. By calculating the weight of TNT required to produce a particular shock wave of equal magnitude to that produced by a unit weight of another explosive, the efficiency of explosives can be compared. The energy released in the detonation of one metric ton of TNT is defined to be  $4184 \text{ GJ}$ . For example, a ton of C-4 releases  $5860 \text{ GJ}$  of energy, which means that the heat of reaction ratio for C-4 is  $E_{C-4}/E_{TNT} = 5860/4184 = 1.4$ , which means that  $1 \text{ kg}$  of C-4 is equivalent to  $1.4 \text{ kg}$  of TNT. An equivalent weight of TNT,  $W_{TNT}$ , may be calculated for any explosive with a given weight,  $W_{EXP}$ , by using the ratio of the heat produced during the detonation expressed as

$$W_{TNT} = W_{EXP} \frac{E_{EXP}}{E_{TNT}} \quad (2.1)$$

where  $E_{EXP}$  and  $E_{TNT}$  are the energy released by the explosive in question and TNT, respectively. The TNT equivalence is also helpful when comparing the total explosive mass of common blast threats such as person- and vehicle-borne improvised explosive devices (IEDs), as shown in Table 2.2

Table 2.2: The TNT equivalent mass of various IEDs.

| Description    | TNT eq.<br>[kg] |
|----------------|-----------------|
| Pipe bomb      | 2.4             |
| Suicide Vest   | 9.0             |
| Briefcase bomb | 23.0            |
| Car            | 454.0           |
| Passenger van  | 1814.0          |
| Delivery truck | 4536.0          |
| Semi-trailer   | 27216.0         |



## 2.1.2 Blast Loading

During a detonation, a rapid and stable reaction propagates through the explosive material and converts the material into a hot, dense and high-pressure gas. The volume of this gas is the source of the shock wave propagating in the surrounding air. The shock wave is transmitted spherically while the pressure decreases with the cube of the distance shown in Figure 2.3. The decrease in pressure causes a decay in strength and velocity while increasing the duration of the wave.

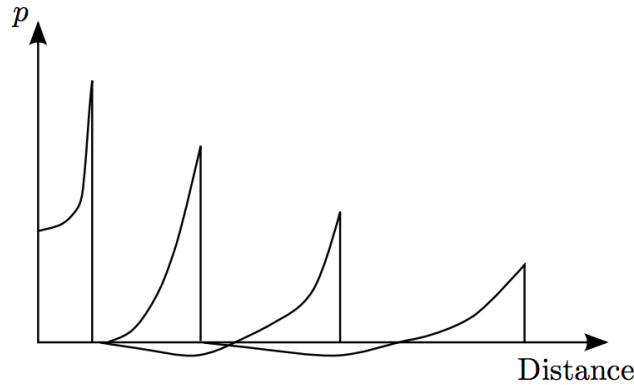


Figure 2.3: Shock wave propagation of a detonation [2].

Figure 2.4 presents an idealized pressure-time history curve of a blast wave often used for design analysis purposes. At a short time after the explosion,  $t_a$ , the pressure increases from the atmospheric pressure,  $P_a$ , to the peak incident overpressure,  $P_{so}$ . The pressure decays exponentially as the shock front expands before reaching the atmospheric pressure to constitute the positive phase of the blast wave. A negative phase follows, causing a reversal of flow back to the explosion center. The positive phase has a duration of  $t_+$  and the negative phase a duration of  $t_-$ .

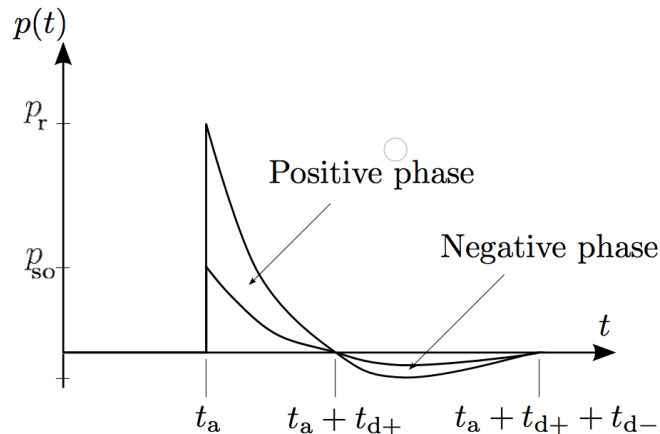


Figure 2.4: Idealized pressure-time curve of a blast wave. Illustration based on [2].

When a blast wave interacts with a structure which is not parallel to the wave direction, the wave is reflected and reinforced. The reflected pressure,  $P_r$ , is always higher than the incident pressure at the same distance from the explosion as shown in Figure 2.4. Therefore, the reflected peak pressure is used for design purposes. Since the positive phase is associated with the most significant structural damages, the negative phase is often neglected. Eq. 2.2

shows the Friedlander equation, which is widely used and represents the idealized positive pressure-time history from Figure 2.4.

$$P(t) = P_a + P_r \left(1 - \frac{t}{t_+}\right) e^{-\frac{bt}{t_+}} \quad (2.2)$$

where  $b$  is the exponential decay coefficient. The specific impulse,  $i_{r+}$ , of the blast wave is given as the area under the positive pressure-time curve expressed as

$$i_{r+} = \int_{t_a}^{t_a+t_+} P_r(t) dt \quad (2.3)$$

With the analytic solution for the Friedlander equation defined as

$$i_{r+} = \frac{P_r t_+}{b^2} [b - 1 + e^{-b}] \quad (2.4)$$

### 2.1.3 Blast Loads in Structural Design

In structural design and blast load predictions a useful tool is the comparison of various explosives at different stand-off distances. The comparison is performed through the application of scaling laws where smaller scale experiments can contribute to the prediction of large-scale explosions. A conventional approach is the use of Hopkinson-Cranz scaling [6, 7], also known as cube-root scaling. The law states that charges of the same material with similar geometry, but of different mass will produce similar blast waves at equal scaled distances and times, given that the charges are detonated in the same atmosphere. If  $R$  is the stand-off distance,  $E$  is the total energy of explosive detonation, and  $W$  is the total weight of the reference explosive source, then the properties of the shock wave for the reference explosion may be related to those arising from another charge of weight,  $W_1$ , with a total released energy,  $E_1$ , located at a distance,  $R_1$ , by the expression.

$$\frac{R}{R_1} = \left(\frac{E}{E_1}\right)^{1/3} = \left(\frac{W}{W_1}\right)^{1/3} \quad (2.5)$$

If  $W_1$  and  $E_1$  are chosen as a unit of mass or energy, the scaled distance  $Z$  and the scale factor  $\Lambda$  are introduced as

$$Z = R_1 = \frac{R}{E^{1/3}} = \frac{R}{W^{1/3}} = \Lambda R \quad (2.6)$$

A schematic presentation of the Hopkinson-Cranz scaling is shown in Figure 2.5, where a transducer located a distance  $R$  from the center of the explosive charge, with characteristic dimension  $d$ , will experience a pressure  $P$ , duration  $t_+$  and a characteristic time history resulting in the specific impulse  $i_+$ . The scaling law then states that a transducer positioned  $\Lambda R$  from the center of a similar explosive charge of the characteristic dimension  $\Lambda d$  would experience a blast wave of similar form with magnitude  $P$ , duration  $\Lambda t_+$  and specific impulse  $\Lambda i_+$ .

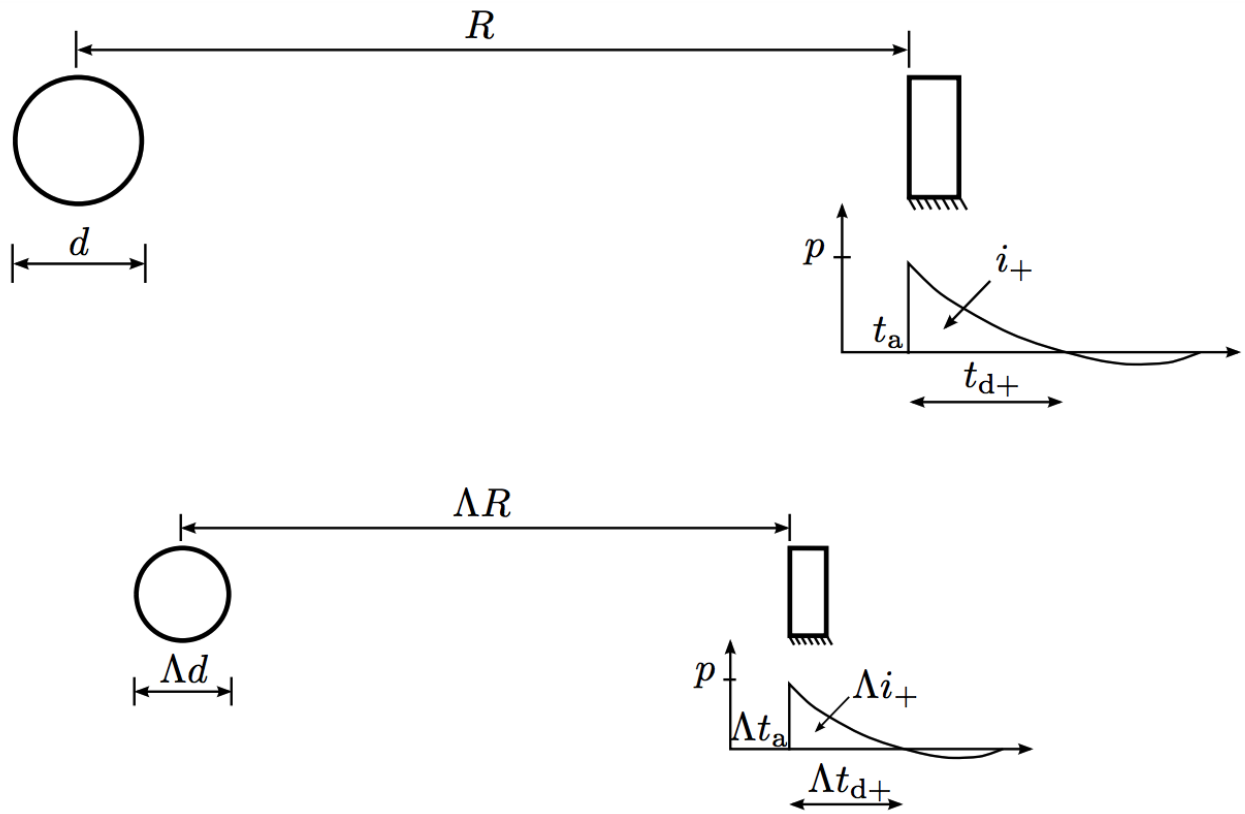


Figure 2.5: Schematic presentation of Hopkinson-Cranz wave scaling [2].

The scaled distance  $Z$  presented is also commonly used to categorize loading scenarios into three categories; close-in detonations defined by  $0 \leq Z \leq 0.5$ , near-field detonations defined by  $0.5 < Z \leq 2.0$  and far-field detonations defined by  $2.0 < Z$ . Contact or close-in detonation are characterized by high magnitudes of pressures in the order of 10 to 30  $GPa$ . These types of detonations typically involve highly localized effects on the structure, with failure modes of the structure categorized by shear, spalling, punching or petalling. Both near-field and far-field detonations are characterized by a more distant blast wave that involves the compression of atmospheric air only. The near-field loading involves a non-uniform spatial distribution of the pressure on the surface and may involve both global and local effects, while far-field detonations generally result in a global response, exclusively. It is noteworthy that the categorizations explained above may be misleading, in the sense that a small charge detonating close to a target may yield a similar  $Z$ -value as a large charge detonating much further away, while their impact on the structural target varies greatly. In blast-resistance design, the categorizations may indicate the necessary complexity in design. Scaled parameters can also be used in structural design concerning blast loading by the application of the empirical equations of Kingery and Bulmash [8], which provide relations to compare several blast parameters.

The research by Kingery and Bulmash, in which experimental data from idealized conditions were gathered and curve-fitted to higher-order polynomial equations for the necessary blast parameters from a TNT equivalent charge using the Hopkinson-Cranz scaling laws, is seen in Figure 2.6. The empirical data is based on detonations of TNT equivalent weights ranging from 1 to 400000  $kg$ . The Kingery and Bulmash relations are an empirical method that presents an idealized representation of blast loads for design purposes and have a significant advantage compared to other methods regarding time consumption. The method can be used as a starting point of a blast load analysis before more elaborate analyses and methods are considered.

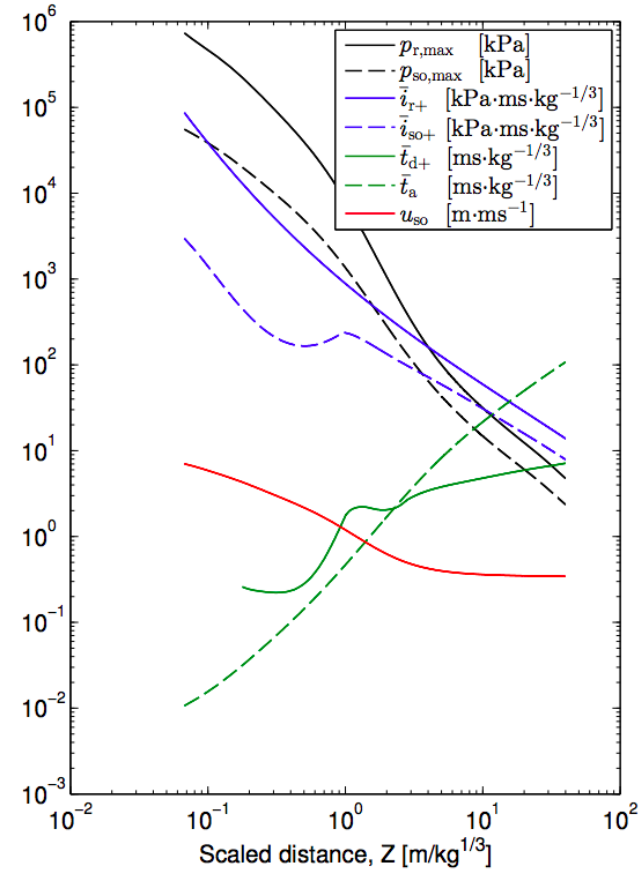


Figure 2.6: Kingery and Bulmash relations for some important blast parameters [8].

In a previous study conducted by Aune [2] in the SIMLab Shock Tube Facility (SSTF) rigid plates were exposed to a firing pressure range similar to the one seen in Table 2.3, where the maximum reflected pressure on the rigid plates was recorded. In this thesis, a similar firing pressure range was investigated, and the approximate TNT equivalents at a standoff distance of 25 *m* for the reflected pressure according to Kingery and Bulmash are listed in Table 2.3. Noticeably, the Kingery Bulmash relations suggests that the firing pressure of 35 *bar* resulting in a maximum reflected pressure of 1187.7 *kPa* is equivalent to the shock wave from a small delivery truck filled with TNT at a standoff distance of 25 *m*.

Table 2.3: The TNT equivalent mass of various SSTF firing pressures at a standoff distance of 25 *m*.

| Firing Pressure<br>[ <i>bar</i> ] | Reflected Pressure<br>[ <i>kPa</i> ] | TNT eq.<br>[ <i>kg</i> ] |
|-----------------------------------|--------------------------------------|--------------------------|
| 10                                | 462.6                                | 836.5                    |
| 15                                | 620.5                                | 1139.3                   |
| 25                                | 825.9                                | 1526.0                   |
| 35                                | 1187.7                               | 2194.3                   |

### 2.1.4 Structural Response

Flexible structures exposed to various intensities of blast loading display different dynamic responses. Three damage modes were identified, illustrated in Figure 2.7, by Menkes and Opta [9], Teeling-Smith and Nurick [10] and Olson et al. [11] for clamped aluminum beams, clamped circular plates and clamped square plates, respectively. Mode I shows large inelastic deformations, Mode II displays tensile tearing at the supports and Mode III is caused by shear failure at the supports. Mode I is observed up to a critical value of impact velocities, where a further increase of the impact velocities is observed to trigger Mode II. Further, when another critical value is reached Mode III will be triggered [2].

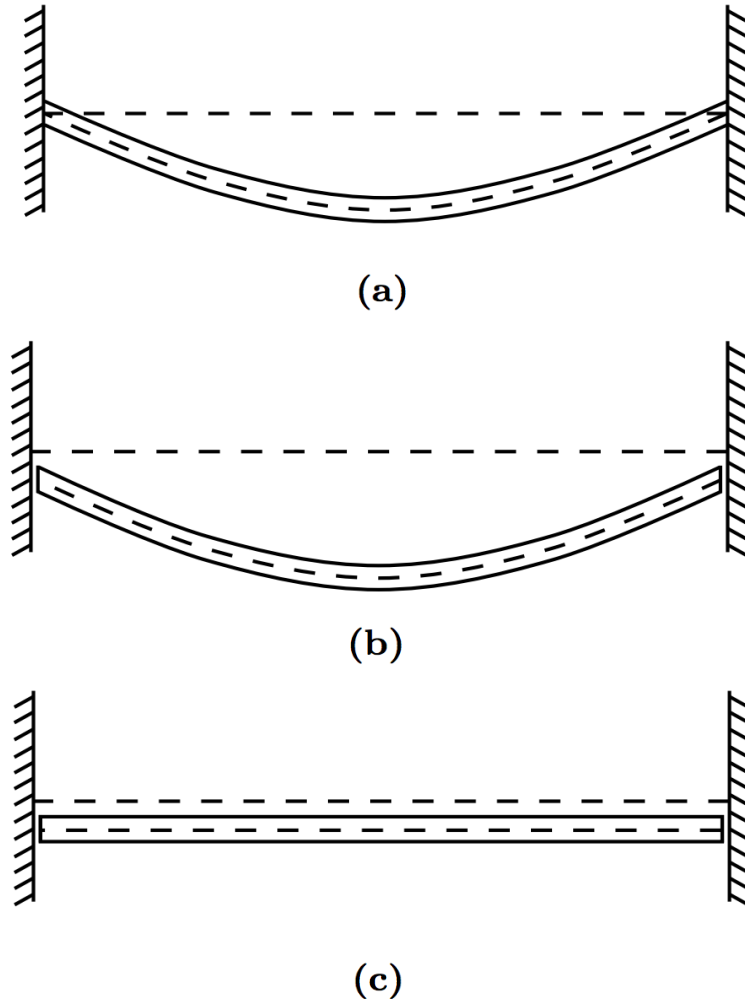


Figure 2.7: Failure modes for impulsively loaded beams and plates: (a) Mode I - Large inelastic deformation, (b) Mode II - Tensile tearing at supports and (c) Mode III - Shear failure at supports [2].

### 2.1.5 Fluid-structure Interaction

Structures exposed to blast loading may experience significant blast-structure interaction. This interaction occurs when the structural surface being impacted by the blast wave and the wave itself are not parallel. The impacted structure typically behaves like either a rigid or a deformable surface. Fluid-structure interaction (FSI) is observed when the impacted surface is allowed to deform or move [2]. Therefore, FSI effects are more pronounced for flexible structures. Taylor [12] suggested that lightweight structures undertake less momentum compared to a heavier more rigid structure when exposed to the same blast intensity. In other words, the motion of the reflecting surface reduces the pressure acting on it. Previous research has shown that FSI effects can reduce the blast load acting on the structure, with this effect being more pronounced for large deformations [2]. The reduction of the blast load is related to both the induced velocity of the impacted structure and the deformed shape. Lightweight and flexible structures experience both a higher induced velocity and a dynamic response as seen in Figure 2.7a) with a possible overlapping of the dynamic response and the positive phase duration. By the utilization of ductile materials in the design of flexible structures, which allows finite deformations, FSI may reduce the transmitted impulse and serve as alternative load paths. Given that the structural members can sustain the deformation without experiencing failure the blast wave is partially absorbed through various deformation mechanisms [2].

Methods and procedures used in blast-resistance design can vary considerably in complexity, accuracy, computational cost and efficiency. Regarding explicit non-linear finite element analysis, an uncoupled approach is a widely preferred procedure in today's blast-resistance design. Blast load construction is then often done from empirical data or through computational fluid dynamics in a Eulerian reference system. This provides a spatial and temporal pressure distribution over the problem boundary, which is applied to computational structural dynamics to calculate the corresponding dynamic response. The fundamental assumption of the uncoupled approach is that the behavior of the blast loading is not changed due to structural motion and visa versa. Considering non-linear effects in both geometry and material behavior, an uncoupled approach may yield undesired deviations in numerical simulations. In a study conducted by Børvik et al. [13], considerable variations in the predictive capabilities of uncoupled and coupled methods in typical industrial applications were observed. While coupled methods have the potential of increased accuracy regarding dynamic response, an uncoupled approach is considered to provide conservative and sufficiently accurate results, while keeping computational costs low.

## 2.2 SIMLab Shock Tube Facility

In this thesis, the blast loading scenarios in the experimental program were created in the SIMLab Shock Tube Facility (SSTF), which will be briefly described in this section. For an in-depth description, the reader is referred to work by Aune et al. [14]. The use of a shock tube to investigate the response of structures in blast environments is a practically and experimentally valuable alternative to explosive detonations. The shock tube produces shock waves under controlled laboratory conditions, where the shock strength is determined by the initial conditions. Properties of the planar shock wave acting on a structure can be studied by placing a test object inside or at the end of the tube. It has been verified by several researchers at the Department of Structural Engineering at NTNU, that the shock tube can produce repeatable uniform shock waves that have similar pressure-time characteristics as an actual far field explosive detonation [2, 3, 15, 16, 17, 18].

### 2.2.1 Design

The SSTF is made up of several modular sections, as illustrated in Figure 2.8 and 2.10a, joined together using bolted connections at the end flanges of each part. Between the parts, rubber O-rings are used to ensure sealing at the joints. Each part is carried by a support structure on steel wheels for convenient assembly and disassembly of the tube. This provides flexibility in varying the length of the driven section. The SSTF is made from P355NH stainless steel and is designed according to ISO-2768-1. The overall length of the tube is 18.36 *m* and is divided into the following sections:

- The driver section
- The firing section
- The driven section
- The window section
- Expansion 1
- Expansion 2
- The dump tank

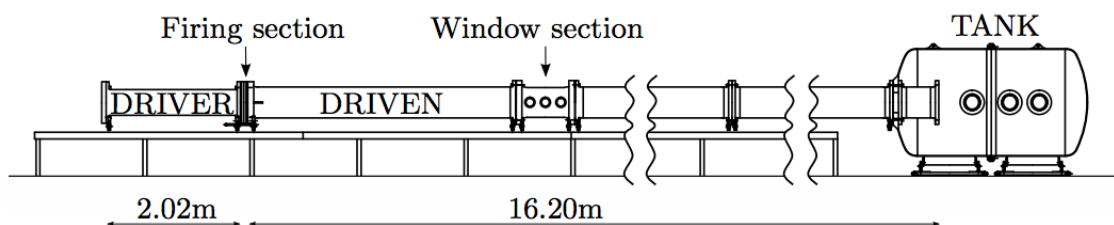


Figure 2.8: Illustration of the SSTF sections seen from the side [2].

The driver section has a total length of 2.02 *m* and has an inner diameter of 0.331 *m*. It is possible to use aluminum inserts to vary the length of the section in increments of 0.25 *m*.

Next to the driver section is the firing section with a length of 0.14 m. The firing section is made up of several intermediate pressure chambers separated by membranes, shown in Figure 2.10b. These membranes are made from the polyester Melinex, but membranes of other materials are also available. Membranes of different thickness and capacity can be chosen and combined depending on the desired firing pressure. Two of the intermediate pressure chambers are pressurized simultaneously in the firing section with approximately  $2/3$  and  $1/3$  of the driver pressure. This creates a stepwise pressure differential between the driver section and the driven section, as seen in Figure 2.9. When the driver section reaches the desired pressure, the membranes are ruptured to initialize the shock wave. To rupture the membranes, the pressure chamber closest to the driver section is vented. This results in the pressure differential loading the membranes past their capacity. However, venting causes a slight increase in the volume of the driver section, which further leads to a slight drop in driver pressure. It is, therefore, necessary to pressurize the driver section higher than the desired firing pressure.

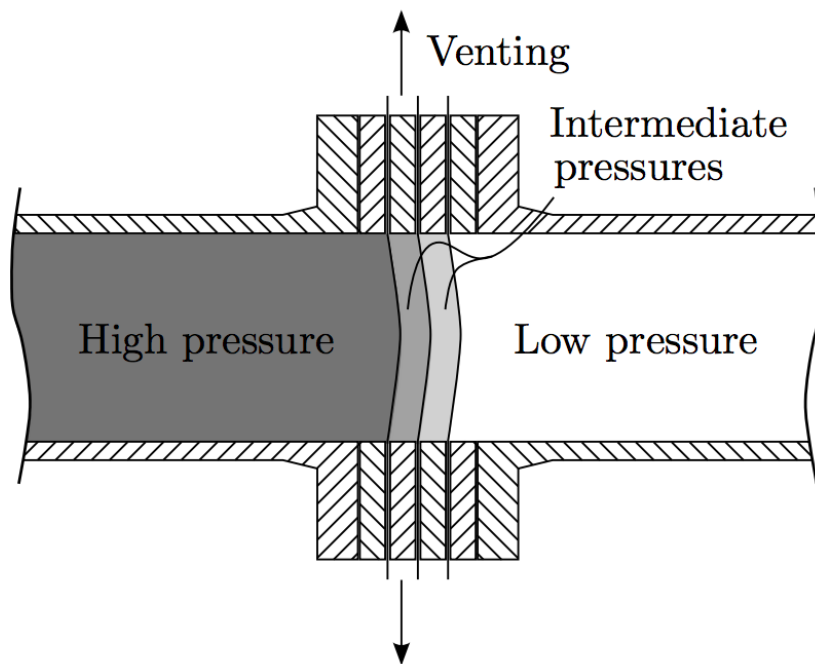


Figure 2.9: Sketch of cross-section of SSTF at firing section immediately before firing [2].

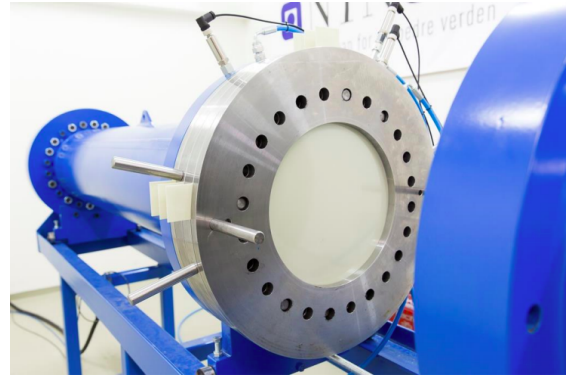
The driven section starts out as a circular tube, with an inner diameter of 0.331 m. Along the next 0.6 m the cross-section of the tube transitions into a square cross-section with inner dimensions of 0.3 m x 0.3 m, capsuled by the circular outer. The transition was made to enable the installation of test objects in threaded holes in the tube floor, and to accommodate plane parallel windows in the following window section, which simplifies the use of optical techniques, as seen in Figure 2.10d. The window section is used to investigate the interaction and flow around objects. The driven section is extended beyond the window section by extension 1 and extension 2.

The driven section ends with a clamping rig for test specimens inside of a dump tank, as seen in Figure 2.10c. The tank has a volume of 5.1 m<sup>3</sup> with an internal diameter of 1.6 m. The increase in volume enables the mounting of larger test specimens exposed to localized blast loading at the end of the driven section. The increase in volume also lowers the pressure and contains the shock wave to protect surrounding equipment and personnel.

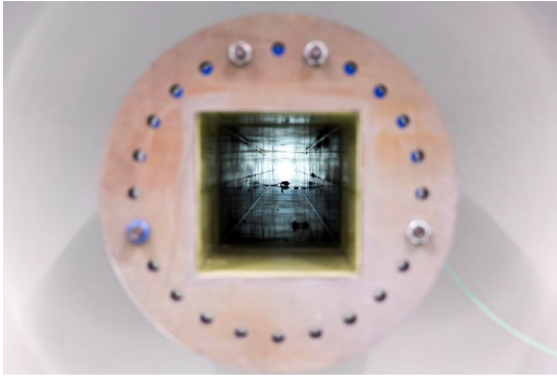




(a) Overview of S STF, seen from the driver section



(b) Firing section, seen from driven section



(c) Internal cross-section of driven section



(d) Window section

Figure 2.10: Pictures of SIMLab Shock Tube Facility [2].

## 2.2.2 Shock Wave

When the membranes rupture, a uniform shock wave starts propagating down the driven section of the tube. The development of the shock wave is illustrated in Figure 2.11. Figure 2.11a shows a simplified shock tube with a driver section with constant pressure,  $p_4$ , a firing section with one membrane and a driven section with constant pressure,  $p_1$ . In Figure 2.11b the pressure differential just before the membranes rupture is illustrated. When the membranes are loaded past their capacity the incident shock wave is released into the driven section as seen in Figure 2.11c. The pressure behind the shock front,  $p_2$ , is moving down the tube with the contact surface between the gas in the driver and the driven section moving in the same direction with a lower velocity. A rarefaction moves in the opposite direction of the shock wave and is reflected in the back of the driver section, as seen in Figure 2.11d. This results in the rarefaction moving in the same direction as the shock wave with pressure  $p_3$  behind it. When the incident shock wave reaches the end of the driven section, the wave is reflected, and we get a reflected shock wave moving back towards the driver section with the pressure behind it increased to  $p_5$ , as illustrated in Figure 2.11e.

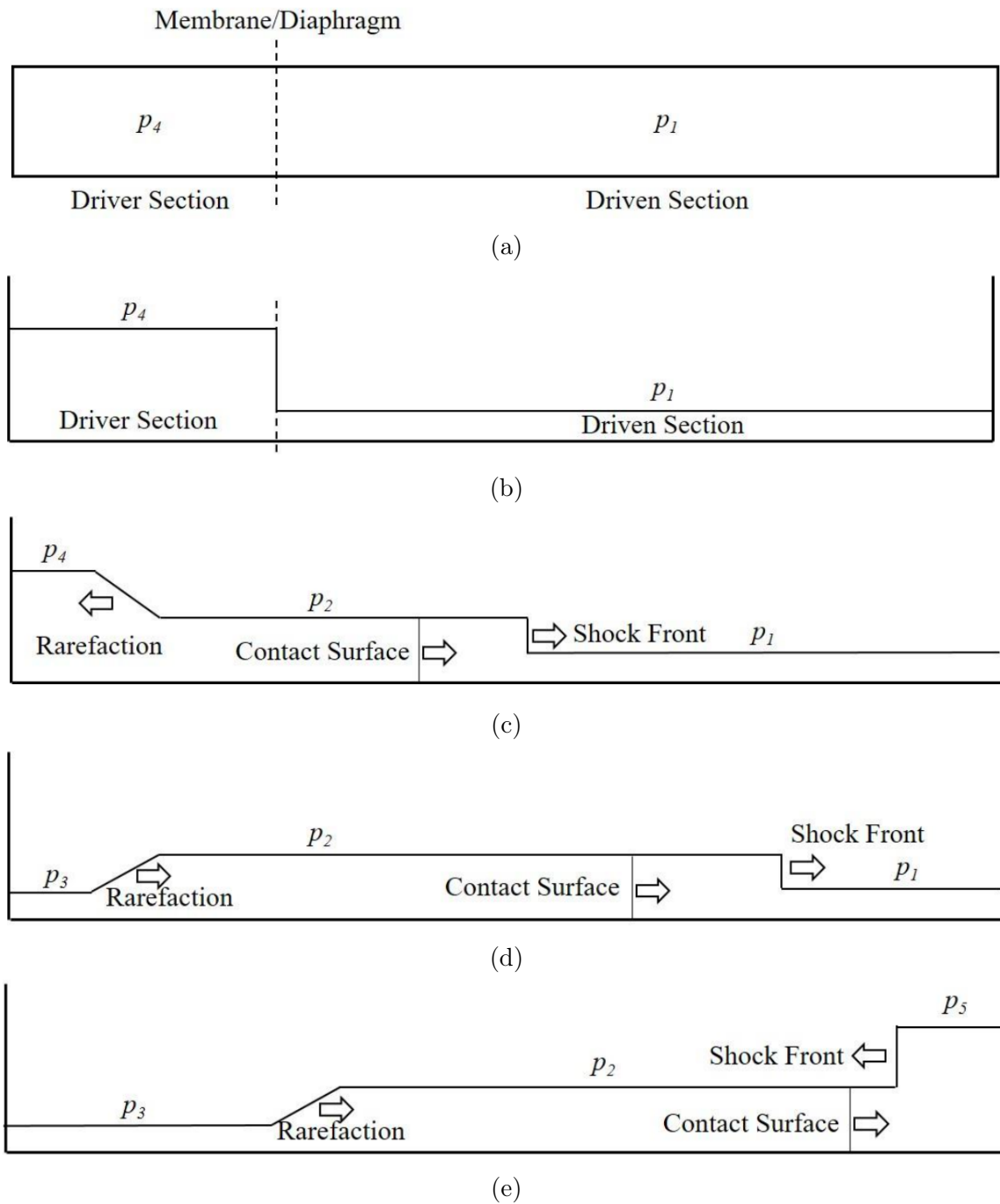


Figure 2.11: Shock wave propagation in a shock tube [19].

The interaction between reflected waves and wavefronts causes pressure peaks throughout the pressure history in the experiment. At high driver pressures, the interactions may result in secondary and tertiary peaks during the positive phase of the pressure-time history, as seen in Figure 2.12.

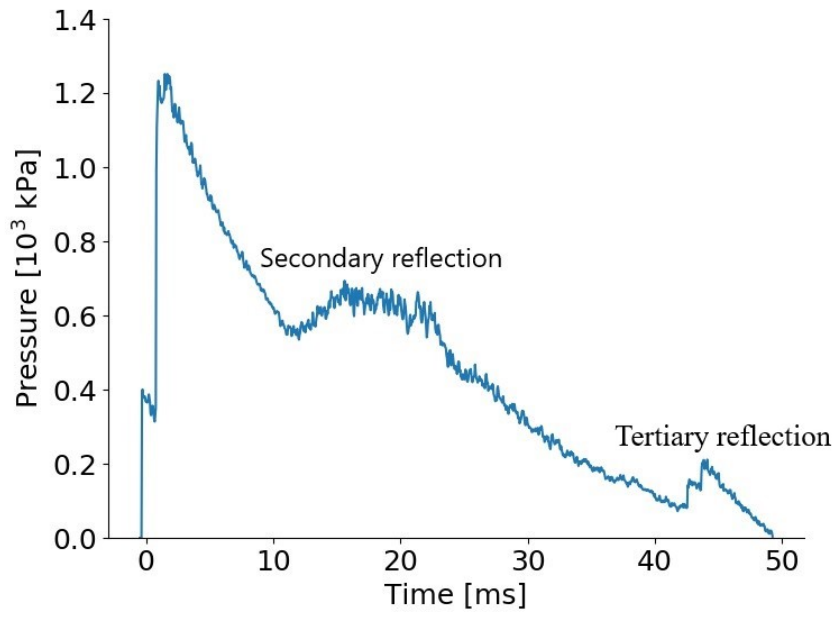


Figure 2.12: Pressure-time history curve with secondary and tertiary reflection in the shock tube.

## 2.3 Digital Image Correlation

Digital Image Correlation (DIC) is a non-contact optical technique for measuring strain and displacement. The accelerated advances of digital storage capacity, computer hardware and high-resolution imaging over the last decade have made DIC a widespread experimental measuring technique. DIC works by comparing digital photographs of a component or test specimen at different stages of deformation. By tracking blocks of pixels, surface displacement can be measured as well as the construction of full-field 2D or 3D deformation vector fields and strain maps. DIC requires the pixel blocks to be unique and random regarding contrast and intensity levels to work properly. Often the photographed materials natural surface texture is sufficient for DIC to work, while in some cases speckle pattern paint is applied to ensure unique and random surface pattern. DIC is mainly a post-processing technique, but can also be applied to live track material points during experiments [20].

High-resolution images taken with high frequency can provide data reflecting the real response of the material. This is an advantage compared to displacement measured by a load cell, which has to be corrected for machine stiffness and only measures the global response of the material. The fact that DIC is a non-contact method also makes it preferable compared to, for example, an extensometer when measuring a material reaching failure. However, large deformations may present difficulties when tracked by DIC.

By using two cameras, DIC can be used to track 3D deformations. For 3D tracking camera angles and camera positions have to be calibrated in advance. During calibration a set of initial images are used to establish a relationship between image coordinates and 3D target coordinates, as shown in Figure 2.13

During post-processing a mesh is applied to the initial configuration of the component, using a DIC software. The mesh is related to the position of individual unique points and greyscale patterns on the material. A tracking algorithm embedded in the DIC software is then used to track the movement of the said unique points from image to image and deform the mesh accordingly. The measured deformations of the mesh provide the deformation and strain outputs. In this thesis the DIC software eCorr [21] developed by E. Fagerholt at SIMLab, NTNU, is used to measure the response of the test specimens during all experiments.

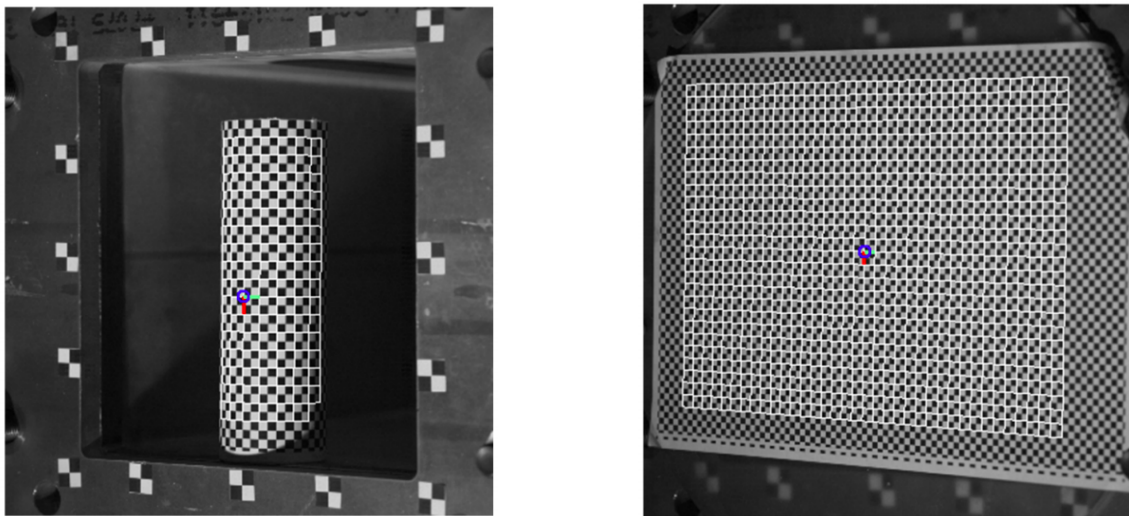


Figure 2.13: Cylindrical calibration target (left) and glass-plate calibration target (right) with meshes where the nodes represent extracted corners, with known target coordinates, used to calibrate camera models [2].

## 2.4 Foam

Foams are three-dimensional cellular materials with either open or closed cell structure [22, 23], as shown in Figure 2.14. While the cells are connected by sharing struts in open cell foams, the cells are connected by sharing walls in closed cell foams. The latter seals the gas inside each cell and makes closed cell foams more rigid than open cell foams [24]. Foams are widely used in energy absorbing applications due to high weight-to-strength ratio and cost efficiency. These are usually metallic and polymeric foams, where compression causes a progressive collapse of the core material - an excellent energy absorbing quality. A common application of foam is in sandwich panels, which traditionally take the form of a structure with a foam core layer encapsulated by face sheets on either side. Sandwich components are widely used in protection, construction, aircraft and automotive businesses due to the combination of high energy absorption and the panels ability to maintain integrity during loading.

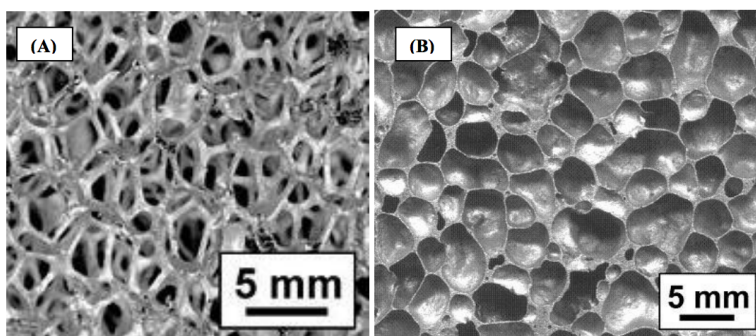


Figure 2.14: Typical microscopic cell structure of open (left) and closed (right) cell foams [25].

### 2.4.1 Mechanical Properties

The behavior of foams subjected to dynamic loading has been investigated in numerous studies and summarized by Sun and Li [24]. Since different notation is applied in different studies, the notation used in this study follows the notation used by Sun and Li.

The compression of foams exhibits three distinct regimes - the pre-collapse, plateau and densification regime as seen in Figure 2.15. During the pre-collapse stage, the stress increases linearly with strain as a result of elastic deformation of cell walls. A local maximum is reached, generally known as the collapse initiation strain,  $\varepsilon_{c0}$ , representing the initiation of the new deformation mechanism of cell wall failure in the plateau stage. Progressive collapse of cell walls is initiated where the stress is relatively constant over a large strain range that ends at the densification initiation strain,  $\varepsilon_{d0}$ . Further compression from the densification initiation strain causes more cell walls to collapse and densify the material further. In this regime, the slope of the stress-strain curve increases rapidly as the strain approaches the asymptote defined by the densification strain,  $\varepsilon_d$ . Figure 2.15 shows a schematic diagram of the stress-strain curve of foam and the presented parameters.

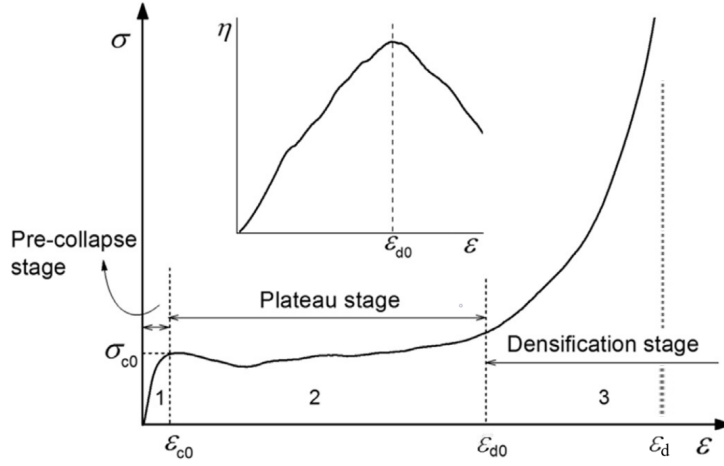


Figure 2.15: Schematic diagram of a foam stress-strain curve under compression loading. Illustration based on [24].

The densification initiation strain can be obtained from the energy absorption efficiency method presented by Li et al. [26], where the energy absorption efficiency,  $\eta$ , is defined as

$$\eta(\varepsilon) = \frac{1}{\sigma(\varepsilon)} \int_0^\varepsilon \sigma(\varepsilon) d\varepsilon \quad (2.7)$$

The densification initiation strain corresponds to the strain at maximum energy absorption efficiency seen in Figure 2.15, i.e

$$\left. \frac{d\eta(\varepsilon)}{d\varepsilon} \right|_{\varepsilon=\varepsilon_{d0}} = 0 \quad (2.8)$$

The average plateau stress,  $\sigma_p$ , can be obtained by energy equivalence in the plateau stage as

$$\sigma_p = \frac{\int_{\varepsilon_{c0}}^{\varepsilon_{d0}} \sigma(\varepsilon) d\varepsilon}{\varepsilon_{d0} - \varepsilon_{c0}} \quad (2.9)$$

Stress oscillation may occur in the plateau stage, and the plateau stage behavior varies for different foams [24]. Strain softening or strain hardening characteristics can also be observed in the plateau stage as seen in Figure 2.16 [26].

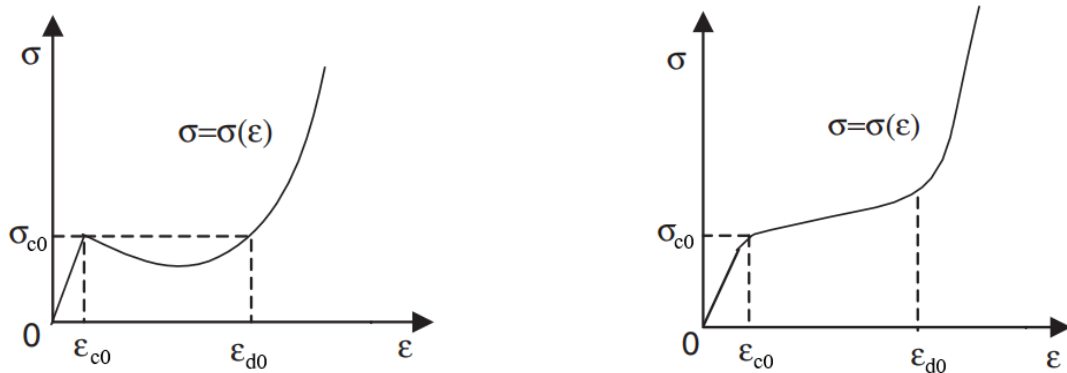


Figure 2.16: Strain softening and hardening characteristics of foams. Illustration based on [26].

## 2.5 Constitutive Models

In this section, the constitutive models applied in numerical simulations for aluminum, steel, and foam are presented. A variation of the Deshpande-Fleck model is utilized for the description of foam behavior, while the description of aluminum and steel is done through a thermoelastic-thermoviscoplastic material model based on the constitutive model of Johnson and Cook.

### 2.5.1 Foam

The material behavior of foam can be described by several models, such as Schreyer et al. [27], Ehlers et al. [28], Miller [29] and Deshpande and Fleck [30]. Several different models are also implemented in LS-DYNA. A selection of these models was validated through a study done by Hanssen et al. [31]. The constitutive model chosen to describe the behavior of the polymeric foam in this study was a variation of the Deshpande-Fleck model, with the inclusion of fracture and a statistical variation of density, suggested and implemented in LS-DYNA by Reyes et al. [32]. The model was chosen for its simplicity and because it has previously been used in similar studies on polymeric foams subjected to dynamic loading [3, 33], which yielded accurate results in numerical validations.

The Deshpande-Fleck model [30] is seen as an extension of von Mises yield criterion, where the yield function depends on both deviatoric and hydrostatic stresses. The yield function,  $f$ , is defined as

$$f = \hat{\sigma} - Y \quad (2.10)$$

where  $Y$  is the yield stress and  $\hat{\sigma}$  is the equivalent stress. The yield stress is defined as

$$Y = \sigma_{c0} + R(\hat{\epsilon}) \quad (2.11)$$

where  $\sigma_{c0}$  is the collapse initiation stress and  $R(\hat{\epsilon})$  is the strain hardening as a function of the equivalent strain  $\hat{\epsilon}$ .

The equivalent stress can be expressed as

$$\hat{\sigma}^2 = \frac{1}{[1 + (\alpha/3)^2]} [\sigma_{eq}^2 + \alpha^2 \sigma_m^2] \quad (2.12)$$

where  $\sigma_{eq}$  is the equivalent von Mises stress,  $\sigma_m$  is the mean stress, and  $\alpha$  is a function describing the shape of the yield surface, as seen in Figure 2.17.  $\alpha$  varies with the plastic coefficient of contraction,  $v_p$ , and is defined as

$$\alpha^2 = \frac{9(1 - 2v_p)}{2(1 + v_p)} \quad (2.13)$$

The equivalent von Mises stress and the mean stress is defined by Eq. 2.14 and 2.15, respectively,

$$\sigma_{eq} = \sqrt{\frac{3}{2} \sigma'_{ij} \sigma'_{ij}} \quad (2.14)$$

$$\sigma_m = \frac{1}{3}\sigma_{kk} \quad (2.15)$$

where  $\sigma'_{ij}$  is the deviatoric stress and  $\sigma_{kk}$  is the sum of the principal stresses. The strain hardening function is expressed as

$$R(\hat{\varepsilon}) = \gamma \frac{\varepsilon}{\varepsilon_d} + \alpha_2 \ln \left[ \frac{1}{1 - (\varepsilon/\varepsilon_d)^\beta} \right] \quad (2.16)$$

where  $\gamma$  is a linear strain-hardening coefficient,  $\alpha_2$  is a non-linear scale factor,  $\beta$  is a non-linear shape factor,  $\varepsilon$  is the true strain and  $\varepsilon_d$  is the densification strain. If the plastic coefficient of contraction is assumed to be zero the analytical expression for the densification strain can be expressed as

$$\varepsilon_d = -\ln \left[ \frac{\rho_f}{\rho_{f0}} \right] \quad (2.17)$$

where  $\rho_f$  is the density of the foam and  $\rho_{f0}$  are the density of the base material.

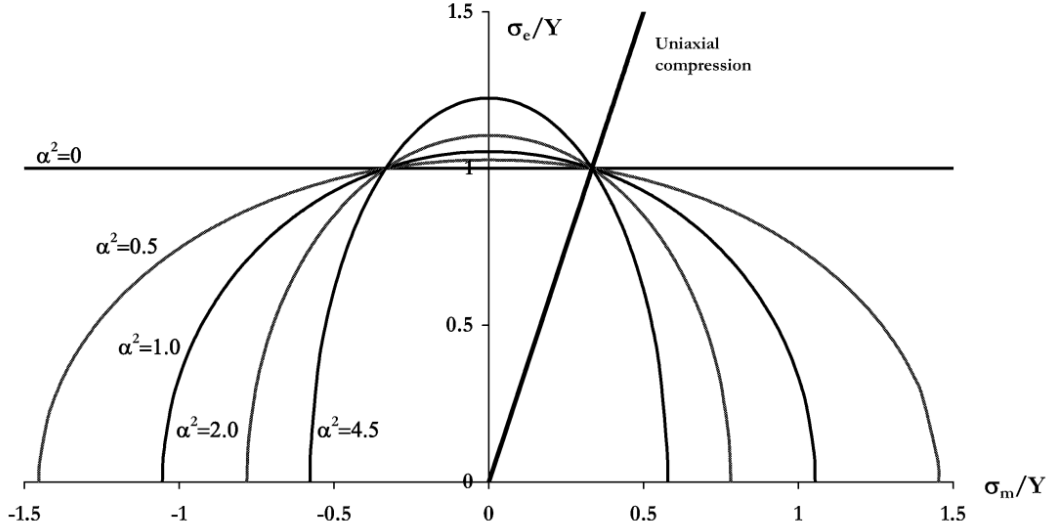


Figure 2.17: Influence of  $\alpha$  on yield surface [32]

## 2.5.2 Aluminum and Steel

The constitutive model chosen to describe the aluminum and steel material was suggested by Børvik et al. [34]. The model is a thermoelastic-thermoviscoplastic material model well suited for the large plastic strains and high strain rates associated with blast loading scenarios. It is based on the constitutive model and fracture strain model of Johnson and Cook [35], and on continuum damage mechanics as proposed by Lemaitre [36]. The model includes von Mises yield criterion, linear thermoelasticity, the associated flow rule, non-linear isotropic strain hardening, strain-rate hardening, temperature softening due to adiabatic heating, isotropic ductile damage, and failure. The Cockcroft-Latham fracture criterion [37] is used to describe fracture.



The definition of the yield function,  $f$ , is

$$f = \sigma_{eq} - (\sigma_0 + R(p)) \quad (2.18)$$

where  $\sigma_0$  is the yield stress,  $R(p)$  is the isotropic hardening and  $\sigma_{eq}$  is the equivalent von Mises stress. The equivalent stress can be expressed as

$$\sigma_{eq} = \left[ \sigma_0 + \sum_{i=1}^2 Q_i (1 - e^{-C_i p}) \right] [1 - T^{*m}] [1 + \dot{p}^*]^c \quad (2.19)$$

where  $p$  is equivalent plastic strain,  $\dot{p}^*$  is a dimensionless strain rate,  $T^*$  is a normalized temperature,  $Q_i$ ,  $C_i$ ,  $c$  and  $m$  are material constants. The dimensionless strain rate is defined as

$$\dot{p}^* = \frac{\dot{p}}{\dot{p}_0} \quad (2.20)$$

where  $\dot{p}_0$  is a user-defined reference strain rate and  $\dot{p}$  is the equivalent plastic strain rate. The normalized temperature is expressed as

$$T^* = \frac{T - T_r}{T_m - T_r} \quad (2.21)$$

where  $T$  is the absolute temperature,  $T_r$  is the room temperature and  $T_m$  is the melting temperature of the material. The first term of the expression for the equivalent stress is a two-term Voce hardening rule. The next term is a temperature correction term, while the last term is a strain rate correction term. Temperature change due to adiabatic heating effects can be expressed as

$$\Delta T = \int_0^p \chi \frac{\sigma_{eq}}{\rho C_p} dp \quad (2.22)$$

where  $\rho$  is the material density,  $C_p$  is the specific heat, and  $\chi$  is the Taylor-Quinney coefficient representing the proportion of plastic work converted into heat. Cockcroft-Latham fracture criterion is widely used to describe ductile fracture [37] and defined as

$$\omega = \frac{1}{W_c} \int_0^p \max(\sigma_1, 0) dp \quad (2.23)$$

where  $\omega$  is the damage parameter,  $W_c$  the fracture parameter and  $\sigma_1$  is the maximum principal stress.  $\sigma_1$  is defined positively in tension and equal zero in compression causing failure only to occur for tensile stresses. Fracture occurs when the damage parameter reaches unity for all integration points in an element, and the element is eroded.

## 2.6 State-of-the-Art

In this section, a summary of selected research done on the energy absorption capabilities of various sandwich configurations is presented. Additionally, studies conducted on the mechanical properties of polymeric foams are summarized.

### 2.6.1 Sandwich Structures

A surge in research on blast resistance and protective capabilities of structural component has been observed in recent years, due to an increased amount of terrorist attacks using explosives against civilian targets. In the broad research field of blast resistance, studies on sandwich components have been conducted on a vast variation and combination of skins and cores, where aluminum foam is a widely used core material in sandwich panels. There are many findings on the increased protective capabilities of a sandwich component compared to single plates. In this section, a variety of studies, and their findings, on sandwich components are presented.

Sandwich configurations constructed with steel skins and aluminum foam cores exposed to impact and blast loading has been studied in various scientific frameworks. Radford et al. [38] studied clamped sandwich panels with aluminum foam cores exposed to mid-span impact of a metal foam projectile. The dynamic response of the sandwich panels was compared to single plates of stainless steel with the same areal mass, as seen in Figure 2.18. It was found that the sandwich panels had a higher shock resistance than the single plates and that there was a positive correlation between shock resistance and the sandwich core thickness. Similarly, Liu et al. [39] studied the performance of sandwich components with aluminum foam cores and steel skins exposed to blast loading. Again, a comparison with single steel plates was carried out, which showed that the peak load was reduced by 60 to 65 % for the sandwich components compared to the single plates.

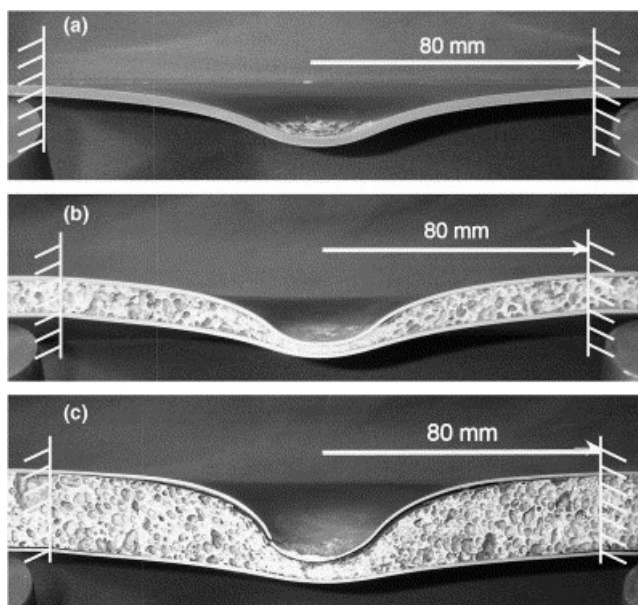


Figure 2.18: Cross-sectional view of single steel plate (top) and sandwich components with aluminum foam cores (center and bottom) exposed to mid-span impact of metal foam projectile [38].

The importance of foam density on blast resistance has also motivated studies on the field of foam-based sandwich components with various densities exposed to blast loading. Hassan et al. [40] found that damage within the sandwich panels became more severe as the density of the foam core was increased. For the lowest density foam, the core did not experience fracture or debonding over the range of loads considered. Instead, the panel absorbed energy through plastic deformation of skins and compression of the foam core. When higher density foams were used, fracture was observed in addition to debonding at the skin-core interface.

Regarding energy absorption, a variation of foam density over the thickness of the core has been researched in a variety of studies. Wang et al. [41] studied the blast resistance of sandwich configurations with composite skins and stepwise graded styrene foam cores. Two configurations were investigated, one configuration with low/middle/high and one with middle/low/high-density layers. It was found that core configured in ascending order outperformed the latter in blast resistance. Significant compression of the foam core was observed in the ascending configuration, while disintegration of the core layers and fracture in the front skin was observed in the other configuration, as seen in Figure 2.19. Aluminum honeycombs are an alternative to foam as an energy absorbing core. Shiqiang et al. [42] investigated the effect of stepwise graded aluminum honeycomb as a sandwich core in a blast resistance capability evaluation, where aluminum was used as skin material. It was found that the blast resistance capability of the sandwich configurations was moderately sensitive to the arrangement of core densities. However, for the graded panels with a descending relative density core arrangement, the plastic energy dissipated in the core and the force attenuation were larger than in the ungraded configuration.

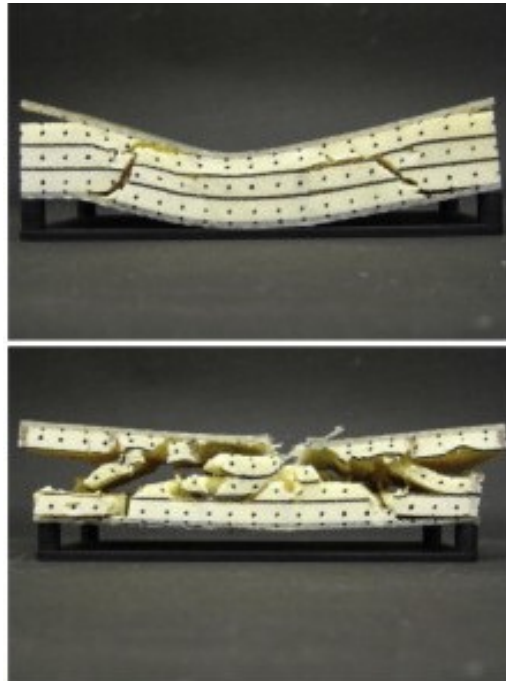


Figure 2.19: Cross-sectional view of sandwich panels with low/middle/high (top) and middle/low/high-density (bottom) foam core configurations exposed to blast loading studied by Wang et al. [41].

Optimizing the blast resistance of a sandwich component is of great interest for protective applications. Qi et al. [43] performed a multi-objective optimization of aluminum foam-cored sandwich panels, with respect to blast resistance. Different combinations of AA2024 T3 aluminum alloy, AS3678-250 mild steel and rolled homogeneous armor steel was used as skins in the panels. It was found that the sandwich component with an aluminum front skin and a rolled homogeneous armor steel back skin outperformed the other sandwich configurations regarding maximum back skin deflection and areal specific energy absorption. Additionally, it was observed that boundary conditions and standoff distance between the explosive and the target surface both had a significant influence on the dynamic response of sandwich panels. Minimizing maximum back skin deflection and maximizing areal specific energy absorption was found to be conflicting goals from the optimization, thus different blast loading scenarios should be considered during the design of such sandwich panels for robust blast resistance.

## 2.6.2 Foam Materials

To be able to optimize and evaluate the protective capabilities of sandwich structures utilizing foam as a core is of importance to understand the mechanical properties of the foam material under the given blast load scenarios. In this thesis extruded polystyrene (XPS) foam will be used as a core material and is therefore of great interest. There is, however, a lack of research conducted on the mechanical properties of XPS. Considering the lack of research on XPS foam, findings from research on other polymeric foams with transferable properties and concepts will be presented.

The foam core of a sandwich component may be under high strain rate conditions during blast loading. A wide range of studies suggests strain rate sensitivity for polymeric foams under compression loading [44, 45, 46, 47, 48, 49], where the strain rate dependence may be observed as an increase in elastic modulus, compressive strength, or decrease of densification strain. Ouellet et al. [44] studied the compressive response of polymeric foams under quasi-static, medium and high strain rate conditions, where the strain rates ranged from 0.0087 to 2500  $s^{-1}$ . In literature, a large amount of compression data is available; however, most data addresses strain rates up to 250  $s^{-1}$ , where higher strain rate data only investigates modest levels of compression. Oullet et al. found that strain rate effects become more pronounced at rates above approximately 1000  $s^{-1}$ . In a study of strain rate effects on elastic and early cell-collapse of polystyrene foam, Song et al. [45] found that the collapse stress increased nearly linearly with the logarithm of the strain rate, and the elastic modulus was seen to increase with strain rate. However, Chen et al. [46] found that the elastic modulus of expanded polystyrene did not exhibit apparent strain rate dependency over the range of 1 to 280  $s^{-1}$ . In the study by Chen et al. it was also found that the compressive strength of expanded polystyrene increased rapidly with strain rates over 113  $s^{-1}$  and a slight decrease of the densification strain over the same strain rate range.

The impact of density on the mechanical properties of polymeric foam has also been investigated in several studies. Bouix et al. [47] studied the behavior of polypropylene under dynamic loading, where it was shown that the strain rate hardening phenomenon was more pronounced for higher density foams. This phenomenon is according to Bouix et al. correlated to the micro-inertia effects, which are more pronounced on thicker cell walls during the dynamic buckling of the foam cells. Chen et al. [46] found that the static strength and elastic modulus of expanded polystyrene increased with density, where higher density expanded polystyrene exhibited higher energy absorption capabilities than lower density ones. Avalle et al. [50] conducted a study on polymeric foams under compressive loading, characterized by the use of the energy-absorption diagram. It was shown that the maximum efficiency identifies the condition for optimal energy absorption of the foam, while the maximum stress reached a value limited through other design considerations. In the study by Avalle et al. it is suggested that a foam with an optimum value of density can be found for various applications. In other words, the utilization of a low-density foam, too porous for the loading conditions will result in the densification stage being reached, which will exponentially increase the force before the energy has been dissipated. However, a foam with a density too high for the loading conditions may result in a high force without utilizing the full plateau region, as shown in Figure 2.20 [50].

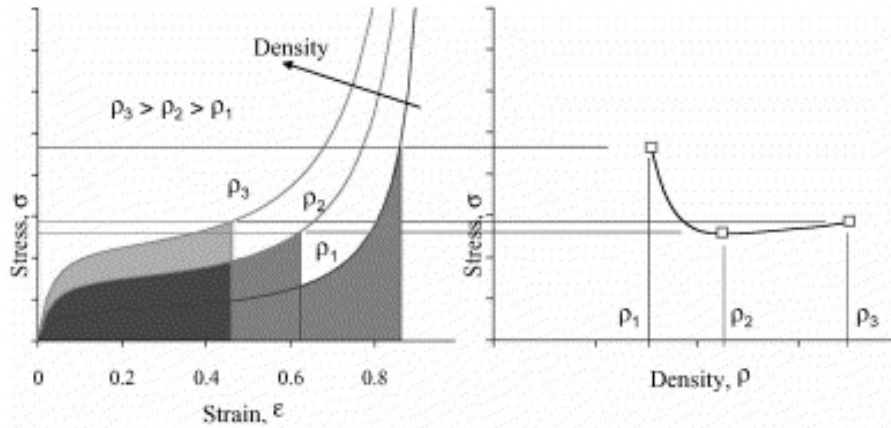


Figure 2.20: Energy diagram of typical foams of different density obtained from the same solid material [50].

# Chapter 3

## Preliminary Numerical Work

Physical experiments are expensive, time-consuming and usually limited to small-scale testing, while numerical simulations can be applied to full-scale models, where implementation of modifications require less extensive work and are far cheaper. Numerical simulations also provide valuable results outside the limitations of the experimental setup. In this chapter, a preliminary study aimed to establish and evaluate a reference model, to suggest a firing pressure range for the experimental program and evaluate different options for boundary conditions in the test setup is presented.

All simulations in this chapter were performed on sandwich components with aluminum skins and an XPS-250 core. Results of back skin midpoint displacement, maximum and average force, impulse and energy absorption values are presented and investigated. The midpoint displacement was extracted at the last time step of the simulations. The contact force between the back skin and back clamping frame was extracted to obtain the force-time curves, where the impulse is the area under the curve, and the average force is the impulse divided by the end time. The energy absorption is extracted as the internal energy of each part in the component.

### 3.1 LS-DYNA

In this thesis, the finite element solver LS-DYNA is used for numerical simulations. LS-DYNA is a general-purpose finite element program created by Livermore Software Technology Corporation (LSTC). It offers a large database of material models, contact algorithms, and element formulations. Moreover, it is frequently employed in crash and impact simulations due to its strong capabilities in highly nonlinear and transient dynamic analysis with explicit time integration.

The energy balance has to be studied after a simulation is completed to investigate the reliability of the results [51], defined as

$$E_{total} = E_{kin}^0 + E_{int}^0 + W_{ext} \quad (3.1)$$

where  $E_{kin}^0$  is the initial kinetic energy,  $E_{int}^0$  is the initial internal energy and  $W_{ext}$  is the external work. The total energy,  $E_{total}$ , is defined as

$$E_{total} = E_{kin} + E_{int} + E_{si} + E_{rw} + E_{damp} + E_{hg} \quad (3.2)$$

where  $E_{kin}$  is the current kinetic energy,  $E_{int}$  is the current internal energy,  $E_{si}$  is the current sliding interface energy,  $E_{rw}$  is the current rigid wall energy,  $E_{damp}$  is the current damping energy and  $E_{hg}$  is the current hourglass energy.

The energy balance is usually studied through the energy ratio expressed as

$$eratio = \frac{E_{total}}{E_{total}^0 + W_{ext}} \quad (3.3)$$

which is equal to unity if the energy is preserved. A deviation exceeding a couple of percents indicate an error in the model and require further investigation by the user.

## 3.2 Reference Model

The establishment of the reference model concerning the component geometry is based on earlier experimental and numerical studies conducted on sandwich panels in the SIMLab Shock Tube Facility at NTNU, such as the study performed by Sigurdsson [3]. The sandwich panel geometry and clamping frame geometry is shown in Figure 3.1 and will be further presented together with the experimental test set-up in Section 5.1. The thickness of the skins, foam and clamping frames are 0.8, 50.0 and 25.0 *mm*, respectively.

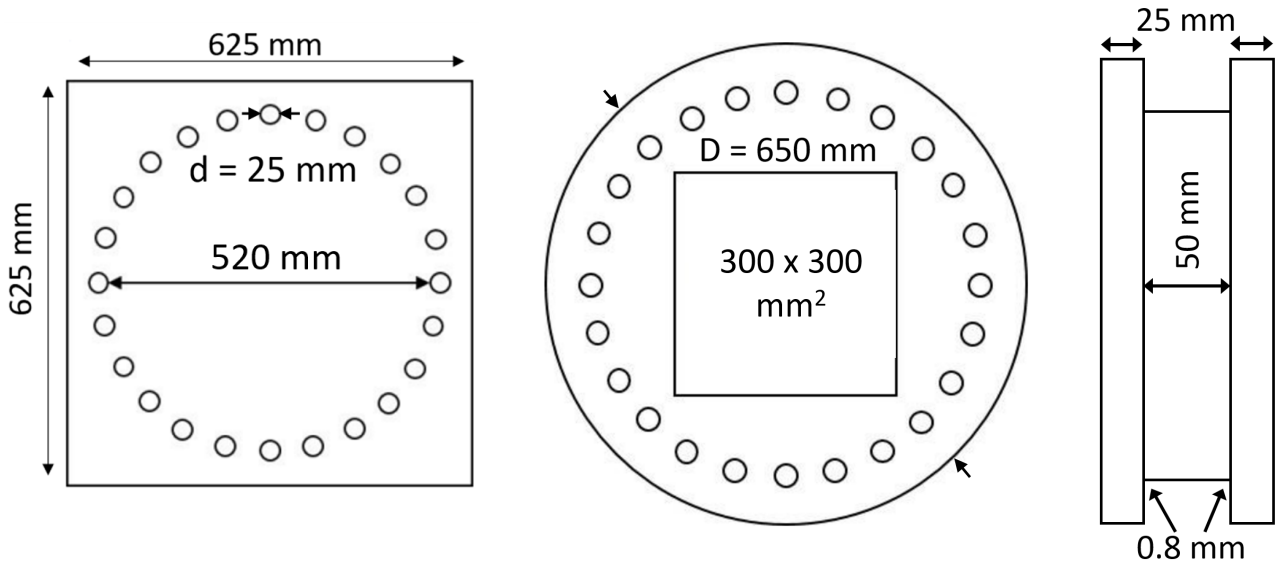


Figure 3.1: Sandwich panel geometry (left) and clamping frame geometry (right). This illustration is based on [2].

The reference model developed based on the geometry presented above, was is divided into six parts; three for the rig and three for the sandwich panel. The rig was modeled with two clamping frames and twelve bolts. The sandwich panel was modeled with two skins and a foam core. The reference model can be seen from the side in Figure 3.2 and a front view is displayed in Figure 3.3. Both steel clamping frames and the bolts were modeled with linear elastic properties, using the elastic material model *Mat 001* in LS-DYNA, with a stiffness of 210 *GPa*, following the assumption of no plastic deformation in these components. The front clamping frame was constrained in the longitudinal direction of the bolts to mimic the behavior of the shock tube.

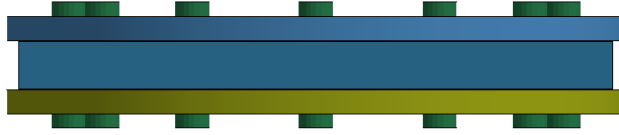


Figure 3.2: Front view of the sandwich reference model.

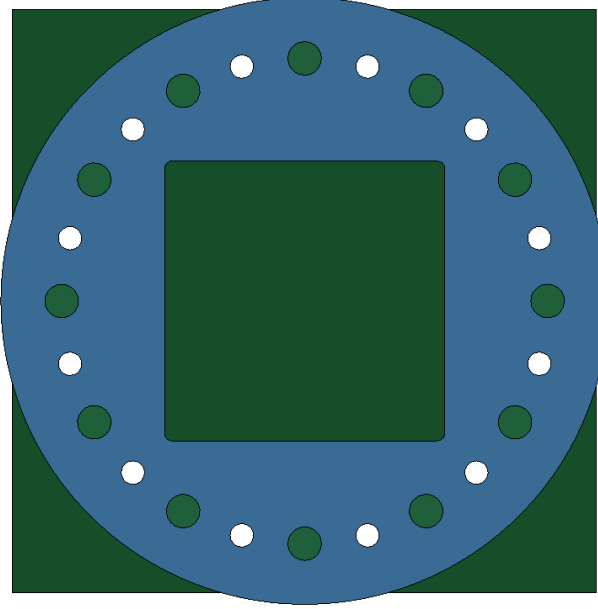


Figure 3.3: Top view of the sandwich reference model.

The aluminum and steel skins were modeled with Børvik et al.'s [34] constitutive model presented in Section 2.5.2 implemented as the material model *Mat 107* in LS-DYNA. Cockcroft-Latham fracture criterion was utilized to describe fracture. Since no material tests were performed at this stage of the study, aluminum and steel material parameters were taken from earlier studies performed at SIMLab [2] and are presented in Table 3.1.

Table 3.1: Material parameters for the constitutive relation for aluminum and steel [2].

| Material    | $\sigma_0$<br>[MPa] | $Q_1$<br>[MPa] | $C_1$<br>[-] | $Q_2$<br>[MPa] | $C_2$<br>[-] | $c$<br>[-] | $m$<br>[-] | $\dot{p}_0$<br>[s <sup>-1</sup> ] | $W_c$<br>[MPa] |
|-------------|---------------------|----------------|--------------|----------------|--------------|------------|------------|-----------------------------------|----------------|
| AA1050-H14  | 80.0                | 31.2           | 1090.0       | 12.2           | 20.4         | 0.014      | 1.0        | $5 * 10^{-4}$                     | 60             |
| DOCOL 600DL | 325.7               | 234.8          | 56.2         | 445.7          | 4.7          | 0.01       | 1.0        | $5 * 10^{-4}$                     | 555            |

The XPS foam was modeled with a variation of the Deshpande-Fleck material model, *Mat 154* in LS-DYNA, with material parameters obtained by Berdal and Bjørge [33]. XPS-250, XPS-400 and XPS-700 was modelled with nominal densities of 33, 37 and 50  $kg/m^3$  as presented in Table 3.2. No fracture criterion was applied in the foam material model.



Table 3.2: Material parameters for the constitutive relation for XPS foams [33].

| Material | $\rho$<br>[ $kg/m^3$ ] | $E$<br>[ $MPa$ ] | $\sigma_{c0}$<br>[ $MPa$ ] | $\gamma$<br>[-] | $\varepsilon_d$<br>[-] | $\alpha_2$<br>[-] | $\beta$<br>[-] |
|----------|------------------------|------------------|----------------------------|-----------------|------------------------|-------------------|----------------|
| XPS-250  | 33.0                   | 13.71            | 0.257                      | 0.771           | 3.36                   | 26.43             | 5.51           |
| XPS-400  | 37.0                   | 18.47            | 0.412                      | 0.707           | 3.68                   | 38.96             | 5.05           |
| XPS-700  | 50.0                   | 23.45            | 0.732                      | 0.287           | 3.46                   | 56.87             | 4.70           |

*Automatic surface to surface* contact algorithm was applied between all components with both static and dynamic friction coefficient set to 0.1. The friction coefficient has not been appropriately investigated. The soft penalty formulation was applied for all components in contact with foam, while a standard penalty formulation was used between all other components. The foam and skins were meshed with an element size of 5 mm. Four-node Langrangian shell elements with Belytschko-Tsay element formulation was utilized, with Gauss quadrature rule and five integration points through the thickness of 0.8 mm for the skins. Ten eight-node constant stress solid elements were used through the thickness of 50 mm for the foam. Hourglass stiffness of type 3, *Flanagan-Belytschko*, with exact volume integration and a coefficient of 0.05 was utilized in the model.

The blast loading was implemented as a uniformly distributed pressure-time history obtained experimentally in the shock-tube facility on massive steel plates by Aune [2]. This is a simplification, as the plates studied in this thesis are not considered rigid. The pressure-time history curves were idealized using curve-fitting of the Friedlander equation, Eq. 2.2, with the Friedlander parameters presented in Table 3.3 and the pressure-time history curve presented in Figure 3.4 [2]. Note that R77\_P35 is obtained by two curve fits to take the secondary reflection into account, where only the curve fit from the primary to the secondary peak is presented in Table 3.3.

Table 3.3: Friedlander parameters to the idealized pressure-time history curves.

| Name    | Firing Pressure<br>[ $bar$ ] | $p_{r,max}$<br>[ $kPa$ ] | $t_+$<br>[ $ms$ ] | b<br>[-] | $i_{r+}$<br>[ $kPams$ ] |
|---------|------------------------------|--------------------------|-------------------|----------|-------------------------|
| R77_P10 | 10                           | 446.20                   | 35.40             | 1.57     | 4904.50                 |
| R77_P15 | 15                           | 606.60                   | 44.10             | 2.03     | 7510.00                 |
| R77_P25 | 25                           | 795.20                   | 68.70             | 2.04     | 12383.30                |
| R77_P35 | 35                           | 1105.20                  | 73.90             | 1.90     | 16613.40                |

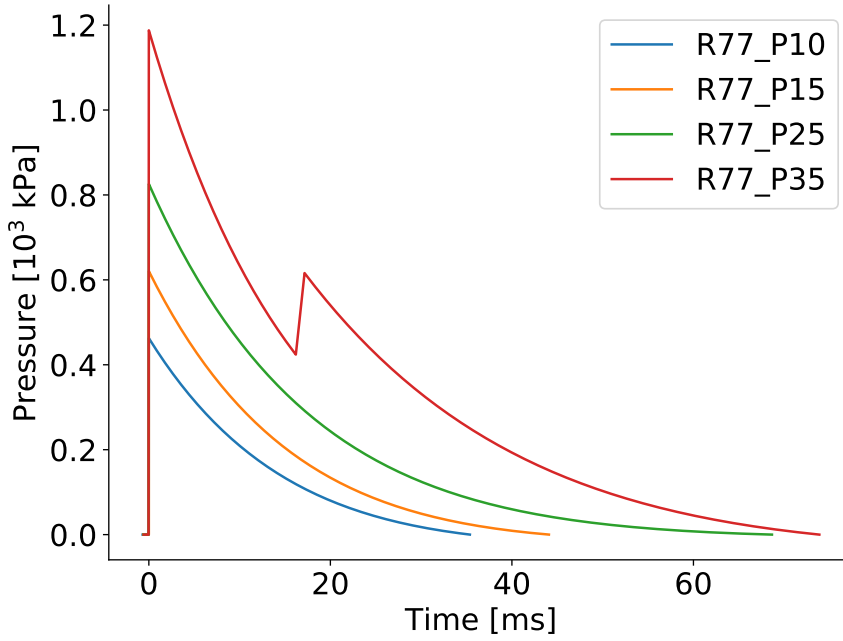


Figure 3.4: Idealized pressure-time curves used to describe blast loads in the numerical models.

### 3.3 Experimental Firing Pressure

Experimentally, it is desired to obtain results with significant deformation of the specimen without reaching fracture. Therefore, a preliminary numerical study was performed to suggest firing pressure range for the experimental program. Simulations were performed for aluminum skins without foam cores and aluminum front skins and steel back skins without foam cores exposed to different firing pressures while investigating the recorded damage parameter. The midpoint displacement is included for aluminum skins to validate the convergence of deformation. Considering a previous study on single aluminum plates by Aune [17] the double skins were expected to fracture due to stress localization along the edges of the clamping frame. Stress localization is a highly mesh dependent phenomenon. Therefore a study of the mesh sensitivity was performed by decreasing the element size stepwise to a shell thickness of 0.8 mm. Fracture occurs when the damage parameter,  $\omega$ , in Cockcroft-Latham fracture criterion presented in Section 2.5.2 reaches unity. Note that the fracture parameter,  $W_c$ , is also mesh dependent and was calibrated to an element size of 0.8 mm [2]. The damage parameter was extracted as "Misc History Variable #1" in LS-DYNA.

### 3.3.1 Aluminum Skins

Table 3.4 presents the maximum value of the damage parameter and the physical location on the back skins when varying the nominal firing pressure. No fracture was observed while varying the firing pressure from 10 to 25 *bar* in the reference model with a mesh size of 5 *mm*. It is observed that the maximum value of the damage parameter was recorded in the middle of the blast-exposed area for all specimen modeled with this meshing. Decreasing the mesh size to 2 *mm* affected the value of the damage parameter slightly, while the location of the maximum damage was changed towards the edges of the clamping frame. Decreasing the mesh size to 0.8 *mm* shows a significant increase in the maximum damage value due to a stress localization along the edges of the clamping frame being captured as seen in Figure 3.5. A damage parameter of 0.91 is obtained in the most refined model exposed to 15 *bar* firing pressure, while fracture is obtained when exposing the model to 25 *bar* firing pressure. The mesh refinement seems only to affect the midpoint displacement to a small degree.

Table 3.4: Back skin midpoint displacement,  $u_{BS}$ , maximum damage parameter value,  $\omega_{max}$ , and location for numerical simulations of aluminum skins without foam cores, with varying mesh sizes and firing pressures,  $P_f$ .

| Element Size<br>[ <i>mm</i> ] | $P_f$<br>[ <i>bar</i> ] | $u_{BS}$<br>[ <i>mm</i> ] | $\omega_{max}$<br>[—] | Location    |
|-------------------------------|-------------------------|---------------------------|-----------------------|-------------|
| 5.0                           | 10                      | 39.29                     | 0.26                  | Middle      |
|                               | 15                      | 49.98                     | 0.38                  | Middle      |
|                               | 25                      | 65.06                     | 0.55                  | Middle      |
| 2.0                           | 10                      | 37.74                     | 0.29                  | Side/Middle |
|                               | 15                      | 47.78                     | 0.38                  | Middle      |
|                               | 25                      | 60.75                     | 0.56                  | Side/Middle |
| 0.8                           | 10                      | 38.33                     | 0.51                  | Side        |
|                               | 15                      | 48.36                     | 0.91                  | Side        |
|                               | 25                      | -                         | Fracture              | Side        |

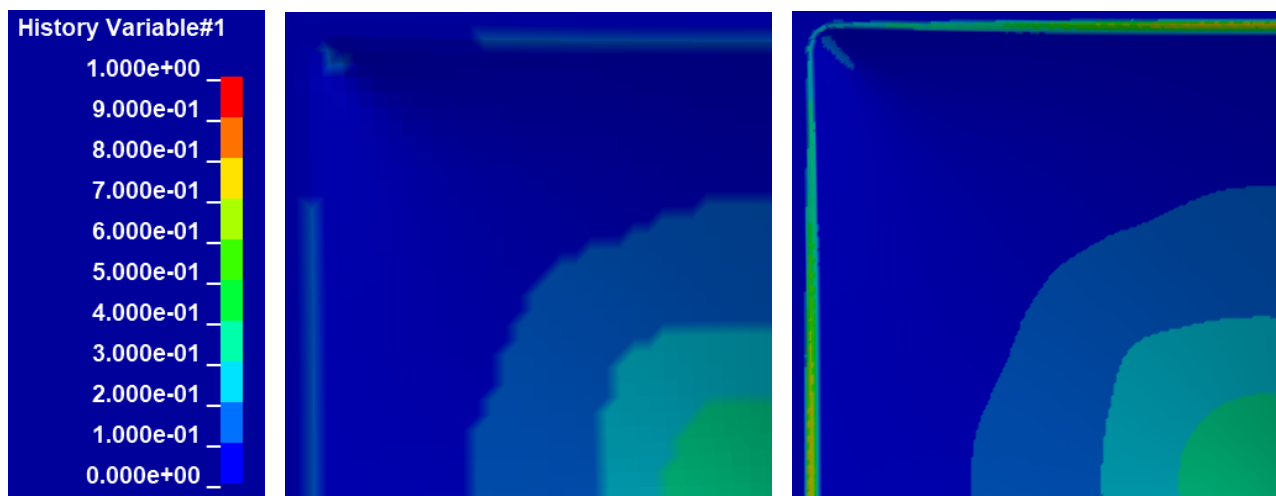


Figure 3.5: Value and distribution of damage parameter on quarter of the blast exposed area for double aluminum skins with a mesh size of 5 *mm* (left) and 0.8 *mm* (right) exposed to a firing pressure of 15 *bar*.

The results illustrate the challenges tied to modeling a mesh dependent mechanism such as strain localization and fracture. The previous study by Aune [17] found that a single aluminum plate reached fracture along the edges of the clamping frame when exposed to 10 *bar* nominal firing pressure. Considering that the fracture parameter used in this study was calibrated for an element size of 0.8 *mm* in [17], the numerical model meshed with the same size should be emphasized when investigating fracture in the component. Fracture is observed when the specimen is exposed to 25 *bar* firing pressure, while a damage parameter of 0.91 was obtained when exposed to 15 *bar* firing pressure. The latter is close to unity, which makes predicting experimental fracture difficult. With the presented results and the findings from [17] as a reference, an experimental program exposing aluminum skins without a foam core to firing pressures of 10 and 15 *bar* was suggested.

### 3.3.2 Aluminum and Steel Skins

Table 3.5 presents the value and the location of the maximum damage parameter recorded during numerical simulations of components with aluminum front skin and steel back skin exposed to different firing pressures. It is observed in Table 3.5 that the distribution of the damage parameter follows a similar pattern as the numerical results for the aluminum skins, where the localization moves towards the edges with increased mesh refinement. However, the values of the damage parameters are far smaller in magnitude, as expected for the aluminum and steel skins. The results suggest that the aluminum and steel skins will not experience fracture exposed to the investigated firing pressures. Therefore, an experimental program exposing components with a front plate of aluminum and a back plate of steel to firing pressures of 25 and 35 *bar* was suggested.

Table 3.5: Back skin midpoint displacement,  $u_{BS}$ , maximum damage parameter value,  $\omega_{max}$ , and location for numerical simulations of aluminum and steel skins without foam cores, with varying mesh sizes and firing pressures,  $P_f$ .

| Element Size<br>[ <i>mm</i> ] | $P_f$<br>[ <i>bar</i> ] | $\omega_{max}$<br>[—] | Location |
|-------------------------------|-------------------------|-----------------------|----------|
| 5.0                           | 25                      | 0.08                  | Middle   |
|                               | 35                      | 0.13                  | Middle   |
|                               | 60                      | 0.20                  | Middle   |
| 2.0                           | 25                      | 0.08                  | Middle   |
|                               | 35                      | 0.15                  | Middle   |
|                               | 60                      | 0.21                  | Side/Mid |
| 0.8                           | 25                      | 0.22                  | Side     |
|                               | 35                      | 0.32                  | Side     |
|                               | 60                      | 0.35                  | Side     |

### 3.4 Boundary Conditions

Previous studies show that the use of a single nut on the bolts to fix sandwich components to the test rig introduces issues related to pre-stress (PS) of the component and uncertain boundary conditions [3]. The foam in the sandwich components experiences compression, even at low levels of torque applied to the nuts, when the nuts are tightened. This behavior is undesirable in the form of having an unknown pre-stress applied to the foam, and that loosely fastened single nuts can cause reduced stiffness of the desired fixed boundary condition of the test rig. Pre-stress in the foam and reduced stiffness of the boundary conditions are sources of error and will be further discussed in Chapter 7.

To address this issue, multiple solutions for boundary conditions were suggested. Experimentally, a fixed boundary condition can be obtained by using two nuts tightened against each other or by using a distance piece (DP) around the bolts, as seen in Figure 3.6 (right). Using two nuts is the preferred solution considering it requires less pre-experimental work than the use of a distance piece. However, it has not been experimentally confirmed that the two nuts locked against each other will not loosen during the impact of the shock wave. Numerically, the desired boundary condition is obtained by modeling the bolts with one nut in each end as one part as seen in Figure 3.6. This representation mimics the boundary condition obtained by tightening two nuts against each other experimentally and is used in the reference model.

A distance piece is a hollow steel cylinder placed around the bolts to fix the distance between the clamping frames or between the skins in the sandwich panel. Both configurations were evaluated numerically and compared to the reference model. In addition, a model with both clamping frames fixed without a distance piece was created as a reference where fixed boundary conditions were ensured.

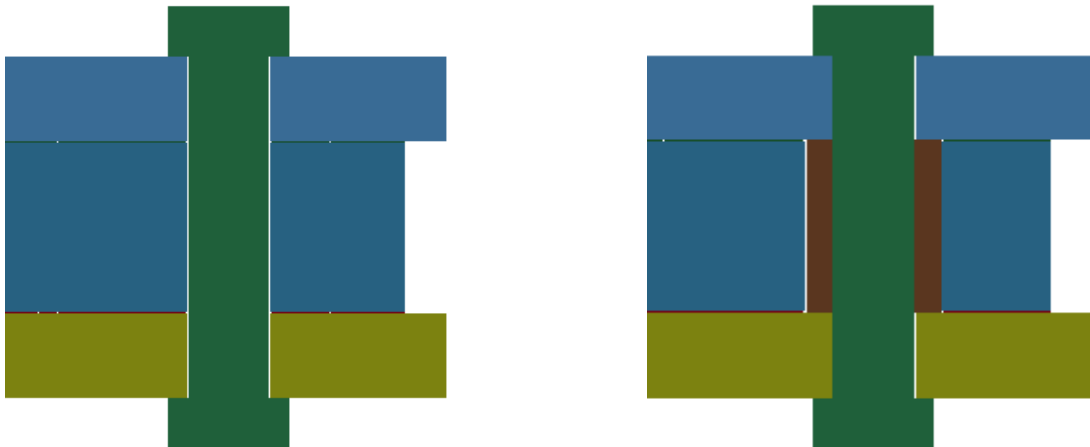


Figure 3.6: Cross-section of a bolt without (left) and with (right) a distance piece.

The numerical results for midpoint displacement and the force histories are presented in Figure 3.7 for the different boundary conditions introduced above. Table 3.6 presents the obtained midpoint displacement, impulse, average and maximum force and the foam core energy absorption. It can be observed that all options yield similar midpoint displacement as the reference model (RM). However, the energy absorbed by the foam core is observed to decrease, and the reaction force increases significantly for the simulations with a distance piece between the skins. This is an undesirable effect in structural protection, and the configuration was discarded. By comparing the numerical results for the other three options, it is seen that all three yields similar results for midpoint displacement, energy absorbed in the foam core and reaction force on the boundary condition. Oscillations can be observed in the force-time curves for all models except the model with fixed clamping frames, due to deformation of the bolts. Moreover, modeling both clamping frames as fixed is considered a valid simplification of the numerically introduced distance piece. The similarity in the numerical results for different boundary conditions suggests that using two nuts or a distance piece in the experimental program will yield similar results.

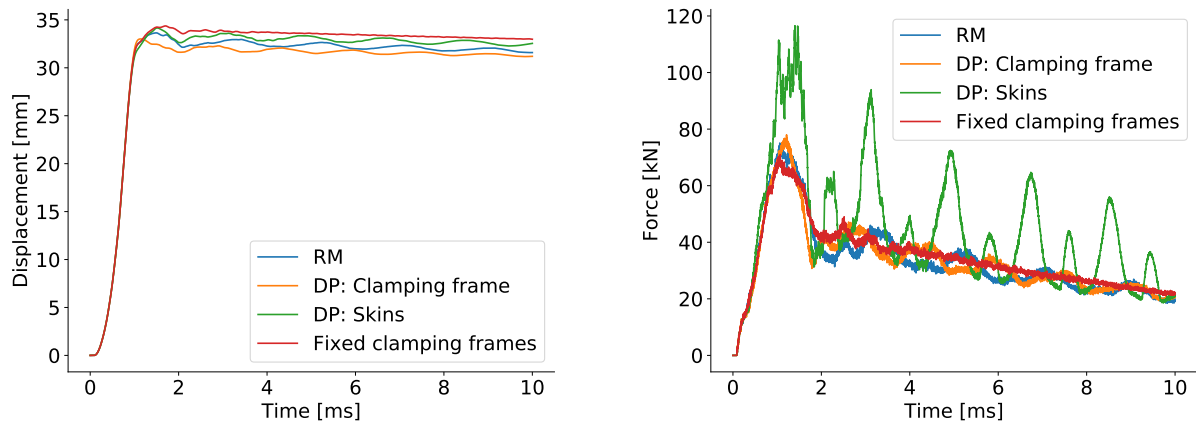


Figure 3.7: Midpoint displacement (left) and force (right) histories for the numerical study on boundary conditions.

Table 3.6: Back skin midpoint displacement,  $u_{BS}$ , impulse, average and maximum force,  $F_{avg}$  and  $F_{max}$ , and energy absorbed in the foam core for boundary condition simulations.

| Simulation            | $u_{BS}$<br>[mm] | Impulse<br>[kNs] | $F_{avg}$<br>[kN] | $F_{max}$<br>[kN] | Absorbed energy<br>[kJ] |
|-----------------------|------------------|------------------|-------------------|-------------------|-------------------------|
| RM                    | 31.59            | 320.60           | 32.96             | 75.09             | 558.88                  |
| DP: Clamping frames   | 31.20            | 332.84           | 33.28             | 77.98             | 565.14                  |
| DP: Skins             | 32.54            | 439.78           | 43.98             | 116.48            | 478.45                  |
| Fixed clamping frames | 32.98            | 343.64           | 34.36             | 71.00             | 568.51                  |

### 3.5 Pre-stress

An investigation on pre-stressed foam cores was conducted since the boundary conditions studied in Section 3.4 would experimentally include some degree of pre-tensioning of the nuts. Previous studies by Sigurdsson [3] suggests a tightening of the nuts of 2  $Nm$  for sandwich panels and 100  $Nm$  for skins. It is assumed that the latter torque would be appropriate for an experimental setup including a distance piece. To mimic this behavior the initial torque was included in the models through applying pre-tensioning stress,  $\sigma_{ps}$ , to the bolts as described by Aune et al. [15]. Eq. 3.4, 3.4 and 3.6 describes the calculation of the pre-tensioning stress

$$F_{ps} = \frac{M_t}{\kappa\varphi} \quad (3.4)$$

$$\sigma_{ps} = \frac{F_{ps}}{A_c} = \frac{F_{ps}}{\frac{1}{4}\pi\varphi^2} \quad (3.5)$$

$$\sigma_{ps} = \frac{4M_t}{\pi\varphi^3\kappa} \quad (3.6)$$

where  $F_{ps}$  is the pre-tensioning force,  $M_t$  the initial torque,  $\kappa$  the thread geometry and friction coefficient,  $\varphi$  the bolt diameter and  $A_c$  the contact area. The recommended value for the coefficient  $\kappa$  is usually 0.18, however, it may vary between 0.10 and 0.23 [15]. In this study, a  $\kappa$  equal to 0.18 was used.

Figure 3.8 shows the midpoint displacement and the force histories for numerical models with and without pre-stress, PS, and with and without a distance piece, DP. Table 3.7 presents the obtained midpoint displacement, impulse, average and maximum force and the energy absorption of the sandwich component. It is observed that introducing pre-stress on the bolts does not significantly affect the midpoint displacement, force transferred to the clamping frame or the absorbed energy of the simulations with or without a distance piece. Therefore, simulations including pre-stress will not be studied any further.

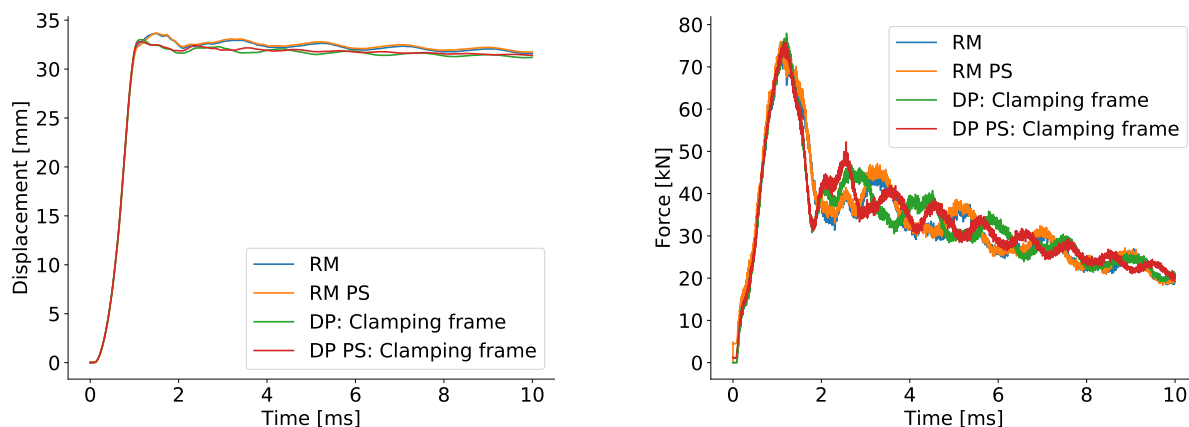


Figure 3.8: Midpoint displacement (left) and force (right) histories for the numerical study on pre-stress, PS, with and without a distance piece, DP.

Table 3.7: Back skin midpoint displacement,  $u_{BS}$ , impulse, average and maximum force,  $F_{avg}$  and  $F_{max}$ , and energy absorbed in the foam core for pre-stressed simulations.

| Simulation             | $u_{BS}$<br>[mm] | Impulse<br>[kNs] | $F_{avg}$<br>[kN] | $F_{max}$<br>[kN] | Absorbed energy<br>[kJ] |
|------------------------|------------------|------------------|-------------------|-------------------|-------------------------|
| RM                     | 31.59            | 329.60           | 32.96             | 75.09             | 1068.39                 |
| RM PS                  | 31.74            | 337.22           | 33.72             | 76.02             | 1053.55                 |
| DP: Clamping frames    | 31.20            | 332.84           | 33.28             | 77.98             | 1055.92                 |
| DP PS: Clamping frames | 31.40            | 335.20           | 33.52             | 75.90             | 1059.58                 |

### 3.6 Friction

Considering no experimental study has been conducted on the static or dynamic friction coefficients between foam and aluminum, foam and steel and steel and aluminum in this study, numerical results for varying the friction coefficients are evaluated. The static and dynamic coefficients of friction are assumed equal in all further simulations. The coefficients were increased and decreased as seen in Table 3.8 and compared with the reference model, RM.

Midpoint displacement and force histories for varying friction is presented in Figure 3.9, while the values obtained are presented in Table 3.9. It is observed that removing all friction causes an increase of 25 % in midpoint displacement compared to the RM. A slight increase in impulse, forces, and energy absorbed is also seen. Increasing the friction coefficients to 0.6 causes a decrease of 15 % in the midpoint displacement, while a slight increase in force and a slight decrease in energy are seen. Similar results are obtained when increasing the friction coefficients to 1.0. This implies that there is an upper boundary where increasing the friction further will not alter the results significantly. The friction coefficient of the reference model was considered to yield acceptable results and was used for further numerical simulations.

Table 3.8: Friction coefficients between the different materials.

| Simulation | Aluminum-Steel<br>[—] | Aluminum-Foam<br>[—] | Steel-Foam<br>[—] |
|------------|-----------------------|----------------------|-------------------|
| RM         | 0.1                   | 0.1                  | 0.1               |
| F1         | 0.0                   | 0.0                  | 0.0               |
| F2         | 0.6                   | 0.6                  | 0.6               |
| F3         | 1.0                   | 1.0                  | 1.0               |



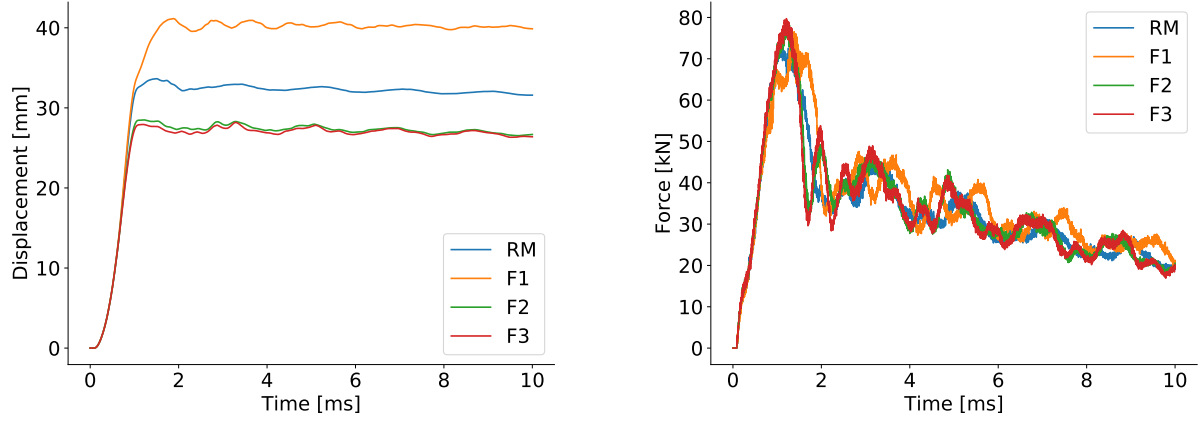


Figure 3.9: Midpoint displacement (left) and force (right) histories for the numerical study on friction.

Table 3.9: Back skin midpoint displacement,  $u_{BS}$ , impulse, average and maximum force,  $F_{avg}$  and  $F_{max}$ , and energy absorbed in the foam core for varying friction coefficients.

| Simulation | $u_{BS}$<br>[mm] | Impulse<br>[kNs] | $F_{avg}$<br>[kN] | $F_{max}$<br>[kN] | Absorbed energy<br>[kJ] |
|------------|------------------|------------------|-------------------|-------------------|-------------------------|
| RM         | 31.59            | 329.60           | 33.00             | 75.09             | 1068.39                 |
| F1         | 39.87            | 351.94           | 35.19             | 76.53             | 1319.22                 |
| F2         | 26.68            | 335.03           | 33.50             | 78.53             | 985.02                  |
| F3         | 26.39            | 334.22           | 32.42             | 79.71             | 977.42                  |

### 3.7 Mesh Sensitivity

In Section 3.3 a refinement of mesh size was performed to study stress localization and fracture of skin specimens without foam cores. It is also desirable to investigate the convergence of numerical results on sandwich components through a mesh sensitivity study. In Table 3.10 the mesh refinement of the sandwich components is tabulated. The numerical model with a mesh size of 0.8 mm and 2.0 mm for the skins and the foam core, respectively, is modeled as only a quarter of the sandwich component. This measure was taken to reduce the computational cost of the numerical simulation.

Table 3.10: Element size for skins and foam.

| Simulation | Skins mesh size<br>[mm] | Foam mesh size<br>[mm] |
|------------|-------------------------|------------------------|
| RM         | 5.0                     | 5.0                    |
| M1         | 2.0                     | 2.0                    |
| M2_Q       | 0.8                     | 2.0                    |

Midpoint displacement and force histories for the reference model and the models with refined meshes are compared in Figure 3.10 while Table 3.11 presents corresponding values obtained. It is observed that the midpoint displacement of model M1 and M2\_Q increase with 2 and 5 %, respectively, with mesh refinement, compared to the reference model. The same trend is observed for the impulse, reaction force, and energy absorbed where mesh refinement causes a slight increase in the presented values. The deformation profiles of the RM and the M2\_Q models can be seen in Figure 3.11. A slight change in deformation profile might cause the deviations presented above. The results provided by the reference model with a mesh size of 5.0 mm is considered relatively converged and fairly accurate. Based on these results and considering the computational cost of the model with refined meshed, the reference model is preferred and will be used for further numerical simulations.

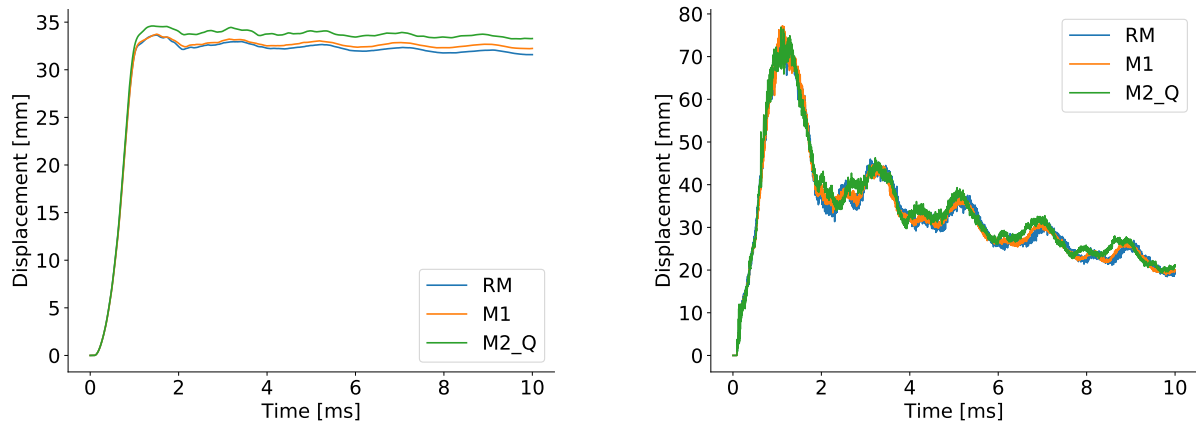


Figure 3.10: Midpoint displacement (left) and force (right) histories for the numerical study on mesh sensitivity.

Table 3.11: Back skin midpoint displacement,  $u_{BS}$ , impulse, average and maximum force,  $F_{avg}$  and  $F_{max}$ , and energy absorbed in the foam core for varying mesh refinement.

| Simulation | $u_{BS}$<br>[mm] | Impulse<br>[kNs] | $F_{avg}$<br>[kN] | $F_{max}$<br>[kN] | Absorbed energy<br>[kJ] |
|------------|------------------|------------------|-------------------|-------------------|-------------------------|
| RM         | 31.59            | 329.60           | 32.96             | 75.09             | 1068.39                 |
| M1         | 32.24            | 330.43           | 33.04             | 77.18             | 1100.99                 |
| M2_Q       | 33.27            | 338.31           | 33.83             | 76.88             | 1141.32                 |

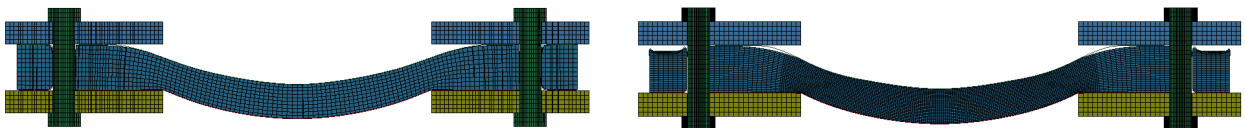


Figure 3.11: Deformation profiles of the reference model, RM, (left) and the most refined mesh, M2\_Q, (right) after 10 ms.

## 3.8 Main Findings

In this section, the main findings of the preliminary study are summarized.

- Using a mesh size of 5 *mm* does not capture the stress localization along the edges of the clamping frames. A mesh size of 0.8 *mm* is necessary to capture the phenomenon and mimic fracture in the aluminum skins without a foam core.
- For experiments with aluminum skins without a foam core, a firing pressure range of 10 and 15 *bar* was suggested.
- For experiments with aluminum front skins and steel back skins a firing pressure range of 15 and 35 *bar* was suggested.
- Fixing the sandwich panels using two nuts is desired during conduction of experiments.
- Using a distance piece between the clamping frames only affect the solution slightly.
- Fixing both clamping frames is a sufficient simplification to modeling the distance piece between the clamping frames.
- Using a distance piece between the skins will reduce the energy absorbed by the foam and increase the reaction forces on the boundary conditions significantly. Therefore, the configuration discarded.
- Pre-stressed nuts only affect the numerical solution slightly and will not be included in further studies.
- Increased friction decreases displacement and energy absorption. Removing friction drastically increases the deformation and energy absorption of the simulations while the reaction force is only slightly affected.
- Mesh refinement increases the displacement and energy absorption with a slight change in the deformation profile. The reference model is considered fairly converged and is preferred to the models with refined meshes considering computational cost. Therefore, an element size of 5 *mm* will be utilized in further studies.

# Chapter 4

## Material Study

In this chapter, the materials used in this thesis are presented. The aluminum alloy used for selected skins are presented through a short general description of the material, stating chemical composition and material constants and through a more thorough presentation of the material tests performed to calibrate the material parameters. For the steel alloy used in this study no material tests were performed, considering the numerous studies done on the material [1, 2]. A brief overview of the steel alloy and a tabulation of the material constants and parameters are presented. For the foam types used as core material in the sandwich panels, no material tests were performed. However, experimental data was obtained from a previously conducted study by Sigurdsson [3] on the material. This data was used to validate the numerical models and to study the energy absorption properties of the material. The compression test data was used by Berdal and Bjørgo [33] to create a density-dependent model which will be used in further studies.

### 4.1 Aluminum

In the current study skins made from 0.8 *mm* thick plates of AA1050-H14 aluminum were used. AA1050A-H14 is a 1000-series aluminum alloy considered commercially pure and is formulated for primary forming into wrought products [52], produced by Hindalco Industries Ltd. It is usually formed by extrusion or rolling. The alloy-series can be strengthened by cold working, but not by heat treatment [53]. It is furnished in the H14 temper to develop a particular degree of intergranular and exfoliation corrosion. The nominal yield stress and ultimate tensile strengths were given by the manufacturer to be 110 *MPa* and 116 *MPa* respectively. The chemical composition of the alloy is shown in Table 4.1. Table 4.2 presents the physical material constants for aluminum used in the material models.

Table 4.1: Chemical composition of AA1050A-H14 [18].

| Si [%] | Fe [%] | Cu [%] | Mn [%] | Mg [%] | Zn [%] | Ti [%] | Al [%] |
|--------|--------|--------|--------|--------|--------|--------|--------|
| 0.030  | 0.360  | 0.001  | 0.002  | 0.000  | 0.003  | 0.010  | Rest   |

Table 4.2: Physical material constants for AA1050-H14 [1].

| $E$<br>[GPa] | $\nu$<br>[-] | $\rho$<br>[kg/m <sup>3</sup> ] | $\alpha$<br>[K <sup>-1</sup> ] | $C_p$<br>[J/kgK] | $\chi$<br>[-] | $T_r$<br>[K] | $T_m$<br>[K] |
|--------------|--------------|--------------------------------|--------------------------------|------------------|---------------|--------------|--------------|
| 70           | 0.33         | 2705                           | $1.2 \times 10^{-5}$           | 452              | 0.9           | 293          | 893          |

To establish the material properties of the AA1050-H14 aluminum alloy used in the shock tube experiments, nine uni-axial tensile tests of UT-200 flat dog bone components created from the aluminum skins were performed at room temperature. Three tests were carried out for the 0-degree, 45-degree and 90-degree direction of the material, relative to the rolling direction. The nominal geometry of the specimens is shown in Figure 4.1. The apparatus used for the tensile tests was an Instron 5985 with a load cell of 250 kN. The tests were performed by fixing one end of the specimens while pulling the other. Both sides of the dog bone specimens were attached to the machine with a bolt through a hole in the specimen. The machine applied a displacement at a rate of 1.0 mm/min until the specimens reached fracture. Reaction force and displacement were measured by the machine, while a camera was used to capture the deformation of the test specimens. Displacement data retrieved from the Instron machine was disregarded due to error sources such as machine stiffness. The strain was obtained from image analysis using 2D-DIC with the software eCorr. Data for force and strain was post-processed to obtain the stress-strain relationship.

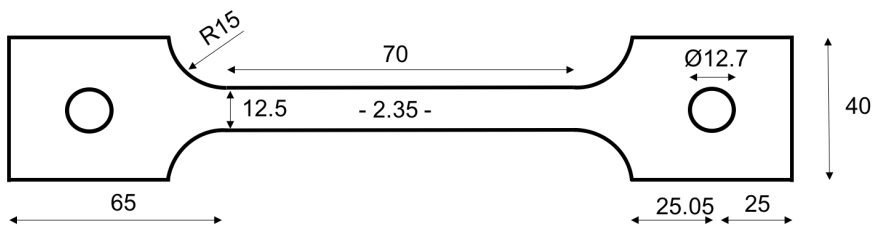


Figure 4.1: Dimensions of UT-200 flat dog bone test specimen.

#### 4.1.1 Digital Image Correlation

DIC is an optical method that measures changes in an images series [54]. In this thesis, the DIC software eCorr was used to generate strain plots and local strain values in nodes. The specimens were painted with a random speckle pattern to improve the accuracy of the results. A camera was placed such that the optical axis was normal to the dog bone specimen surfaces. Using eCorr, a mesh of Q4 elements was placed on the test specimens in their initial configuration. By tracking the development in the pictures, the software calculated displacements and strains in the nodes of the mesh. Inaccuracies are usually due to grayscale noise in the recorded images. The results can be improved by creating a vector over the uniform middle part of the specimen as a virtual extensometer to even out the deviations in the nodes.

#### 4.1.2 Material Model

An elastic-plastic material model was used to predict the response of the aluminum alloy AA1050-H14 in this study. Von Mises yield criterion was considered in the material model due to its appliance to ductile materials and since it is widely used for uni-axial tension tests [55].

Von Mises assumes an isotropic, isochoric, isothermal and rate independent material where yielding is independent of the hydrostatic pressure. Several studies suggest an anisotropic behavior for extruded aluminum alloys [56]. Therefore three directions relative to the rolling of the material were tested and used for material model calibration. The work hardening was described using Voce hardening law. The tensile test data was processed and curve fitted to calibrate the hardening model for the three different directions. Cockcroft-Latham [37] fracture criterion was added to the material model and calibrated with trial and error numerically by comparison of the material model and the experimental results.

### 4.1.3 Elastic Properties

The force data obtained during the tensile tests were used to calculate engineering stress,  $\sigma_e$ . Engineering stress is a measurement of stress based on force and the initial cross-section area of the specimen as seen in Eq. 4.1, which means it disregards the area reduction during the elastic, and more significantly, during the plastic deformation. Calculated engineering stress for all material tests is shown in Figure 4.2. Notice that the third test for the 0-degree direction was disregarded due to an error in the experimental setup for that particular test. Spikes in the stress-strain curves can be observed. These were caused by yield in the specimen at the interaction between the bolt and the holed part of the specimen. However, the spikes are insignificant to the shape of the curves and will, for further calibration procedures, be disregarded. As seen in Figure 4.2, the variations within the material test for each direction are small. The second test for each direction was picked as a representative presentation of the behavior in each direction. These three tests will be used for further illustration of the calibration procedure described below.

True stress and true strain were calculated to include the deformation of the specimen and describe the response accurately. In Figure 4.3 it can be observed that the engineering stress is similar to the true stress in the elastic region but significantly lower in the plastic zone. This effect is due to the elevated changes to the specimens area in the plastic zone compared to the elastic zone. These measurements were derived assuming that the volume of the specimen was conserved, an isochoric material, as seen in Eq. 4.2 and that plastic deformation zone is far greater than elastic deformation zone. Eq. 4.3 and Eq. 4.4 were used to calculate true stress,  $\sigma_t$ , and true strain,  $\varepsilon_t$ , respectively, until necking. Necking is initiated at maximum force recorded.

$$\sigma_e = \frac{F}{A_0} \quad (4.1)$$

$$A = \frac{A_0 L_0}{L} \quad (4.2)$$

$$\sigma_t = \sigma_e(1 + \varepsilon_e) \quad (4.3)$$

$$\varepsilon_t = \ln(1 + \varepsilon_e) \quad (4.4)$$

Young's Modulus,  $E$ , yield stress,  $\sigma_0$ , and Poisson's Ratio,  $\nu$ , was not calibrated in this study, instead generally accepted values of 70 GPa, 80 MPa and 0.33, respectively, was used in further calculations [2, 56].

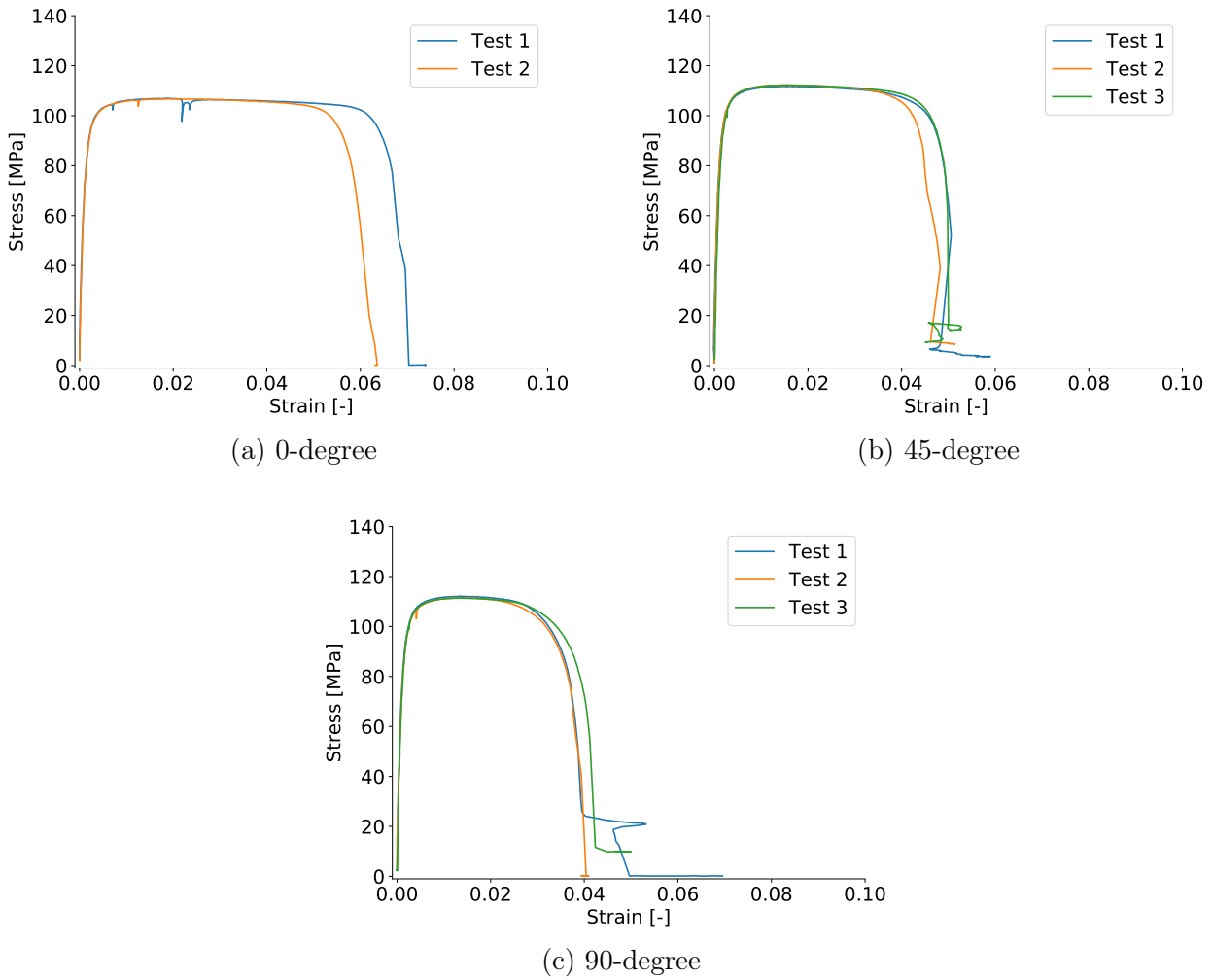


Figure 4.2: Engineering stress plotted with engineering strain for all tension tests for AA1050-H14 in the 0-degree, 45-degree and 90-degree direction, relative to the rolling direction of the material.

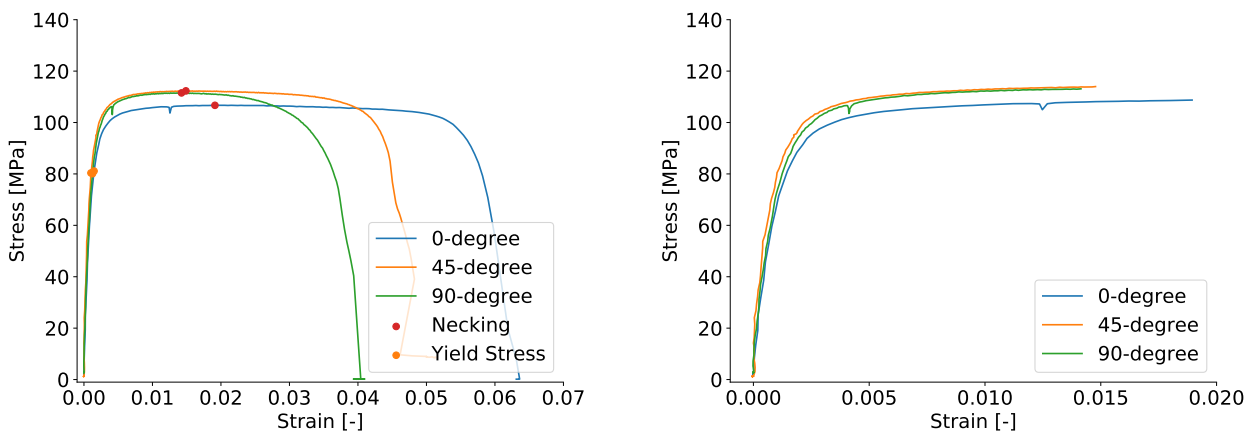


Figure 4.3: Engineering stress, necking and yield stress plotted with engineering strain (left) and true stress plotted with true strain (right) for selected tension tests for AA1050-H14.

#### 4.1.4 Plastic Properties

During blast loading, the aluminum skins may undergo large plastic deformation. Therefore, it is instrumental to have information about the material's plastic behavior. The performed tensile tests only provide information pre-necking which occurs at maximum force, at approximately 0.01 to 0.02 elongation for all three directions. At necking, a biaxial stress state is introduced which distorts the results for uniaxial behavior. Therefore, the post-necking behavior was disregarded. The plastic strains,  $\varepsilon_{pl}$ , were obtained by subtracting elastic strains from the true strains as seen in Eq. 4.5, and was the basis for calibrating the hardening model.

$$\varepsilon_{pl} = \varepsilon - \varepsilon_{el} \quad (4.5)$$

The true stress-plastic strain curve was approximated using a nonlinear least squares solver. Voce hardening law was used to describe the work hardening of the material, where the least square solver provides the hardening parameters to the optimized curve fit. Due to the large deformations during the shock tube experiments, significantly larger strains than necking are expected. The stress post-necking is unknown but can be approximated by extrapolating the hardening laws as seen in Figure 4.4 (right). The Voce law is based on a series of exponential functions where  $Q_i$  and  $C_i$  are optimized for each part of the series, shown in Eq. 4.6. The curve fits of the hardening law for all three directions are shown in Figure 4.4 (left). Two exponential functions were sufficient to provide an accurate fitting of the curves. Extrapolated results are seen in Figure 4.4 (right) while Table 4.3 shows the optimized hardening parameters for Voce hardening law.

$$\sigma = \sigma_0 + \sum_{i=1}^n Q_i (1 - e^{-C_i p}) \quad (4.6)$$

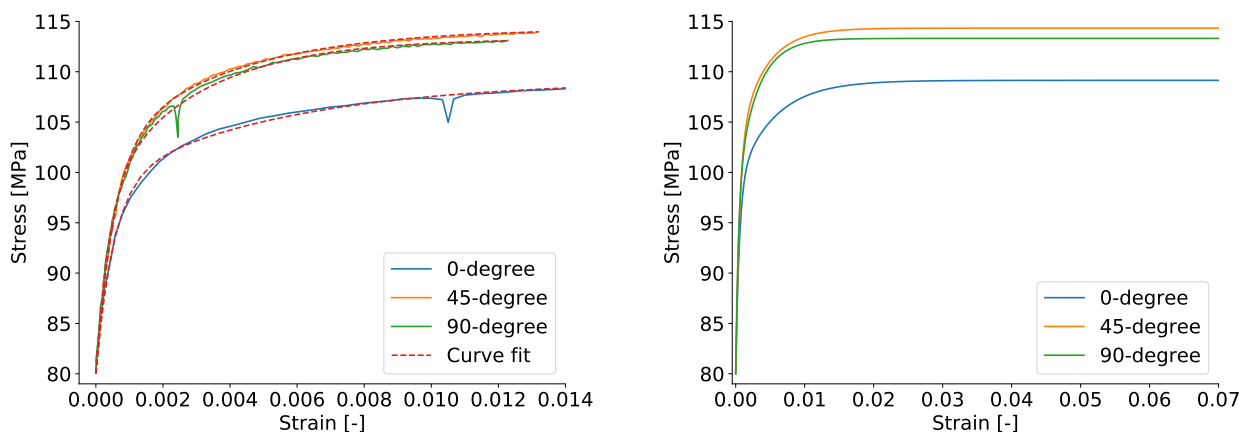


Figure 4.4: Curve fits for Voce hardening law for all three directions (left) and extrapolated curve fits for strains post necking (right).



Table 4.3: Curve fitted Voce hardening law material model parameters for 0-degrees, 45-degrees and 90-degrees relative to the rolling direction of aluminum alloy AA1050-H14.

| Direction | $Q_1$ | $C_1$   | $Q_2$ | $C_2$  |
|-----------|-------|---------|-------|--------|
| 0-degree  | 18.65 | 1884.49 | 10.36 | 185.73 |
| 45-degree | 21.66 | 1702.63 | 11.66 | 251.62 |
| 90-degree | 17.79 | 2427.84 | 15.16 | 339.68 |

#### 4.1.5 Numerical Validation

A numerical model of the test specimen was created to validate the calibrated material model, as seen in Figure 4.5. The same constitutive model, element formulation and hourglass control as described in Section 3.2 was applied to the numerical model of the dog bone specimen. The geometry of the test specimen can be seen in Figure 4.1. The holed parts and the gauge section of the specimen are meshed with an element size of 3.0 mm and 0.8 mm, respectively. Fixed boundary conditions were applied to the left hole, while a velocity was applied to the right hole equivalent to a translation of 5 mm during 151 seconds.

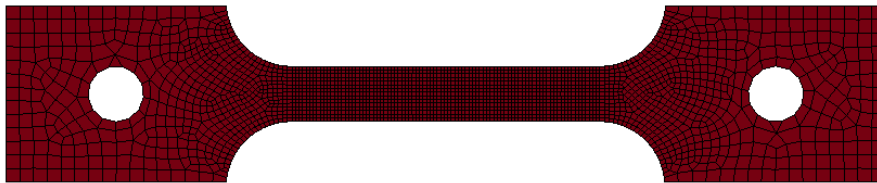


Figure 4.5: Numerical model of test specimen UT-200 flat dog bone.

The material parameters applied to the model described above can be seen in Table 4.4. Note that the Johnson-Cook hardening parameter,  $c$ , is equal zero to obtain the quasi-static condition of the material tests using a time-scaled numerical model. The Cockcroft-Latham fracture parameters were obtained by trial and error for the three material directions. Note that necking is a mesh sensitive phenomenon and that the element exposed to the largest plastic work, the critical element, is always located inside the neck [15]. Therefore, the fracture parameter is highly mesh dependent and is calibrated for the element size of the tensile test. Results on mesh refinement on aluminum skins without foam core presented in Section 3.3 shows that mesh size is a dominant factor when modeling fracture, but only affects the midpoint displacement to a small degree. Since the main scope of this study is to investigate the structural response of sandwich panels exposed to blast loading and not fracture, the fracture criterion calibrated for an element size of 0.8 mm is assumed sufficient.

Table 4.4: Material parameters for the constitutive relation for AA1050-H14.

| Direction | $\sigma_0$<br>[MPa] | $Q_1$<br>[MPa] | $C_1$<br>[-] | $Q_2$<br>[MPa] | $C_2$<br>[-] | $c$<br>[-] | $m$<br>[-] | $\dot{p}_0$<br>[s <sup>-1</sup> ] | $W_c$<br>[MPa] |
|-----------|---------------------|----------------|--------------|----------------|--------------|------------|------------|-----------------------------------|----------------|
| 0-degree  | 80.0                | 18.65          | 1884.49      | 10.36          | 185.73       | 0.0        | 1.0        | $5 * 10^{-4}$                     | 60.0           |
| 45-degree | 80.0                | 21.66          | 1702.63      | 11.66          | 251.62       | 0.0        | 1.0        | $5 * 10^{-4}$                     | 45.0           |
| 90-degree | 80.0                | 17.79          | 2427.84      | 15.16          | 339.68       | 0.0        | 1.0        | $5 * 10^{-4}$                     | 25.0           |

The numerical work based on the obtained material parameters compared with the experimental results is presented in Figure 4.6. An agreement is observed pre-necking, while post-necking the numerical results display a more sudden and complete fracture characteristic than the experimental results. The model is assumed sufficient to study the structural response of sandwich panels exposed to blast loading.

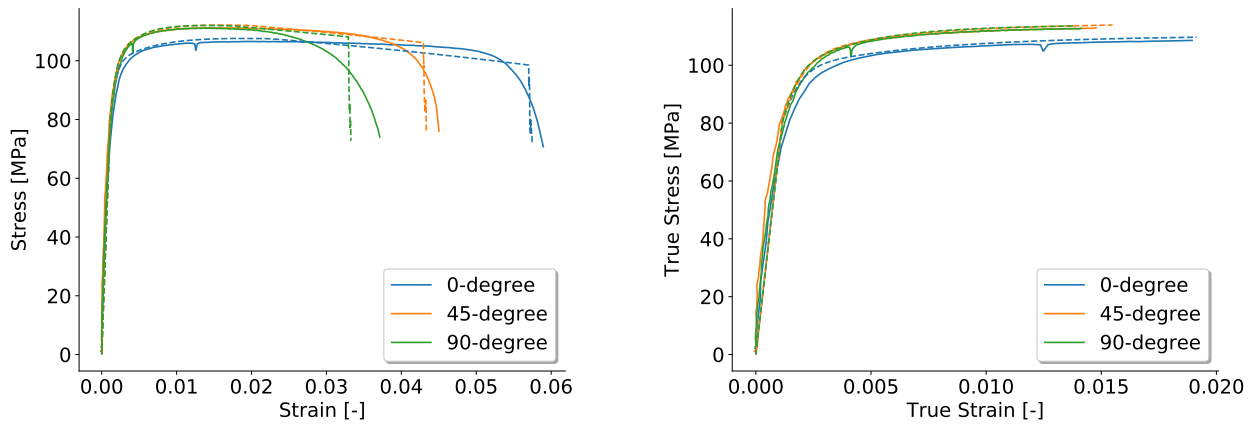


Figure 4.6: Numerical (dashed line) and experimental comparison of engineering stress-strain curves (left) and true stress-strain curves (right).

## 4.2 Steel

In the current study skins made from 0.8 mm thick plates of DOCOL 600DL steel were used. DOCOL 600DL is a dual-phase, cool-rolled steel, manufactured by Swedish Steel Ltd (SSAB). The heat treatment of the steel gives a two-phase structure with ferrite and martensite. The ferrite gives the steel good formability, and the martensite gives high strength properties [57]. The chemical composition of the material is given in Table 4.5. Table 4.6 presents the physical material constants for the steel used in the material models.

Table 4.5: Chemical composition of DOCOL 600DL [18].

| C [%] | Si [%] | Mn [%] | P [%] | S [%] | Al [%] | Fe [%] |
|-------|--------|--------|-------|-------|--------|--------|
| 0.10  | 0.40   | 1.50   | 0.010 | 0.002 | 0.040  | Rest   |

Table 4.6: Physical material constants for DOCOL 600DL steel [2].

| $E$<br>[GPa] | $\nu$<br>[-] | $\rho$<br>[kg/m <sup>3</sup> ] | $\alpha$<br>[K <sup>-1</sup> ] | $C_p$<br>[J/kgK] | $\chi$<br>[-] | $T_r$<br>[K] | $T_m$<br>[K] |
|--------------|--------------|--------------------------------|--------------------------------|------------------|---------------|--------------|--------------|
| 210          | 0.33         | 7850                           | $1.2 * 10^{-5}$                | 452              | 0.9           | 293          | 1800         |

No material test was performed on DOCOL 600DL in this study, as the material has been thoroughly studied in previous work [1]. Necessary material parameters for DOCOL 600DL was obtained from a study by Holmen et al. [1] and are presented in Table 4.7.

Table 4.7: Material parameters for the constitutive relation for DOCOL 600DL steel [1].

| $\sigma_0$<br>[MPa] | $Q_1$<br>[MPa] | $C_1$<br>[-] | $Q_2$<br>[MPa] | $C_2$<br>[-] | $c$<br>[-] | $m$<br>[-] | $\dot{p}_0$<br>[s <sup>-1</sup> ] | $W_c$<br>[MPa] |
|---------------------|----------------|--------------|----------------|--------------|------------|------------|-----------------------------------|----------------|
| 325.7               | 234.8          | 56.2         | 445.7          | 4.7          | 0.01       | 1.0        | $5 * 10^{-4}$                     | 60             |

## 4.3 Foam

In the current study, the foam cores used in the sandwich panels are made from 50.0 *mm* thick plates of XPS foam produced by Sundolitt, with three different densities, namely XPS-250, XPS-400 and XPS-700 with nominal densities of 33, 37 and 50  $kg/m^3$ , respectively. XPS is a closed cell foam which is mainly used as insulation due to its low thermal conductivity. The foam is produced from molten polystyrene mixed with a gas phase before it is extruded through a nozzle to obtain the wanted shape. Since XPS is a highly flammable material, a flame retardant has to be added before it is used as thermal insulation [58] or in protective applications. Since the main objective of this study is the structural response to blast load, this will not be further addressed.

No material test was performed for the foam types in this study. However, experimental data for compression tests from XPS-250, XPS-400 and XPS-700 was obtained from a previous study by Sigurdsson [3]. The results from the previously conducted study were used to validate the numerical foam compression model, facilitate an investigation of the densification initiation strain of the foam types and introduce a density-dependent model.

### 4.3.1 Material Parameters

The material parameters  $\sigma_{c0}$ ,  $\alpha_2$ ,  $\beta$ ,  $\gamma$  and  $\varepsilon_d$  can be obtained by inverse modeling by trial and error in the optimization software LS-OPT in combination with LS-DYNA results. LS-OPT uses a least-square method to match the experimental curve with a similar curve from LS-DYNA. This method has been used in previous work by Berdal and Bjørgero [33] based on extensive experimental data on XPS foams by Sigurdsson [3]. The resulting material parameters are shown in Table 4.8. Note that the collapse initiation strain,  $\sigma_{c0}$ , is the same material parameter as the yield stress,  $\sigma_y$ , from Berdal and Bjørgero [33] which is also the same material parameter as the plateau stress,  $\sigma_p$ , from LS-DYNA keyword user's manual [59].

Table 4.8: Material parameters for the constitutive relation for XPS-foams [33].

| Material | $\rho$<br>[ $kg/m^3$ ] | $E$<br>[ $MPa$ ] | $\sigma_{c0}$<br>[ $MPa$ ] | $\alpha_2$<br>[-] | $\beta$<br>[-] | $\gamma$<br>[-] | $\varepsilon_d$<br>[-] |
|----------|------------------------|------------------|----------------------------|-------------------|----------------|-----------------|------------------------|
| XPS-250  | 33.0                   | 13.71            | 0.257                      | 26.43             | 5.51           | 0.771           | 3.36                   |
| XPS-400  | 37.0                   | 18.47            | 0.412                      | 38.96             | 5.05           | 0.707           | 3.68                   |
| XPS-700  | 50.0                   | 23.45            | 0.732                      | 56.87             | 4.70           | 0.287           | 3.46                   |

### 4.3.2 Numerical Validation

A numerical model of the specimen used in compression tests was created to validate the material parameters obtained by Berdal and Bjørgero [33]. The same constitutive model, element formulation and hourglass control as described in Section 3.2 was applied to the numerical model of the compression test specimen. The geometry of the foam specimens were cubic, with dimensions 50x50x50  $mm^3$  [3]. The model was meshed with an element size of 2.5 *mm*. To simulate the compression test setup, two rigid plates were modeled, as seen in Figure 4.7. The bottom plate was given fixed boundary conditions, while a velocity of 80 *m/s* was applied to the top plate for 0.6 seconds.

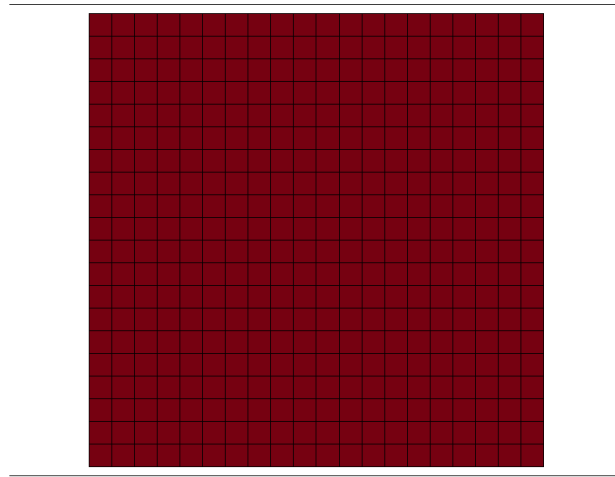


Figure 4.7: Numerical foam compression test model.

Figure 4.8 shows the true stress-strain curves for numerical and experimental compression tests for all three XPS-variations. It is observed that the numerical results are in good agreement with the experimental results for all three XPS-variations.

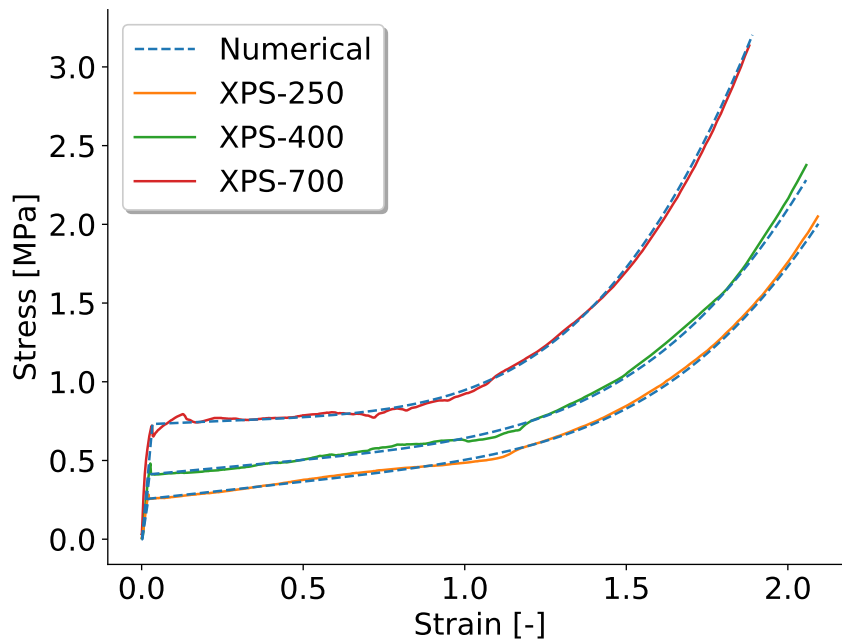


Figure 4.8: True stress-strain curves from compression tests for XPS-250, XPS-400 and XPS-700 (solid lines) and numerical validation results (dashed lines) using material parameters from Table 4.8.

### 4.3.3 Plastic Properties

The collapse initiation stress,  $\sigma_{c0}$ , and the collapse initiation strain,  $\varepsilon_{c0}$ , is obtained at the first stress peak and are usually used to indicate the yield strength. An offset yield point of 0.3 % strain might be used to determine the initial yield strength, but it requires the knowledge of elastic modulus which may vary with strain and needs considerable extra effort to obtain accurate measurements [24].

The densification initiation strain,  $\varepsilon_{d0}$ , was obtained from the energy absorption efficiency method [26], where the densification initiation strain corresponds to maximum energy absorption efficiency. The energy absorption efficiency,  $\eta$ , is defined as

$$\eta(\varepsilon) = \frac{1}{\sigma(\varepsilon)} \int_0^\varepsilon \sigma(\varepsilon) d\varepsilon \quad (4.7)$$

where  $\sigma$  is the true stress and  $\varepsilon$  is the true strain. The average plateau stress,  $\sigma_p$ , is obtained by the energy equivalence in the plateau stage, defined as

$$\sigma_p = \frac{\int_{\varepsilon_{c0}}^{\varepsilon_{d0}} \sigma(\varepsilon) d\varepsilon}{\varepsilon_{d0} - \varepsilon_{c0}} \quad (4.8)$$

The experimental and numerical efficiency-strain curves obtained by Eq. 4.7 for XPS-250, XPS-400 and XPS-700 foams are presented in Figure 4.9.

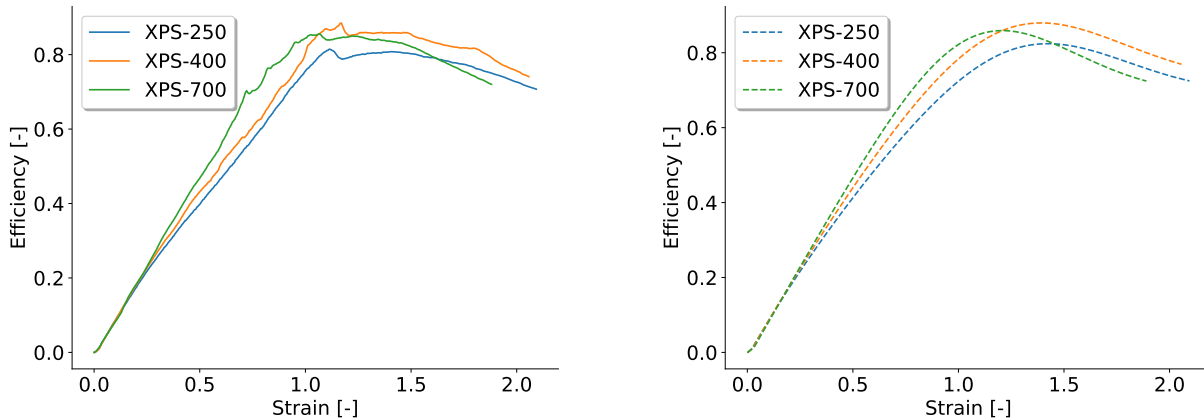


Figure 4.9: Energy absorption efficiency plotted with true strain for experimental data (left) and numerical simulations (right) for XPS-250, XPS-400 and XPS-700.

In any foam applications involving energy absorption and protection, the densification strain plays an important role [26]. Table 4.9 and 4.10 presents the collapse initiation strain, densification initiation strain and plateau stress for the experimental and numerical results. It is observed that the numerical plateau stress is around 10 % higher than the experimental values, while the densification initiation strain is up to 30 % higher than the experimental values. The parameters obtained from the numerical results will be used in comparison to numerical values from component tests in Chapter 6.

Table 4.9: Experimental energy absorption efficiency parameters for XPS-foams.

| Foam    | $\varepsilon_{c0}$<br>[-] | $\varepsilon_{d0}$<br>[-] | $\sigma_p$<br>[MPa] |
|---------|---------------------------|---------------------------|---------------------|
| XPS-250 | 0.02                      | 1.11                      | 0.38                |
| XPS-400 | 0.03                      | 1.17                      | 0.53                |
| XPS-700 | 0.03                      | 1.07                      | 0.80                |

Table 4.10: Numerical energy absorption efficiency parameters for XPS-foams.

| Foam    | $\varepsilon_{c0}$<br>[-] | $\varepsilon_{d0}$<br>[-] | $\sigma_p$<br>[MPa] |
|---------|---------------------------|---------------------------|---------------------|
| XPS-250 | 0.02                      | 1.43                      | 0.44                |
| XPS-400 | 0.03                      | 1.39                      | 0.58                |
| XPS-700 | 0.04                      | 1.21                      | 0.84                |

#### 4.3.4 Density-Dependent Model

A density-dependent model was calibrated by Berdal and Bjørge [33] to study densities outside of the density range of the experimental program. The model is based on the study by Hanssen et al. [31] on aluminum foam. Note that the density-dependent model by Berdal and Bjørge is calibrated to the material parameters obtained by direct calibration and not the material parameters obtained with LS-OPT as used in this thesis.

The material parameters were obtained by a power law expression including the foam density, defined as

$$E, \sigma_{c0}, \alpha_2, \beta, \gamma = C_0 + C_1 \left( \frac{\rho_f}{\rho_{f0}} \right)^n \quad (4.9)$$

where  $\rho_f$  is the foam density,  $\rho_{f0}$  is the foam base material density,  $C_0$ ,  $C_1$  and  $n$  are constants for each material parameter.

While the densification strain utilized in this thesis was obtained by optimization with LS-OPT, the densification strain in the density-dependent model was calculated with the theoretical expression presented in Section 2.5.1, and as defined by Eq. 4.10. Therefore, a deviation in the densification strain is expected.

$$\varepsilon_d = -\ln \left[ \frac{\rho_f}{\rho_{f0}} \right] \quad (4.10)$$

The calibrated constants for the density-dependent material model, obtained by Berdal and Bjørge [33], is presented in Table 4.11. Note that the calibration of Young's modulus was not stated in [33] and was therefore calibrated from Eq. 4.9. The material parameters obtained with the density-dependent model for XPS-250, XPS-400, and XPS-700 are presented in Table 4.12.

Table 4.11: Constants for the density-dependent material model for XPS foam based on power law curve fit [33].

|       | $E$      | $\sigma_{c0}$ | $\alpha_2$ | $1/\beta$ | $\gamma$ |
|-------|----------|---------------|------------|-----------|----------|
| $C_0$ | -2000.00 | 0.00          | 10.01      | 0.17      | 0.00     |
| $C_1$ | 2091.93  | 700           | 1.62       | 54.81     | 1.074e-4 |
| $n$   | 0.011    | 2.27          | -0.39      | 2.11      | -2.62    |

Table 4.12: Density-dependent material parameters for XPS-250, XPS-400 and XPS-700.

| Material   | $\rho$<br>[ $kg/m^3$ ] | $E$<br>[ $MPa$ ] | $\sigma_{c0}$<br>[ $MPa$ ] | $\alpha_2$<br>[-] | $\beta$<br>[-] | $\gamma$<br>[-] | $\varepsilon_d$<br>[-] |
|------------|------------------------|------------------|----------------------------|-------------------|----------------|-----------------|------------------------|
| XPS-250_dd | 33.0                   | 14.71            | 0.279                      | 16.16             | 4.82           | 0.837           | 3.45                   |
| XPS-400_dd | 37.0                   | 17.32            | 0.366                      | 15.89             | 4.58           | 0.614           | 3.33                   |
| XPS-700_dd | 50.0                   | 23.98            | 0.726                      | 15.24             | 3.83           | 0.279           | 3.03                   |

The density-dependent stress-strain curves are compared with the experimental results for validation in Figure 4.10. It is observed that the density-dependent model captures the general shape of the stress-strain curves for strains lower than 1.5, but the initial collapse stress deviates slightly from the initial numerical work for XPS-250 and XPS-400. The deviations between the experimental results and the numerical density-dependent results increase for larger strains.

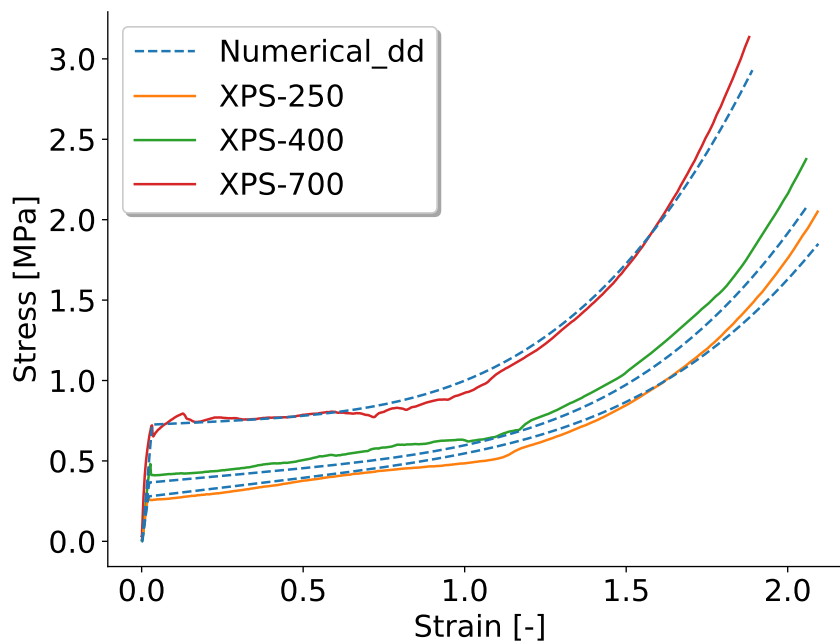


Figure 4.10: Stress-strain curves from compression tests for XPS-250, XPS-400 and XPS-700 (solid lines) and density-dependent numerical model validation results (dashed lines) using material parameters from Table 4.12.



The calculated energy absorption efficiency parameters for the density-dependent model for XPS-250, XPS-400 and XPS-700 are presented in Table 4.13. From a comparison with Table 4.10, it is observed that the collapse initiation strains are fairly similar, the densification initiation strains increase with around 10 % and the plateau stress increase slightly for XPS-250 and XPS-700 while decrease for XPS-400.

Table 4.13: Numerical energy absorption efficiency parameters for XPS-250, XPS-400 and XPS-700 obtained with the density-dependent model.

| Foam       | $\varepsilon_{c0}$<br>[-] | $\varepsilon_{d0}$<br>[-] | $\sigma_p$<br>[MPa] |
|------------|---------------------------|---------------------------|---------------------|
| XPS-250_dd | 0.02                      | 1.55                      | 0.51                |
| XPS-400_dd | 0.02                      | 1.43                      | 0.54                |
| XPS-700_dd | 0.03                      | 1.31                      | 0.89                |

Material parameters for XPS foam with density varying from 30 to 100  $kg/m^3$  are presented in Table 4.14. Densities lower than 30  $kg/m^3$  gave undesired stress-strain behavior and was therefore discarded. Note that Berdal and Bjørge's density-dependent model is based on a study by Hanssen et al. [31] on varying density for aluminum foam. Therefore, extrapolation outside of the tested densities has limited validity.

Table 4.14: Material parameters for XPS foam with density varying from 30 to 100  $kg/m^3$ .

| Simulation | Density<br>[ $kg/m^3$ ] | $E$<br>[E Pa] | $\sigma_{c0}$<br>[MPa] | $\gamma$<br>[-] | $\beta$<br>[-] | $\alpha_2$<br>[-] | $\varepsilon_d$<br>[-] |
|------------|-------------------------|---------------|------------------------|-----------------|----------------|-------------------|------------------------|
| D30        | 30.0                    | 12.56         | 0.224                  | 1.082           | 4.99           | 16.40             | 3.55                   |
| D40        | 40.0                    | 18.89         | 0.430                  | 0.510           | 4.43           | 15.73             | 3.26                   |
| D50        | 50.0                    | 23.81         | 0.713                  | 0.285           | 3.85           | 15.25             | 3.04                   |
| D60        | 60.0                    | 27.84         | 1.079                  | 0.177           | 3.31           | 14.90             | 2.85                   |
| D70        | 70.0                    | 31.25         | 1.530                  | 0.118           | 2.84           | 14.61             | 2.70                   |
| D80        | 80.0                    | 34.21         | 2.072                  | 0.082           | 2.43           | 14.38             | 2.57                   |
| D90        | 90.0                    | 36.83         | 2.708                  | 0.061           | 2.08           | 14.19             | 2.45                   |
| D100       | 100.0                   | 39.17         | 3.439                  | 0.046           | 1.79           | 14.02             | 2.34                   |

The numerical stress-strain and efficiency-strain curves for XPS foam with density varying from 30 to 100  $kg/m^3$  are presented in Figure 4.11 with associated energy absorption efficiency parameters presented in Table 4.15. It is observed that densities higher than 60  $kg/m^3$  does not have a local maximum efficiency and therefore not a densification initiation strain. This is a consequence of the shape of the stress-strain curves which does not include the distinguished plateau and densification regime. This emphasizes the limitations of the density-dependent model and will be further discussed in Chapter 7. However, the density-dependent model is assumed sufficient to study the general trends of sandwich components with varying foam core density.

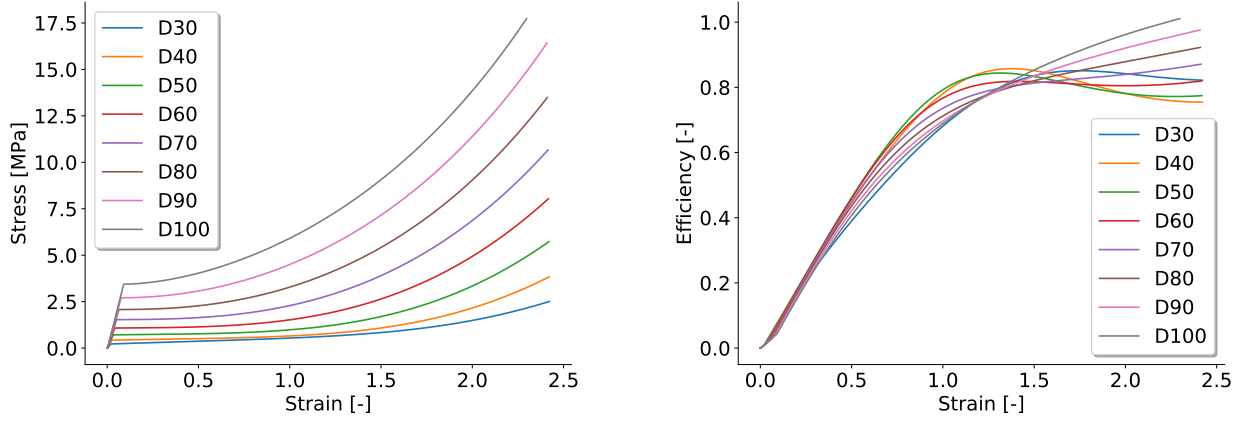


Figure 4.11: True stress (left) and energy absorption efficiency (right) plotted with true strain for XPS foam with density varying from 30 to 100  $kg/m^3$ .

Table 4.15: Numerical density-dependent energy absorption efficiency parameters for XPS foam with density varying from 30 to 100  $kg/m^3$ .

| Simulation | $\rho$<br>[ $kg/m^3$ ] | $\varepsilon_{c0}$<br>[-] | $\varepsilon_{d0}$<br>[-] | $\sigma_p$<br>[ $MPa$ ] |
|------------|------------------------|---------------------------|---------------------------|-------------------------|
| D30        | 30.0                   | 0.02                      | 1.74                      | 0.54                    |
| D40        | 40.0                   | 0.03                      | 1.38                      | 0.58                    |
| D50        | 50.0                   | 0.03                      | 1.31                      | 0.87                    |
| D60        | 60.0                   | 0.04                      | 1.41                      | 1.39                    |
| D70        | 70.0                   | 0.05                      | -                         | -                       |
| D80        | 80.0                   | 0.07                      | -                         | -                       |
| D90        | 90.0                   | 0.08                      | -                         | -                       |
| D100       | 100.0                  | 0.09                      | -                         | -                       |

## 4.4 Main Findings

In this section, the main findings of the material study are summarized.

- Material tests for the AA1050-H14 aluminum alloy on the 0-degree, 45-degree and 90-degree direction of the material, relative to the rolling direction provided accurate material parameters for further numerical work.
- The Cockcroft-Latham fracture parameter was calibrated by trial and error for each material direction of the AA1050-H14 aluminum alloy.
- A validation of material parameters obtained from [33] for XPS-250, XPS-400 and XPS-700 showed good agreement between experimental and numerical compression tests.
- Experimental and numerical energy adsorption efficiency parameters, such as the densification initiation strain and the average plateau stress was found for XPS-250, XPS-400 and XPS-700.
- Calibration and validation of a density-dependent material model was performed, which showed good agreement between experimental results and results provided by the density-dependent model for small strains, with the deviation growing with increased strains.
- The density-dependent material model was used to obtain material parameters for densities outside the experimental range. The density-dependent model was observed to give unsatisfying material behavior for densities below  $30 \text{ kg/m}^3$  and was therefore discarded.
- No densification initiation strain could be obtained for densities above  $60 \text{ kg/m}^3$ , with the density-dependent model due to no distinct plateau and densification regime in the stress-strain curves.

# Chapter 5

## Experimental Work

In this chapter the experimental work conducted and the obtained results are presented. The results serve as a basis of comparison for numerical simulations and as an indicator of mechanisms in sandwich components consisting of two skins and a foam core. All experiments were performed at the shock tube facility at SIMLab, NTNU. Experimental data from a previous study performed in the same facility conducted by Sigurdsson [3] is included for comparison and completeness of the experimental results.

### 5.1 Experimental Setup and Program

The shock tube facility was used to recreate loading conditions similar to those that occur during explosive detonations. The shock tube offers a controlled alternative to a detonation of explosives, which makes the replication of the experiments and the experimental conditions easier. The experimental program consists of fourteen separate experiments, where five were performed on skin configurations without a foam core tested at different firing pressures. The remaining nine experiments were performed on sandwich components with a variation of firing pressure, foam density and skin configurations. Three foam variations, XPS-250, XPS-400, and XPS-700, with nominal densities of 33, 37 and 50  $kg/m^3$ , respectively, and with a nominal thickness of 50.0  $mm$ , were used as core materials in the sandwich panels. Each foam variation was tested with both AA1050-H14 skins and a combination of an AA1050-H14 front skin and a DOCOL 600DL back skin. The skins had a nominal thickness of 0.8  $mm$ . The sandwich panels with aluminum skins were subjected to 10 and 15  $bar$  firing pressure, while the sandwich panels with an aluminum front skin and steel back skin were subjected to 35  $bar$  firing pressure. No bonding agent was used between the foam and the skins. The primary goal of the experiments was to investigate the response of the sandwich panels, with regards to a variety of foam core material and skin configuration, under blast load conditions, and to get a basis of comparison for further numerical analyses and validation. The test program is summarized in Table 5.1 and 5.2.

A skin combination of aluminum front and back skin will be abbreviated as "Al", and a combination of an aluminum front and steel back skin will be abbreviated "AlS" for the rest of this thesis.

Table 5.1: Experimental program for Al configurations in the shock tube facility.

| Test Name     | Core Material | Skin Material | Firing Pressure<br>[bar] |
|---------------|---------------|---------------|--------------------------|
| S_Al_P10      | -             |               |                          |
| SW_Al_250_P10 | XPS-250       | AA1050-H14    | 10                       |
| SW_Al_400_P10 | XPS-400       |               |                          |
| SW_Al_700_P10 | XPS-700       |               |                          |
| S_Al_P15      | -             |               |                          |
| SW_Al_250_P15 | XPS-250       | AA1050-H14    | 15                       |
| SW_Al_400_P15 | XPS-400       |               |                          |
| SW_Al_700_P15 | XPS-700       |               |                          |
| S_Al_P25      | -             | AA1050-H14    | 25                       |

Table 5.2: Experimental program for AIS configurations in the shock tube facility.

| Test Name      | Core Material | Skin Material             | Firing Pressure<br>[bar] |
|----------------|---------------|---------------------------|--------------------------|
| S_AIS_P25      | -             | AA1050-H14 and DOCOL 600L | 25                       |
| S_AIS_P35      | -             |                           |                          |
| SW_AIS_250_P35 | XPS-250       | AA1050-H14 and DOCOL 600L | 35                       |
| SW_AIS_400_P35 | XPS-400       |                           |                          |
| SW_AIS_700_P35 | XPS-700       |                           |                          |

The foam cores and the skins were pre-drilled with twenty-four bolt holes as shown in Figure 5.1 (left). The dimensions and the mass of the foam cores were recorded to calculate real densities for the specimens and can be seen in Appendix A. Generally, the measured real densities showed agreement with the nominal densities. However, deviations were present, which is likely due to challenges related to the cutting process of the foam specimens. To impose fixed boundary conditions, the sandwich components and the skins were clamped to the end of the driven section of the SSTF, presented in Section 2.2, using a clamping frame and twelve bolts. In the clamped configuration, a 300 mm x 300 mm area of the test specimen were exposed to the shock wave, as seen in Figure 5.1 (middle). The thickness of the skins, the foam core and the clamping frames are illustrated in Figure 5.1 (right).

As discussed in Section 3.4, previous studies indicate that using a single nut to fix sandwich panels to the test rig have introduced challenges related to tightening the nuts without applying stress to the foam core [3] and still maintaining fixed boundary conditions. As presented in Section 3.4, two solutions were proposed; the use of two nuts or a distance piece between the clamping frame and the test rig. For the solution including two nuts, the inner nut would be fastened with a torque wrench set to 2 Nm, while the outer nut would be locked against the first nut with a torque wrench set to 100 Nm, as seen in Figure 5.2. Considering the pre-experimental work related to the solution including distance pieces, the solution including two nuts was preferred and used for initial experiments. A physical inspection of the tautness of the two nuts after the conduction of two experiments on sandwich components, lead to the conclusion that the solution provided sufficient tautness of the nuts and the distance piece proposal was discarded for further experimental work.

Pressure sensors placed along the driven section are used to measure the shock wave as it propagates towards the test component. Sensor number P01-1 and P01-2 are placed closest to the test specimen, as seen in Figure 5.3 (right). The pressure data recorded was used to obtain the peak pressure before and after the shock wave hit the test specimen, and to determine the time of impact. Two Phantom v1610 high-speed cameras were used to capture the structural response of the backside of the test specimen. One camera was placed on each side of the dump tank as seen in Figure 5.3. The recording rate of the cameras was set to 37000 *fps* with an image resolution of 768 x 800 pixels, for all experiments.

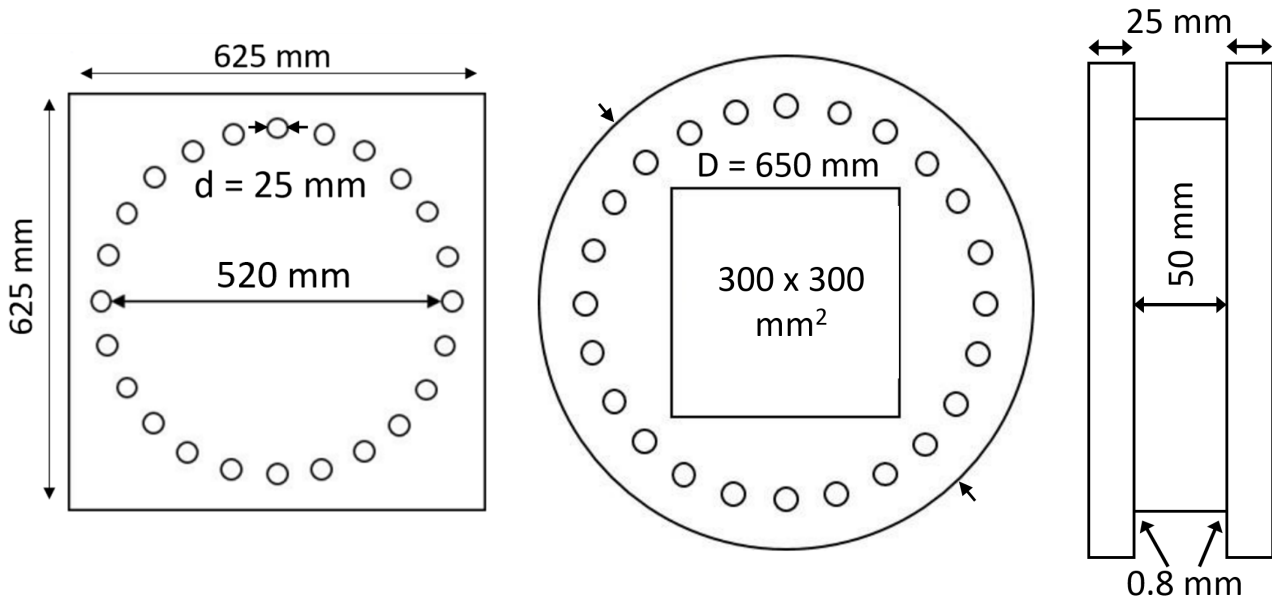


Figure 5.1: Top view of component (left) and clamping frame geometry (middle) and side view of the clamped component (right). Illustration based on [2].

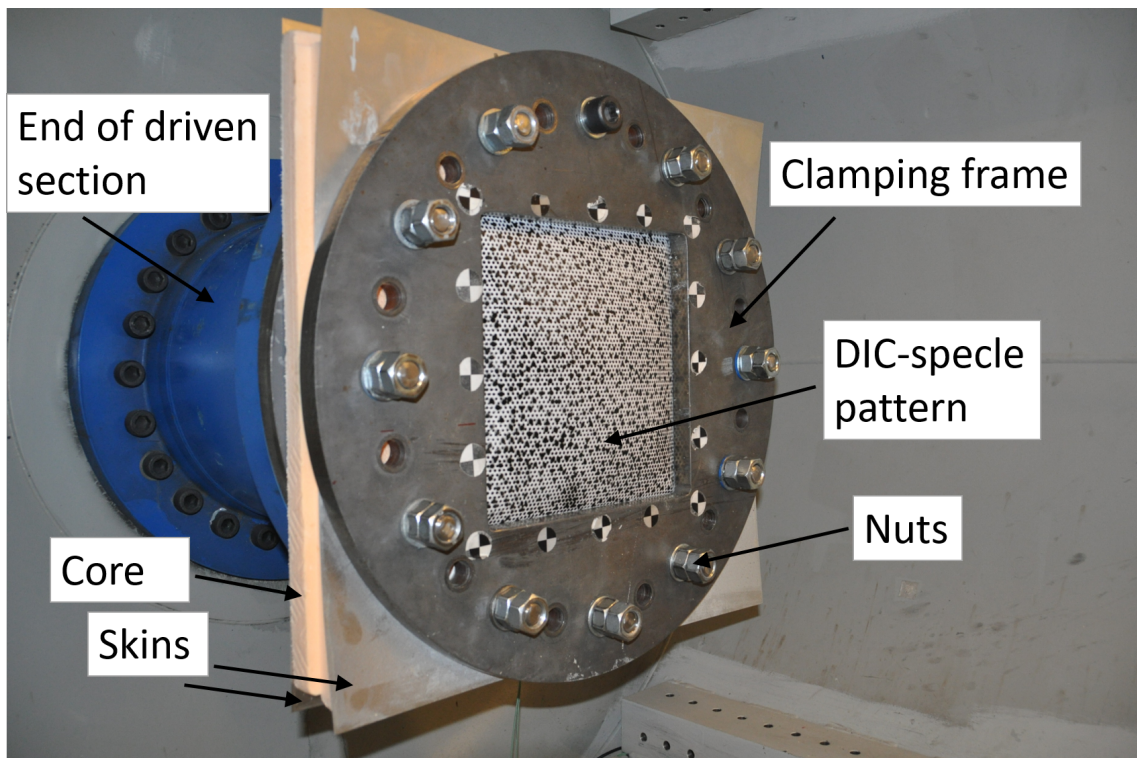


Figure 5.2: Picture of clamping configuration for sandwich panels in test rig.

## 5.2 Three-Dimensional Digital Image Correlation

Three-dimensional digital image correlation (3D-DIC) is a technique used in post-processing of experimental results. 3D-DIC can be used to obtain displacements and strains from high-speed camera images. It is an accurate and fast technique that can track large displacements and capture local deformations. It is dependent on sufficient image quality and accurate camera calibrations to obtain accurate results. The two high-speed cameras used in this thesis was positioned as seen in Figure 5.3 and synchronized with pressure transducers.

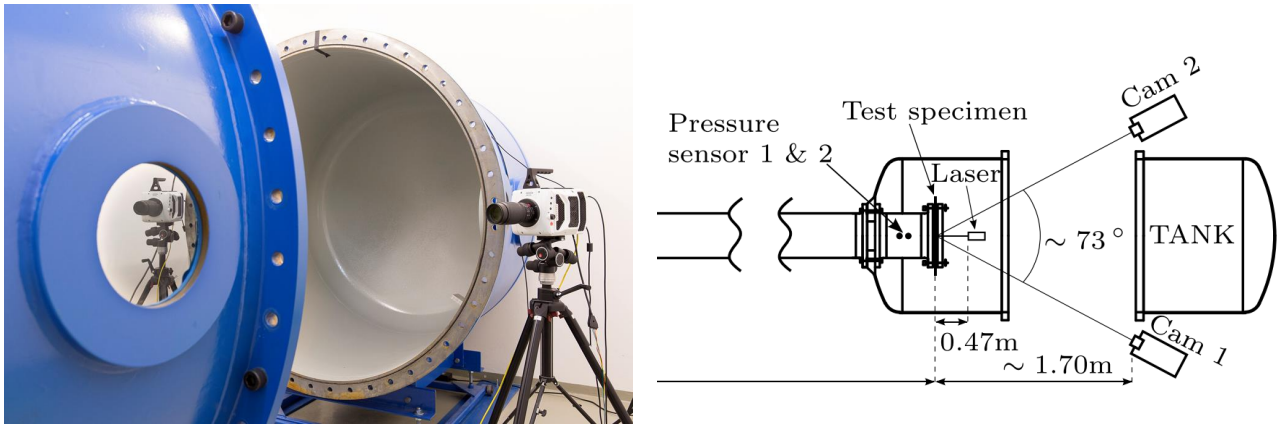


Figure 5.3: Picture (left) and schematic illustration (right) of SSTF camera setup [2].

The back skin of the specimens was painted with a speckle pattern shown in Figure 5.2 to ensure uniqueness of grey scale values in the elements during DIC-analysis. To analyze the pictures using 3D-DIC, the software eCorr was used. The software utilizes finite element formulations to calculate displacements and strains in the mesh applied during analysis. An illustration of the 3D-DIC processes and results obtained can be seen in Figure 5.5. For a more in-depth and general explanation of 3D-DIC techniques and procedures, the reader is referred to work by Fagerholt et al. [54].

Midpoint displacements were extracted by using point tracking of a subset approximately placed in the middle of the skin. To correct for movements of the shock tube due to recoil from the shock wave, tracking of subsets on the clamping frame was added. Subsets are marked as squares in Figure 5.5. The displacement of the rig was averaged and subtracted from the midpoint displacement during post-processing. Deformation profiles were extracted at four different times during the deformation processes. Maximum midpoint displacement and a corresponding point in time were obtained from the 3D-DIC analysis. Next, the times for 3/4, 2/4 and 1/4 of the specified maximum midpoint displacement was extracted together with deformation profiles corresponding to those points in time during the deformation evolution. The deformation profiles were collected horizontally across the specimen by defining a vector from the checkerboard stickers at each side of the clamping frame as seen in Figure 5.5 (left).

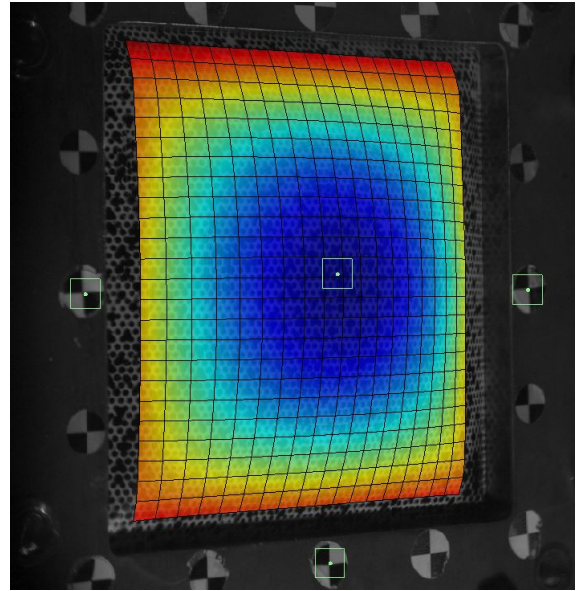
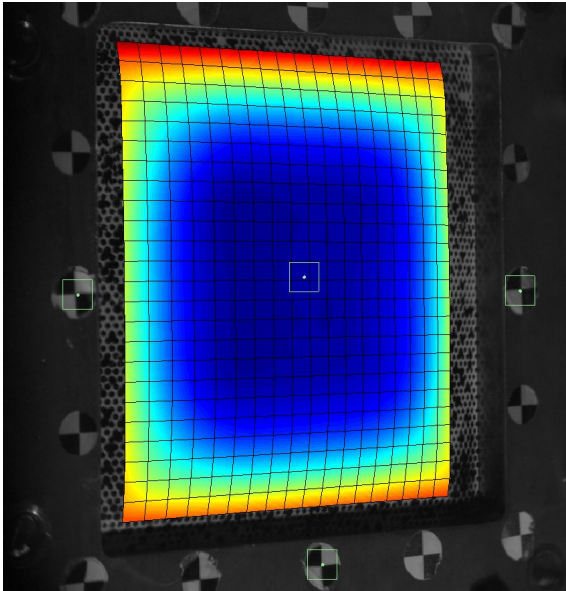
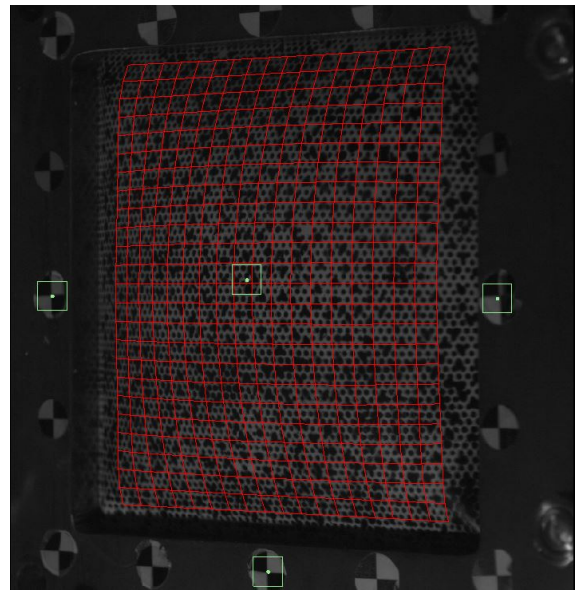
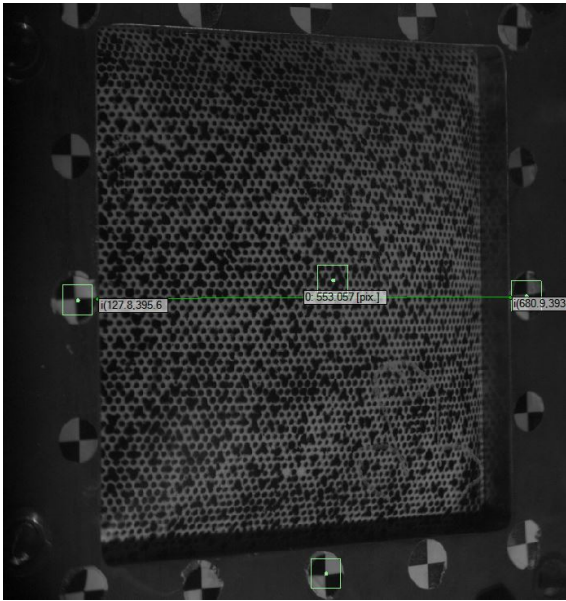


Figure 5.5: Pictures from both cameras, with vector and subsets (top left), mesh and subsets (top right), and mesh and field map showing deformation evolution (bottom left and right).



## 5.3 Results

The experimental program performed in this thesis provides results on pressure history, midpoint displacement and deformation profiles. Results for tests on Al skins are presented in Section 5.3.1, Al sandwich panels in Section 5.3.2, AIS skins in Section 5.3.3 and results on AIS sandwich panels in Section 5.3.4.

All experiments are presented with pressure histories synchronized with midpoint displacements and deformation profiles extracted at maximum midpoint displacement and  $1/4$ ,  $2/4$ ,  $3/4$  of maximum midpoint displacements. The displacement levels at which the profiles are extracted are illustrated as points on the midpoint displacement curves with the same colors as the profile plots. For the experiments where fracture was reached, a dotted horizontal line is plotted to illustrate at what approximate deformation level fracture was initiated. This gives an overall presentation of the individual results of each experiment.

Further, an investigation of pressure histories was conducted, which is presented in Section 5.3.5 and 5.3.6, followed by a closer comparison and examination of midpoint displacement in Section 5.3.7 and 5.3.8 for Al components and AIS components, respectively.

A physical measurement of the midpoint displacement of the tested specimens was recorded. This measurement was recorded as a rough validation of the results obtained through the 3D-DIC analysis, and be further discussed in Section 5.3.7 and 5.3.8. As seen in Figure 5.6, a bar was placed on the horizontal middle bolts in contact with the clamping frame to have a fixed reference for all measurements. A caliper was used to measure the distance from the bar to the deformed back skin of the test specimen.

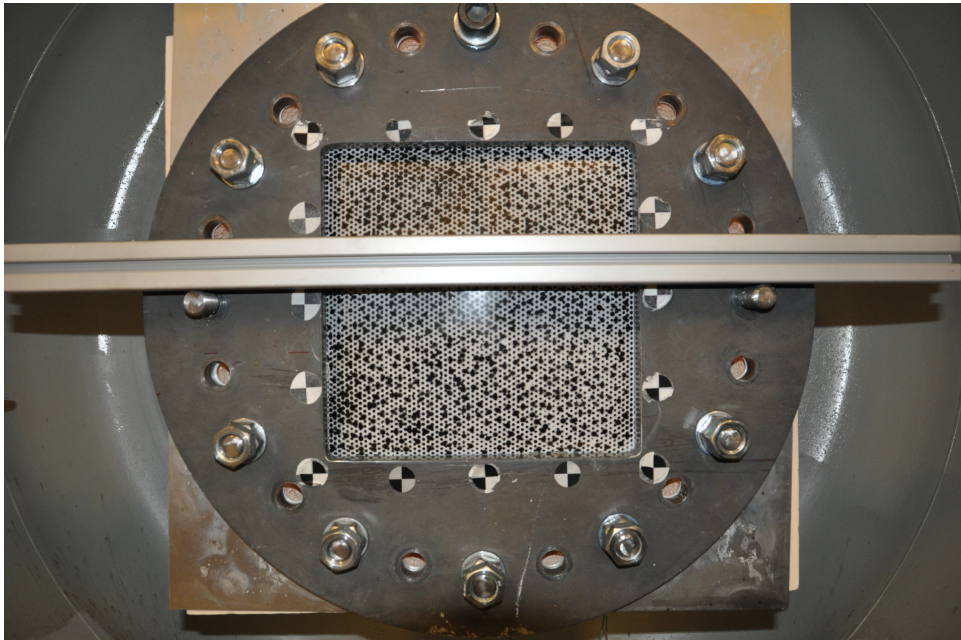
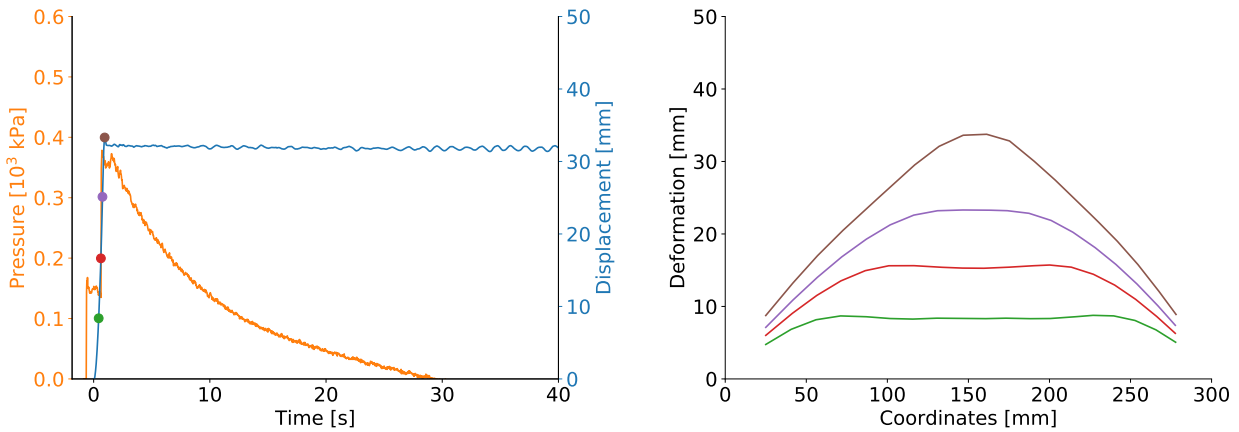
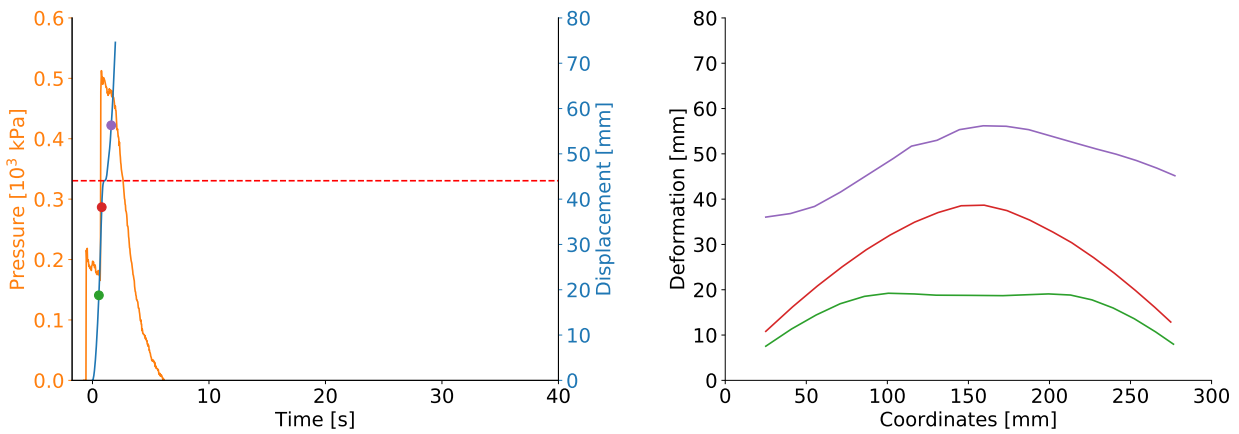


Figure 5.6: Measuring technique of midpoint displacement post-experiment.

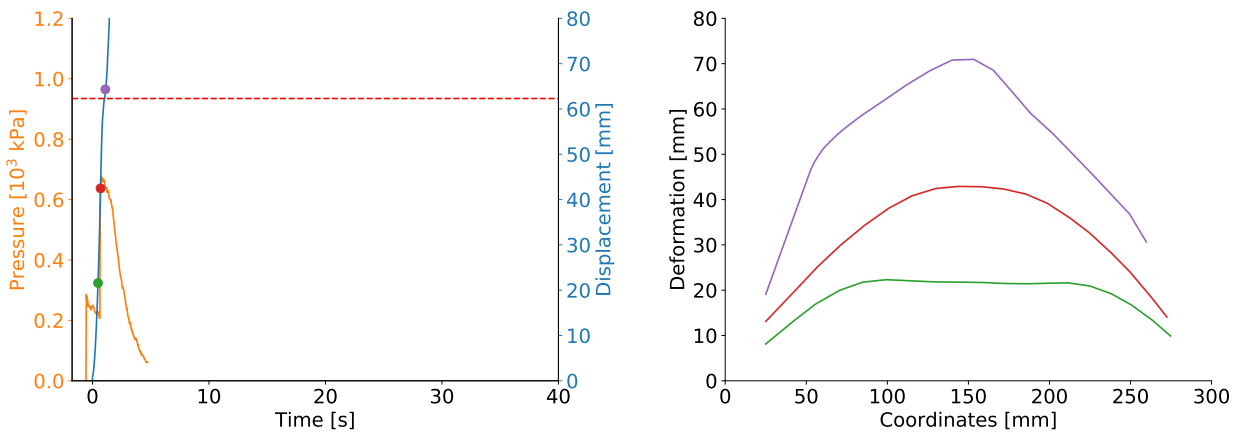
### 5.3.1 Skins - Aluminum



(a) S\_Al\_P10



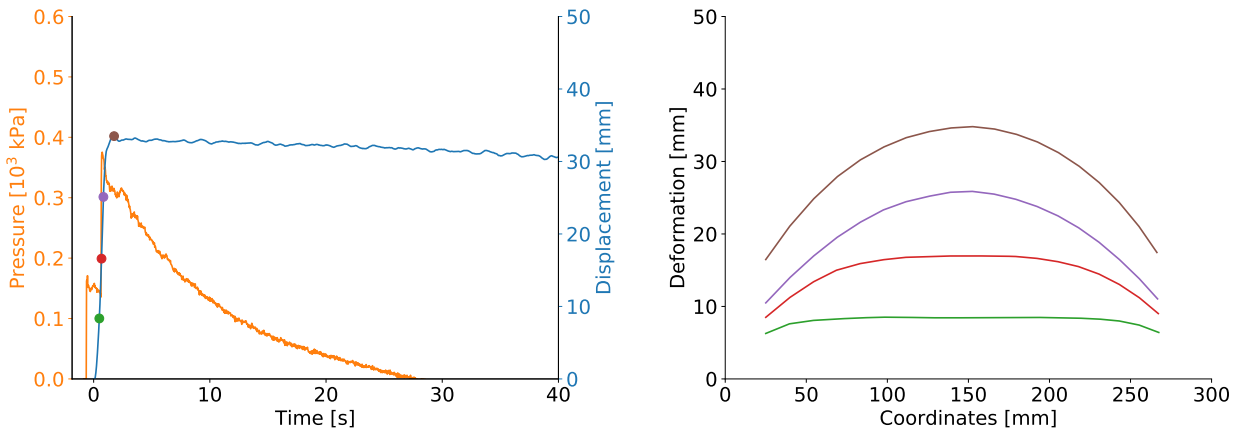
(b) S\_Al\_P15



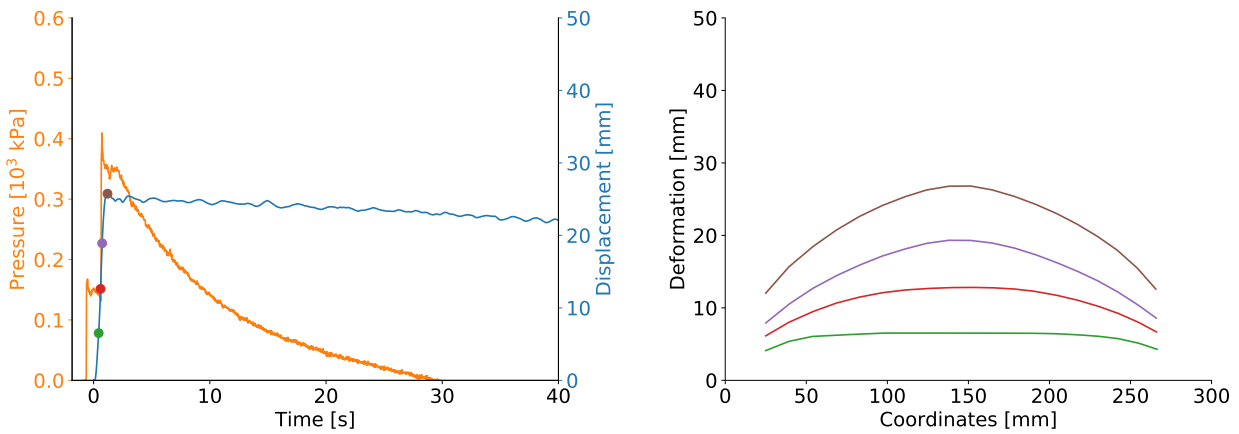
(c) S\_Al\_P25

Figure 5.7: Pressure recorded at sensor P01-1 and midpoint deflection (left) and deformation profiles at 1/4, 2/4, 3/4, and max deflection (right) for Al skins, without a foam core, exposed to 10 (top), 15 (middle) and 25 bar (bottom) firing pressure.

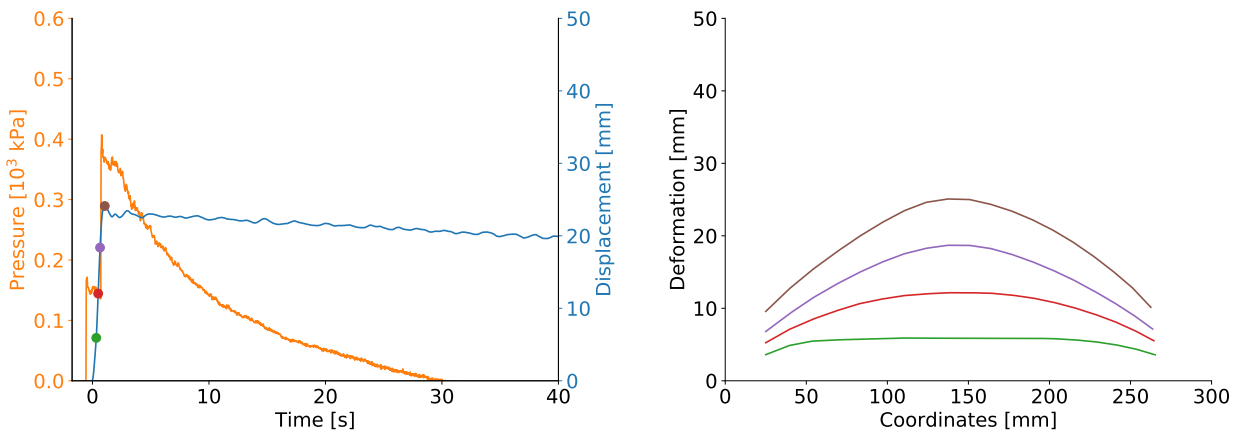
### 5.3.2 Sandwich Panels - Aluminum Skins



(a) SW\_Al\_250\_P10

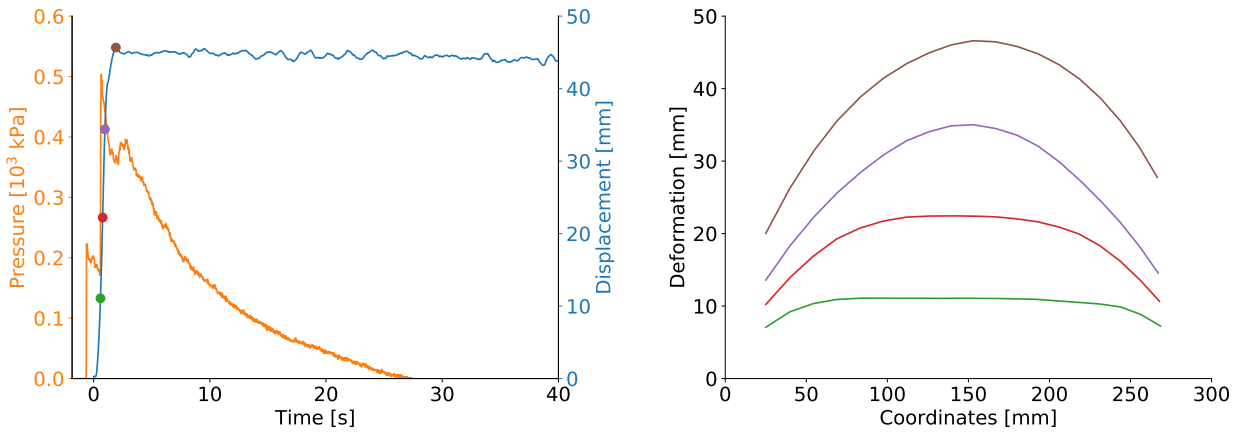


(b) SW\_Al\_400\_P10

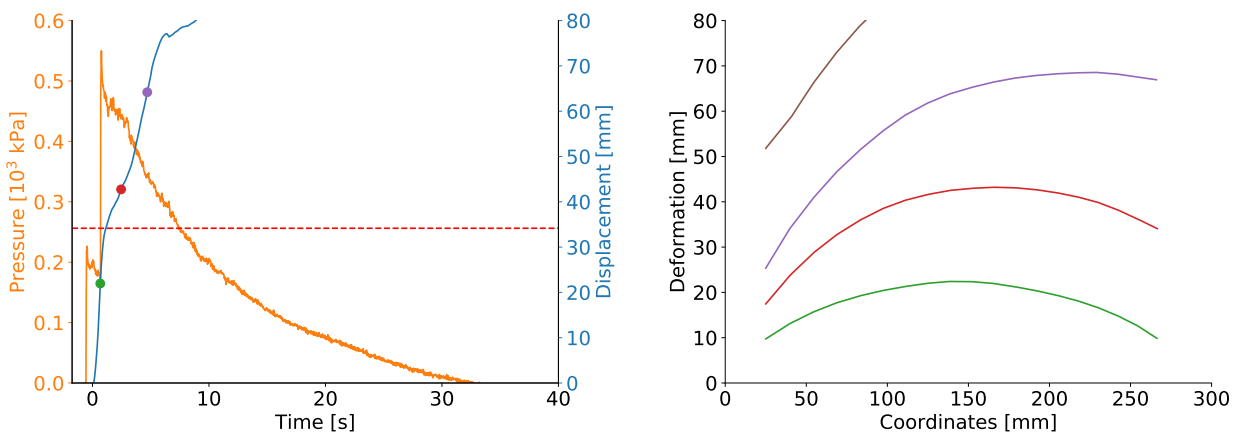


(c) SW\_Al\_700\_P10

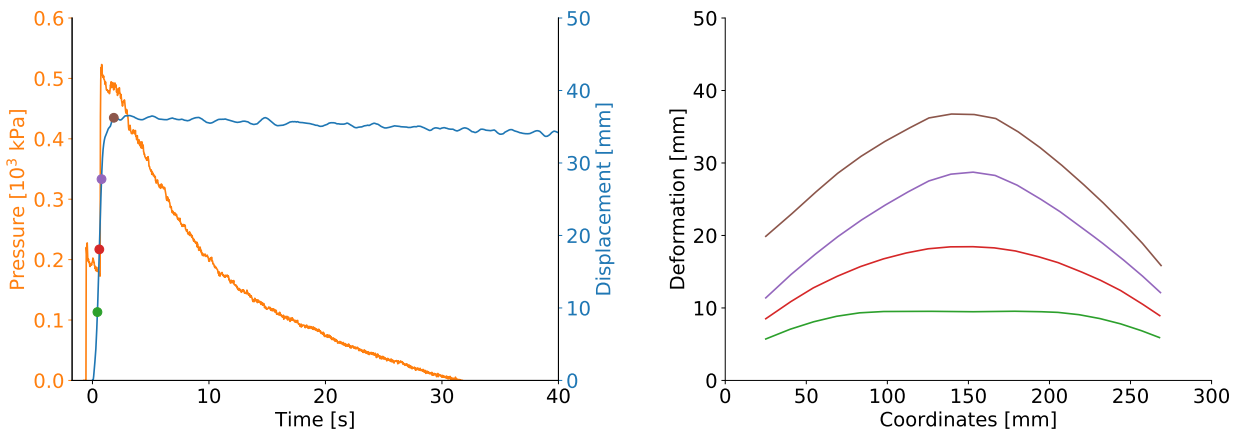
Figure 5.8: Pressure recorded at sensor P01-1 and midpoint deflection (left) and deformation profiles at 1/4, 2/4, 3/4, and max deflection (right) for Al sandwich panels with XPS-250 (top), XPS-400 (middle) and XPS-700 (bottom) as core material, exposed to 10 *bar* firing pressure.



(a) SW\_Al\_250\_P15



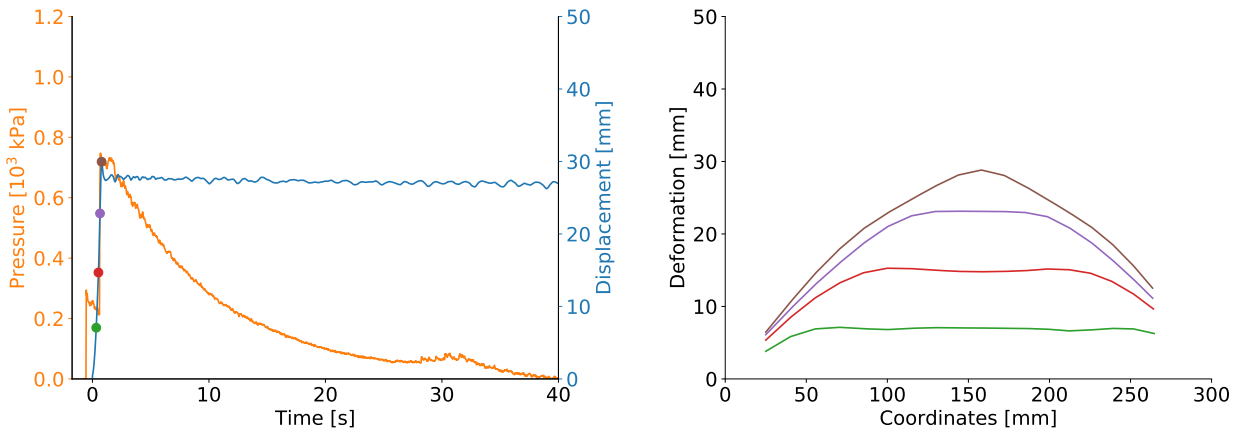
(b) SW\_Al\_400\_P15



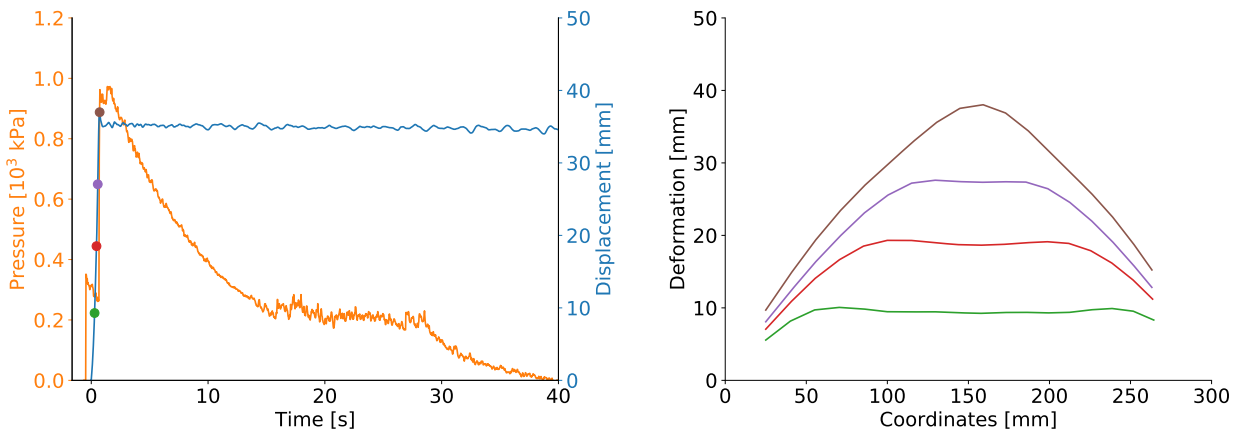
(c) SW\_Al\_700\_P15

Figure 5.9: Pressure recorded at sensor P01-1 and midpoint deflection (left) and deformation profiles at 1/4, 2/4, 3/4, and max deflection (right) for Al sandwich panels with XPS-250 (top), XPS-400 (middle) and XPS-700 (bottom) as core material, exposed to 15 *bar* firing pressure.

### 5.3.3 Skins - Aluminum and Steel



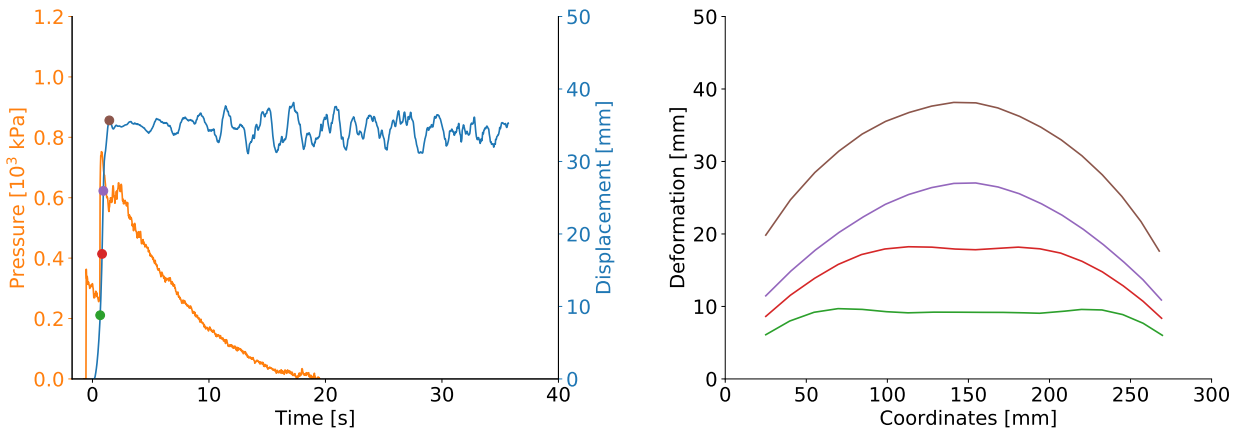
(a) S\_AIS\_P25



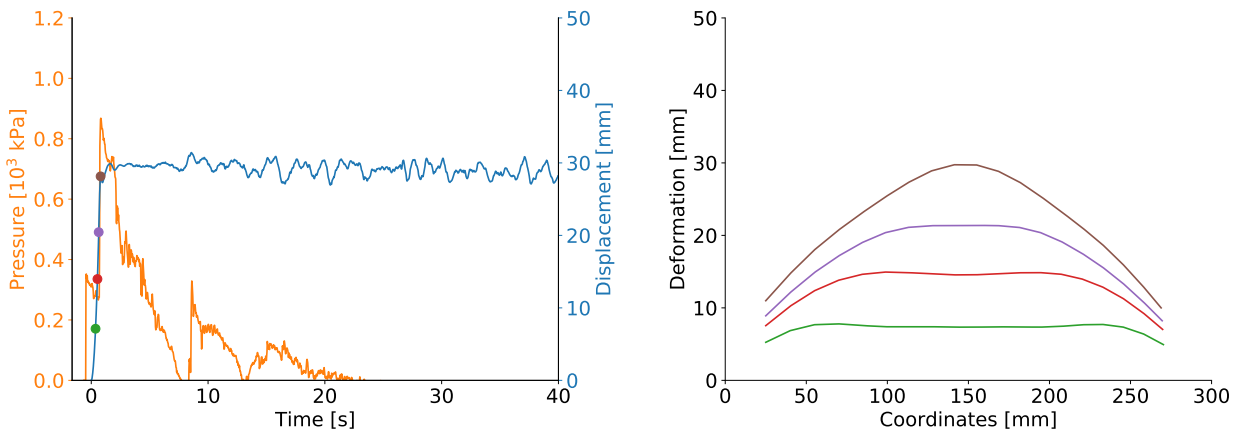
(b) S\_AIS\_P35

Figure 5.10: Pressure recorded at sensor P01-1 and midpoint deflection (left) and deformation profiles at 1/4, 2/4, 3/4, and max deflection (right) for AIS skins, without foam cores, exposed to 25 (top) and 35 *bar* (bottom) firing pressure.

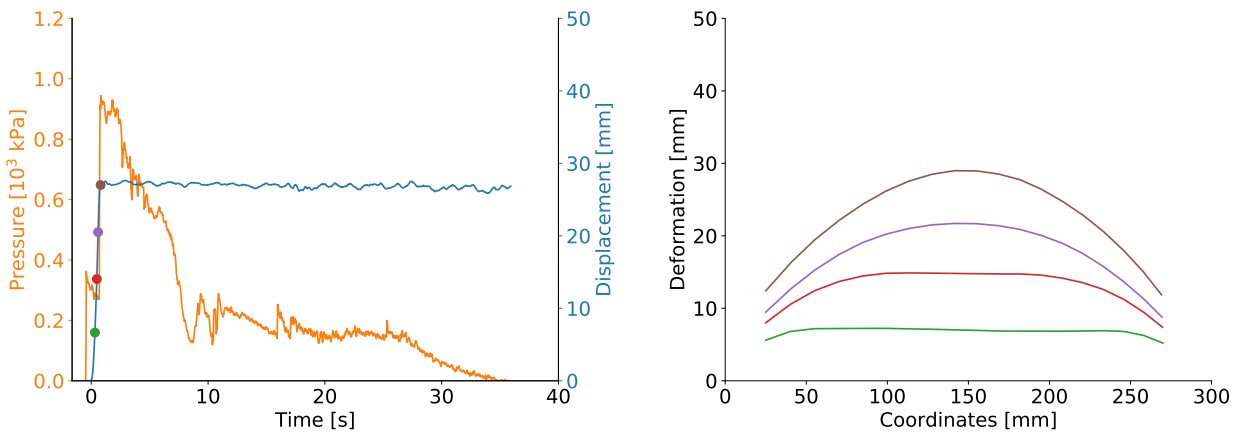
### 5.3.4 Sandwich Panels - Aluminum and Steel Skins



(a) SW\_AIS\_250\_P35



(b) SW\_AIS\_400\_P35



(c) SW\_AIS\_700\_P35

Figure 5.11: Pressure recorded at sensor P01-1 and midpoint deflection (left) and deformation profiles at 1/4, 2/4, 3/4, and max deflection (right) for AIS sandwich panels with XPS-250 (top), XPS-400 (middle) and XPS-700 (bottom) as core material, exposed to 35 bar firing pressure.

### 5.3.5 Pressure Load - Aluminum Skins

Figure 5.12 presents pressure-time curves for all Al experiments and Table 5.3 presents the recorded firing, incident and reflected peak pressure. It is clear from Table 5.3 that the accuracy of the applied firing pressure is good. For the experiments exposed to 10 and 15 *bar* firing pressure the maximum deviations, for experiments with the same nominal firing pressure, in recorded firing pressure and incident pressure are 3 and 2 %, respectively. This indicates that the state of the shock wave is close to identical for experiments with the same nominal firing pressure prior to impact. More substantial deviations can be observed for recorded reflected pressure, for experiments exposed to the same nominal firing pressure. The biggest deviation for the experiments exposed to 10 and 15 *bar* firing pressure is approximately 10 %. The differences in reflected peak pressure may be due to the different deformations of the test specimens and FSI effects, considering that more substantial deformation results in a dissipation of reflected pressure. Additionally, larger deformation in sandwich components leads to more leakage of pressure to the dump tank. Note that fracture occurred when the Al skin specimen was subjected to 15 *bar* firing pressure, which explains the rapid drop in recorded pressure seen in Figure 5.12 (right).

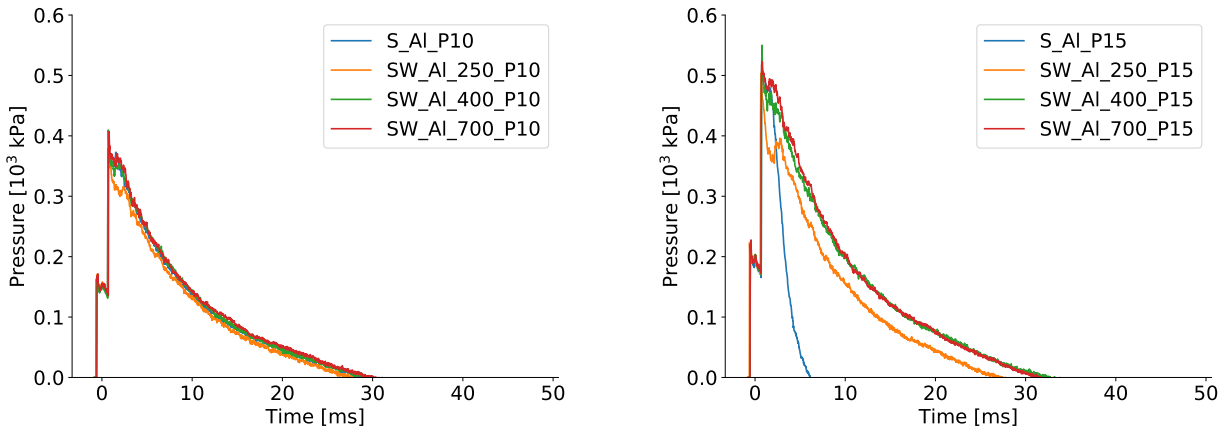


Figure 5.12: Pressure-time curves for Al configurations exposed to a nominal firing pressure of 10 (left) and 15 *bar* (right).

Table 5.3: Nominal and recorded firing,  $P_{f,n}$  and  $P_{f,r}$ , incident,  $P_i$ , and reflected,  $P_r$ , pressure recorded for Al components.

| Test Name     | $P_{f,n}$<br>[kPa] | $P_{f,r}$<br>[kPa] | $P_i$<br>[kPa] | $P_r$<br>[kPa] |
|---------------|--------------------|--------------------|----------------|----------------|
| S_AI_P10      | 1000               | 1021.15            | 167.85         | 378.42         |
| SW_AI_250_P10 |                    | 1040.99            | 170.90         | 375.37         |
| SW_AI_400_P10 |                    | 1039.77            | 167.85         | 409.55         |
| SW_AI_700_P10 |                    | 1039.46            | 171.51         | 407.10         |
| S_AI_P15      | 1500               | 1524.40            | 218.51         | 512.70         |
| SW_AI_250_P15 |                    | 1568.35            | 223.39         | 503.54         |
| SW_AI_400_P15 |                    | 1570.79            | 226.44         | 549.93         |
| SW_AI_700_P15 |                    | 1567.74            | 227.66         | 523.07         |
| S_AI_P25      | 2500               | 2514.42            | 291.05         | 718.44         |

### 5.3.6 Pressure Load - Aluminum and Steel Skins

Figure 5.13 presents pressure-time curves for all AIS experiments and Table 5.4 presents the recorded firing, incident and peak reflected pressure. It can be seen that, for the same nominal firing pressure, the deviation in recorded firing pressure is approximately 0.1 %, while the deviations of the recorded incident pressure are 3 %. Regarding the reflected pressure, the biggest deviation is observed to be approximately 30 %, within the same nominal firing pressure. The AIS skins without a foam core experienced the highest reflected pressures with the recorded values decreasing with foam density. The deviations are likely caused by the same factors as for the Al experiments described in Section 5.3.5. Additionally, the differences are influenced by the increased firing pressure and the increased stiffness of the back skin.

Noise is observed in the pressure recordings for all sandwich panels seen in Figure 5.13. This is likely due to the large and somewhat uneven deformation of the front skin, in combination with pressure leakage into the dump tank. Significant drops in pressure are seen after the reflected peak pressure for the sandwich panel with an XPS-400 core. The reason for this is currently unknown, but the first drop of pressure is similar to the behavior observed for experiment S\_Al\_P15, seen in Figure 5.12, which experienced complete fracture. The sandwich panel with an XPS-400 core might have experienced increased pressure leakage compared to the other sandwich panels causing the distinct pressure drop. The following peak after the drop in the pressure-time curve could be caused by a secondary reflection encountering the specimen, resulting in further leakage. An excellent example of a secondary reflection is seen in the pressure-time curve for experiment S\_AIS\_P35, illustrated in Figure 5.13.

A physical inspection of the tested components, post-experiment, indicated that sandwich panels with XPS-250 and XPS-400 cores experienced suction seen in Figure 5.12, causing the front skin to deform in the opposite direction of the shock wave. This phenomenon is known as reversed snap buckling [2] and can be observed in Figure 5.14, showing the deformation of the front skin of experiment SW\_AIS\_250\_P35.

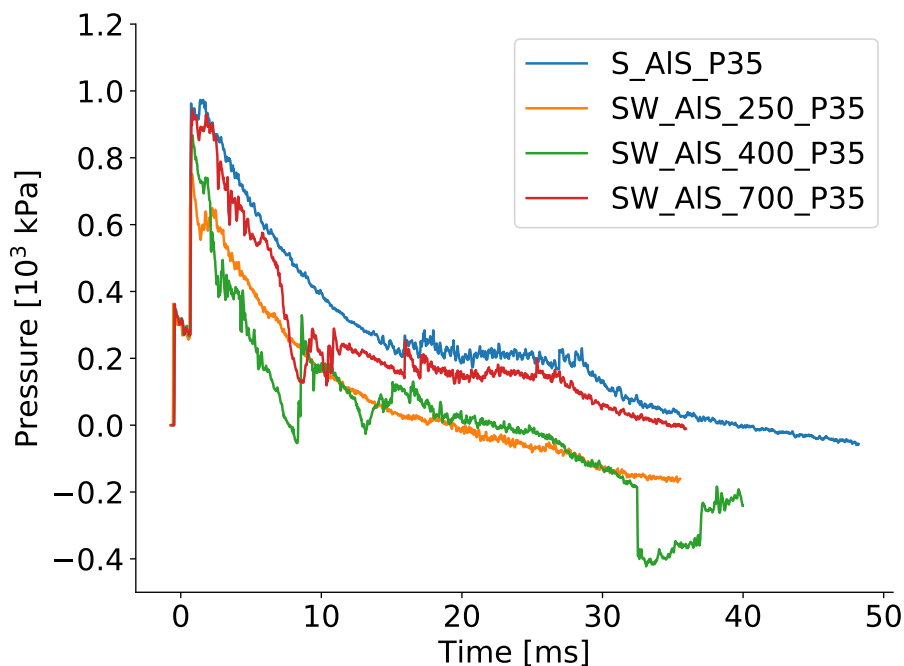


Figure 5.13: Pressure-time curves for AIS configurations exposed to a nominal firing pressure of 35 bar.



Table 5.4: Nominal firing pressure,  $P_{f,n}$ , recorded firing pressure,  $P_{f,r}$ , incident pressure,  $P_i$ , and reflected pressure,  $P_r$ , pressure recorded for AIS components.

| Test Name      | $P_{f,n}$<br>[kPa] | $P_{f,r}$<br>[kPa] | $P_i$<br>[kPa] | $P_r$<br>[kPa] |
|----------------|--------------------|--------------------|----------------|----------------|
| S_AIS_P25      | 2500               | 2503.13            | 295.97         | 783.38         |
| S_AIS_P35      |                    | 3816.34            | 351.56         | 972.90         |
| SW_AIS_250_P35 | 3500               | 3816.34            | 363.16         | 752.56         |
| SW_AIS_400_P35 |                    | 3821.22            | 352.17         | 867.92         |
| SW_AIS_700_P35 |                    | 3815.73            | 362.55         | 944.21         |

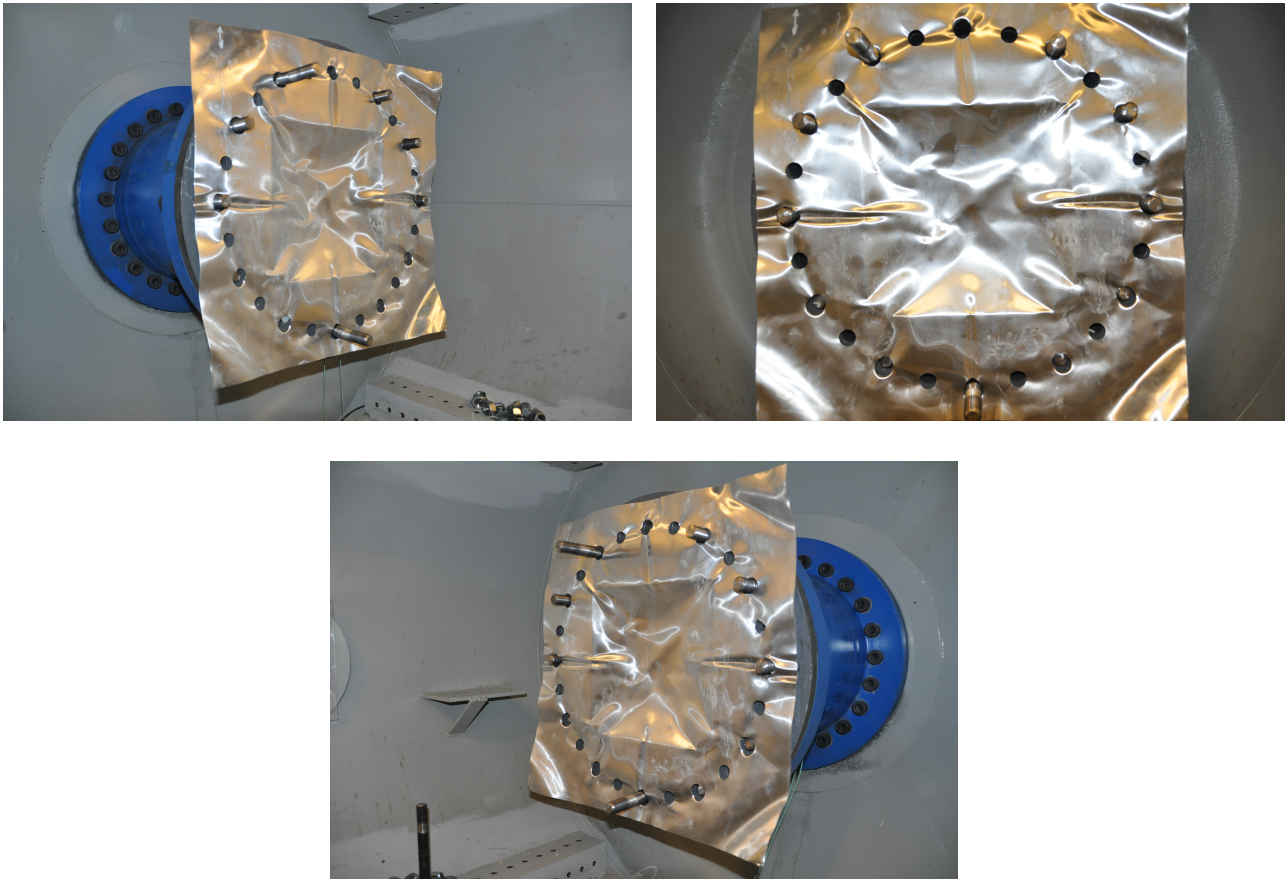


Figure 5.14: Reversed snap buckling effect of front skin on AIS sandwich component with XPS-250 foam core exposed to 35 bar firing pressure.

### 5.3.7 Midpoint Displacement - Aluminum Skins

Figure 5.15 presents midpoint displacements for Al components exposed to firing pressure of 10 (left) and 15 *bar* (right). In Table 5.5 maximum midpoint displacements recorded in the 3D-DIC analysis, midpoint displacements physically measured after the experiments and the difference between the two are presented. The physically measured displacement was obtained as shown in Figure 5.6. It can be observed that the measured midpoint displacements are consistently lower than the recorded DIC max midpoint displacements, with the measurements regarding the specimens exposed to 15 *bar* pressure having a slightly lower difference than the ones exposed to 10 *bar*. These results are in general agreement with expectations of elastic deformation effects decreasing the midpoint displacement after loading. The physical measure of midpoint displacement was recorded as a rough validation for the midpoint displacements obtained with 3D-DIC techniques. Note that no physical measurement of midpoint displacement was recorded on experiment S\_Al\_P10. Additionally, no deformation was recorded on SW\_Al\_P15 or SW\_Al\_400\_P15 because, in both cases, the specimens reached fracture. The experiment with Al skins without a foam core exposed to 25 *bar* firing pressure was also performed, which reached fracture. Considering that no Al sandwich panels were exposed to a firing pressure of 25 *bar*, the results are not presented in this section.

The midpoint displacement plots presented in Figure 5.15a suggests a trend where there is a negative correlation between the density of the foam core and displacement levels. There is also a significant gap of 7.75 *mm* and 9.38 *mm* between the sandwich component with an XPS-250 foam core and the panels having cores of XPS-400 and XPS-700, respectively. It is also seen that the experiment with Al skins without a foam core reached a similar displacement level as the one having an XPS-250 core subjected to 10 *bar* firing pressure, with a difference of 0.19 *mm*.

The displacement trend mentioned above is partially supported by the results from the experiments exposed to a firing pressure of 15 *bar*. In Figure 5.15b and Table 5.5 it is observed that there is a gap of 9.43 *mm* between the maximum midpoint deformation of the sandwich component with an XPS-250 core and an XPS-700 core. This is in good agreement with the results from the same sandwich configurations exposed to a firing pressure of 10 *bar*. The fact that experiment S\_Al\_P15 and SW\_Al\_400\_P15 reached fracture at 15 *bar* firing pressure suggests that there exists a capacity limit regarding firing pressure, before fracture, for this specific sandwich configuration somewhere in the interval 10 to 20 *bar* firing pressure. Material imperfections or production defects might also affect the capacity of the sandwich configurations. It is worth mentioning that experiment SW\_Al\_700\_P15 also experienced minor fracture along the edges of the back skin that was in contact with the clamping frame. The Al skins without foam cores exposed to 15 and 25 *bar* reached complete failure, in both skins, along the edges in contact with the clamping frame. Figure 5.17 shows the fracture of experiment SW\_Al\_400\_P15 and SW\_Al\_700\_P15.

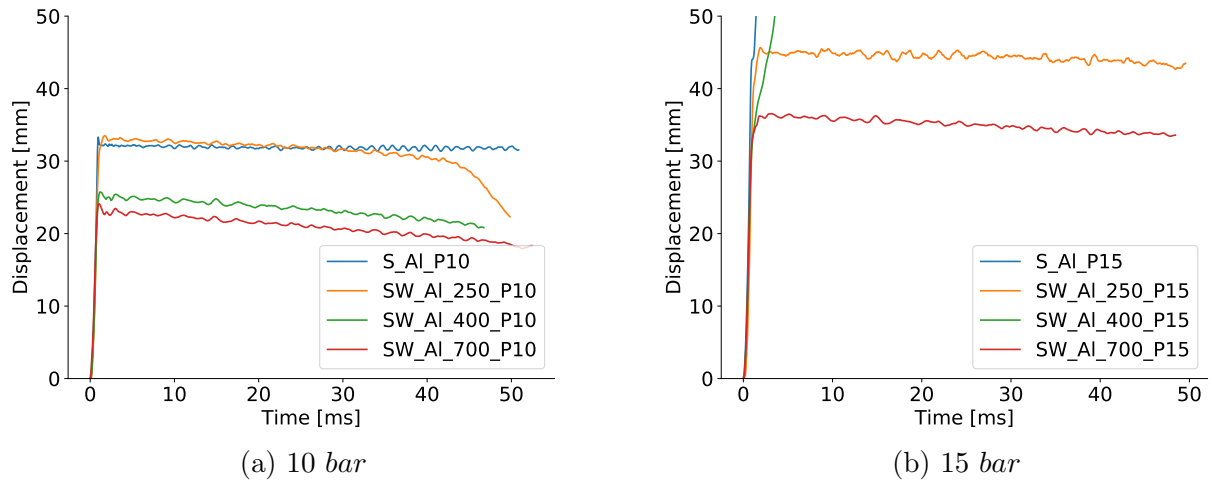


Figure 5.15: Midpoint displacement extracted from 3D-DIC analysis for Al components exposed to a nominal firing pressure of 10 (left) and 15 bar (right).

Table 5.5: Midpoint displacement provided by 3D-DIC analysis,  $u_{max}$ , physically measured midpoint displacement,  $u_m$ , and the deviation between them for Al components.

| Test Name     | $P_f$<br>[bar] | DIC $u_{max}$<br>[mm] | Measured $u_m$<br>[mm] | $u_{max} - u_m$<br>[mm] | $\frac{u_{max} - u_m}{u_{max}}$ |
|---------------|----------------|-----------------------|------------------------|-------------------------|---------------------------------|
| S_AI_P10      | 10             | 33.31                 | No Measurement         | -                       | -                               |
| SW_AI_250_P10 |                | 33.50                 | 28.70                  | 4.80                    | 14.32 %                         |
| SW_AI_400_P10 |                | 25.75                 | 22.00                  | 3.75                    | 14.56 %                         |
| SW_AI_700_P10 |                | 24.11                 | 19.85                  | 4.26                    | 17.68 %                         |
| S_AI_P15      | 15             | Fracture              | Fracture               | -                       | -                               |
| SW_AI_250_P15 |                | 45.67                 | 43.30                  | 2.37                    | 5.18 %                          |
| SW_AI_400_P15 |                | Fracture              | Fracture               | -                       | -                               |
| SW_AI_700_P15 |                | 36.24                 | 33.50                  | 2.74                    | 7.55 %                          |

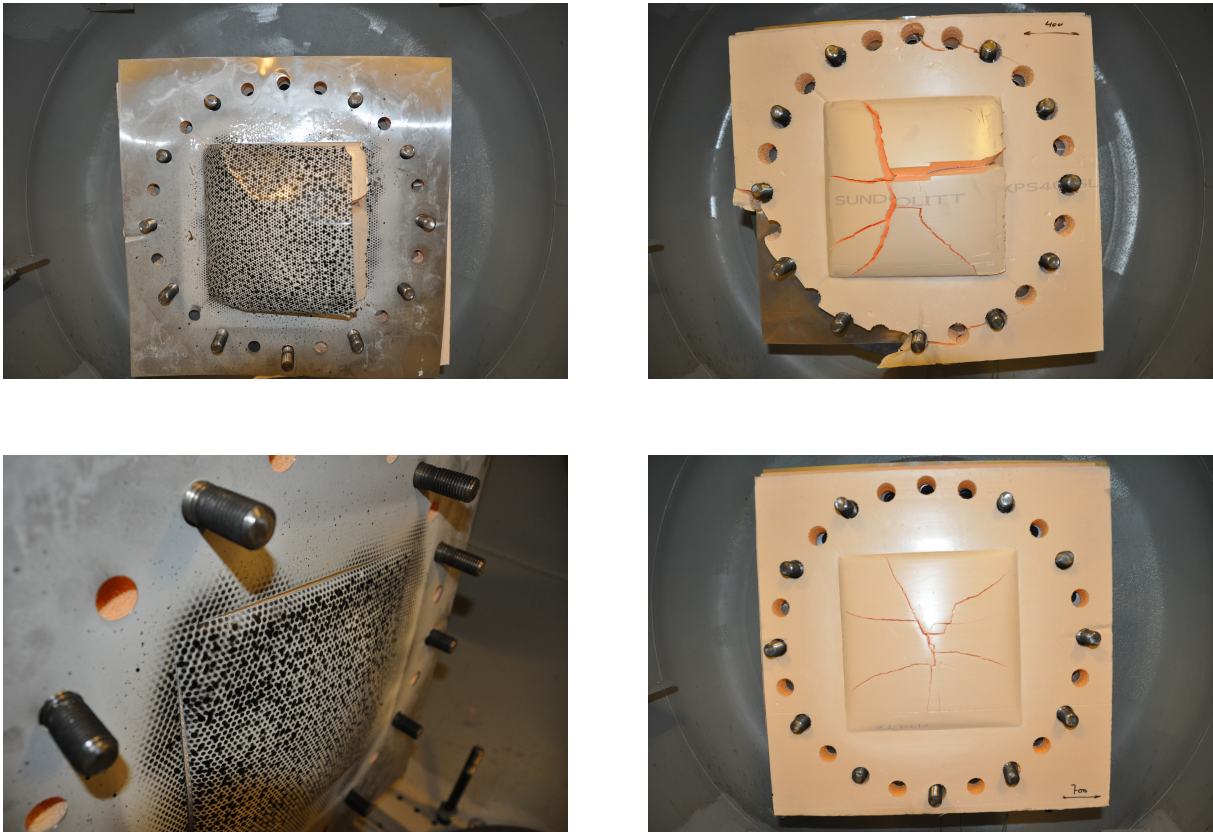


Figure 5.17: Fracture levels in back skin (left) and foam (right) of Al sandwich components with XPS-400 (bottom) and XPS-700 (top) foam core exposed to 15 *bar* firing pressure.

### 5.3.8 Midpoint Displacement - Aluminum and Steel Skins

In Figure 5.18 (right) midpoint displacements for AIS sandwich panels with foam cores of XPS-250, XPS-400 and XPS-700 are presented for firing pressure of 35 *bar*. In Figure 5.18 (left) the results from an AIS configuration without foam cores exposed to firing pressures of 25 and 35 *bar* are presented. Table 5.6 presents maximum midpoint displacements recorded in the 3D-DIC analysis, midpoint displacements physically measured after the experiments, and the difference between the two. In Table 5.6 it can be observed that the measured midpoint displacements are consistently lower than the recorded DIC max midpoint displacements, as previously seen for the Al configurations in Section 5.3.7. The difference calculated for the AIS experiments is generally slightly lower than the ones recorded for the Al experiments due to the steel skins being significantly stiffer than the aluminum skins.

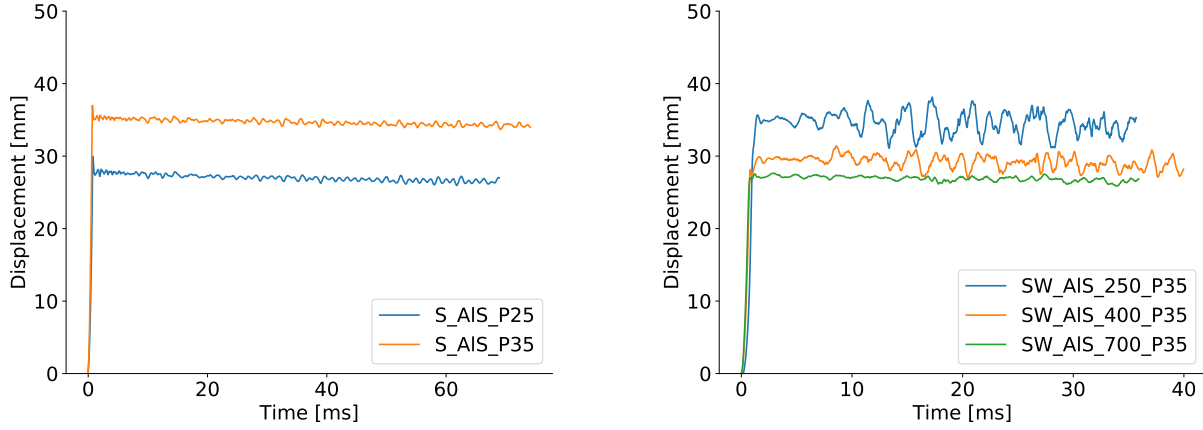


Figure 5.18: Midpoint displacement extracted from 3D DIC analysis for AIS components without a foam core (left) and for AIS sandwich panels (right).

Table 5.6: Midpoint displacement provided by 3D-DIC analysis,  $u_{max}$ , physically measured midpoint displacement,  $u_m$ , and the deviation between them for AIS specimens exposed to a nominal firing pressure,  $P_f$ , of 25 and 35 *bar*.

| Test Name      | $P_f$<br>[ <i>bar</i> ] | DIC $u_{max}$<br>[ <i>mm</i> ] | Measured $u_m$<br>[ <i>mm</i> ] | $u_{max} - u_m$<br>[ <i>mm</i> ] | $\frac{u_{max} - u_m}{u_{max}}$<br>% |
|----------------|-------------------------|--------------------------------|---------------------------------|----------------------------------|--------------------------------------|
| S_AIS_P25      | 25                      | 29.96                          | 27.50                           | 2.46                             | 8.22 %                               |
| S_AIS_P35      |                         | 36.99                          | 34.47                           | 2.52                             | 6.82 %                               |
| SW_AIS_250_P35 | 15                      | 35.67                          | 31.77                           | 3.90                             | 10.93 %                              |
| SW_AIS_400_P35 |                         | 28.14                          | 26.95                           | 1.19                             | 4.24 %                               |
| SW_AIS_700_P35 |                         | 27.00                          | 26.80                           | 0.20                             | 0.75 %                               |

The trend seen for the Al experiments where there is a negative correlation between foam density and displacement levels is also present for the AIS experiments. For midpoint displacement, differences of 7.52 *mm* and 8.67 *mm* between the sandwich component with an XPS-250 foam core and the panels having cores of XPS-400 and XPS-700, respectively, can be seen. A similar maximum midpoint displacement is observed for the skins without a foam core and the sandwich panel with an XPS-250 core, coinciding with results obtained for Al components. The oscillations observed in Figure 5.18 (right) are unrealistic considering the blast load scenario in question. These oscillations are likely due to vibrations in the Plexiglas plates in the dump tank providing a view for the high-speed cameras. It is suspected that large deformations cause pressure leakage from the driven section of the shock tube into the dump tank, which caused the Plexiglas to vibrate. The most interesting information from the midpoint displacement curves is the data before, and right after maximum deformation, therefore the oscillations are insignificant and are disregarded in the further investigation of the results.

### 5.3.9 Scanned Deformation Profiles

To extract additional information about the structural behavior of the sandwich panels exposed to blast loading, a selection of front and back skins were scanned with a ROMER Absolute Arm (RAA), produced by Hexagon AB [60]. The RAA is a portable measuring arm with RS4 laser scanner designed for 3D data capture across a range of surfaces and applications. The RAA includes a laser scanner, with a laser width of 150 mm able to capture 752000 points per second, to produce a point cloud with coordinates in x-,y- and z-plane. The point cloud was later post-processed to filter out outliers and to extract data describing deformation profiles of the components. The sandwich panels exposed to 35 bar firing pressure was excluded from the laser measurements because of the reversed snap buckling behavior of the front skin, while experiment SW\_Al\_400\_P15 was excluded from the laser measurements because of fracture. The deformation profiles of all scanned sandwich panels are shown in Figure 5.19. Table 5.7 presents the RAA extracted measurements of midpoint displacement of front skin, back skin, and the difference in midpoint displacement of the back skin physically measured and scanned with RAA. Middle and average side compression of the foam core was calculated from the RAA deformation profiles and are also presented in Table 5.7.

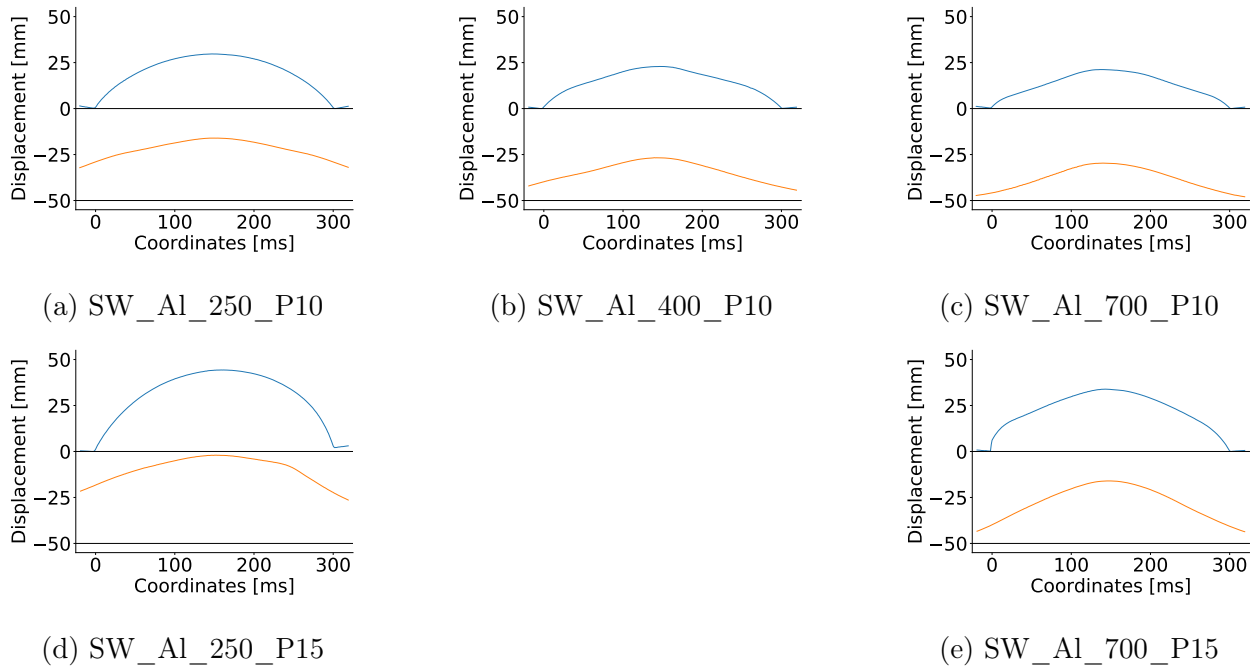


Figure 5.19: Deformation profiles for Al sandwich components exposed to 10 (top) and 15 bar (bottom) firing pressure, obtained by with RAA.

Table 5.7: Front and back skin midpoint displacement,  $u_{FS}$  and  $u_{BS}$ , and middle and average side foam compression,  $C_{mid}$  and  $C_{side}$ , for Al sandwich components investigated with RAA.

| Test Name     | $P_f$<br>[bar] | $u_{FS}$<br>[mm] | $u_{BS}$<br>[mm] | $\frac{u_{BS} - u_m}{u_{BS}}$ | $C_{mid}$<br>[mm] | $C_{side}$<br>[mm] |
|---------------|----------------|------------------|------------------|-------------------------------|-------------------|--------------------|
| SW_Al_250_P10 |                | 33.97            | 29.71            | 3.39 %                        | 4.26              | 20.69              |
| SW_Al_400_P10 | 10             | 23.26            | 22.89            | 3.90 %                        | 0.37              | 9.74               |
| SW_Al_700_P10 |                | 20.34            | 21.21            | 6.43 %                        | -0.88             | 3.37               |
| SW_Al_250_P15 |                | 47.98            | 44.32            | 2.30 %                        | 3.66              | 30.98              |
| SW_Al_250_P15 | 15             | 34.00            | 33.89            | 1.15 %                        | 0.12              | 8.98               |

The RAA scanned specimens were measured by reattaching them to a single clamping frame with bolts placed on a table. The setup for the laser measurement can be seen in Figure 5.20. Ideally, the skins should have been scanned while mounted in the test rig, under more similar conditions. When interpreting the resulting deformation profiles and comparing them to other measurements the conditions which the data was extracted has to be taken into consideration. The possibility of sliding between the front skin and the bolts during the experiments are not accounted for in the scanned results, neither are the elastic deformation differences between the fully clamped panels during experiments and the reattachment used for the scanning procedure.

In Table 5.7 it can be seen that the midpoint displacement recorded by the RAA and the physically measured midpoint displacements are relatively similar. This is expected due to both measurements being taken after the experimental loading in contrast to the 3D-DIC which measured the maximum midpoint displacement during testing. For the midpoint displacements of the front and the back skins a similar trend as observed in Section 5.3.7, where a negative correlation between the midpoint displacement and the density of the foam core, can be observed. It can also be seen that the gap in midpoint displacement between the components with foam cores of XPS-250 and the ones with a core of XPS-400 and XPS-700, is present. Concerning deformation profile shape, it can be seen in Figure 5.19 that the experiments with a core of XPS-250 experienced a rounder and more distributed shape than the two other foam cores. This is also reflected in the measurement of the increased compression on the edge of the component. This trend can also be observed in the Section 5.3.1 and 5.3.2, where deformation profiles of the back skin at maximum midpoint displacement obtained from the 3D-DIC analysis are presented. It is also noticeable that the obtained values for midpoint compression are low. This is not in agreement with the foam compression visually observed in the experiments. This is suspected to be due to the conditions present when the skins were scanned with the RAA.

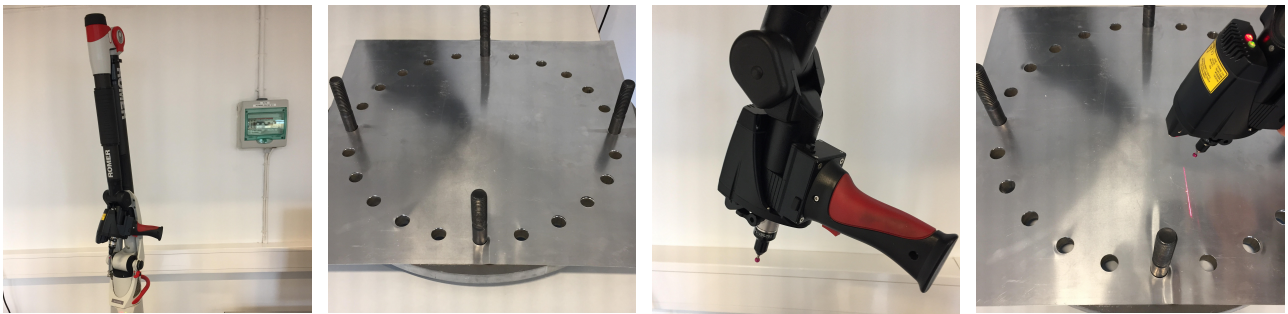


Figure 5.20: Setup for measurements using the RAA.

## 5.4 Previous Study

For completeness of the experimental results and as a reference to similar previous work, the results from the experimental program performed by Sigurdsson [3] are included. This includes data from five tests conducted on sandwich panels with steel skins and XPS foam cores performed in a similar way as described in Section 5.1. There are, however, a set of differences. The images recorded was captured by the same camera models but with a recording rate of 24000 *fps* instead of 36000 *fps*, used in this study. The images were reanalyzed using 3D-DIC in this study for consistency and validation. The pressure histories were recorded by the same sensors. However, these have been renamed from 409 and 410 to P01\_2 and P01\_1, respectively. To fasten the test component with foam cores to the test rig, only one nut was used, instead of two used in this study. The major difference was, however, the experimental program, summarized in Table 5.8. One of the tests was performed with a steel front and back skin without a foam core exposed to a firing pressure of 60 *bar*. Only one foam type was used as foam core, XPS-250, with a nominal density of 33 *kg/m*<sup>3</sup>. Three of the test components were sandwich configuration with steel front and back skins and XPS-250 as foam cores exposed to firing pressures of 35, 60 and 75 *bar*. The sandwich component exposed to 35 *bar* was also tested without a front skin. The results are presented similarly as described in Section 5.3, with an overall presentation of the individual results, and with closer examination and comparison of midpoint displacement and pressure.

Table 5.8: Experimental program carried out by Sigurdsson [3].

| Test Name                          | Core Material | Skin Material                      | Driver Pressure<br>[ <i>bar</i> ] |
|------------------------------------|---------------|------------------------------------|-----------------------------------|
| SW_S_250_P35_1Skin<br>SW_S_250_P35 | XPS-250       | DOCOL 600L back skin<br>DOCOL 600L | 35                                |
| S_S_P60<br>SW_S_250_P60            | -<br>XPS-250  | DOCOL 600L                         | 60                                |
| SW_S_250_P75                       | XPS-250       | DOCOL 600L                         | 75                                |



### 5.4.1 Results

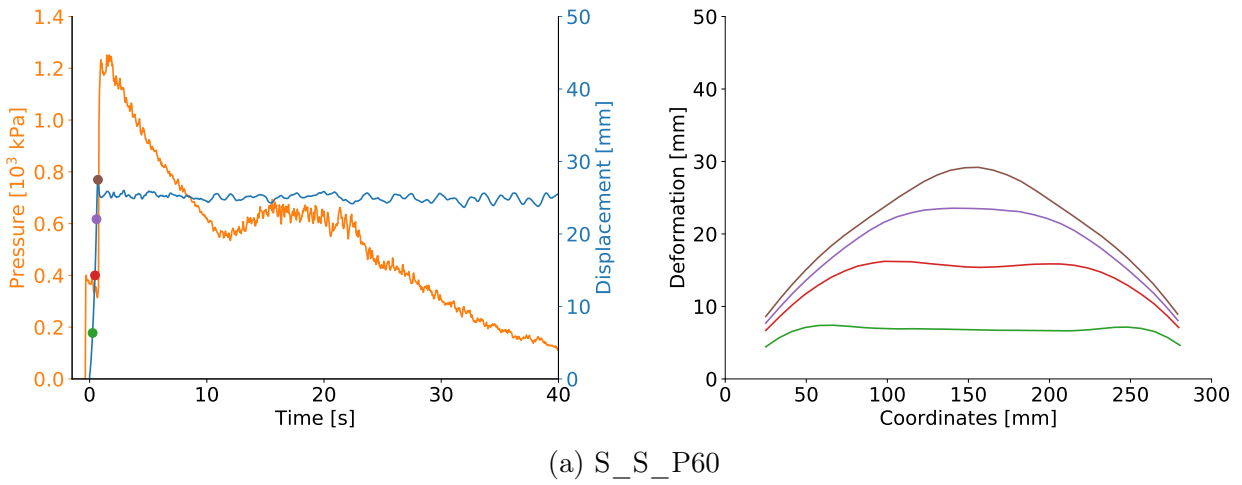


Figure 5.21: Pressure and midpoint displacement (left) and deformation profiles at 1/4, 2/4, 3/4, and max deflection (right) for steel front and back skins without a foam core, exposed to 60 *bar* firing pressure.

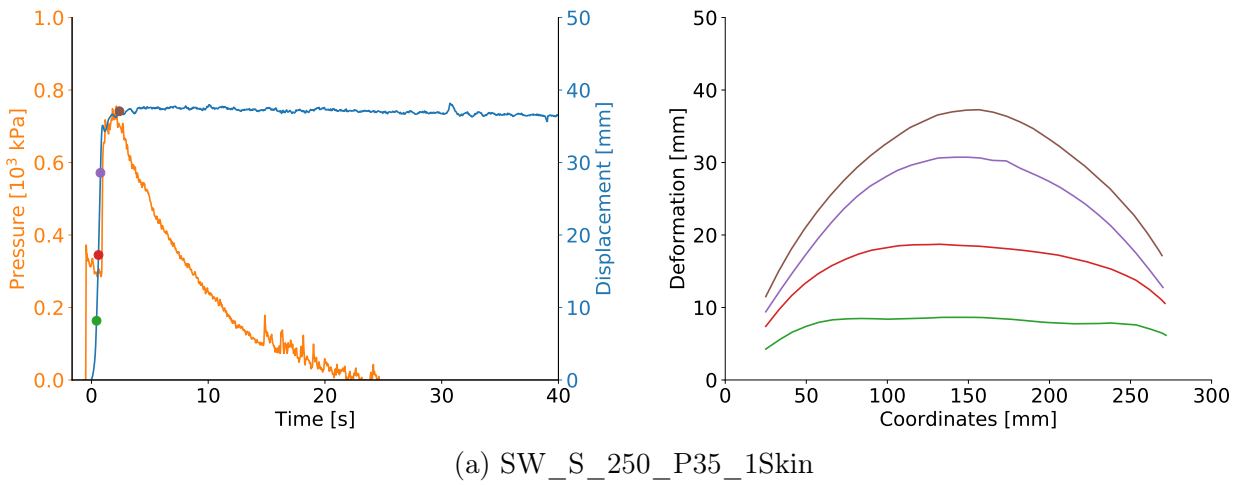
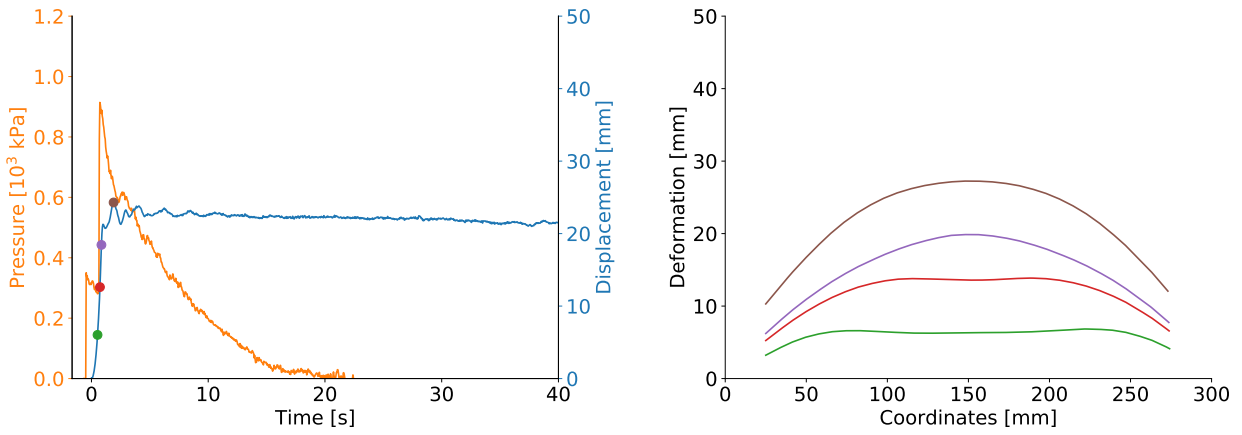
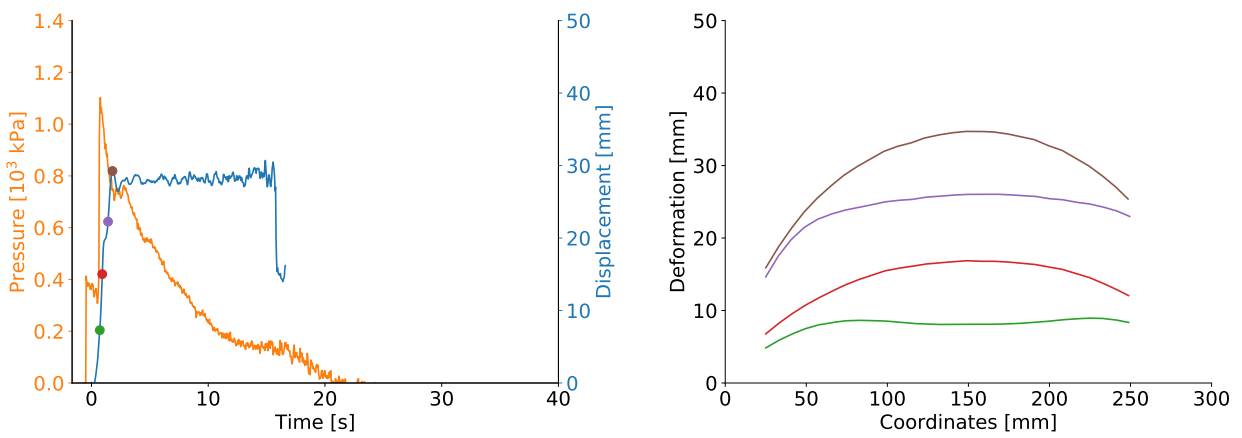


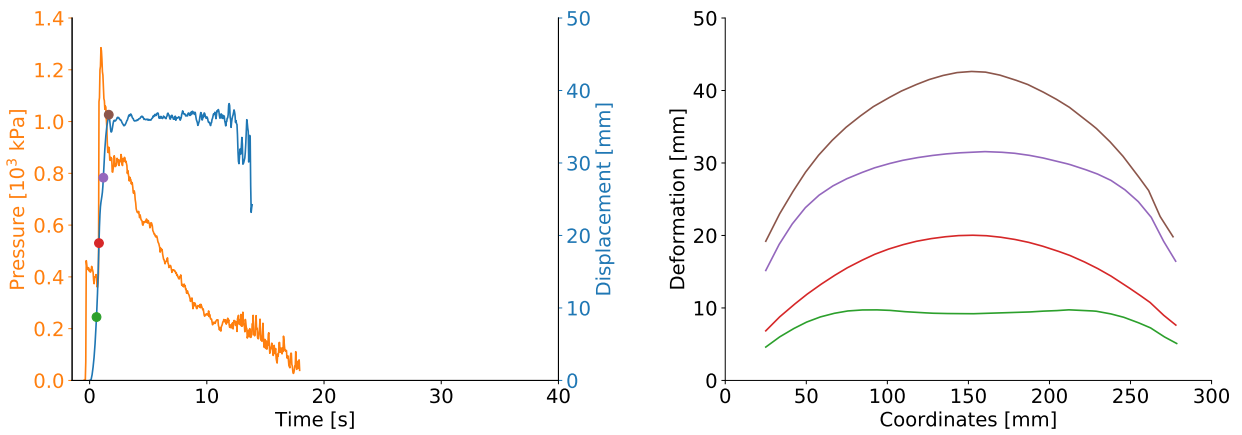
Figure 5.22: Pressure and midpoint displacement (left) and deformation profiles at 1/4, 2/4, 3/4, and max deflection (right) for a sandwich panel without front skin, with steel back skin exposed to 35 *bar* firing pressure.



(a) SW\_S\_250\_P35



(b) SW\_S\_250\_P60



(c) SW\_S\_250\_P75

Figure 5.23: Pressure and midpoint displacement (left) and deformation profiles at 1/4, 2/4, 3/4, and max deflection (right) for sandwich panels with steel front and back skins exposed to 35 (top), 60 (middle) and 75 *bar* (bottom) firing pressure.

## Pressure Load and Midpoint Displacement

The recorded pressure-time curves from the study by Sigurdsson [3] are presented in Figure 5.24 (left) with recorded firing, incident and peak pressure values listed in Table 5.9. It is observed that recorded firing pressures are close to identical to nominal firing pressure, for components exposed to 35 and 60 *bar* firing pressure. The deviation between nominal and recorded incident pressure for 35 and 60 *bar* firing pressure is approximately 5 %. The deviation in recorded peak reflected pressure between the two experiments with 35 *bar* firing pressure is approximately 20 %. This deviation is likely due to the removed front skin in one of the experiments. The drop in reflected pressure for the sandwich component exposed to 60 *bar* may have been caused by the reduced stiffness introduced by the foam core. A secondary and a tertiary peak can be seen in the pressure curve for experiment S\_S\_P60. The pressure curves in Figure 5.9 (left) are similar to the pressure curves for AIS components in Section 5.3.6, where the main difference is the large deformation of the aluminum front skin.

The recorded midpoint displacements are presented in Figure 5.24 (right) and Table 5.9. It can be observed that the midpoint displacement histories for experiment SW\_S\_250\_P60 and SW\_S\_250\_P75 are cut off before the other displacement histories. This is likely due to vibrations of the Plexiglas between the high-speed camera and the test specimen because of pressure leakage into the dump tank. These results are similar to the oscillations observed in Section 5.3.8. However, the increased firing pressures resulted in warping of the images captured. The distortion of images lead to diverged and incomplete results from the 3D-DIC analysis [3]. Similar to the experiments conducted in this study, the sandwich component with an XPS-250 foam core had a maximum midpoint displacement similar to the steel skins, without a foam core, exposed to the same firing pressure of 60 *bar*. It is also noticeable that the sandwich panels with steel back and front skins exposed to increased firing pressure exhibited a smaller increase in maximum midpoint displacement than the Al sandwich panels. The increase in maximum midpoint displacement between experiment SW\_S\_250\_P35 and experiment SW\_S\_250\_P60 and SW\_S\_250\_P75 are 16.94 % and 33.73 %, respectively. The difference between experiment SW\_Al\_250\_P10 and SW\_Al\_250\_P15 is 26.65 %, for an increase of 5 *bar* firing pressure, compared to an increase of 25 and 35 *bar* firing pressure for the components with steel skins.

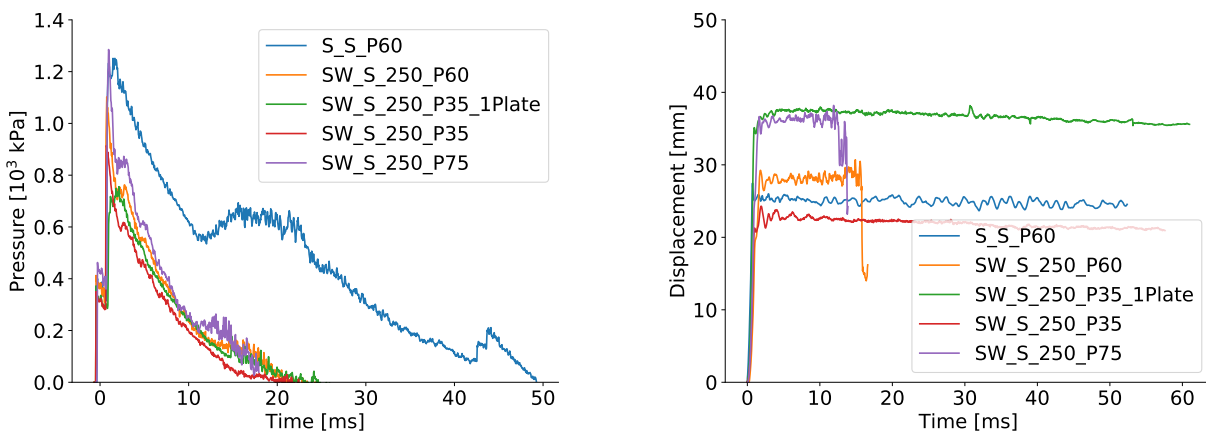


Figure 5.24: Pressure recorded at sensor 410 (left) and midpoint displacement extracted from 3D-DIC analysis (right) for the experiments performed by Sigurdsson.

Table 5.9: Nominal firing pressure,  $P_{f,n}$ , recorded firing pressure,  $P_{f,r}$ , incident pressure,  $P_i$ , reflected pressure,  $P_r$ , and midpoint displacement,  $u_{max}$ , for experiments performed by Sigurdsson.

| Test Name          | $P_{f,n}$<br>[kPa] | $P_{f,r}$<br>[kPa] | $P_i$<br>[kPa] | $P_r$<br>[kPa] | DIC $u_{max}$<br>[mm] |
|--------------------|--------------------|--------------------|----------------|----------------|-----------------------|
| SW_S_250_P35_1Skin | 3500               | 3811.76            | 372.31         | 755.62         | 37.08                 |
| SW_S_250_P35       |                    | 3811.76            | 350.34         | 914.31         | 24.29                 |
| S_S_P60            | 6000               | 6203.50            | 400.39         | 1251.20        | 27.47                 |
| SW_S_250_P60       |                    | 6208.69            | 412.60         | 1102.30        | 29.25                 |
| SW_S_250_P75       | 7500               | 7806.64            | 462.65         | 1285.40        | 36.66                 |

## 5.5 Main Findings

In this section, the main findings of the experimental work conducted are summarized.

- Recorded firing pressure and incident pressure, for experiments exposed to the same nominal firing pressure, varies only to a small extent. Deviations between peak reflected pressure for equal nominal firing pressure was observed due to a difference in deformation levels and fluid-structure interaction effects.
- Significant drops in the pressure data obtained from the AIS experiments subjected to a firing pressure of 35 *bar* were observed. The large deformations of the aluminum front skin might cause an increased pressure leakage compared to the other panels exposed to equal firing pressure.
- For the AIS experiments exposed to 35 *bar* firing pressure oscillations in the results were observed, likely due to vibrations of the Plexiglas between the high-speed camera and the test component caused by pressure leakage.
- Reversed buckling behavior of the front skin was observed for AIS sandwich panels with XPS-250 and XPS-400 foam core exposed to 35 *bar* firing pressure.
- Results suggest a trend where there exists a negative correlation between foam density and displacement levels. A gap between Al components with XPS-250 and XPS-400/700 foam cores was obtained when exposed to a firing pressure of 10 *bar*.
- Similar deformation level was observed for the Al skins without a foam core and the Al sandwich panel with XPS-250 foam core, subjected to a firing pressure of 10 *bar*.
- Al sandwich panels and Al skins without foam cores exposed to 15 *bar* firing pressure suggest similar trends as the Al experiments subjected to 10 *bar* firing pressure. However, the results are less conclusive because of the presence of fracture in multiple experiments.
- The Al experiments conducted on 10 and 15 *bar* suggests that there is a capacity limit of the tested Al components, regarding firing pressure, between 10 and 20 *bar*.
- AIS sandwich panels exhibit similar behavioral trends as Al sandwich components.
- A selection of skins from sandwich components were scanned with the RAA scanning arm, which produced accurate measurements of skin deformation, post-experiment. However, the conditions which the skins were scanned caused uncertainties related to a quantitative comparison of the results obtained through this method and other measuring techniques.
- A qualitative comparison of the deformation profiles obtained from the scanning procedure and 3D-DIC analysis was performed, which showed good agreement in deformation shape. Compared to the Al components with XPS-400 and XPS-700 foam cores, a rounder and more distributed deformation shape for the sandwich panel with a core of XPS-250 was found.
- For completeness of the experimental work, results from a study conducted by Sigurdsson [3] was included, where some of the same trends concerning deformation and recorded pressure were seen.

# Chapter 6

## Numerical Work

The numerical work, excluding the preliminary study and numerical validation of material tests, are described in this chapter. As a reference model, the same model as introduced and described in Section 3.2 was used, except for updated material parameters for aluminum, obtained through the material tests described in Section 4.1. The numerical results obtained with updated material parameters are presented in Section 6.1. Further, the numerical model is validated by comparison to experimental results in Section 6.2. The validation of the numerical model allowed further investigation of properties of the structural response not captured by the current experimental setup. These properties are presented in Section 6.3. The numerical results of interest are the compression and strains in the foam core, the energy absorption, the energy distribution between skins and foam, and the contact force between the components and the back clamping frames. Section 6.4 aims to evaluate and optimize sandwich configurations under different blast load scenarios by separately varying foam thickness and foam density, before varying both the thickness and density while keeping the mass of the foam core constant.

### 6.1 Updated Material Parameters for Aluminum

In Section 4.1 material tests for the AA1050-H14 aluminum alloy were performed at 0-degree, 45-degree and 90-degree direction of the material, relative to the rolling direction. The aluminum is assumed isotropic in the numerical model. Therefore, numerical simulations of an Al component, without and with a foam core of XPS-250 core exposed to a firing pressure of 10 *bar*, were performed with the different material parameters calibrated to the different material directions. The resulting midpoint displacement histories from simulations with material parameters calibrated for 0-degree, 45-degree, 90-degree and the material parameters used in the preliminary study are presented in Figure 6.1, together with the results for the corresponding experiments. It can be observed that the different material parameters yield similar results, where the numerical simulation with the material parameters from the 0-degree calibration yields the largest maximum midpoint displacement for both components, which is a conservative result. It was concluded that the calibrated material parameters for the 0-degree direction will be used in further simulations. The material parameters can be seen in Table 6.1.

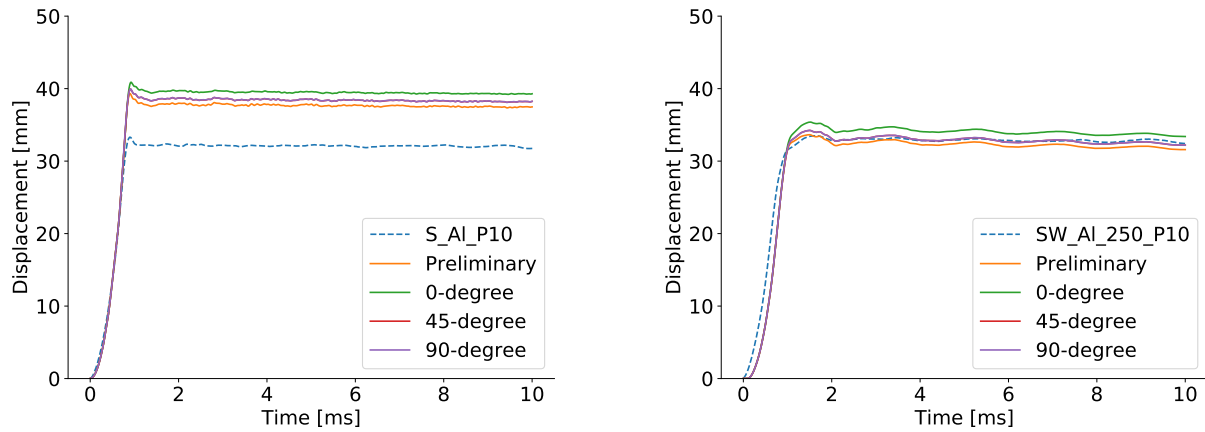


Figure 6.1: Midpoint displacement histories obtained from experimental work, numerical simulations with material parameters calibrated for aluminum AA1050-H14 in three directions and simulations with the material parameters used in the preliminary numerical work. Al configurations, without (left) and with (right) XPS-250 core, exposed to 10 *bar* firing pressure are shown.

Table 6.1: Material parameters for the constitutive relation for AA1050-H14 at 0 degree direction of the material.

| Material | $\sigma_0$<br>[MPa] | $Q_1$<br>[MPa] | $C_1$<br>[-] | $Q_2$<br>[MPa] | $C_2$<br>[-] | $c$<br>[-] | $m$<br>[-] | $\dot{p}_0$<br>[s <sup>-1</sup> ] |
|----------|---------------------|----------------|--------------|----------------|--------------|------------|------------|-----------------------------------|
| AA1050   | 80.0                | 18.65          | 1884.49      | 10.36          | 185.73       | 0.014      | 1.0        | $5 * 10^{-4}$                     |

## 6.2 Validation of Reference Model

The experimental setup for the test program performed in this study provides a limited amount of information on the structural behavior of the sandwich panels as a whole. The two sources of information are the pressure sensors and the two high-speed cameras capturing the behavior of the back skin. The sensors provide a fairly accurate measure of the blast load impacting the component, and the high-speed cameras combined with a 3D-DIC analysis provide accurate results on midpoint displacement and deformation profile evolution of the back skin. It is, however, desirable to investigate other properties of the structural response, such as the behavior of the front skin, foam compression, energy absorbed in the different parts of the sandwich panel and the force transferred to the clamping frame. These properties can be investigated through numerical simulations. However, it is essential to evaluate the accuracy of the numerical model in question before extracting and investigating properties not captured by the experimental setup. In the following section, the reference model is validated through comparison of numerical and experimental results on pressure histories, midpoint displacements, and deformation profiles.

### 6.2.1 Pressure Load

It is observed in Figure 6.2 and 6.3 that the pressure time history applied to describe the blast load scenario in the numerical simulations overestimate the pressure measured during the experiments. While the general shape of the curve is similar, the increased peak pressure and increased duration of the numerical curve provides a conservative presentation of the pressure load. A secondary reflected pressure peak is observed in the pressure-time history of experiment S\_AI\_S\_P25, which is not included in the idealized curve for this pressure. The secondary reflected peak pressure is included in the idealized curve for 35 *bar* firing pressure, but the experimental results are difficult to compare due to the noise in the recorded data, which is described in Section 5.3.6.

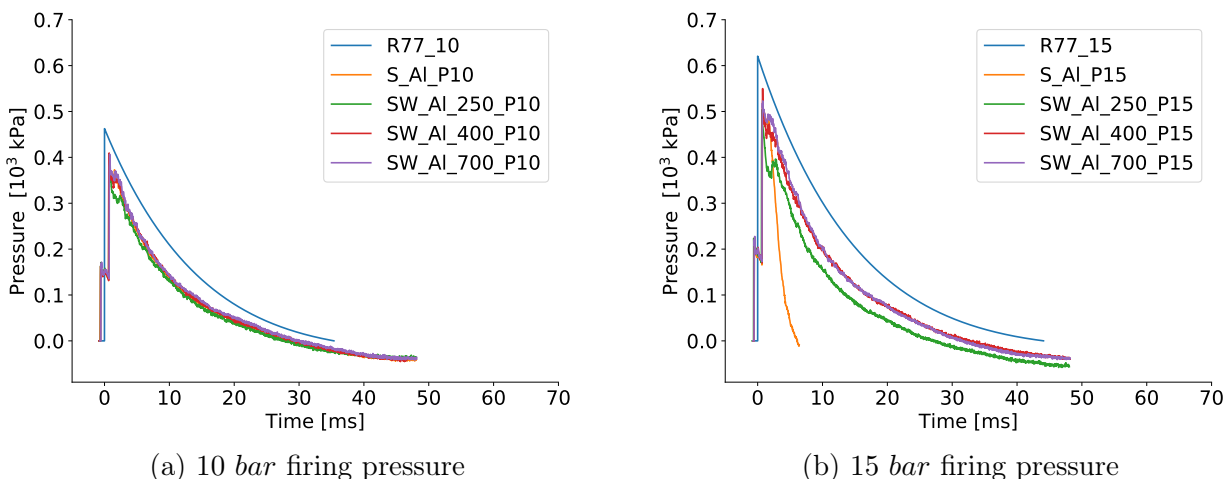


Figure 6.2: Lines "R77\_10" and "R77\_15" show idealized pressure curves used in numerical simulations. The remaining lines show recorded pressure curves at sensor P01\_1 for experiments with the same nominal firing pressure as the numerical simulations.



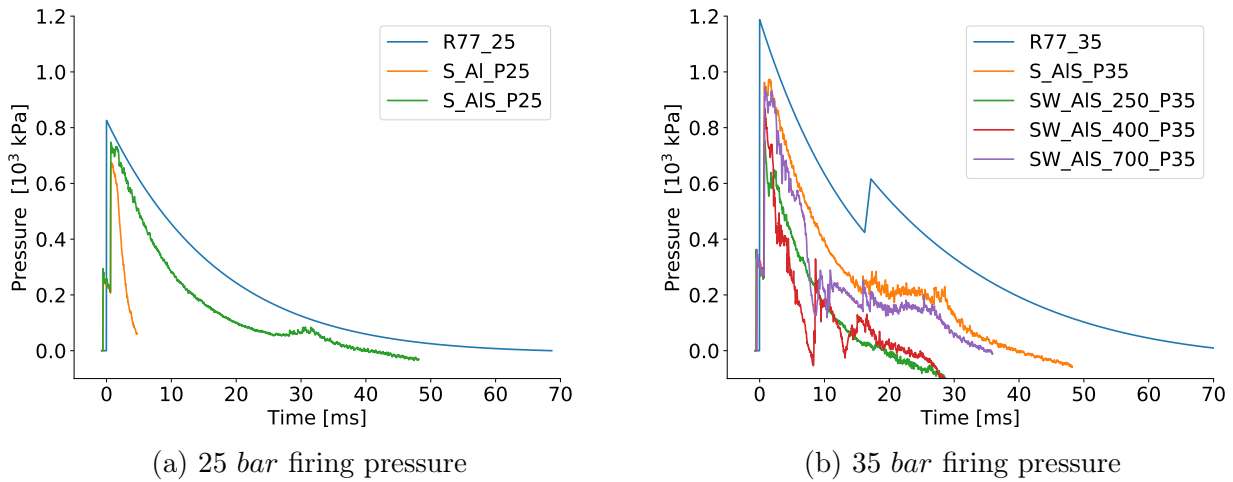


Figure 6.3: Lines "R77\_25" and "R77\_35" show idealized pressure curves used in numerical simulations. The remaining lines show recorded pressure curves at sensor P01\_1 for experiments with the same nominal firing pressure as the numerical simulations.

Table 6.2 presents the experimental and numerical values of the reflected peak pressures. It can be seen that the numerical peak reflected pressure is 10 to 20 % higher than the experimentally recorded values for firing pressures of 10, 15 and 25 *bar*. For the experiments subjected to 35 *bar* firing pressure, the numerical peak pressure is 15 to 35 % higher. The combination of high firing pressure, low-density foam and AIS skin configuration presents the largest deviation of reflected peak pressure. Generally, all the experimentally recorded peak pressures are smaller in magnitude than in the idealized pressure curves used for numerical simulations. This is expected since the idealized curves are constructed based on pressure recorded on rigid plates [2]. The deformation of the components in this experimental program causes a decrease in the recorded peak pressure to a various extent as discussed in Section 5.3.5. The idealized pressure curves are considered a conservative, controlled and fairly accurate representation of the actual pressure curves.

Table 6.2: Values of applied numerical,  $P_{max,n}$ , and experimentally,  $P_{max,e}$ , recorded peak reflected pressure and the deviation between them.

| Test Name      | $P_{max,n}$<br>[kPa] | $P_{max,e}$<br>[kPa] | $P_{max,n} - P_{max,e}$<br>[kPa] | $\frac{P_{max,n} - P_{max,e}}{P_{max,n}}$ |
|----------------|----------------------|----------------------|----------------------------------|---|
| S_Al_P10       |                      | 378.42               | 84.19                            | 18.20 %                                   |
| SW_Al_250_P10  | 462.61               | 375.37               | 87.24                            | 18.86 %                                   |
| SW_Al_400_P10  |                      | 409.55               | 53.06                            | 11.47 %                                   |
| SW_Al_700_P10  |                      | 407.10               | 55.51                            | 12.00 %                                   |
| S_Al_P15       |                      | 512.70               | 107.82                           | 17.38 %                                   |
| SW_Al_250_P15  | 620.52               | 503.54               | 116.98                           | 18.85 %                                   |
| SW_Al_400_P15  |                      | 549.93               | 70.59                            | 11.38 %                                   |
| SW_Al_700_P15  |                      | 523.07               | 97.45                            | 15.70 %                                   |
| S_Al_P25       | 825.94               | 675.05               | 150.89                           | 18.27 %                                   |
| S_AIS_P25      |                      | 747.68               | 78.26                            | 9.48 %                                    |
| S_AIS_P35      |                      | 972.90               | 214.79                           | 18.08 %                                   |
| SW_AIS_250_P35 | 1187.69              | 752.56               | 435.13                           | 36.64 %                                   |
| SW_AIS_400_P35 |                      | 867.92               | 319.77                           | 26.92 %                                   |
| SW_AIS_700_P35 |                      | 944.21               | 243.48                           | 20.50 %                                   |

## 6.2.2 Midpoint Displacement - Aluminum Skins

A comparison of numerical and experimental midpoint displacement for the Al components are shown in Figure 6.4 and in Table 6.3. The simulations follow a pattern similar to the experimental results described in Section 5.3.7, where the midpoint displacement increases with decreasing foam density. At 10 bar firing pressure, generally, the numerical simulations yield greater levels of displacement with a maximum displacement of about 10 to 20 % greater than the experimental values. An exception is observed for SW\_Al\_250\_P10, which only displayed an increase of 0.45 %. The reason for this exception is not currently known. The overestimation of midpoint displacement by numerical simulations is in agreement with the findings of Aune et al. [18].

While experiment SW\_Al\_400\_P15 and S\_Al\_P15 experienced fracture in the experimental study, the numerical and experimental results for experiment SW\_Al\_250\_P15 and SW\_Al\_700\_P15 have a difference of less than 2.5 %. It is observed that both simulations experience a midpoint displacement lower than the experimental results for most of their displacement history. Note that experiment SW\_Al\_700\_P15 reached some degree of fracture, as discussed in Section 5.3.7. In contrast to the experiments, the numerical simulations for experiment SW\_Al\_400\_P15 and S\_Al\_P15 did not exhibit fracture. As discussed in Section 3.3, fracture is mesh dependent. The results suggest that the coarse mesh of the reference model does not capture the stress localization from the tensile tearing along the edge of the clamping frame which might cause the obtained behavior. Mesh refinement is necessary when studying components loaded close to their capacity. However, all simulations capture the shape of the midpoint displacement histories of the experiments in an accurate way.

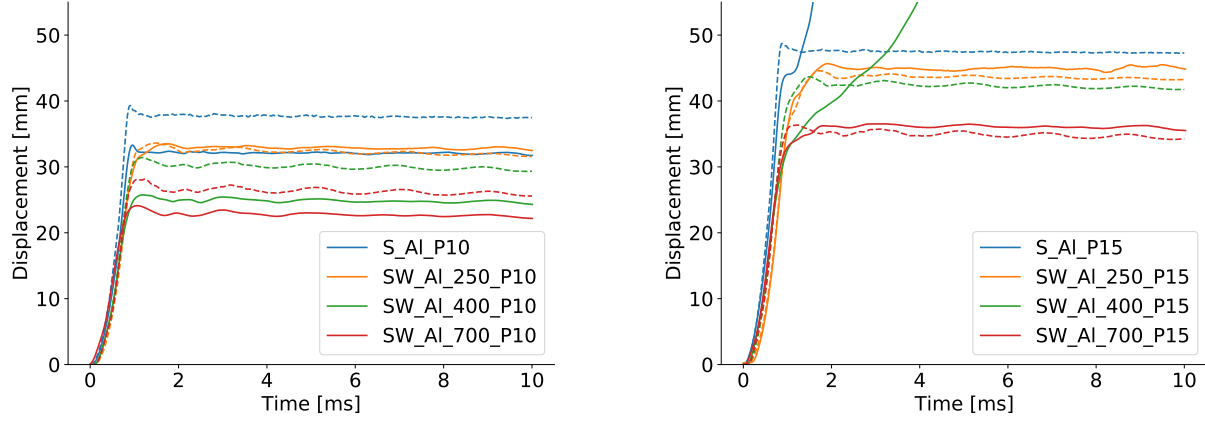


Figure 6.4: Numerical (dashed lines) and experimental (solid lines) midpoint displacement for Al components exposed to a nominal firing pressure of 10 *bar* (left) and 15 *bar* (right).

Table 6.3: Numerical,  $u_n$ , and experimental,  $u_e$ , maximum midpoint displacement and the deviation between them for Al components exposed to a nominal firing pressure of 10 *bar* and 15 *bar*.

| Test Name     | Numerical $u_n$<br>[mm] | Experimental $u_e$<br>[mm] | $u_n - u_e$<br>[mm] | $\frac{u_n - u_e}{u_n}$ |
|---------------|-------------------------|----------------------------|---------------------|-------------------------|
| S_Al_P10      | 39.31                   | 33.31                      | 6.00                | 15.27 %                 |
| SW_Al_250_P10 | 33.65                   | 33.50                      | 0.15                | 0.45 %                  |
| SW_Al_400_P10 | 31.42                   | 25.75                      | 5.68                | 18.06 %                 |
| SW_Al_700_P10 | 28.16                   | 24.11                      | 4.05                | 14.38 %                 |
| S_Al_P15      | 48.73                   | Fracture                   | -                   | -                       |
| SW_Al_250_P15 | 44.59                   | 45.67                      | -1.08               | -2.42 %                 |
| SW_Al_400_P15 | 43.68                   | Fracture                   | -                   | -                       |
| SW_Al_700_P15 | 36.36                   | 36.24                      | 0.12                | 0.33 %                  |

### 6.2.3 Midpoint Displacement - Aluminum and Steel Skins

The numerical and experimental midpoint displacement results of the AIS components are presented in Figure 6.5 and in Table 6.4. The AIS configurations also display increased midpoint displacements in the numerical results compared to the experimental results. The numerical simulations of the AIS configuration, without the foam core, is found to have an increase of 11 to 13 % midpoint displacement while the AIS sandwich components display an increase of 17 to 35 %. The experimental and numerical midpoint displacement behavior for the AIS sandwich components exposed to 35 *bar* is similar to the behavior of the Al sandwich components exposed to 10 *bar*, concerning an increase in midpoint displacement with decreased foam density. However, the simulations of the AIS configuration display a behavior where there is a gap present between the component with a foam core of XPS-400 and XPS-700, in contrast to the formerly mentioned gap between XPS-250 and XPS-400 in the experiments.

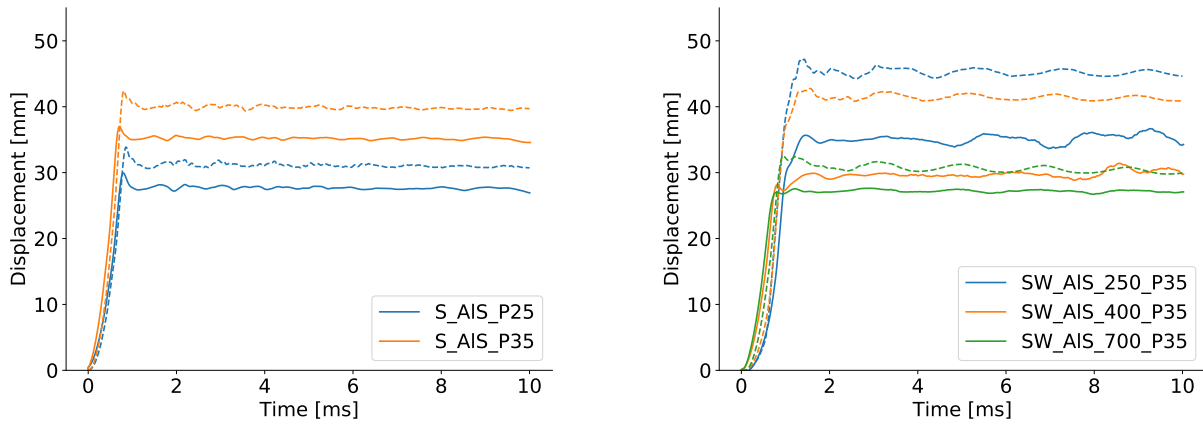


Figure 6.5: Numerical (dashed lines) and experimental (solid lines) midpoint displacement for AIS skins, without foam cores, exposed to a nominal firing pressure of 25 and 35 *bar* (left) and for AIS sandwich components exposed to a nominal firing pressure of 35 *bar* (right).

Table 6.4: Numerical,  $u_n$ , and experimental,  $u_e$ , maximum midpoint displacement for AIS components exposed to a nominal firing pressure of 25 and 35 *bar* and 35 *bar*, respectively.

| Test Name      | Numerical $u_n$<br>[mm] | Experimental $u_e$<br>[mm] | $u_n - u_e$<br>[mm] | $\frac{u_n - u_e}{u_n}$ |
|----------------|-------------------------|----------------------------|---------------------|-------------------------|
| S_AIS_P25      | 33.88                   | 29.96                      | 3.91                | 11.55 %                 |
| S_AIS_P35      | 42.39                   | 36.99                      | 5.40                | 12.74 %                 |
| SW_AIS_250_P35 | 47.21                   | 35.67                      | 11.54               | 24.44 %                 |
| SW_AIS_400_P35 | 42.78                   | 28.14                      | 14.64               | 34.21 %                 |
| SW_AIS_700_P35 | 32.55                   | 27.00                      | 5.55                | 17.05 %                 |

## 6.2.4 Deformation Profiles - Aluminum Skins

The experimental deformation profiles are extracted at maximum midpoint displacement, 3/4, 2/4 and 1/4 of maximum midpoint displacement. Additionally, profiles illustrating maximum displacement for the numerical simulations are shown. The numerical deformation profiles are extracted at similar deformation levels and not the exact same time, to be able to compare the evolution of the deformation shape between experiments and simulations. A comparison of deformation profiles at the same moment in time would be less useful considering the steepness of the slope between impact and maximum displacement.

In Figure 6.6 and Figure 6.7 the evolution of the deformation profiles obtained from numerical simulations and 3D-DIC analysis are presented. Figure 6.6 shows the development for Al skins without a foam core exposed to 10 and 15 *bar* firing pressure, while Figure 6.7 displays the results for Al sandwich components with varying foam cores exposed to 10 and 15 *bar* firing pressure. Figure 6.6a shows agreement between the numerical and experimental evolution of deformation shape. It is noticeable that the numerical simulation exhibits a rounder deformation shape at the given deformation levels. However, the shape of maximum displacement for both numerical and experimental profiles are fairly similar regarding roundness. The results show that the displacement initiates at the edges of the component and propagates towards the plate centers. This mechanism is more noticeable for skins without a foam core than sandwich panels. The behavior was accurately captured numerically for all experiments. In Figure 6.7 it is observed that there is general agreement between experimental and numerical deformation profiles, except for experiment SW\_Al\_400\_P15, where the sandwich component experienced fracture during testing.

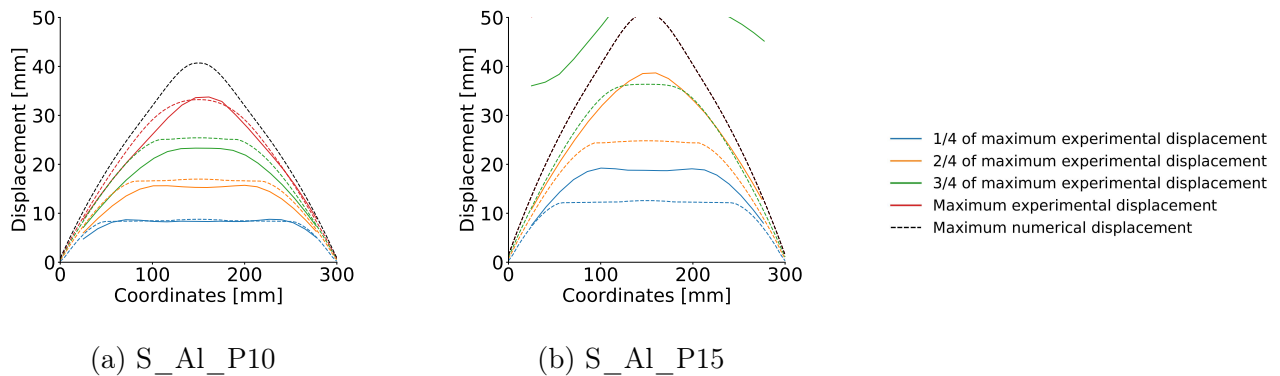
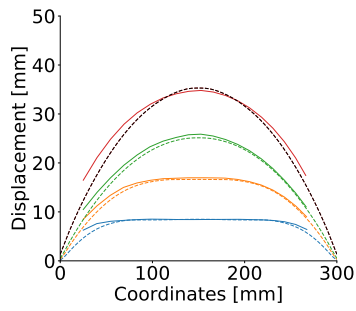
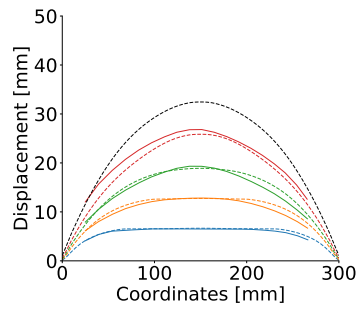


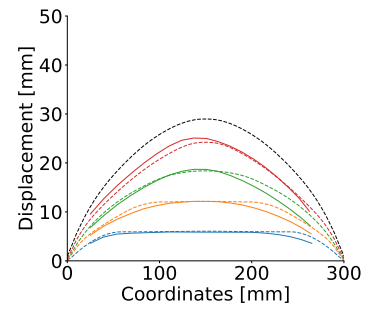
Figure 6.6: Numerical (dashed lines) and experimental (solid lines) deformation profiles for Al skins without foam cores exposed to a nominal firing pressure of 10 *bar* (left) and 15 *bar* (right).



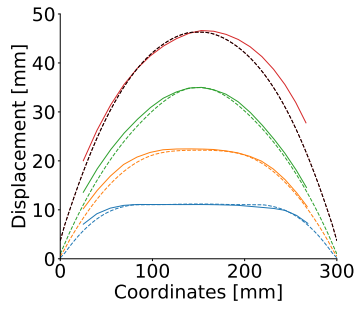
(a) SW\_Al\_250\_P10



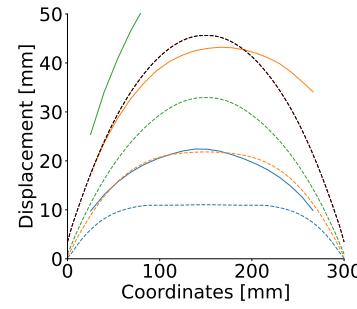
(b) SW\_Al\_400\_P10



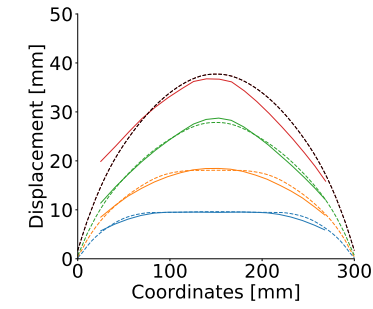
(c) SW\_Al\_700\_P10



(d) SW\_Al\_250\_P15



(e) SW\_Al\_400\_P15



(f) SW\_Al\_700\_P15

Figure 6.7: Numerical (dashed lines) and experimental (solid lines) deformation profiles for Al sandwich components with XPS-250 (left), XPS-400 (center) and XPS-700 (right) as core material exposed to a nominal firing pressure of 10 *bar* (top) and 15 *bar* (bottom).

## 6.2.5 Deformation Profiles - Aluminum and Steel Skins

In Figure 6.8 and Figure 6.9 the evolution of the deformation profiles obtained from numerical simulations and 3D-DIC analysis of AIS components are presented. Figure 6.8 shows the development for AIS skins without a foam core exposed to 25 and 35 *bar* firing pressure, while Figure 6.8 displays the results for AIS sandwich components with varying foam cores exposed to 35 *bar* firing pressure. Small deviation between experimental and numerical results, except the maximum numerical deformation profile, is observed in Figure 6.8. In Figure 6.9 it is noticeable that the maximum simulated deformation profile deviates from the experimental one, with some margin, with experiment SW\_AIS\_400\_P35 standing out. Looking at the shapes exclusively, where the deformation initiates at the edges and propagates towards the center, there is good agreement between experimental and numerical results.

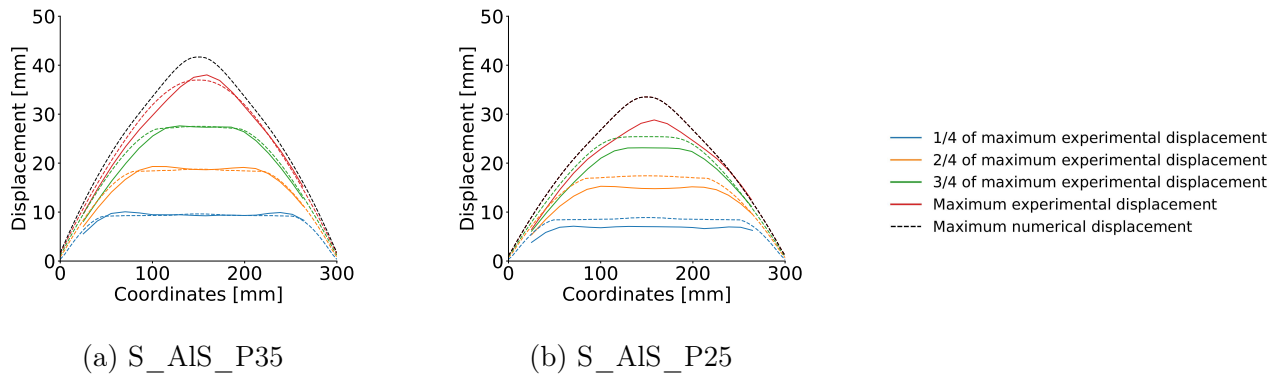


Figure 6.8: Numerical (dashed lines) and experimental (solid lines) deformation profiles for AIS skins without foam cores exposed to a nominal firing pressure of 35 *bar* (left) and 25 *bar* (right).

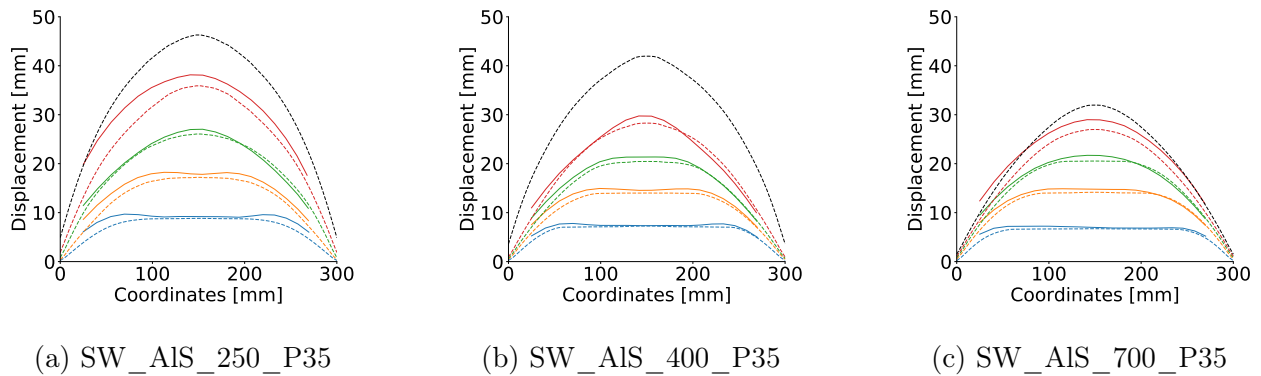


Figure 6.9: Numerical (dashed lines) and experimental (solid lines) deformation profiles for AIS sandwich components with XPS-250 (left), XPS-400 (center) and XPS-700 (right) as core material exposed to a nominal firing pressure of 35 *bar*.

## 6.3 Further Numerical Results

In this section, the properties of the sandwich components structural response not captured by the experimental setup will be presented and investigated. The compression and strains of the foam core, the energy absorbed and distribution between skins and foam core and the reaction force is presented to evaluate the energy absorption capabilities of the sandwich panels. In addition to numerical simulations of the configurations included in the experimental program, Al and AlS configurations exposed to 25 *bar* firing pressure was included for the completeness of the results and more meaningful comparisons. It is worth mentioning that the Al configuration would, experimentally, most likely reach fracture. However, fracture was not observed in the numerical simulations due to the coarse mesh of the reference model, as discussed in Section 3.3. The results are included, but not emphasized because of the somewhat nonphysically large deformations without fracture.

### 6.3.1 Foam Compression

The foam core compression was obtained from the numerical front skin and back skin deformation profiles. Figure 6.10 illustrates the deformation profiles of all sandwich components tested in the experimental program. Figure 6.10a, 6.10b, 6.10c, 6.10d and 6.10f also displays the results from the scanning performed with the RAA, described in Section 5.3.9. Figure 6.12 shows the cross section of numerical models for Al sandwich components with foam cores of XPS-250 and XPS-700 exposed to 15 *bar* firing pressure.

The difference between the results obtained through numerical simulations and the results obtained with the RAA can be seen in Figure 6.10. Significant deviations can be observed between the results from the RAA scanning and the numerical results. Generally, the numerically recorded deformation of the back skin is in agreement with the scanned results. However, recordings of the front skin deformation deviate significantly, which leads to significant differences in recorded foam compression at the middle and sides of the components. This is likely due to the difference in conditions described in Section 5.3.9, such as the fact that the scanned results were obtained post-experiment allowing elastic effects to take place, while the numerical results were extracted within 10 *ms* of the blast loading impacting the components.

The foam compression in the middle of the components, seen in Table 6.5, was obtained by calculating the difference between maximum midpoint displacement for the front and back skin and then subtracting it from the initial foam thickness of 50 *mm*. The same procedure was followed to obtain the average foam compression at the edge of the blast-exposed area, seen in Table 6.5. The numerical deformation profiles in Figure 6.10 and the numbers associated with the calculated results, shown in Table 6.5, were extracted at the last time step in the numerical results, unlike the maximum values studied in Section 5.3.7 and 5.3.8.



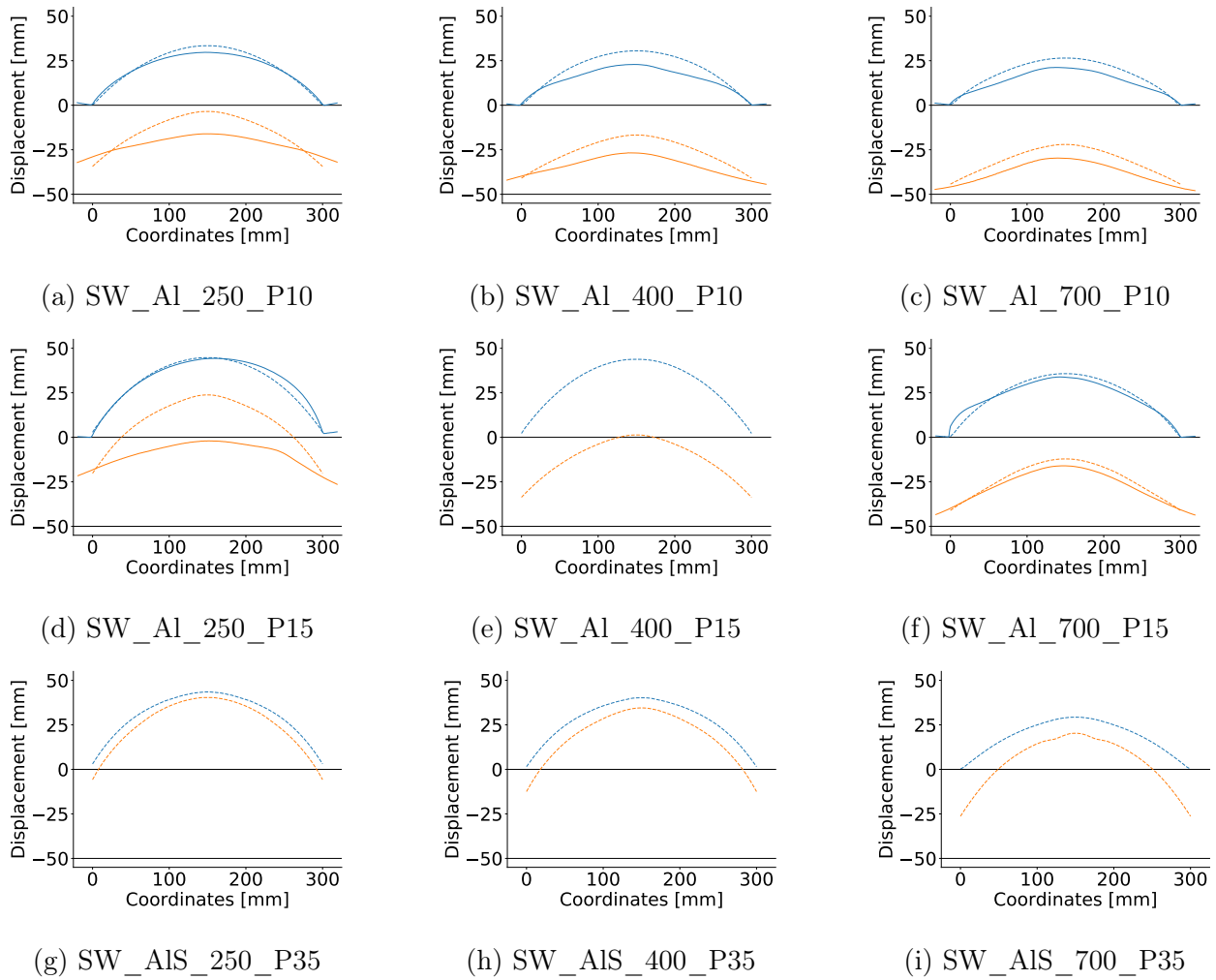


Figure 6.10: Numerical (dashed lines) and experimental (solid lines) deformation profiles for sandwich components with XPS-250 (left), XPS-400 (center) and XPS-700 (right) as core material exposed to a nominal firing pressure of 10 (top), 15 (center) and 35 *bar* (bottom).

Table 6.5: Numerical front and back skin midpoint displacement,  $u_{FS}$  and  $u_{BS}$ , and middle and side foam core compression,  $C_{mid}$  and  $C_{side}$ , for sandwich components extracted from deformation profiles.

| Test Name      | $u_{FS}$<br>[mm] | $u_{BS}$<br>[mm] | $C_{mid}$<br>[mm] | $C_{side}$<br>[mm] |
|----------------|------------------|------------------|-------------------|--------------------|
| SW_Al_250_P10  | 46.48            | 33.39            | 13.09             | 15.53              |
| SW_Al_400_P10  | 33.25            | 30.51            | 2.74              | 8.68               |
| SW_Al_700_P10  | 27.96            | 26.47            | 1.49              | 5.21               |
| SW_Al_250_P15  | 73.79            | 44.71            | 29.08             | 26.95              |
| SW_Al_400_P15  | 51.30            | 43.78            | 7.52              | 14.12              |
| SW_Al_700_P15  | 37.84            | 35.73            | 2.11              | 8.44               |
| SW_Al_250_P25  | 106.70           | 67.80            | 38.90             | 35.04              |
| SW_Al_400_P25  | 81.06            | 56.64            | 24.42             | 25.05              |
| SW_Al_700_P25  | 55.65            | 51.11            | 4.54              | 10.28              |
| SW_AIS_250_P25 | 74.15            | 28.90            | 45.26             | 35.23              |
| SW_AIS_400_P25 | 64.54            | 23.89            | 40.65             | 23.24              |
| SW_AIS_700_P25 | 33.98            | 23.31            | 10.67             | 7.28               |
| SW_AIS_250_P35 | 90.33            | 43.47            | 46.87             | 41.17              |
| SW_AIS_400_P35 | 84.48            | 40.18            | 44.31             | 36.00              |
| SW_AIS_700_P35 | 70.26            | 29.28            | 40.98             | 23.46              |

Figure 6.11 presents the numerical middle foam compression of all sandwich components. It is observed that the foam compression is decreasing with increased foam density for all panels. The same trend is observed for the foam compression at the edge of the blast-exposed area, seen in Table 6.5. At 10 and 15 *bar* firing pressure, the difference between XPS-250 and XPS-700 foam is significant, while for the sandwich components exposed to 35 *bar* firing pressure the differences in numerically recorded foam compression is smaller. The combination of a high firing pressure, a relatively soft and ductile aluminum front skin and a stiff steel back skin caused the foam to compress up to 93.74 % of the thickness, where the foam is approaching the densification stage explained in Section 2.4. This mechanism causes a rapid rise in the stress-strain curve, which explains the small variations in foam compression with increasing density for the sandwich components exposed to 35 *bar* firing pressure, seen in Figure 6.11.

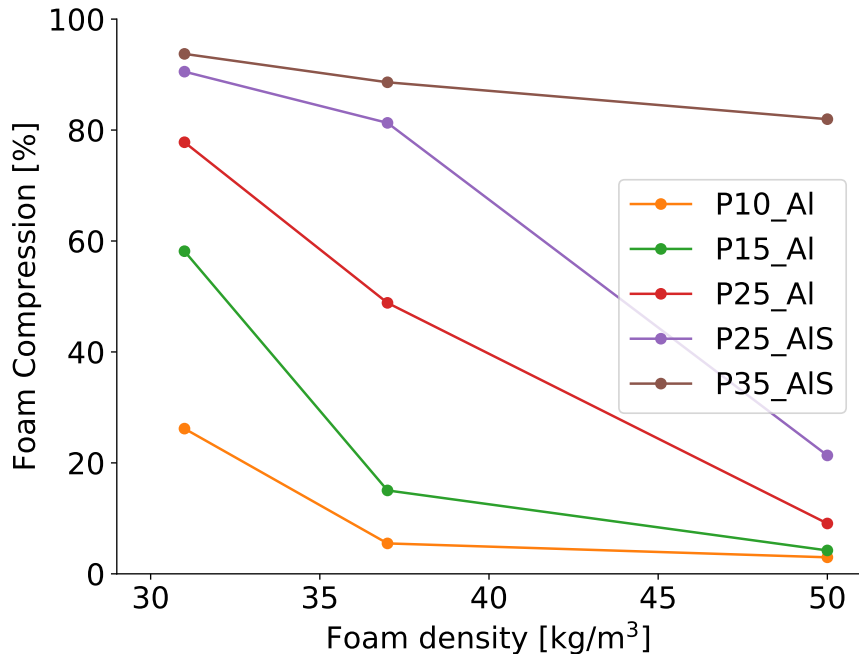


Figure 6.11: Percentage of foam core compression for sandwich components exposed to 10, 15, 25 and 35 *bar* firing pressure.

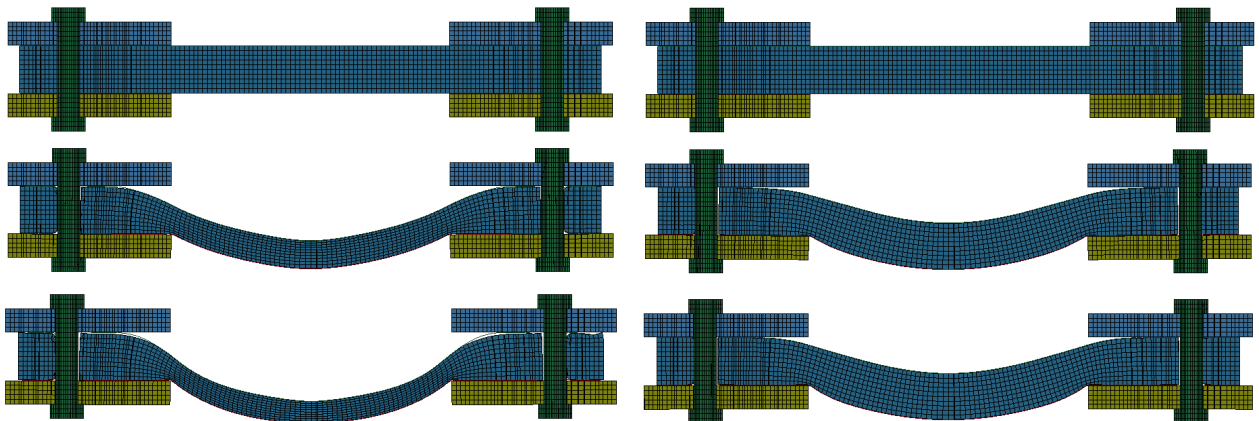


Figure 6.12: Cross section of Al sandwich panels with foam core of XPS-250 (left) and XPS-700 (right) after 0 *ms* (top), 1 *ms* (middle) and 2 *ms* (bottom) at 15 *bar* firing pressure.

### 6.3.2 Strain

The strain,  $\epsilon$ , in the foam core is an interesting measurement in the evaluation of a sandwich components ability to effectively absorb energy. The recorded strains can be related to the densification initiation strain, which is an important parameter describing the compression behavior of a foam, described in Section 2.4. Figure 6.13 presents the effective plastic strain distribution in the XPS-250 core of an Al sandwich panel exposed to 15 *bar* firing pressure from a front view, back view, and middle cross-section. It is observed that the maximum effective plastic strain is located at the corner of the front side exposed to the blast loading. However, the distribution is seen to be fairly uniform in-plane and through the thickness. Therefore, extracting the effective plastic strain at the middle, front element in the numerical model is assumed a sufficient measure of the effective plastic strain in the blast-exposed area through the thickness. The true strain value is obtained by adding the yield strain obtained in Section 4.3.3 to the extracted effective plastic strain. The recorded values for strain and the densification initiation strain for all sandwich components are presented in Table 6.6.

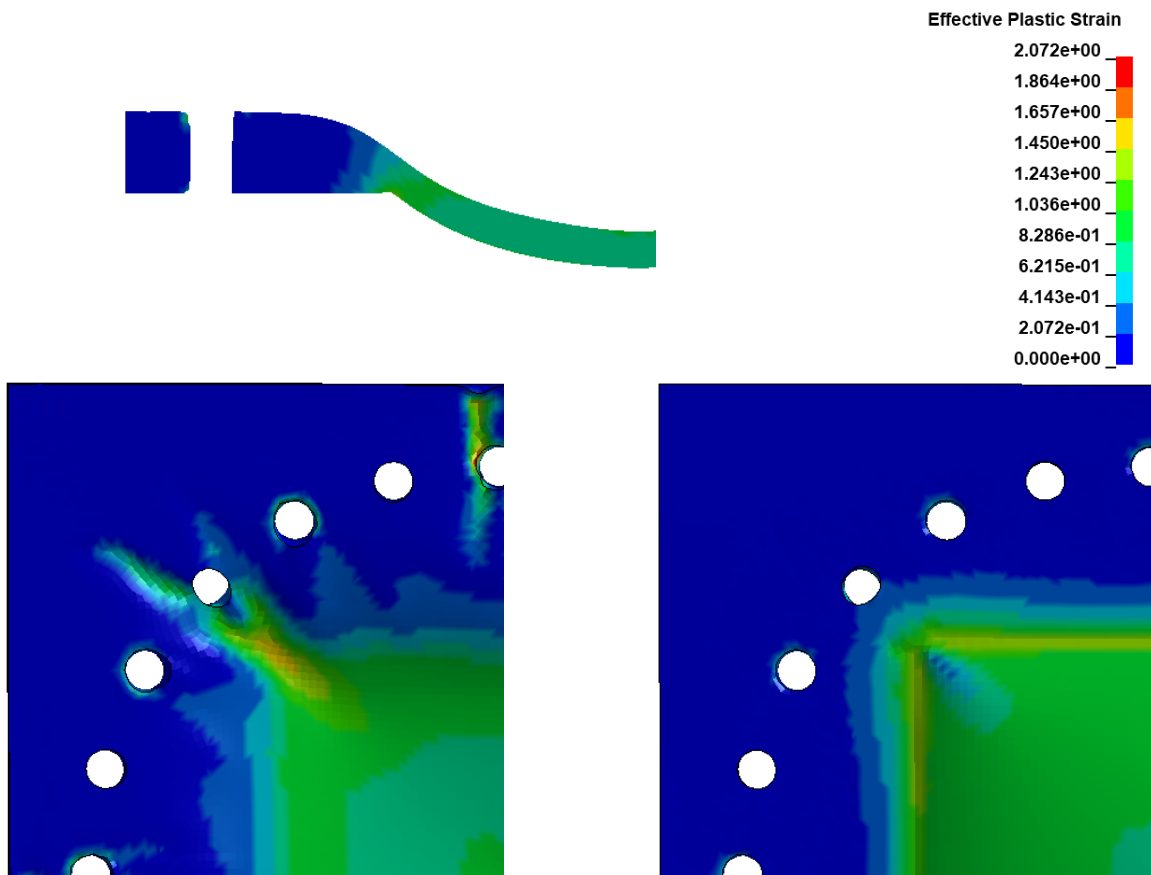


Figure 6.13: Effective plastic strain distribution for one quarter of a Al sandwich panel at middle cross-section (top), front side (bottom left) and back side (bottom right) exposed to 15 *bar* firing pressure.

Table 6.6: Strains in foam core, densification initiation strains and their deviation for sandwich components at 10, 15, 25 and 35 *bar* firing pressure.

| Test Name      | $\varepsilon$<br>[—] | $\varepsilon_{d0}$<br>[—] | $\frac{\varepsilon}{\varepsilon_{d0}}$ |
|----------------|----------------------|---------------------------|--|
| SW_AI_250_P10  | 0.39                 | 1.43                      | 27.34 %                                |
| SW_AI_400_P10  | 0.13                 | 1.39                      | 9.64 %                                 |
| SW_AI_700_P10  | 0.09                 | 1.21                      | 7.02 %                                 |
| SW_AI_250_P15  | 0.88                 | 1.43                      | 61.26 %                                |
| SW_AI_400_P15  | 0.37                 | 1.39                      | 26.26 %                                |
| SW_AI_700_P15  | 0.10                 | 1.21                      | 8.35 %                                 |
| SW_AI_250_P25  | 1.38                 | 1.43                      | 96.36 %                                |
| SW_AI_400_P25  | 0.86                 | 1.39                      | 61.65 %                                |
| SW_AI_700_P25  | 0.15                 | 1.21                      | 12.56 %                                |
| SW_AIS_250_P25 | 2.13                 | 1.43                      | 148.74 %                               |
| SW_AIS_400_P25 | 1.57                 | 1.39                      | 115.18 %                               |
| SW_AIS_700_P25 | 0.32                 | 1.21                      | 26.12 %                                |
| SW_AIS_250_P35 | 2.50                 | 1.43                      | 174.62 %                               |
| SW_AIS_400_P35 | 2.05                 | 1.39                      | 147.63 %                               |
| SW_AIS_700_P35 | 1.53                 | 1.21                      | 126.45 %                               |

Figure 6.15 presents the extracted foam core strain compared with the foam core densification initiation strain at the associated stress-strain and efficiency-strain curves from compression tests. The recorded strain values give a reasonable estimation of which structural behavioral regime the foam reaches when subjected to various pressures, whether it is the elastic regime, the plateau stage or densification region. It is observed that XPS-250 and XPS-400 might not be dense enough when exposed to 35 *bar* firing pressure, i.e., the densification region is reached causing a rapid increase in stress. Further, XPS-700 might be too dense when exposed to firing pressures lower than 35 *bar*, i.e., a small portion of the plateau region is utilized for energy absorption. Note that the strains obtained in the numerical work include significantly higher strain rates than the compression test. More accurate results would be obtained by performing compression tests at higher strain rates or applying a strain rate dependent model to the problem, which will be further discussed in Chapter 7.

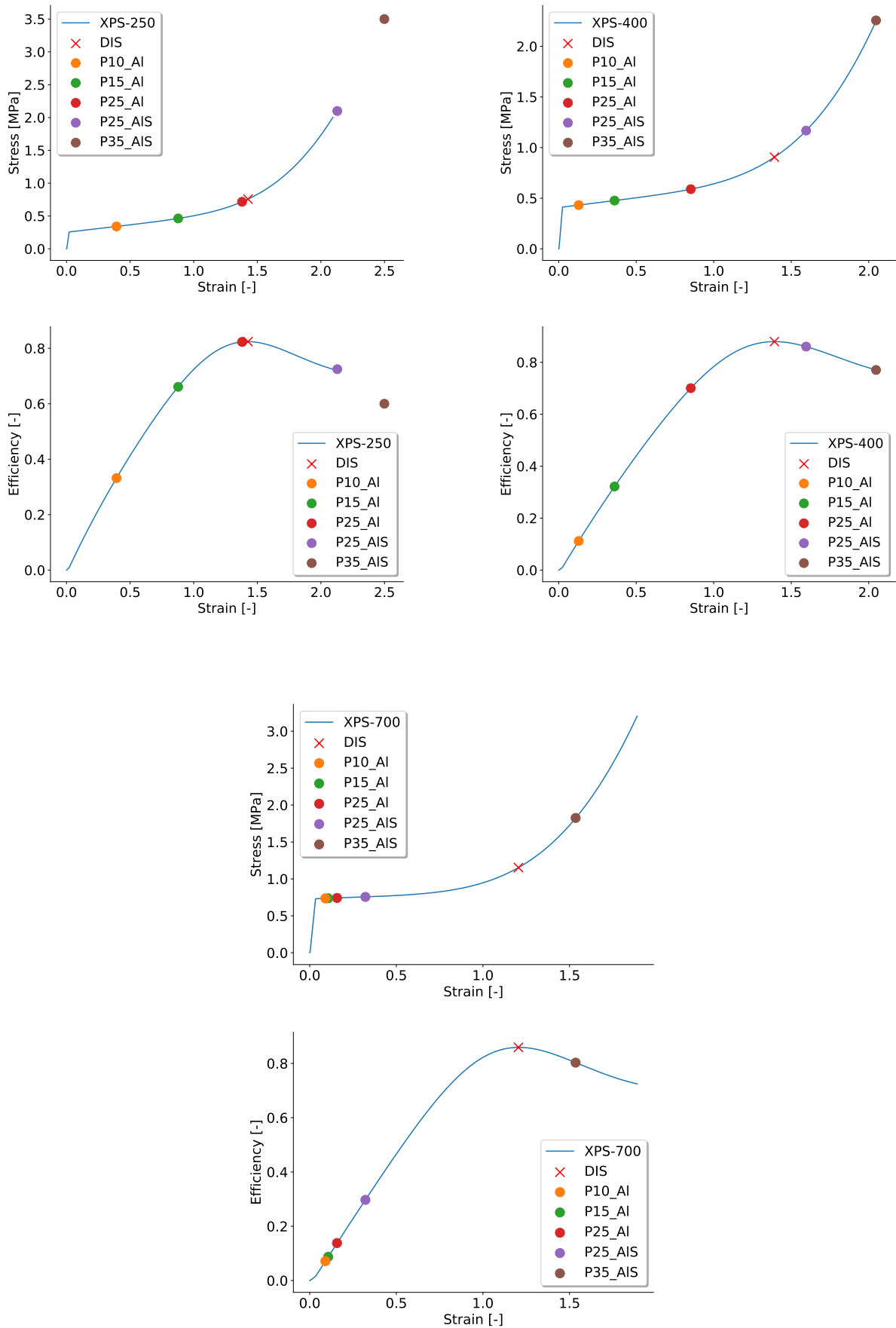


Figure 6.15: Foam core strain values and densification initiation strain presented at compression test stress-strain and efficiency-strain curves for XPS-250 (top and middle left), XPS-400 (top and middle right) and XPS-700 (bottom).

### 6.3.3 Energy Absorption

Energy absorption is an essential parameter in the evaluation of protective properties of a sandwich structure. Since the current experimental setup did not facilitate calculations or recordings of energy absorption, the energy absorption was studied numerically. The absorbed energy is extracted as the internal energy of each part. Figure 6.16 presents the energy absorption for Al components subjected to 10, 15 and 25 *bar* firing pressure (left), and AIS components exposed to 25 and 35 *bar* firing pressure (right). Sandwich panels with low-density foam absorbed most energy and the energy absorbed is decreasing with increased foam density. Regarding components without foam cores, Al specimens showed energy absorbed equally divided between the two skins, while for AIS specimens the back skin absorbed a larger fraction of energy.

Figure 6.17 presents the energy fraction absorbed in the foam core for Al sandwich panels subjected to 10, 15 and 25 *bar* firing pressure (left), and AIS panels exposed to 25 and 35 *bar* firing pressure (right). For Al sandwich panels, it is observed that the fraction of energy absorbed in the foam core decreased with increased foam density, while an increase for the AIS sandwich panels is observed. Both configurations subjected to 25 *bar* exhibit a maximum foam energy absorption fraction with XPS-400 foam core. In Section 6.3.1 the foam compression of the high-density foam panels subjected to 10 and 15 *bar* firing pressure is small, while the compression value for panels exposed to 35 *bar* is above 80% with small variations. It can be observed, in Figure 6.15, that the strain values obtained for the numerical simulations exposed to 35 *bar* exceed the densification initiation strain, which means the foam is in the densification region of the stress-strain curve. It is observed that components with XPS-400 core exposed to 25 *bar* firing pressure exhibit strains close to the densification initiation strain which explains the observed maximum foam absorption fraction. The numbers, #, in the bar charts are explained in Table 6.7 together with the total absorbed energy and the energy fraction distribution between the skins and the foam.

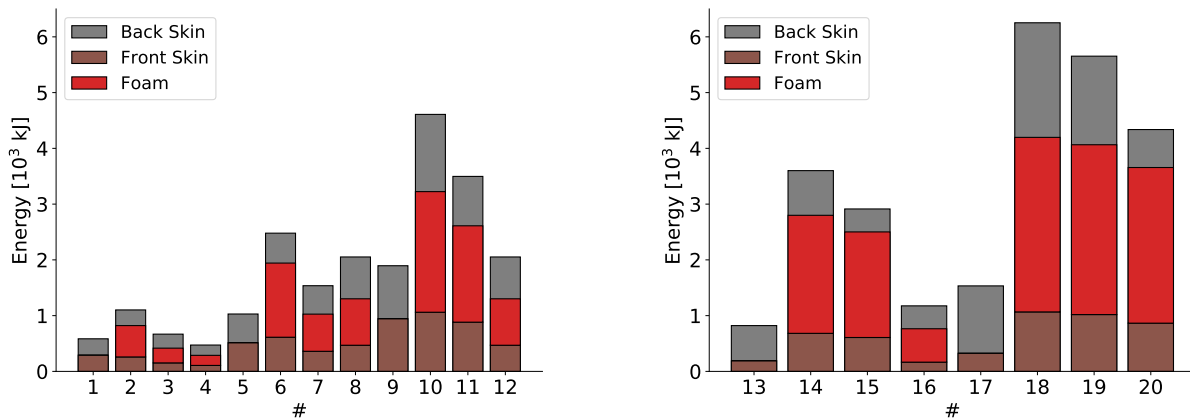


Figure 6.16: Energy absorption in front skin, foam and back skin for Al components (left) and for AIS components (right).

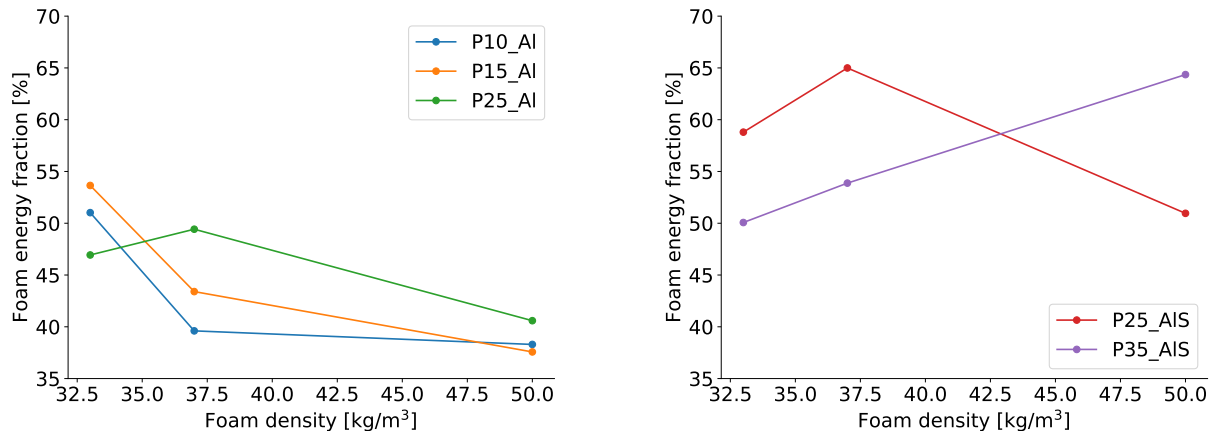


Figure 6.17: Fraction of energy absorbed in the foam core of Al sandwich panels (left) and AIS sandwich panels (right).

Table 6.7: Fraction of energy absorbed in front skin (FS), foam core and back skin (BS) and total energy absorbed for components exposed to 10, 15, 25 and 35 bar firing pressure.

| #  | Test Name      | FS fraction<br>[-] | Foam fraction<br>[-] | BS fraction<br>[-] | Absorbed energy<br>[kJ] |
|----|----------------|--------------------|----------------------|--------------------|-------------------------|
| 1  | S_Al_P10       | 0.50               | -                    | 0.50               | 584.45                  |
| 2  | SW_Al_250_P10  | 0.24               | 0.51                 | 0.25               | 1102.19                 |
| 3  | SW_Al_400_P10  | 0.23               | 0.40                 | 0.38               | 668.00                  |
| 4  | SW_Al_700_P10  | 0.23               | 0.38                 | 0.39               | 472.48                  |
| 5  | S_Al_P15       | 0.50               | -                    | 0.50               | 1029.14                 |
| 6  | SW_Al_250_P15  | 0.25               | 0.54                 | 0.22               | 2479.10                 |
| 7  | SW_Al_400_P15  | 0.23               | 0.43                 | 0.33               | 1536.65                 |
| 8  | SW_Al_700_P15  | 0.23               | 0.38                 | 0.39               | 947.54                  |
| 9  | S_Al_P25       | 0.50               | -                    | 0.50               | 1894.95                 |
| 10 | SW_Al_250_P25  | 0.23               | 0.47                 | 0.30               | 4609.10                 |
| 11 | SW_Al_400_P25  | 0.25               | 0.49                 | 0.25               | 3496.94                 |
| 12 | SW_Al_700_P25  | 0.23               | 0.41                 | 0.37               | 2052.13                 |
| 13 | S_AIS_P25      | 0.23               | -                    | 0.77               | 821.40                  |
| 14 | SW_AIS_250_P25 | 0.19               | 0.59                 | 0.33               | 3600.66                 |
| 15 | SW_AIS_400_P25 | 0.21               | 0.65                 | 0.14               | 2913.27                 |
| 16 | SW_AIS_700_P25 | 0.14               | 0.51                 | 0.35               | 1175.31                 |
| 17 | S_AIS_P35      | 0.21               | -                    | 0.79               | 1533.38                 |
| 18 | SW_AIS_250_P35 | 0.17               | 0.50                 | 0.33               | 6252.30                 |
| 19 | SW_AIS_400_P35 | 0.18               | 0.54                 | 0.28               | 5653.50                 |
| 20 | SW_AIS_700_P35 | 0.20               | 0.64                 | 0.16               | 4337.48                 |



### 6.3.4 Specific Energy Absorption

The specific energy absorption is obtained by dividing the absorbed energy by the mass of the numerical sandwich model. Figure 6.18 presents the specific energy absorption where double skins specimen are represented with zero foam density. Sandwich panels with low-density foam absorb the most specific energy, and the absorption decreases with increased foam density which is also obtained studying the energy absorption in Section 6.3.3. For firing pressures of 10 and 15 *bar*, this effect is more pronounced than for firing pressures of 25 and 35 *bar*. It is also seen that the specific energy absorbed by components without a foam core is more similar to components with low-density foam core for lower firing pressures with a higher specific energy absorption than the high-density foams due to low foam activation. It is observed that the Al skins, without a foam core, at 15 *bar* absorbs more specific energy than the AIS component, without foam core, exposed to a pressure of 35 *bar* due to the high weight of the steel back skin. However, it is worth mentioning that the Al skins without foam core exposed to 25 *bar* reached fracture experimentally, but not numerically due to the coarse mesh of the reference model. Therefore, the Al sandwich panel exposed to 25 *bar*, displays a somewhat nonphysically large deformation and energy absorption, which can be seen in Figure 6.18.

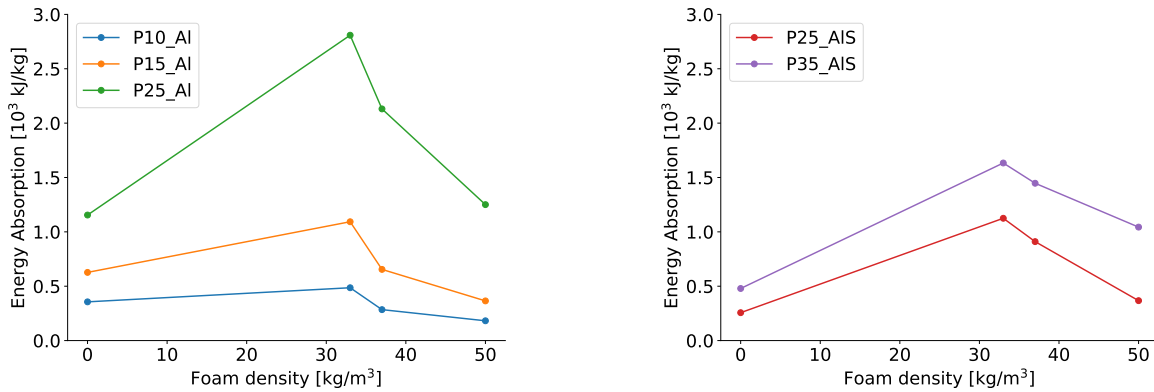


Figure 6.18: Specific energy absorption for components with Al skins (left) AIS skins (right), where specimens without a foam core are marked with zero foam density.

Table 6.8: Mass of the components, total energy absorbed and specific energy absorption for components exposed to 10, 15, 25 and 35 *bar* firing pressure.

| Test Name      | Mass<br>[ <i>kg</i> ] | Absorbed energy<br>[ <i>kJ</i> ] | Specific energy<br>[ <i>kJ/kg</i> ] |
|----------------|-----------------------|----------------------------------|-------------------------------------|
| S_Al_P10       | 1.641                 | 584.45                           | 356.13                              |
| SW_Al_250_P10  | 2.268                 | 1102.19                          | 485.93                              |
| SW_Al_400_P10  | 2.347                 | 668.00                           | 284.59                              |
| SW_Al_700_P10  | 2.596                 | 472.48                           | 181.98                              |
| S_Al_P15       | 1.641                 | 1029.14                          | 627.10                              |
| SW_Al_250_P15  | 2.268                 | 2479.10                          | 1092.93                             |
| SW_Al_400_P15  | 2.347                 | 1536.65                          | 654.67                              |
| SW_Al_700_P15  | 2.596                 | 947.54                           | 364.96                              |
| S_Al_P25       | 1.641                 | 1894.95                          | 1154.67                             |
| SW_Al_250_P25  | 2.268                 | 4609.10                          | 2808.51                             |
| SW_Al_400_P25  | 2.347                 | 3496.94                          | 2130.83                             |
| SW_Al_700_P25  | 2.596                 | 2052.13                          | 1250.44                             |
| S_AIS_P25      | 3.200                 | 821.40                           | 251.61                              |
| SW_AIS_250_P25 | 3.828                 | 3600.66                          | 1124.87                             |
| SW_AIS_400_P25 | 3.907                 | 2913.27                          | 910.14                              |
| SW_AIS_700_P25 | 4.156                 | 1175.31                          | 367.18                              |
| S_AIS_P35      | 3.200                 | 1533.38                          | 479.05                              |
| SW_AIS_250_P35 | 3.828                 | 6252.30                          | 1633.30                             |
| SW_AIS_400_P35 | 3.907                 | 5653.50                          | 1447.01                             |
| SW_AIS_700_P35 | 4.156                 | 4337.48                          | 1043.64                             |

### 6.3.5 Reaction Force

The reaction force is obtained as the resultant contact force between the back skin and the clamping frame. The force-time curves for all components are presented in Figure 6.19 and 6.20. The back clamping frame was not fixed in the direction of the deformation, which explains the oscillations in the force histories. In Table 6.9 the impulse, average and maximum force are presented, where the impulse is calculated as the area under the force-time curve. Components without foam cores experience high-frequency oscillations with large initial peaks which results in a maximum force with a magnitude twice as large as the maximum force for the sandwich panels. The average force is generally seen to increase with increased foam density, which again results in an increased impulse with an increase in foam density. However, a decrease in maximum force with, foam density, is seen for the sandwich components exposed to 35 *bar* firing pressure, which is suspected to be due to higher levels of foam compression. It is worth mentioning that variations within average force for sandwich panels exposed to the same nominal firing pressure are relatively small.

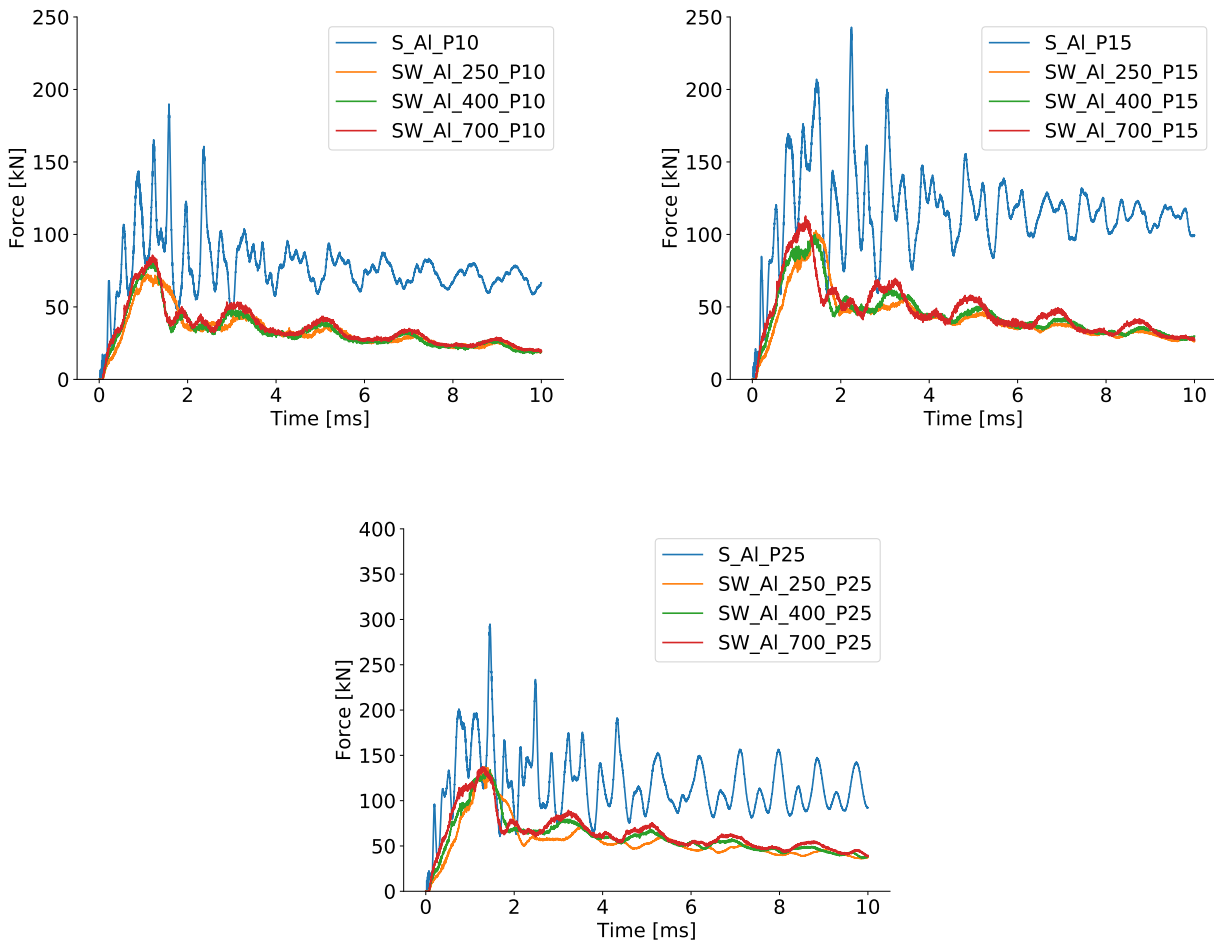


Figure 6.19: Force-time history curves for Al components subjected to 10 and 15 *bar* (top) and 25 *bar* (bottom) firing pressure.

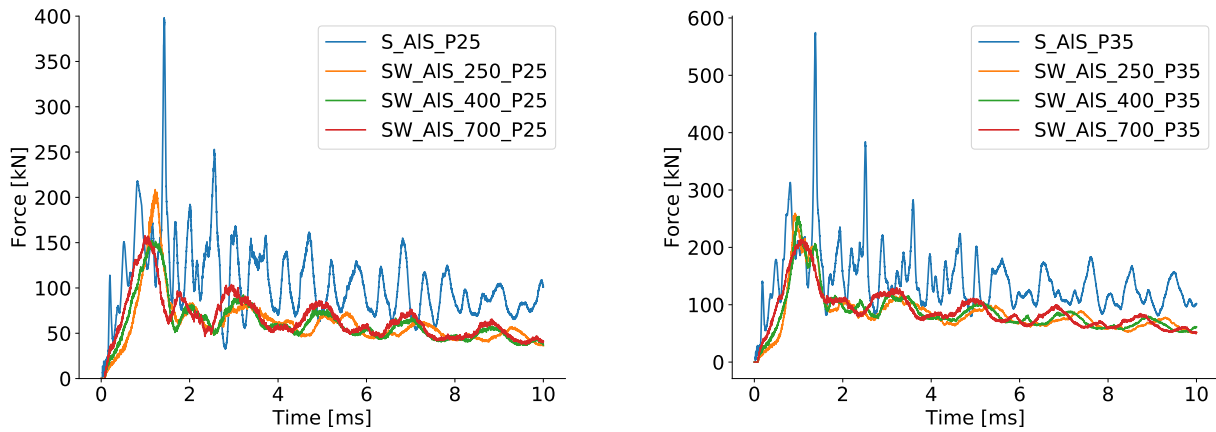


Figure 6.20: Force-time history curves for AIS components subjected to 25 *bar* (left) and 35 *bar* (right) firing pressure.

Table 6.9: Impulse, average force and maximum force for components exposed to 10, 15, 25 and 35 *bar* firing pressure.

| Test Name      | Impulse<br>[ <i>kNs</i> ] | Average force<br>[ <i>kN</i> ] | Max force<br>[ <i>kN</i> ] |
|----------------|---------------------------|--------------------------------|----------------------------|
| S_AI_P10       | 0.770                     | 77.04                          | 189.97                     |
| SW_AI_250_P10  | 0.328                     | 32.81                          | 72.61                      |
| SW_AI_400_P10  | 0.330                     | 33.04                          | 81.66                      |
| SW_AI_700_P10  | 0.354                     | 35.39                          | 85.70                      |
| S_AI_P15       | 1.155                     | 115.48                         | 242.92                     |
| SW_AI_250_P15  | 0.427                     | 42.68                          | 102.67                     |
| SW_AI_400_P15  | 0.451                     | 45.07                          | 99.98                      |
| SW_AI_700_P15  | 0.474                     | 47.38                          | 112.72                     |
| S_AI_P25       | 1.169                     | 116.88                         | 294.91                     |
| SW_AI_250_P25  | 0.555                     | 55.54                          | 137.37                     |
| SW_AI_400_P25  | 0.602                     | 60.15                          | 134.17                     |
| SW_AI_700_P25  | 0.639                     | 63.94                          | 137.27                     |
| S_AIS_P25      | 1.052                     | 105.23                         | 398.24                     |
| SW_AIS_250_P25 | 0.615                     | 61.46                          | 208.59                     |
| SW_AIS_400_P25 | 0.614                     | 61.36                          | 152.30                     |
| SW_AIS_700_P25 | 0.657                     | 65.66                          | 157.34                     |
| S_AIS_P35      | 1.416                     | 141.63                         | 574.43                     |
| SW_AIS_250_P35 | 0.840                     | 84.03                          | 259.47                     |
| SW_AIS_400_P35 | 0.860                     | 85.98                          | 253.84                     |
| SW_AIS_700_P35 | 0.895                     | 89.46                          | 213.61                     |

## 6.4 Parameter Study

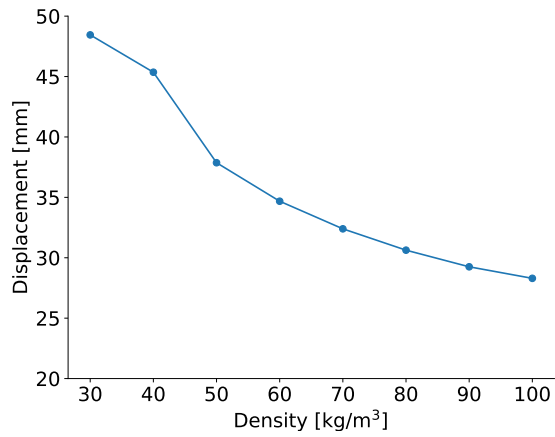
In this section, a parametric study investigating the change of back skin displacement, average force, total and specific energy absorbed, distribution of energy absorption, foam compression and strain with varying density and thickness is presented. First, a variation of density, while keeping the thickness constant is presented. Second, a variation of foam core thickness for XPS-250, XPS-400, and XPS-700 is presented. Finally, a variation of thickness and density, keeping the foam core mass constant, is presented. Numerical results were obtained for Al sandwich panels exposed to 10, 15 and 25 *bar* firing pressure and for AIS sandwich configurations exposed to 25 and 35 *bar* firing pressure. The general trends, commonalities and interesting observations for the parametric study will be presented with selected illustrative plots. For a more comprehensive presentation of the results the reader is referred to Appendix C.

### 6.4.1 Density

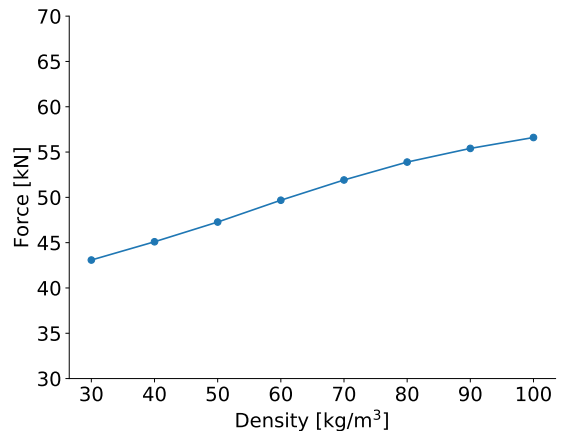
The density-dependent model presented in Section 4.3.4 is applied to obtain material parameters for a foam density range that spans from 30 to 100  $kg/m^3$ . It was also attempted to obtain material parameters for densities below 30  $kg/m^3$ . However, the resulting stress-strain curves provided by the density-dependent model significantly deviated from the stress-strain curves of the other foam densities and was therefore discarded. In Appendix C.1 all results for a variation of foam density can be seen.

Figure 6.21a and 6.21b shows the variation of maximum displacement on the back skin and the average force between the back skin and the back clamping frame for sandwich components exposed to 15 *bar* firing pressure, respectively. The results illustrate the expected trend for all components, where an increase in the density of the foam core gave a decrease in midpoint displacement for the back skin and a simultaneous increase in average force. The increase in average force was seen to be approximately 10 to 20  $kN$  in the different pressure ranges for a variation of foam density. The slope was noticeably steeper for the decrease in displacement in the range of 30 to 60  $kg/m^3$ , with the deformation curves stabilizing with a further increase of density, as seen in Figure 6.21a. These observations agree with the small percentage of foam compression for densities exceeding 60  $kg/m^3$  observed for all components, which can be seen in Appendix C.1. Moreover, this suggests that for the densities beyond 60  $kg/m^3$  there was negligible activation of the foam cores for the sandwich configurations tested in the pressure range of 10 to 35 *bar*.

An interesting observation from the variation of foam density was the changing degree of foam activation, obtained through the percentage of foam compression in the pressure range investigated. In Figure 6.22 the percentage of foam compression for Al and AIS sandwich components exposed to 10 and 15 *bar*, and 25 and 35 *bar* firing pressure, respectively, with a variation of density, are shown. It is seen that sandwich components with the lowest foam density experienced a rapid increase in foam compression before stabilizing at higher pressures. Similar behavior was shown for larger densities, such as 40  $kg/m^3$  and 50  $kg/m^3$ , with the rapid increase taking place at higher load levels than for the lower densities, shown in Figure 6.22. This indicates that the degree of foam activation is highly dependent on blast intensity levels. The small percentage of foam compression for larger densities for the Al configuration might also be due to the softness of the aluminum alloy utilized.

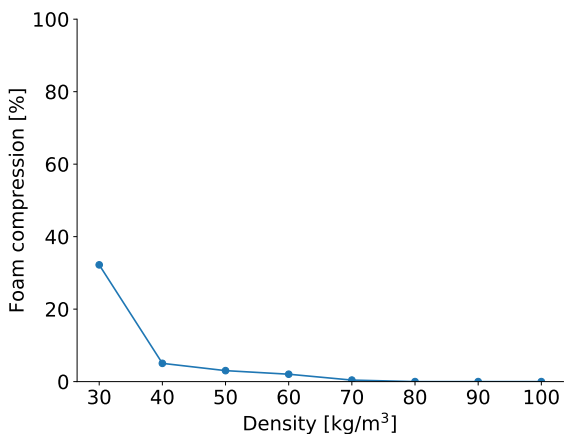


(a) Al - 15 bar

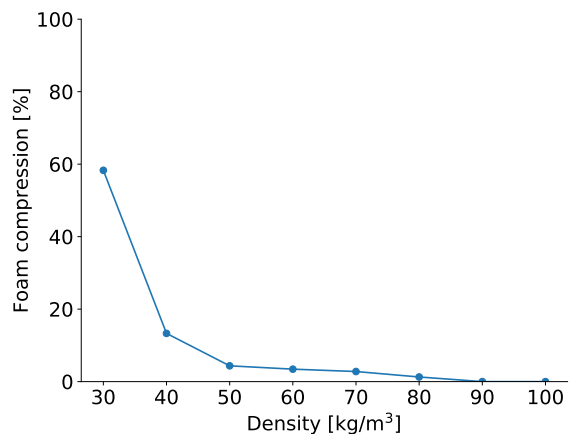


(b) Al - 15 bar

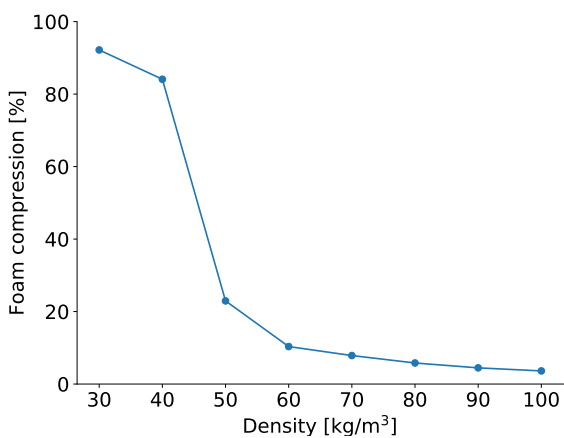
Figure 6.21: Back skin displacement (left) and contact force (right) between component and back clamping frame for a variation of foam core densities in Al components exposed to a firing pressure of 15 bar.



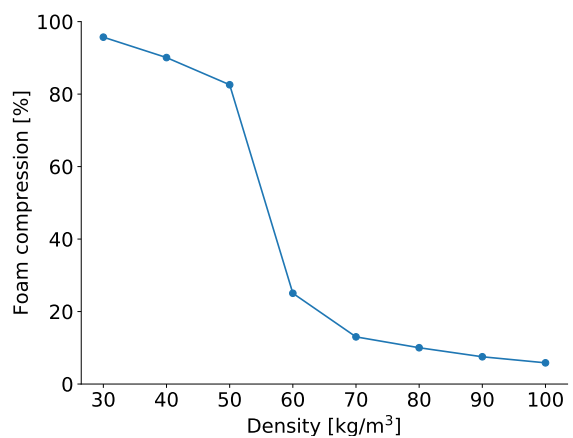
(a) Al - 10 bar



(b) Al - 15 bar



(c) AIS - 25 bar



(d) AIS - 35 bar

Figure 6.22: Foam compression in percent with a variation of foam density for Al and AIS components exposed to 10 and 15 bar (top), 25 and 35 bar (bottom) firing pressure respectively.

To investigate the change of energy absorbed in sandwich components with varying density the energy and specific energy absorption was studied along with the percentage of total energy absorbed by the foam core, back and front skin for all components. A high total energy absorption combined with a high percentage of absorption in the foam core is desirable. Figure 6.23a and 6.23b shows the specific and total energy absorbed in Al and AIS components exposed to firing pressures of 15 and 35 bar, respectively, with a variation of foam core density. For all sandwich configurations at different firing pressures, it was observed that the total energy absorbed decreased for increased foam densities, as seen in Figure 6.23.

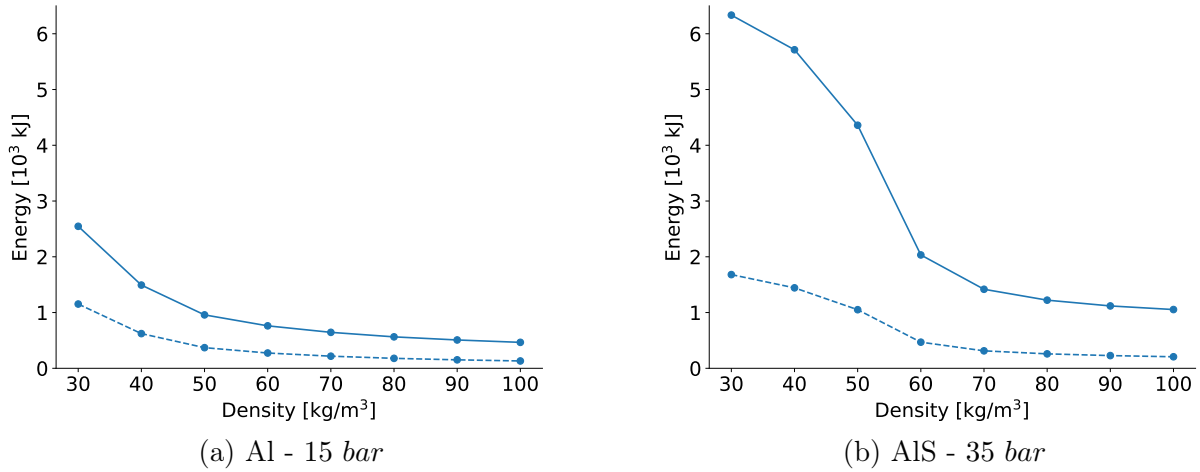
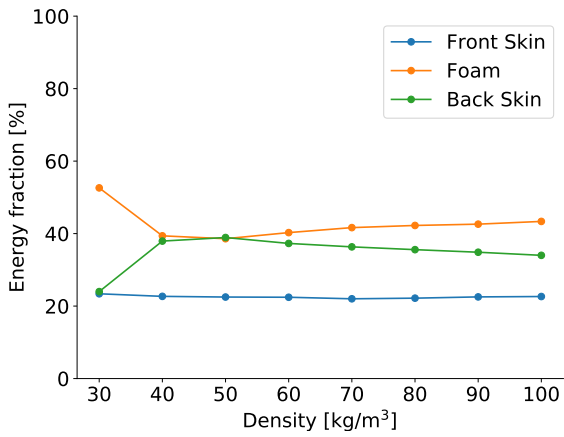
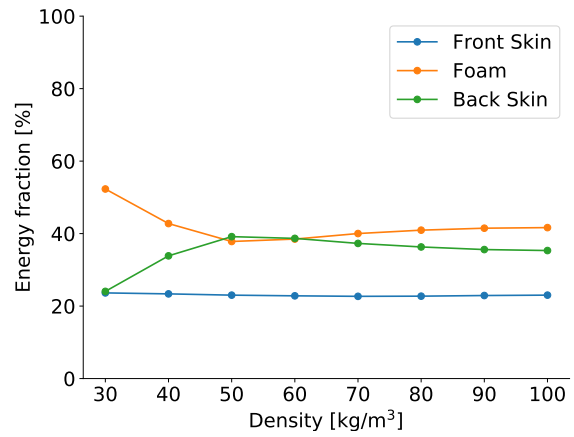


Figure 6.23: Absorbed energy (solid lines) and specific energy absorption (dotted lines) with a variation of foam density for Al and AIS components exposed to a firing pressure of 15 bar (left) and 35 bar (right), respectively.

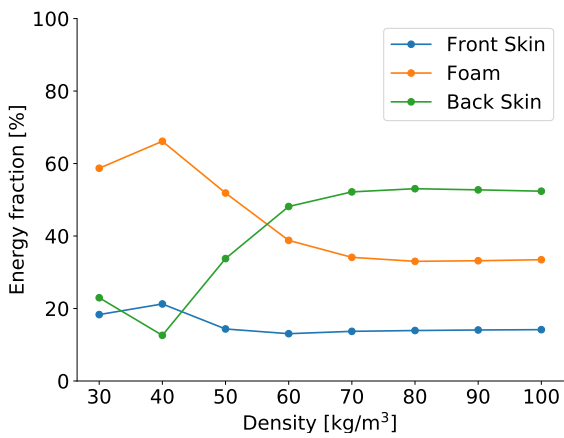
Figure 6.24 shows the percentage of energy absorbed in the front and back skin and the foam core for sandwich components exposed to 10, 15, 25 and 35 bar firing pressure, with a variation of foam density. For sandwich components exposed to 10 and 15 bar firing pressure the lowest foam density provided the most desirable distribution of energy absorbed in the foam core and back skin, as seen in Figure 6.24a and 6.24b. However, for sandwich components exposed to 25 bar firing pressure a maximum and minimum was observed for the percentage of energy absorbed by the foam core and back skin, respectively, at a foam core density of 40 kg/m<sup>3</sup>, shown in Figure 6.24c. This finding suggests an optimal foam density for foam activation regarding energy absorption. Further, the maximum and minimum percentages were found at a foam density of 50 kg/m<sup>3</sup> for a firing pressure of 35 bar, as seen in Figure 6.24d, suggesting that the optimal foam density is increasing with increasing blast intensities.



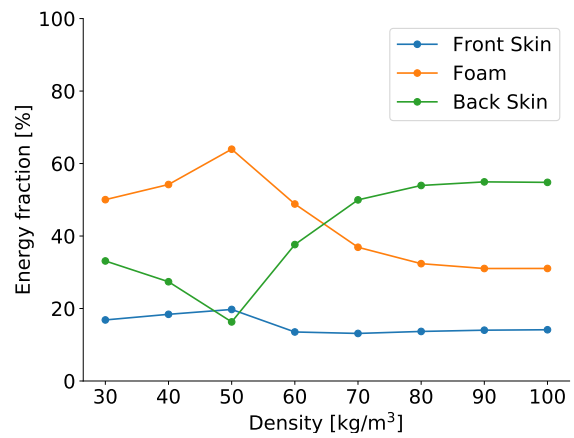
(a) Al - 10 bar



(b) Al - 15 bar



(c) AIS - 25 bar

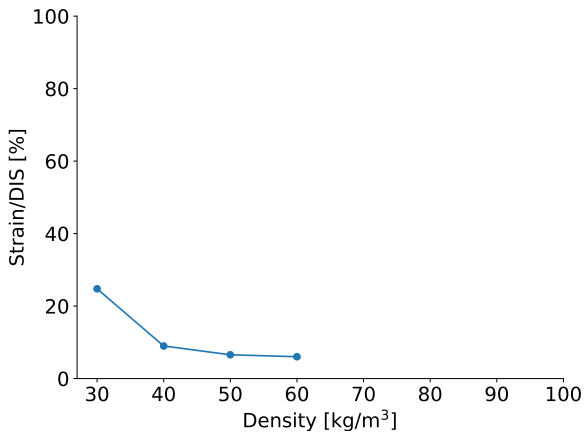


(d) AIS - 35 bar

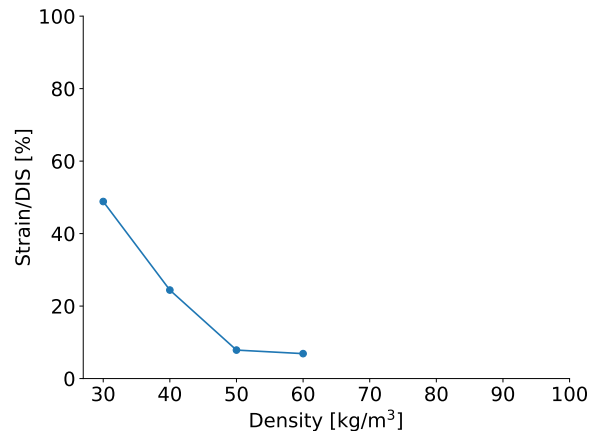
Figure 6.24: Percentage of energy absorbed in the foam core, back and front skin with a variation of foam density for Al and AIS components exposed to a firing pressure of 10 and 15 bar (top), 25 and 35 bar (bottom), respectively.

In Figure 6.25 the percentage of recorded strain compared to the densification initiation strain is shown for a variation of foam density. In Figure 6.25, it is noticeable that the density exhibiting strains closest to the densification initiation strain (DIS), for all firing pressures, corresponds to the density providing the optimal foam core density described above. This supports the proposed relation between the densification initiation strain and the optimal foam density concerning energy absorption, described in Section 6.3.2.

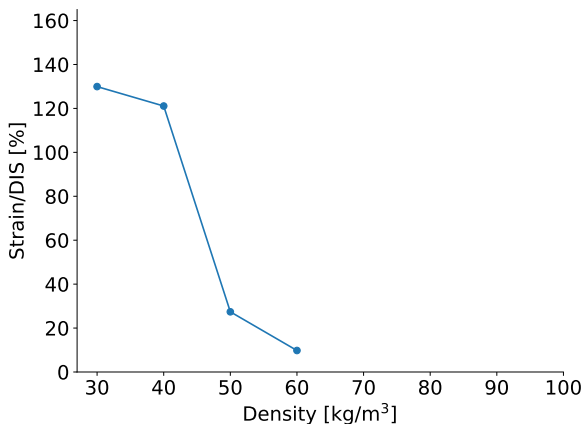




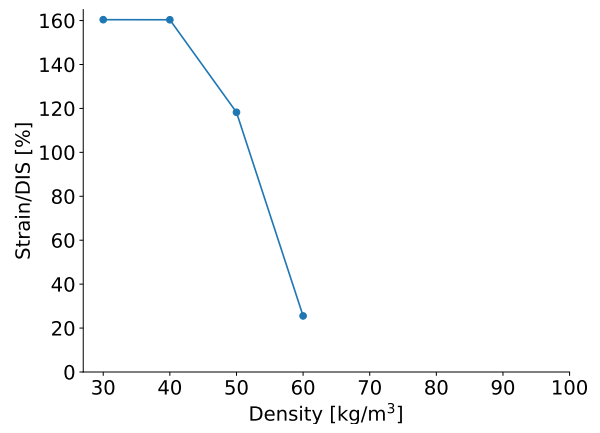
(a) Al - 10 bar



(b) Al - 15 bar



(c) AIS - 25 bar



(d) AIS - 35 bar

Figure 6.25: Foam core strain over densification initiation strain (DIS) in percent with a variation of foam density for Al and AIS components exposed to a firing pressure of 10 and 15 bar (top) and 25 and 35 bar (bottom), respectively.

## 6.4.2 Thickness

In this section a variation of foam thickness for XPS-250, XPS-400 and XPS-700 is presented. The foam thickness studied are 25, 50, 75 and 100 mm. In Appendix C.2 and C.3 the results for the variation of thickness can be seen plotted against density and thickness, respectively.

Figure 6.26a and 6.26b shows the midpoint deformation of the back skin for a variation of foam core thickness of XPS-250, XPS-400 and XPS-700 for Al and AIS components, respectively. It is seen that midpoint displacement of the back skin was reduced with increasing thickness. Additionally, it is observed that for higher pressures the decrease of deformation is smaller, which indicates a higher degree of foam compression.

Figure 6.26c and 6.26d illustrates the variation of average force between the back skin and the back clamping frame with a variation of foam core thickness for Al and AIS components subjected to firing pressures of 10 and 35 bar, respectively. In Figure 6.26c, the variation of average force is observed to be small for lower pressures. However, a slight decrease in average force was observed for increased pressures, as seen in 6.26d. The observations indicate that the average force is not very sensitive to foam thickness, at least not in the investigated blast loading regime.

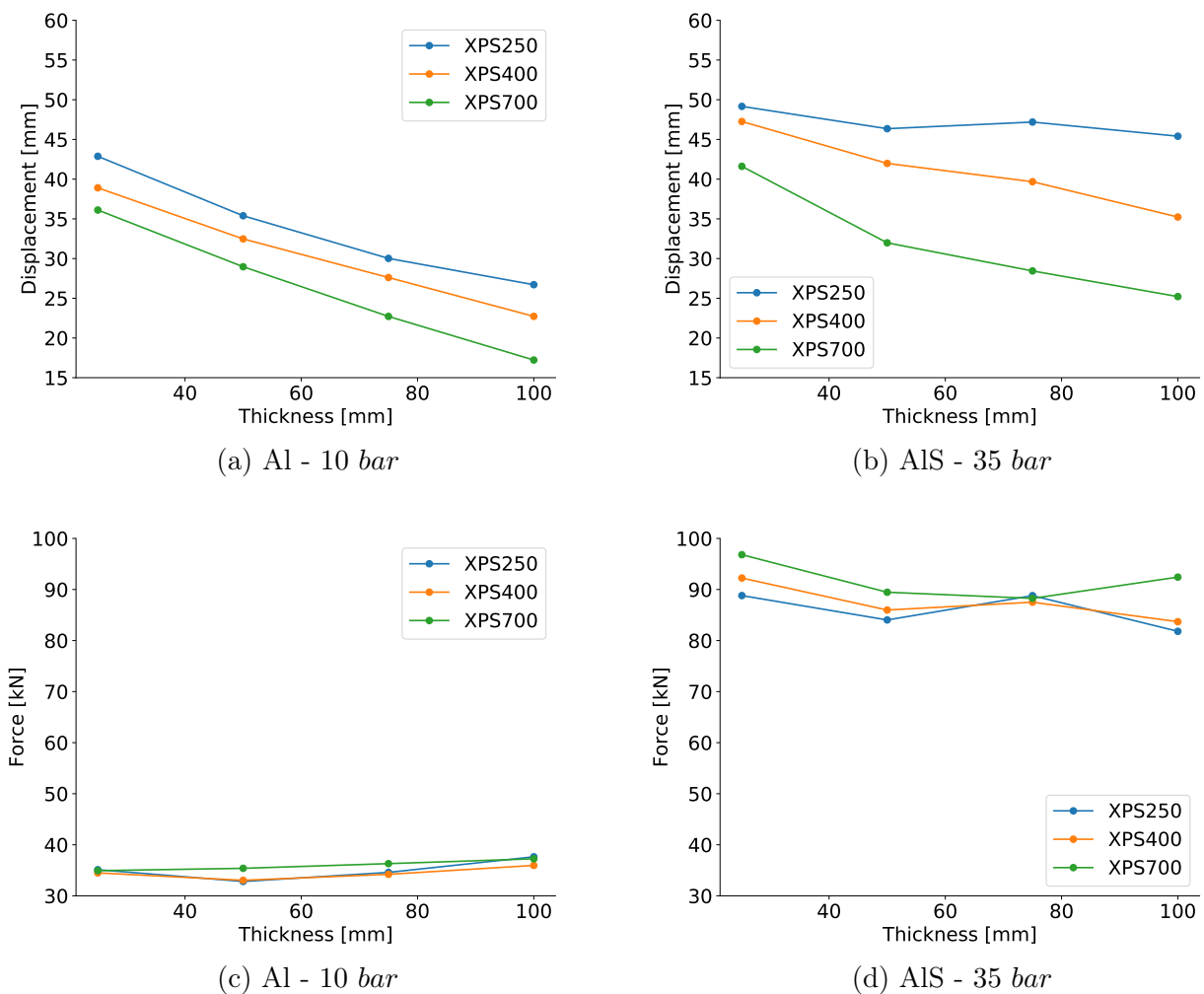


Figure 6.26: Deformation of back skin (top) and average force between back skin and back clamping frame (bottom) with a variation of foam thickness for Al and AIS components exposed to a firing pressure of 15 bar (left) and 35 bar (right), respectively.

The percentage of the total energy absorbed in the foam cores, with a variation of foam thickness for Al and AIS components, is seen in Figure 6.27. An increase in the percentage of energy absorbed in the foam core is seen with increased thickness for XPS-250, XPS-400, and XPS-700.

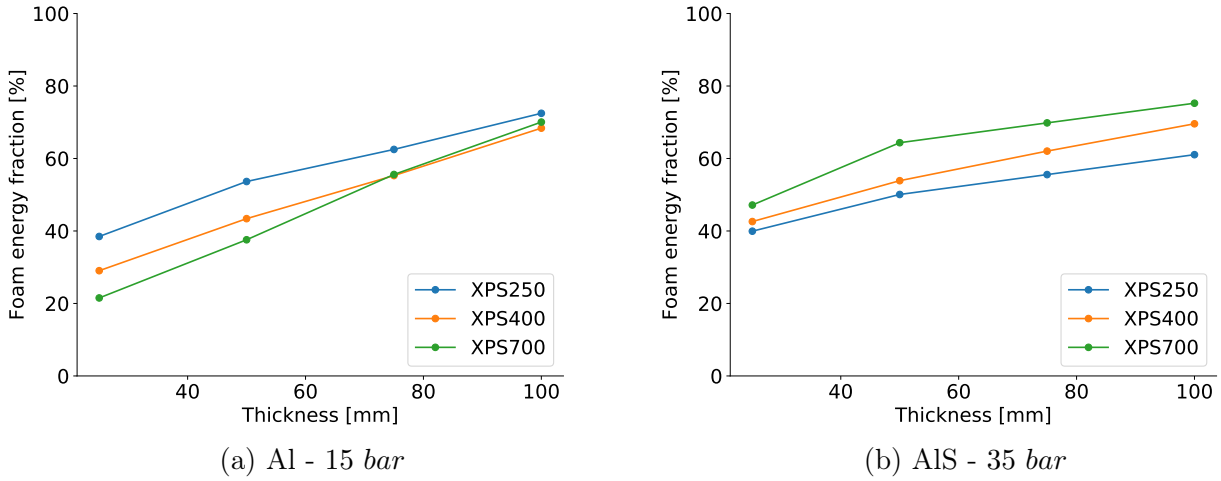
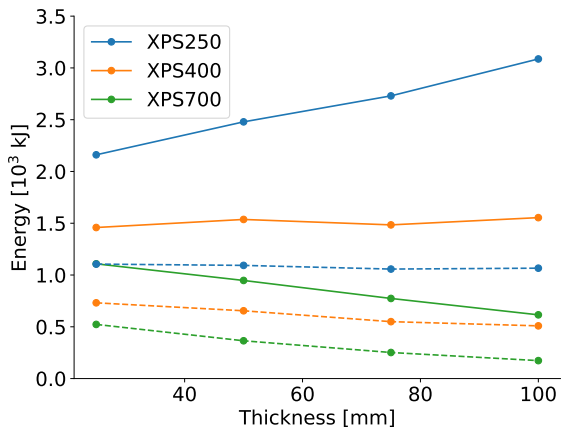
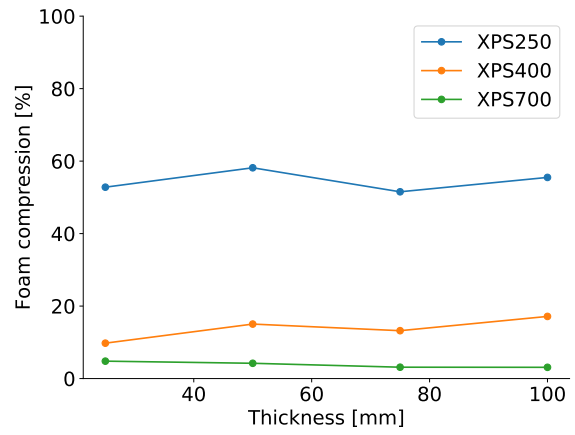


Figure 6.27: Percentage of energy absorbed in the foam core with a variation of foam thickness for Al sandwich components exposed to a firing pressure of 15 *bar* (left) and for AIS sandwich components exposed to a firing pressure of 35 *bar* (right).

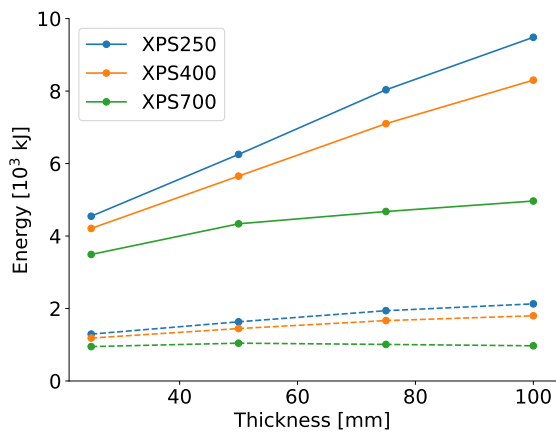
Figure 6.28a and 6.28c show total and specific energy absorbed with a variation of foam core thickness for Al and AIS components exposed to 15 and 35 *bar* firing pressure, respectively. It is seen that the specific energy absorbed is fairly constant for all components with a variation of foam thickness. In Figure 6.28b and 6.28d the percentage of foam compression with a variation of foam thickness for panels exposed to 15 and 35 *bar* can be seen. Interestingly, for low blast intensities and high foam densities, the total energy absorbed seem to be constant or decreasing for increased foam thickness. This effect is likely due to the reduction of back skin displacement, i.e., reduction of energy absorption in the back skin, while the foam cores experience low levels of compression. The increase in total energy absorbed for increasing foam thickness for low densities at low load levels is explained by the high degree of foam activation. When the load level is increased, as seen in Figure 6.28c, an increase in the total energy absorbed can be seen for all components, accompanied with a high level of foam compression, as seen in Figure 6.28d.



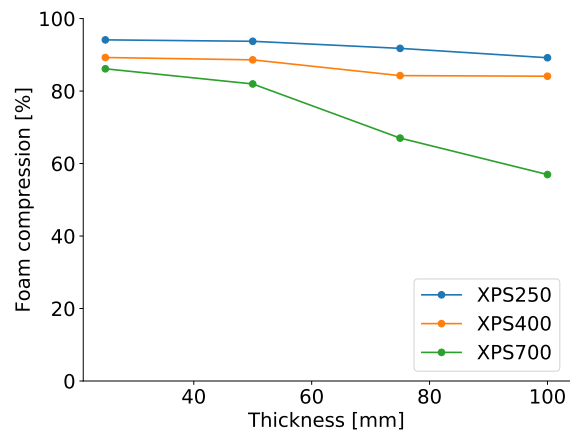
(a) Al - 15 bar



(b) Al - 15 bar



(c) AIS - 35 bar



(d) AIS - 35 bar

Figure 6.28: Absorbed energy (solid lines) and specific energy absorption (dotted lines) (left) and percentage of foam compression (right) with a variation of foam thickness for Al and AIS components exposed to a firing pressure of 15 bar (top) and 35 bar (bottom), respectively.

### 6.4.3 Constant Mass

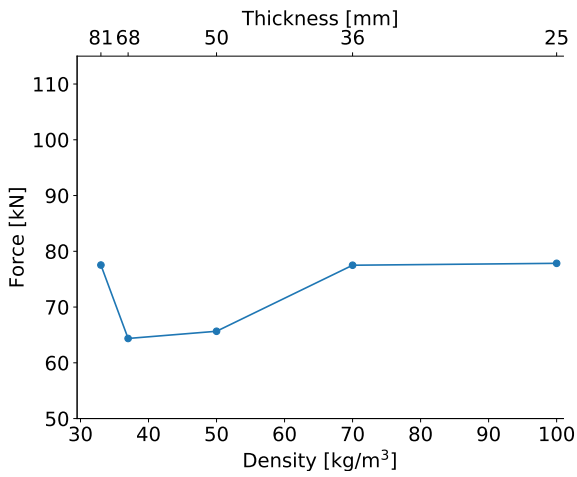
In this section, a variation in foam thickness and density, to keep the mass of the foam core approximately constant, is presented. When both parameters are varied simultaneously the importance of each parameter can be evaluated for different effects. The foam density and thickness spans from 33 to 100  $kg/m^3$  and from 25 to 81  $mm$ , respectively, when the foam mass is kept approximately constant. The variation of thickness and density for the foam core can be seen in Table 6.10. In Appendix C.4 results presenting back skin displacement, average force, total and specific energy absorbed, distribution of energy absorption, foam compression and strain for constant foam mass can be found.

Table 6.10: Foam core thickness, density and mass studied in the parameter study on approximately constant mass.

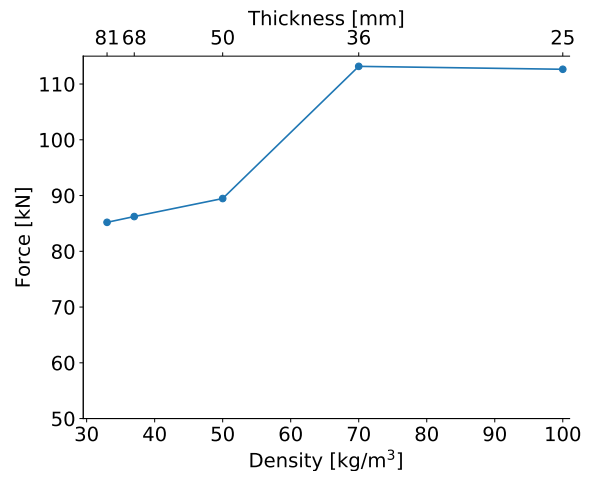
| Thickness<br>[ $mm$ ] | Density<br>[ $kg/m^3$ ] | Mass<br>[ $kg$ ] |
|-----------------------|-------------------------|------------------|
| 81.0                  | 33.0                    | 1.016            |
| 68.0                  | 37.0                    | 0.960            |
| 50.0                  | 50.0                    | 0.955            |
| 36.0                  | 70.0                    | 0.955            |
| 25.0                  | 100.0                   | 0.948            |

For Al components exposed to firing pressures of 10 and 15  $bar$ , only slight differences were observed for deformation of the back skin. The variation of average force between the back skin and the clamping frame for the Al components exposed to 15  $bar$  was observed to be small as well. Figure 6.29a and 6.29b show the average reaction force recorded for a variation of foam density and thickness for AIS components exposed to 25 and 35  $bar$ , respectively. The average force for the AIS components displayed conflicting results, as seen in Figure 6.29. A decrease in force was expected for the components with lower foam densities and larger thickness. A decrease in average force was seen between the component with a core of density 70  $kg/m^3$  and thickness of 36  $mm$  and the core of density 37  $kg/m^3$  and thickness of 68  $mm$ , as seen in 6.29a. However, an increase of average force was seen between the component with a core of density 37  $kg/m^3$  and thickness of 68  $mm$  and the core of density 33  $kg/m^3$  and thickness of 81  $mm$ . The reason for this behavior is not yet known.

Figure 6.30 presents the total and specific energy absorbed with a variation of foam density and thickness for Al and AIS components subjected to 10, 15, 25 and 35  $bar$  firing pressure. A reduction of total and specific energy absorbed can be observed with increasing foam density and decreasing thickness for all components. The reduction is less pronounced for the specific energy absorbed. The observed trend is similar to the change in total and specific energy seen for a variation of density in Section 6.4.1, which indicates that the effect of foam density dominates the total and specific energy absorbed.

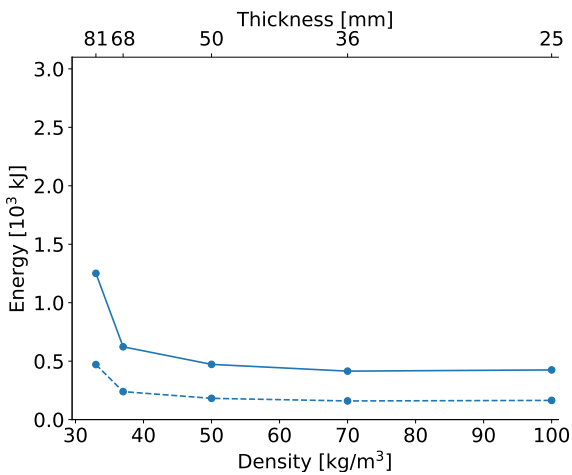


(a) 25 bar

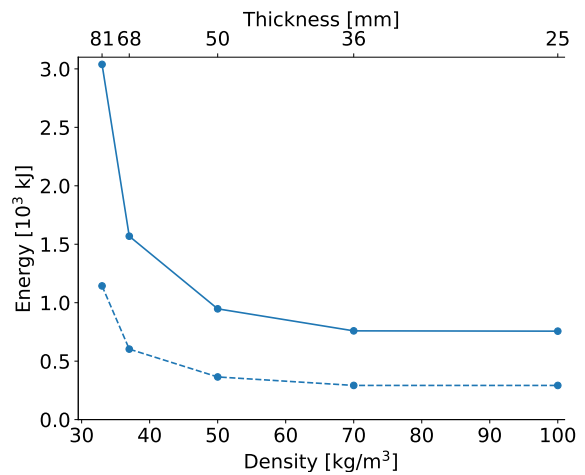


(b) 35 bar

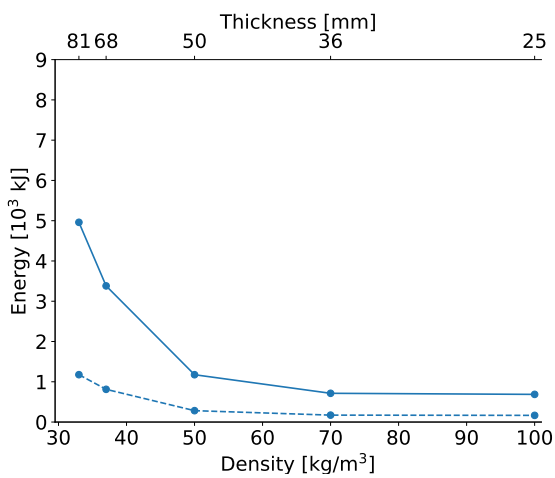
Figure 6.29: Average force between the back skin and back clamping frame with a variation of foam density and thickness with constant foam mass for AIS components exposed to a firing pressure of 25 (left) and 35 bar (right).



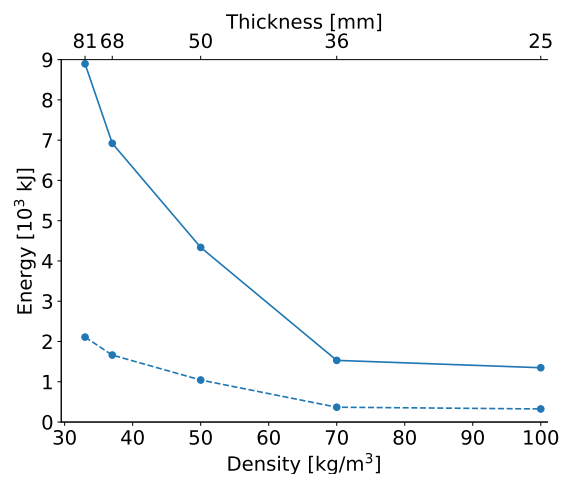
(a) 10 bar



(b) 15 bar



(c) 25 bar



(d) 35 bar

Figure 6.30: Absorbed energy and specific energy absorption with a variation of foam density and thickness with a constant foam mass Al and AIS components exposed to a firing pressure of 10 and 15 bar (top) and 25 and 35 bar (bottom), respectively.

In Figure 6.31 the displacement of the back skin and the percentage of energy absorbed in the back and front skin and the foam core for AIS components can be seen. A minimum is observed for back skin displacement for foam core densities of 37 and 50  $kg/m^3$ . This minimum is also found as a maximum of the percentage of energy absorbed in the foam core and a minimum in the percentage of energy absorbed in the back skin as seen in Figure 6.31. This suggests an ideal foam core density for minimization of back skin displacement and a maximization of the percentage of energy absorbed in the foam core. The downside is, however, the decrease in total energy absorbed.

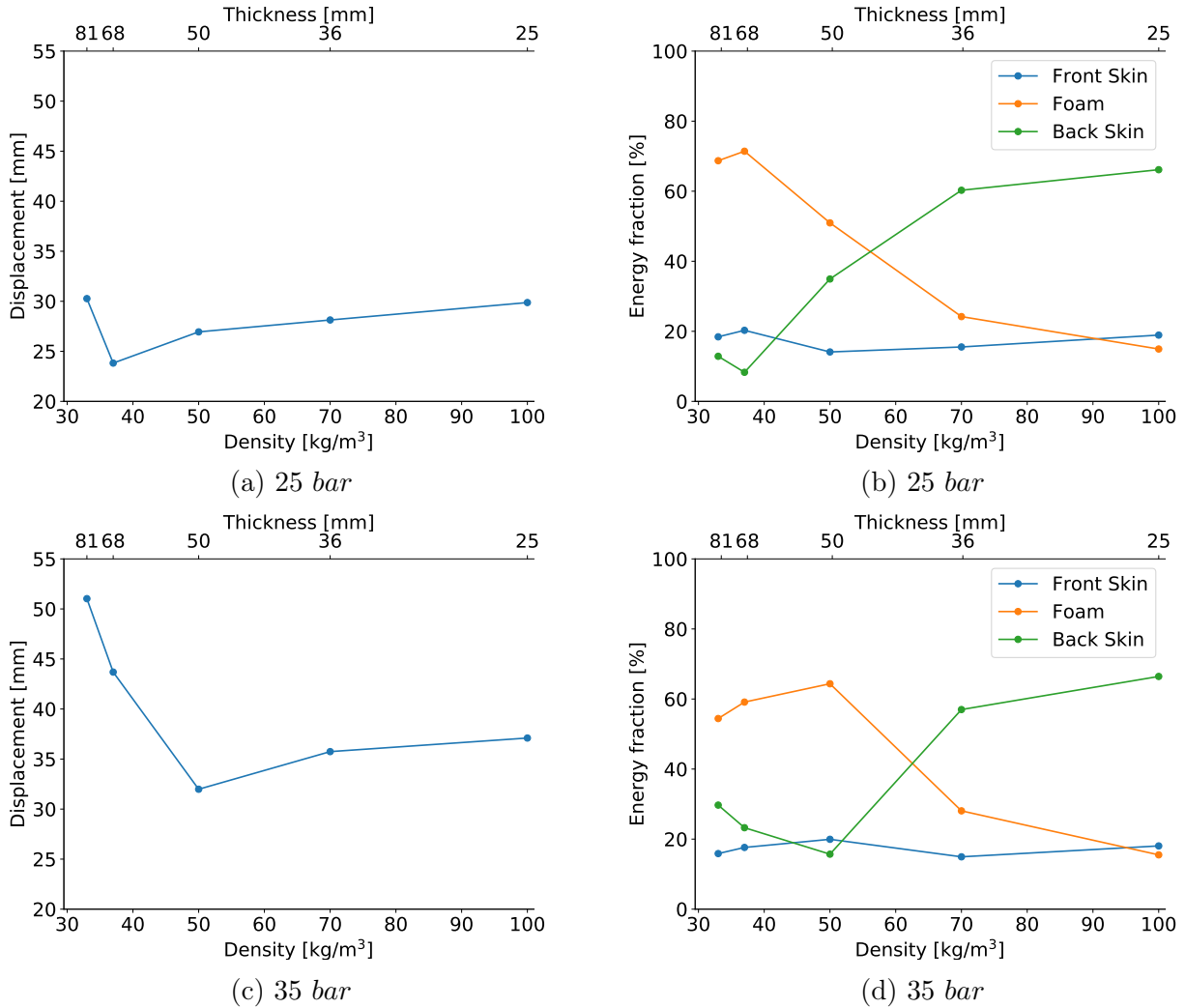


Figure 6.31: Deformation of back skin (left) and percentage of energy absorbed in the foam core, back skin and front skin (right) with a variation of foam density and thickness with a constant foam mass for AIS components exposed to a firing pressure of 25 (top) and 35 bar (bottom).

## 6.5 Main Findings

In this section, the main findings from the validation of the reference model regarding pressure histories, midpoint displacement and deformation profiles are presented. The findings from the study of numerically obtained properties not captured by the experimental setup are also listed. Finally, the findings of the parameter study investigating the effects of varying foam density and foam thickness independently and together, while keeping the foam mass constant, are also presented.

### 6.5.1 Validation of Reference Model

- Validation of numerically applied idealized pressure curves against experimentally recorded pressure histories showed general agreement on the shape of pressure histories with the numerical pressure curves having a slightly larger peak reflected pressure value. The idealized pressure curves were considered a controlled, conservative and fairly accurate representation of the blast loading scenarios.
- A comparison of experimentally and numerically obtained midpoint displacement histories showed good agreement on the shape of the curves obtained. Generally, the midpoint displacement obtained numerically overestimated the experimental displacements, where the effect was more pronounced for higher firing pressures. Some exceptions were observed, where the displacement histories were very similar.
- Deformation profiles obtained numerically and experimentally at similar midpoint deformation levels were compared, which showed good agreement between the two. The deformation evolution initiating at the edges of the blast loaded area and propagating towards the center was captured well numerically.

### 6.5.2 Further Numerical Results

- Further numerical study of foam compression showed significant deviations between the results obtained from the scanning with RAA of skins post-experiment and numerically obtained foam compression, where numerical results showed a decrease of foam compression with an increase in foam core density.
- A comparison of numerically obtained effective plastic strain values and the densification initiation strain obtained from numerical compression tests provided a useful qualitative measure of energy absorption capabilities of the sandwich components.
- Numerical investigation showed a decrease of energy absorbed with an increase of foam core density. For the AIS configuration, an increase in the fraction of energy absorbed in the back skin was observed compared to the Al configuration.
- Foam core energy absorption fraction is obtained to decrease for Al sandwich panels, while an increase for AIS sandwich panel exposed to 35 *bar* is seen. A maximum for foam absorption fraction is obtained for Al and AIS panels with XPS-400 core exposed to 25 *bar* firing pressure.



- When studying the specific energy absorption, the same trends are observed as when studying the energy absorption, but the decrease with foam density is more pronounced. At low load levels, the components without foam cores and with low-density cores have a similar specific energy absorption due to the low foam compression.
- The reaction forces recorded in numerical simulations showed a general increase with the increase of foam density. The variation within average force for sandwich panels subjected to the same firing pressure is fairly small.

### 6.5.3 Parameter Study

- An increase in foam core density showed a decrease in midpoint displacement of the back skin and an increase in average force recorded, with densities above  $60 \text{ kg/m}^3$  showing only slight differences in displacement.
- Foam activation measured in foam compression was seen to have a rapid increase before stabilizing at high levels of compression. This effect was seen to occur at higher firing pressures for higher foam densities.
- When the distribution of energy absorbed was inspected it was seen that for lower levels of firing pressure the percentage of energy absorbed in the foam core was maximized while the percentage of energy absorbed in the back skin was minimized for low foam core densities. This maximum and minimum were observed to correspond to increased foam core densities for increased firing pressure. These maximums and minimums were also observed to correspond to the strain levels closest to the densification initiation strain.
- Trends captured by varying density was also captured when increasing thickness of XPS-250, XPS-400 and XPS-700 foam core.
- An increase in foam core thickness reduced the deformation of the back skin, with the effect being more pronounced at lower levels of firing pressure.
- For increased foam thickness the fraction of energy absorbed in the foam core was observed to increase, while the total energy absorbed decreased for higher foam densities at low firing pressures. For higher pressures, the total energy absorbed increased for all foam densities.
- For a constant foam core mass a minimum in the displacement of the back skin was found for ALS sandwich components. The deformation minimum was seen to correspond to a maximum and minimum in the percentage of energy absorbed in the foam core and back skin, respectively.

# Chapter 7

## Summary and Discussion

This chapter aims to compare and discuss the most important results presented in this thesis. The results from the preliminary study, which aimed to establish and evaluate a reference model, provide a firing pressure range for the experimental program and numerically evaluate different boundary conditions, will be discussed. A discussion of the material tests performed and the material models applied will be presented. The focus will be given to limitations of the setup and conduction of the experimental program, as well as a summary and discussion of the main findings. Conclusively, the numerical work done to validate the reference model and performed during the parameter study will be discussed.

### 7.1 Preliminary Study

A preliminary study was conducted during the early stages of this thesis. A reference model was established, and the effects of parameters such as friction coefficients and mesh size were evaluated. One of the goals for the preliminary study was to determine a firing pressure range for the experiments planned. This was done to avoid undesirable experimental results such as complete fracture and very small deformations. This was especially important for the Al experiments because the aluminum skins were prone to fracture at relatively low firing pressures. The main challenge when suggesting a firing pressure range for the experiments was the highly mesh dependent mechanism of stress localization and fracture in the numerical simulations. The preliminary study also served as an efficient evaluation of the effects of different proposed boundary conditions before the experimental work was carried out.

## 7.2 Material Tests

To increase the accuracy of the numerical model and to obtain a more accurate description of the behavior of the specific batch of AA1050-H14 aluminum alloy, uni-axial tension tests were performed on dog-bone specimens from the same batch as the skins used in the experimental program. From the material tests, it was observed that the 0-degree tests exhibited necking at a lower stress than the 45-degree and 90-degree tests. The 0-degree tests also experienced fracture at a higher strain than the other tests which suggests a more ductile behavior. Due to conservative results for the component test, the material parameters obtained from calibration of the 0-degree tests were used in further numerical simulations. Considering the anisotropic nature of the AA1050-H14 aluminum alloy, the use of an isotropic material model is a simplification of the material behavior. However, it is a reasonable simplification considering the rather similar behavior in the three directions. The fracture criterion was calibrated by trial and error in numerical simulations and can be calibrated more accurately by examination of the critical element in the model. The material parameters used for the steel skins in the thesis was also simplified as isotropic even though studies have shown a slightly anisotropic behavior for the steel DOCOL 600DL [1].

For the three variations of XPS foam used in this study; XPS-250, XPS-400, and XPS-700, no material tests were conducted. However, results from previously performed material tests by Sigurdsson [3] was used to study the densification initiation strain and to validate the numerical models for the compression tests of the foam types. Calibrated material parameters for the XPS foams were taken from a previous study conducted by Berdal and Bjørge [33] and showed good agreement with the experimental results from Sigurdsson's study. The compression tests conducted in [3] was performed with a strain rate of  $10^{-3} s^{-1}$ . One limitation of the variation of the Deshpande-Fleck model utilized is that it does not take strain rate into account. Considering the nature of a blast loaded sandwich panel, higher strain rates than the ones used in [3] is expected, which is confirmed by observation of strain rates of over  $500 s^{-1}$  in the numerical simulations. This discrepancy between the strain rate in the material test and the strain rate expected under blast load scenarios introduces uncertainties regarding the material parameters utilized. Additionally, it reduces the applicability of the calculated densification initiation strain calculated in Section 4.3.3 in an evaluation of the energy absorption capabilities of the numerically investigated sandwich components. To increase the applicability of the densification initiation strain and the accuracy of the material parameters applied in the Deshpande-Fleck model, XPS foam should be tested for increasing strain rates. Another possibility is the implementation of strain rate dependence in the numerical model.

To be able to assess the protective and energy absorption capabilities of foam with a density outside or between the densities used in the experimental program, a density-dependent material model was introduced. For validation, similar densities as XPS-250, XPS-400, and XPS-700 were used as input in the density-dependent model, and numerical results were compared to experimental results from the study done by Sigurdsson [3]. Good agreement and accuracy were observed for the density-dependent model for strains below 1.5, with growing deviations for larger strains. The validity and accuracy of the curve fit used to calibrate the constants of the density-dependent model is uncertain outside of the density range of the experimental material testing program, due to a lack of compression test data on different densities of XPS. Undesired stress-strain behavior was obtained for densities outside a density range of 30 to  $60 kg/m^3$ . To obtain a more accurate curve fit of the constants used in the model a greater variety of foam densities should be experimentally tested. It is also worth mentioning that the derivation of the density-dependent model is based on aluminum foams, instead of polymeric foams, in a study by Reyes et al. [32].

## 7.3 Component Tests

The experimental program of this thesis included fourteen component tests exposed to different firing pressures in the SSTF. The objective of the experimental program was to document, investigate and compare the structural behavior of sandwich components exposed to blast loading. The experimental setup facilitating an object of this nature is fairly complex and has proven to provide valuable insight and results on the structural behavior of different sandwich configurations exposed to blast loading. However, the experimental setup has clear limitations, and the routines directing the conduction of the experiments can also be improved.

Concerning experimental data, the current setup provides information recorded from the pressure sensors and the high-speed cameras. This limits the investigation of the structural behavior to a study of the back skin of the test specimen and the pressure history of the experiment performed. The absence of experimental data on the behavior of the front skin is limiting when investigating trends and evaluating the protective and energy absorption capabilities of a sandwich component. The 3D-DIC analysis is limited to data collection on the back skin, as well. In this thesis, an attempt was made to obtain experimental data on the deformation of the front skin, by introducing the laser scanning of plates post-experiment, where the conditions of the scan were different from the conditions in the test rig in the SSTF. Another limitation is the absence of recorded force and energy absorption during experiments. In the evaluation of protective capabilities, the information of force transferred from a protective component to its boundaries is of great value. The same applies for a quantifiable measure of the energy absorbed in the component, and the percentage of energy absorbed in the different parts of a sandwich panel.

Regarding the routines followed during the conduction of the experimental program, there are several sources of error. In addition to the video captured by the high-speed cameras during the short time interval of blast loading, an image should be captured after the loading and before the dump tank is opened, from the same cameras. This will facilitate a 3D-DIC analysis providing information on deformation at a more permanent stage for the component. The sandwich panels should also be dissected, and a more thorough manual measurement should be obtained of the deformation of the front and back skin and the foam compression at different points on the deformation profile.

For the Al configurations the components exposed to 10 *bar* firing pressure suggested a trend where there was a negative correlation between foam density and maximum midpoint displacement. This was partially supported by the results from the components exposed to 15 *bar* firing pressure. The results were less conclusive for the components exposed to 15 *bar* because fracture was observed. These fracture observations suggest that there exists a capacity limit between 10 and 20 *bar* regarding firing pressure before fracture for a sandwich component with the specific configurations tested. It is also suspected that this limit is higher for a sandwich component with the low-density XPS-250 foam as a core than components utilizing foam cores of higher densities, which is an interesting observation regarding the protective capabilities of this sandwich configuration. The results from the experiments conducted on AlS configurations were seen to support the trends observed for the Al configurations. An interesting observation was that there was no fracture recorded for the AlS components, even for significantly increased firing pressures. This suggests that in a protective application of the sandwich components, a useful measure to avoid fracture would be to utilize a back skin of steel while using an aluminum plate as a front skin to minimize the weight of the component.

Experimental pressure data was recorded during the experiments. The pressure histories for 10, 15, 25 and 35 *bar* firing pressure showed high accuracy between recorded firing pressure and nominal firing pressure. Additionally, minimal variation was observed for the incident pressure recorded for the same nominal firing pressure. These findings suggest an accurate, controlled and repeatable technique of producing blast loading scenarios. Deviations between peak reflected pressure recordings for the same nominal firing pressure was observed and may be due to deformation of the test specimen and fluid-structure interaction effects. Pressure leakage from the driven section to the dump tank was seen to increase with firing pressure and was assumed to cause vibrations in the Plexiglas between the high-speed camera and the test specimen. The vibrations affect the pictures used in the 3D-DIC analysis, causing the nonphysical oscillations in midpoint displacement observed for test specimen exposed to 35 *bar* firing pressure. Similar results were obtained by Sigurdsson for increased firing pressures.

As mentioned, one of the limitations of the experimental setup is the lack of experimental results on the structural behavior of the front skin of the sandwich components. To obtain more extensive data on the back skins and front skins of the tested components a selection of skins were scanned using the RAA scanning arm after the skins were detached from the test rig. The point cloud provided by the scanning procedure produced accurate visualizations of the deformed plates. However, meaningful comparisons were limited due to the results obtained from 3D-DIC analysis illustrated the structural behavior of the back skin during experiments in the test rig, while the scanning was performed after the components were detached from the test rig and deformations due to elastic effects had taken place. This introduced uncertainties concerning the relative displacement between the front and back skin of the sandwich components. Although non-ideal conditions while scanning was present, a qualitative comparison of the deformation profiles obtained with 3D-DIC and the robot arm scan was performed. The comparison showed good agreement regarding deformation shape of the back skin, which suggested a rounder and more distributed deformation shape for the components with a foam core of XPS-250 than the two other XPS-types.

For the completeness of the experimental work done in this thesis, results from a study done by Sigurdsson [3] was included, where some of the previously mentioned trends were captured. In the study done by Sigurdsson, pressure leakage was also present. This was evident from the large oscillations and the incomplete midpoint displacement histories. It was also observed that sandwich panels with steel front and back skins the proportional increase in maximum midpoint displacement for an increase in firing pressure was smaller than for skin configurations including aluminum.

## 7.4 Numerical Work

As a part of the evaluation of the accuracy of the reference model a comparison of experimentally obtained pressure history curves and numerically applied pressure curves were performed. Generally, the idealized pressure curves were observed to have a greater peak reflected pressure and a longer duration of the positive phase. It was also observed that the deviation in peak reflected pressure increased for higher load levels. However, the idealized curves were considered a conservative, consistent and fairly accurate representation of the actual pressure loads compared to the method of extrapolation of experimentally obtained results with a curve fit of the Friedlander equation.

For the Al components exposed to 10 *bar* firing pressure, a consistent agreement between experimental and numerical midpoint displacement results was observed. For the components exposed to 15 *bar* firing pressure, the comparison was less meaningful due to fracture in the experimental components. However, the numerical results for the sandwich components that did not reach fracture captured the shape of the experimental results with similar values of midpoint displacement. Stress localization and fracture are highly mesh dependent. Therefore, a model with a mesh more refined than in the reference model should be utilized to simulate components loaded close to its capacity to obtain more accurate results. The numerical simulation for the components exposed to 25 and 35 *bar* firing pressure showed behavior that generally overestimated the midpoint deformation recorded experimentally. In general, the shape of the midpoint displacement histories was captured by the numerical simulations with sufficient accuracy compared to the experimental data, with a slight overestimation of the deformation level by the numerical simulations.

For additional validation of the numerical model, deformation profiles were compared between numerically obtained results and experimental results obtained with 3D-DIC. It was observed that the numerical results captured the mechanism where the deformation initiated at the edges of the front skin and propagated towards the center. It was generally seen that the relatively simple numerical model achieved accurate and valuable results for a problem of high complexity. Further numerical study of mechanical properties such as foam compression, strain compared to densification initiation strain, energy absorbed and reaction forces gave valuable insight on the behavior of the sandwich configurations at hand and served as a starting point for the following parametric study. In the parametric study conducted, the focus was on variations of the foam core, where foam thickness and foam density were varied separately and then simultaneously where the mass of the foam core was kept constant.

A decrease in deformation of the back skin was found for an increase in both foam density and thickness when the two parameters were varied separately. For the simultaneous variation, a minimum of back skin deformation was found for high pressures. This minimum was seen to correspond to a maximum of the percentage of energy absorbed in the foam core and a minimum of percentage absorbed in the back skin. The findings suggest that an optimal foam core configuration can be found to minimize the deformation and fraction of energy absorbed in the back skin while simultaneously maximizing the activation of the foam core regarding the percentage of energy absorbed. This optimal foam core configuration was also seen to change for a variation of pressure which suggests that an optimal foam configuration is dependent on the subjected pressure. For an optimal foam core configuration for different firing pressures regarding energy absorption, an investigation of the effect of a non-constant (graded) foam density would be interesting.

When performing a parameter study to evaluate the energy absorption capabilities of a sandwich structure, there are a vast amount of parameters to consider. In this study, the goal was to investigate the effects of different foam core variations, to explore trends and general behavioral patterns. A sandwich panel is a complex component, where the combinations of geometries, materials, etc. allows for an infinite number of configurations. Therefore, design and performance requirements are essential in an evaluation or optimization of a sandwich panel. For optimization of components of similar complexities with regards to, for example, back skin deformation, force transferred to the primary structure, energy absorption, total mass of panel, or any combinations of the latter, a comprehensive optimization scheme has to be utilized. The variation of single parameters, one by one, does not give sufficient information to conclude on the protective capabilities of a sandwich component. However, a parametric study of this nature may provide a set of starting points in the design of protective sandwich components.

# Chapter 8

## Conclusion

The primary objective of this thesis was to investigate, both experimentally and numerically, the mechanical response of sandwich components, with foam cores of various densities, to a range of blast loading scenarios. Below, the main findings of the study are shown.

- The preliminary study served to establish a relatively simple, accurate and computational viable reference model and suggest an experimental program.
- Accurate material parameters were obtained from tension tests performed on the AA1050-H14 aluminum alloy. A density-dependent model was introduced to study foam core densities outside and between the densities of the experimental program. The model was utilized to investigate the structural response of sandwich panels but was observed to give unsatisfactory results for densities outside the density range of 30 to 60  $kg/m^3$ .
- Experimental results for sandwich components showed a negative correlation between foam density and displacement levels and rounder and more distributed deformation profiles for sandwich panels with low-density foam cores, which suggest a higher degree of foam activation.
- Fracture in components with aluminum skins subjected to 15 *bar* firing pressure suggests that there exists a firing pressure capacity that lies between 10 and 20 *bar* for this sandwich configuration.
- Recorded pressure histories suggested an accurate reproduction of blast scenarios and showed signs of pressure leakage from the driven section into the dump tank, during experiments.
- The validation of the reference model showed good agreement between numerical and experimental results, with a general overestimation of deformation in the numerical results.
- In the parameter study, the effects of foam density and thickness concerning protective capabilities of sandwich panels were investigated. Results indicating an optimal foam core configuration, for parameters such as back skin displacement, the percentage of energy absorbed in foam core and back skin, was found. The optimal foam core configuration was observed to be dependent on firing pressure.

The general observation is that sandwich panels are complex components that serve as excellent energy absorbents in protective applications if the correct configuration is selected. Numerical simulations were seen to predict the structural response of the components with sufficient accuracy. However, to numerically optimize the energy absorption of sandwich panels an elaborate optimization scheme should be utilized.





# Chapter 9

## Further Work

Due to the range of research fields affecting the work included in this thesis, there are several possible extensions related to its topics. The primary objective of this thesis was to investigate, both experimentally and numerically, the mechanical response of sandwich components, with foam cores of various densities, to a range of blast loading scenarios. The work has naturally been limited by time constraints and the number of material and component tests performed. In Chapter 7 several topics and extensions not covered have been pointed out for further work, many of which stem from challenges encountered during the work. Below, suggestions for further work are listed.

- Perform compression tests on a greater variety of XPS densities to increase accuracy and validity of the density-dependent model. A density-dependent model is a useful tool in the numerical investigation of the mechanical behavior of XPS-foam outside or within the densities of the performed compression tests.
- Perform tension tests on XPS-foam to calibrate an accurate fracture criterion. For more accurate numerical simulations of the behavior of XPS-foam, it is suggested that an energy-based fracture criterion is calibrated from tension tests on the material.
- Perform compression tests on XPS-foam with higher strain rates and utilizing a material model that is strain rate dependent. A discrepancy between the strain rate applied in the compression tests performed on XPS and the strain rate recorded in numerical simulations was found. To address this, it is suggested that compression tests with increased strain rates are performed. It could also be beneficial to incorporate strain rate dependency in the material model. The measures suggested would provide more accurate numerical results and increase the applicability of the densification initiation strain as a parameter for evaluation of energy absorption capabilities in XPS.
- Investigate the behavior of foam cores with non-uniform (graded) density through compression tests. Considering that findings suggested that the optimal foam core density was dependent on firing pressure, it would be beneficial to investigate the mechanical behavior of a graded density foam through compression tests.

- Extend the current experimental setup to be able to record reaction force and provide information about front skin and foam behavior. As mentioned in Section 7.3, the current experimental setup provides limited data with regards to reaction force, front skin and foam behavior. The introduction of windows allowing the high-speed cameras to capture the deflection of the front skin could be a beneficial modification of the current experimental setup.
- Extended post-experiment measuring routines. To obtain more comprehensive experimental data, several additions to post-experimental routines can be made. Using the aforementioned RAA for scanning of the front and back skin should ideally be done when the components are still fastened in the test rig, to achieve more similar conditions to the conditions of the DIC analysis. It is also suggested that a picture is taken with the high-speed camera after applied loading to obtain results on a permanent state of deformation. It is also suggested that the front skin and foam are measured post-experiment by, for example, dissecting the sandwich panels.
- Perform shock tube experiments on additional sandwich configurations. The aluminum alloy used as skin material in this study is a fairly weak aluminum alloy. It is suggested that an aluminum alloy of increased strength is used as skin material in further studies, and as a comparison to the alloy used in this thesis. As mentioned above, a foam core of graded density is an intriguing subject of further studies and should be utilized as a core in sandwich panels tested in SSTF. It was found that the fraction of energy absorbed in the front skin was approximately constant for a majority of the sandwich configurations tested numerically. It is suggested that this observation is tested further empirically and numerically by investigating the substitution of the front skin with a very light membrane material or something of similar capacity to reduce the weight of the component.
- Perform further numerical studies of the strain distribution and magnitude in the sandwich components. In this thesis, the densification initiation strain was proposed as a useful parameter for the evaluation of energy absorption capabilities of sandwich components, by comparison of numerically obtained strains. The strain was extracted at the front center element of the foam core. In further studies, a more comprehensive evaluation of the strain distribution and magnitude should be considered to increase the validity of the densification initiation strain as a useful measure of energy absorption capabilities.
- Conduct an in-depth study of the reaction forces between the sandwich component and back clamping frame. In this thesis, the numerically obtained reaction forces showed significant oscillations. This is suspected to be due to dynamic effects caused by bolt deformations. It is suggested that further studies on the boundary conditions of the back clamping frame regarding force transfer and dissipation are performed.
- Account for FSI in the numerical simulations. The blast load can be modeled more realistically by performing FSI simulations, by accounting for the effect of structural deformation on the applied load and visa versa.
- Introduce and apply a comprehensive optimization tool for numerical studies of sandwich panels. In the parameter study performed in this study, it was observed that there were considerable challenges regarding optimization of a sandwich component because of the vast amount of parameters and suspected cross-linked effects. It is therefore suggested that a comprehensive optimization scheme is introduced to improve the optimization of sandwich components concerning critical variables.

# Bibliography

- [1] J. K. Holmen, O. S. Hopperstad, and T. Børvik. “Low-velocity impact on multi-layered dual-phase steel plates”. In: *International Journal of Impact Engineering* 78 (2015), pp. 161–177.
- [2] V. Aune. “Behavior and modelling of flexible structures subjected to blast loading”. PhD thesis. Department of Structural Engineering, NTNU, 2017.
- [3] B. Sigurdsson. “Foam materials used for energy absorption and damage prevention during blast loading”. Master thesis. Department of Structural Engineering, NTNU, 2016.
- [4] T. Ngo, P. Mendis, A. Gupta, and J. Ramsay. “Blast loading and blast effects on structures - An overview”. In: *Electronic Journal of Structural Engineering* 7.S1 (2007), pp. 76–91.
- [5] V. Aune, T. Børvik, and M. Langseth. “Impact Mechanics - An introduction to blast mechanics”. SIMLab, Department of Structural Engineering, NTNU, 2016.
- [6] B. Hopkinson. “British ordnance board minutes 13565”. In: *The National Archives, Kew, UK* 11 (1915).
- [7] C. Cranz. *Lehrbuch der ballistik*. Vol. 2. Ripol Classic, Moscow, 1917.
- [8] C.N. Kingery and G. Bulmash. *Airblast parameters from TNT spherical air burst and hemispherical surface burst*. US Army Armament and Development Center, Ballistic Research Laboratory, New Jersey, 1984.
- [9] S.B. Menkes and H.J. Opat. “Broken beams”. In: *Experimental Mechanics* 13.11 (1973), pp. 480–486.
- [10] R.G. Teeling-Smith and G.N. Nurick. “The deformation and tearing of thin circular plates subjected to impulsive loads”. In: *International Journal of Impact Engineering* 11.1 (1991), pp. 77–91.
- [11] M.D. Olson, G.N. Nurick, and J.R. Fagnan. “Deformation and rupture of blast loaded square plates — predictions and experiments”. In: *International Journal of Impact Engineering* 13.2 (1993), pp. 279–291.
- [12] G.I. Taylor. “The pressure and impulse of submarine explosion waves on plates”. In: *The scientific papers of GI Taylor* 3 (1963), pp. 287–303.
- [13] T. Børvik, A.G. Hanssen, M. Langseth, and L. Olovsson. “Response of structures to planar blast loads - A finite element engineering approach”. In: *Computers & Structures* 87.9-10 (2009), pp. 507–520.
- [14] V. Aune, E. Fagerholt, M. Langseth, and T. Børvik. “A shock tube facility to generate blast loading on structures”. In: *International Journal of Protective Structures* 7.3 (2016), pp. 340–366.
- [15] V. Aune, G. Valsamos, F. Casadei, M. Larcher, M. Langseth, and T. Børvik. “Numerical study on the structural response of blast-loaded thin aluminium and steel plates”. In: *International Journal of Impact Engineering* 99 (2017), pp. 131–144.
- [16] M. Løken and H. Granum. “Experimental and numerical study on perforated steel plates subjected to blast loading”. Master thesis. Department of Structural Engineering, NTNU, 2016.

- [17] V. Aune, G. Valsamos, F. Casadei, M. Larcher, M. Langseth, and T. Børvik. “Use of damage-based mesh adaptivity to predict ductile failure in blast-loaded aluminium plates”. In: *Procedia Engineering* 197 (2017), pp. 3–12.
- [18] V. Aune, E. Fagerholt, K.O Hauge, K. Olsen, M. Langseth, and T. Børvik. “Experimental study on the response of thin aluminum and steel plates subjected to airblast loading”. In: *International Journal of Impact Engineering* 90 (2016), pp. 106–121.
- [19] S. Downes, A. Knott, and I. Robinson. “Towards a shock tube method for the dynamic calibration of pressure sensors”. In: *Philosophical Transactions of the Royal Society of London A* 372.2023 (2014).
- [20] N. McCormick and J. Lord. “Digital Image Correlation”. In: *Materials today* 13.12 (2010), pp. 52–54.
- [21] eCorr. *eCorr v4.0 Documentation*. URL: <http://folk.ntnu.no/egilf/ecorr/doc/> (visited on 02/01/2018).
- [22] N. Mills. *Polymer foams handbook: engineering and biomechanics applications and design guide*. Elsevier, 2007.
- [23] L.J. Gibson and M.F. Ashby. *Cellular solids: structure and properties*. Cambridge University Press, Cambridge, 1999.
- [24] Y. Sun and Q.M. Li. “Dynamic compressive behaviour of cellular materials: a review of phenomenon, mechanism and modelling”. In: *International Journal of Impact Engineering* 112 (2017), pp. 74–115.
- [25] P.J. Veale. “Investigation of the behavior of open cell aluminum foam”. Master thesis. 1911. University of Massachusetts Amherst, 2014.
- [26] Q.M. Li, I. Magkiriadis, and J. Harrigan. “Compressive strain at the onset of densification of cellular solids”. In: *Journal of cellular plastics* 42.5 (2006), pp. 371–392.
- [27] H.L. Schreyer, Q.H. Zuo, and A.K. Maji. “Anisotropic plasticity model for foams and honeycombs”. In: *Journal of engineering mechanics* 120.9 (1994), pp. 1913–1930.
- [28] W. Ehlers, H. Mullerschön, and O. Klar. “On the behaviour of aluminium foams under uniaxial and multiaxial loading”. In: *Metal Foams and Porous Metal Structures* (1999), pp. 255–262.
- [29] R.E. Miller. “A continuum plasticity model for the constitutive and indentation behaviour of foamed metals”. In: *International Journal of Mechanical Sciences* 42.4 (2000), pp. 729–754.
- [30] V.S. Deshpande and N.A. Fleck. “Isotropic constitutive models for metallic foams”. In: *Journal of the Mechanics and Physics of Solids* 48.6-7 (2000), pp. 1253–1283.
- [31] A.G. Hanssen, O.S. Hopperstad, M. Langseth, and H. Ilstad. “Validation of constitutive models applicable to aluminum foams”. In: *International Journal of Mechanical Sciences* 44.2 (2002), pp. 359–406.
- [32] A. Reyes, O.S. Hopperstad, T. Berstad, A.G. Hanssen, and M. Langseth. “Constitutive modeling of aluminum foam including fracture and statistical variation of density”. In: *European Journal of Mechanics-A/Solids* 22.6 (2003), pp. 815–835.
- [33] S. Berdal and L. Bjørgo. “Impact behavior of foam-based protective structures”. Master thesis. Department of Structural Engineering, NTNU, 2017.
- [34] T. Børvik, O.S. Hopperstad, T. Berstad, and M. Langseth. “A computational model of viscoplasticity and ductile damage for impact and penetration”. In: *European Journal of Mechanics-A/Solids* 20.5 (2001), pp. 685–712.
- [35] G.R. Johnson and W.H. Cook. “A constitutive model and data for metals subjected to large strains, high strain rates and high temperatures”. In: *Proceedings of the 7th International Symposium on Ballistics, The Hague*. 1983, pp. 541–547.
- [36] J. Lemaitre and J.L. Chaboche. *Mechanics of solid materials*. Cambridge University Press, Cambridge, 1994.

- [37] M.G. Cockcroft and D.J. Latham. “Ductility and the workability of metals”. In: *Journal Institute of Metals* 96.1 (1968), pp. 33–39.
- [38] D.D. Radford, G.J. McShane, V.S. Deshpande, and N.A. Fleck. “The response of clamped sandwich plates with metallic foam cores to simulated blast loading”. In: *International Journal of Solids and Structures* 43.7-8 (2006), pp. 2243–2259.
- [39] H. Liu, Z.K. Cao, G.C. Yao, H.J. Luo, and G.Y. Zu. “Performance of aluminum foam - steel panel sandwich composites subjected to blast loading”. In: *Materials & Design* 47 (2013), pp. 483–488.
- [40] M.Z. Hassan, Z.W. Guan, W.J. Cantwell, G.S. Langdon, and G.N. Nurick. “The influence of core density on the blast resistance of foam-based sandwich structures”. In: *International Journal of Impact Engineering* 50 (2012), pp. 9–16.
- [41] E. Wang, N. Gardner, and A. Shukla. “The blast resistance of sandwich composites with stepwise graded cores”. In: *International Journal of Solids and Structures* 46.18-19 (2009), pp. 3492–3502.
- [42] S. Li, X. Li, Z. Wang, G. Wu, G. Lu, and L. Zhao. “Finite element analysis of sandwich panels with stepwise graded aluminum honeycomb cores under blast loading”. In: *Composites Part A: Applied Science and Manufacturing* 80 (2016), pp. 1–12.
- [43] C. Qi, S. Yang, L.J. Yang, Z.Y. Wei, and Z.H. Lu. “Blast resistance and multi-objective optimization of aluminum foam-cored sandwich panels”. In: *Composite Structures* 105 (2013), pp. 45–57.
- [44] S. Ouellet, D. Cronin, and M. Worswick. “Compressive response of polymeric foams under quasi-static, medium and high strain rate conditions”. In: *Polymer testing* 25.6 (2006), pp. 731–743.
- [45] B. Song, W.W. Chen, S. Dou, N.A. Winfree, and J.H. Kang. “Strain-rate effects on elastic and early cell-collapse responses of a polystyrene foam”. In: *International Journal of Impact Engineering* 31.5 (2005), pp. 509–521.
- [46] W. Chen, H. Hao, D. Hughes, Y. Shi, J. Cui, and Zhong-X. Li. “Static and dynamic mechanical properties of expanded polystyrene”. In: *Materials & Design* 69 (2015), pp. 170–180.
- [47] R. Bouix, P. Viot, and J.L. Lataillade. “Polypropylene foam behaviour under dynamic loadings: Strain rate, density and microstructure effects”. In: *International Journal of Impact Engineering* 36.2 (2009), pp. 329–342.
- [48] D.S. Cronin and S. Ouellet. “Low density polyethylene, expanded polystyrene and expanded polypropylene: Strain rate and size effects on mechanical properties”. In: *Polymer Testing* 53 (2016), pp. 40–50.
- [49] A. Yonezu, K. Hirayama, H. Kishida, and X. Chen. “Characterization of the compressive deformation behavior with strain rate effect of low-density polymeric foams”. In: *Polymer Testing* 50 (2016), pp. 1–8.
- [50] M. Avallone, G. Belingardi, and R. Montanini. “Characterization of polymeric structural foams under compressive impact loading by means of energy-absorption diagram”. In: *International Journal of Impact Engineering* 25.5 (2001), pp. 455–472.
- [51] LS-DYNA Support. *Energy data*. 2018. URL: <https://www.dynasupport.com/tutorial/ls-dyna-users-guide/energy-data> (visited on 05/22/2018).
- [52] MakeItFrom. *1050 (A91050) Aluminum*. 2018. URL: <https://www.makeitfrom.com/material-properties/1050-A91050-Aluminum> (visited on 02/01/2018).
- [53] E.A. Avallone, T. Baumeister, and A.M. Sadegh. *Marks’ standard handbook for mechanical engineers. 10*. McGraw-Hill, New York, 2006.
- [54] E. Fagerholt, T. Børvik, and O.S. Hopperstad. “Measuring discontinuous displacement fields in cracked specimens using digital image correlation with mesh adaptation and crack-path optimization.” In: *Optics and Lasers in Engineering* (2013).

- [55] O.S Hopperstad and T. Børvik. “Impact Mechanics - Part 1: Modelling of plasticity and failure with explicit finite element”. SIMLab, Department of Structural Engineering, NTNU, 2017.
- [56] W. Callister and D. Rethwisch. *Materials Science and Engineering - An Introduction*. WILEY, New Jersey, 2013.
- [57] SSAB. *Docol 600DL*. 2018. URL: <https://www.ssab.com/products/brands/docol/products/docol-600dl> (visited on 02/01/2018).
- [58] Y. Delaviz, B. Patel, M. Polasky, R.M. Breindel, R.R. Loh, and M.Z. Weekley. *Method of manufacturing polystyrene foam with polymer processing additives*. US Patent 8,119,701. Feb. 2012.
- [59] *LS DYNA Keywords User’s Manual, Volume 2*.
- [60] Hexagon AB. *ROMER Absolute Arm with integrated scanner*. 2018. URL: <http://www.hexagonmi.com/en-GB/products/portable-measuring-arms/romer-absolute-arm-with-integrated-scanner> (visited on 05/09/2018).

# Appendix A

## Measurements of Foam Density

For the XPS-250, XPS-400 and XPS-700 foam specimens used in the experiments, a nominal density of  $33 \text{ kg/m}^3$ ,  $37 \text{ kg/m}^3$  and  $50 \text{ kg/m}^3$ , respectively, was provided. However, the real densities may deviate from the nominal densities. Table A.1 and A.2 shows measured and calculated real densities for the foam specimens. The 24 pre-drilled holes were also accounted for in the volumetric calculations.

Table A.1: Measurements and calculated density for all foam specimens used as core in sandwich panels with aluminum skins.

| Test Name     | Weight<br>[g] | Height<br>[mm] | Length<br>[mm] | Width<br>[mm] | Density<br>[kg/m <sup>3</sup> ] |
|---------------|---------------|----------------|----------------|---------------|---------------------------------|
| SW_Al_250_P10 | 531.3         | 51.00          | 600.83         | 585.00        | 31.33                           |
| SW_Al_400_P10 | 682.1         | 53.49          | 625.00         | 585.00        | 37.38                           |
| SW_Al_700_P10 | 869.4         | 50.12          | 623.00         | 585.00        | 51.11                           |
| SW_Al_250_P15 | 556.0         | 51.29          | 585.00         | 585.00        | 31.68                           |
| SW_Al_400_P15 | 681.0         | 53.54          | 625.00         | 585.00        | 37.34                           |
| SW_Al_700_P15 | 826.4         | 50.78          | 588.00         | 585.00        | 50.09                           |

Table A.2: Measurements and calculated density for all foam specimens used as core in sandwich panels with aluminum and steel skins.

| Test Name      | Weight<br>[g] | Height<br>[mm] | Length<br>[mm] | Width<br>[mm] | Density<br>[kg/m <sup>3</sup> ] |
|----------------|---------------|----------------|----------------|---------------|---------------------------------|
| SW_AIS_250_P35 | 532.9         | 51.10          | 602.50         | 585.00        | 31.26                           |
| SW_AIS_400_P35 | 674.3         | 50.34          | 603.33         | 585.00        | 37.95                           |
| SW_AIS_700_P35 | 867.3         | 50.27          | 623.67         | 585.00        | 50.68                           |





# Appendix B

## Component Test

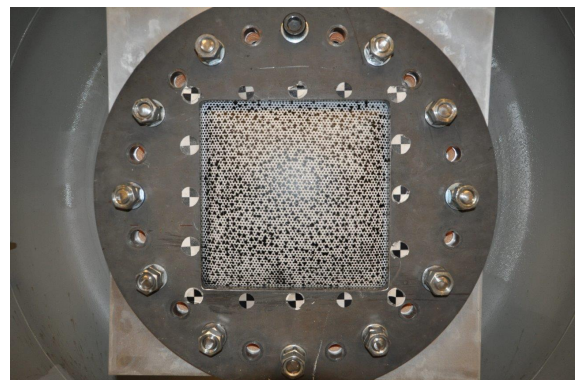
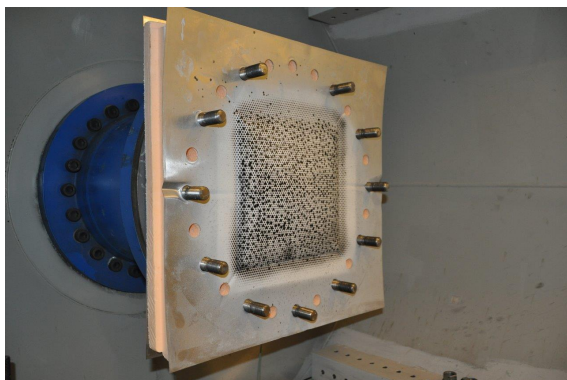
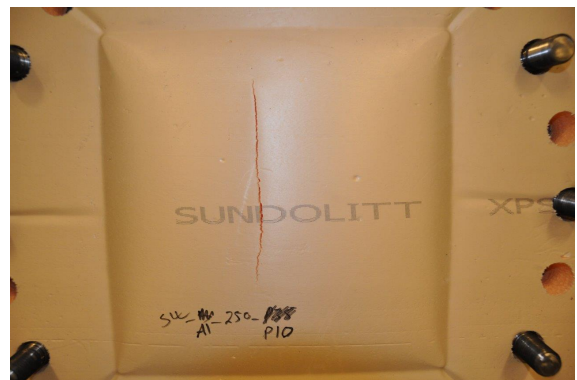


Figure B.3: Picture of front skin (top), foam (middle) and back skin (bottom left) deformation and the clamped component (bottom right) of sandwich panel with aluminum skins and XPS-250 foam core exposed to 10 *bar* firing pressure.

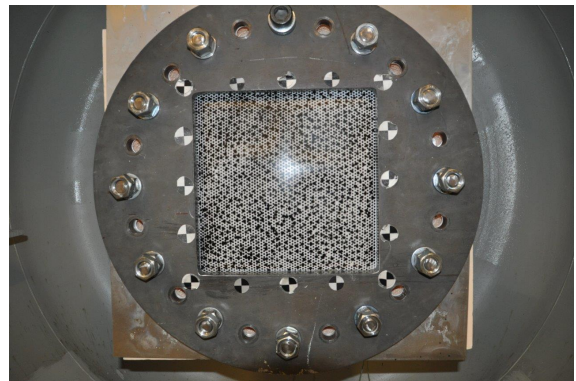
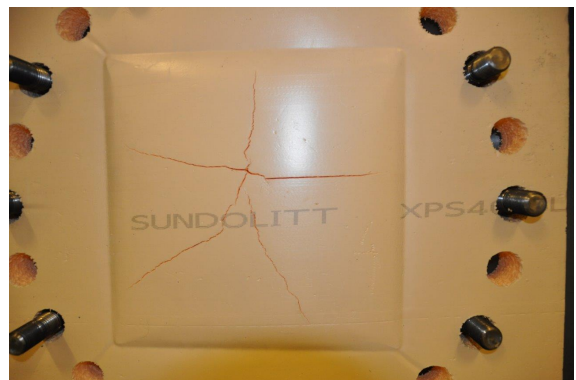
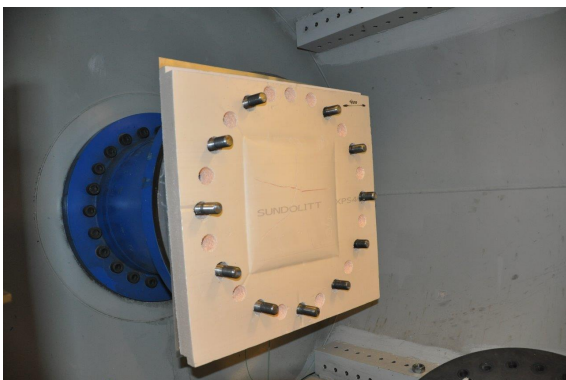
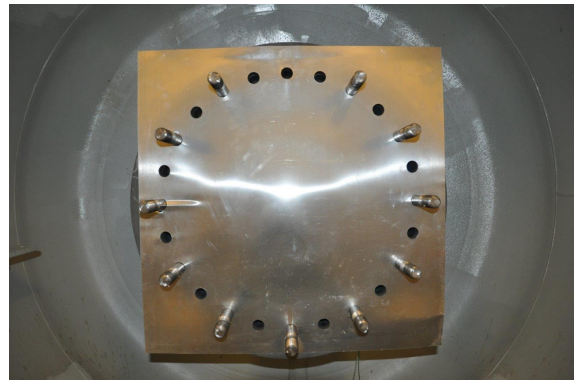
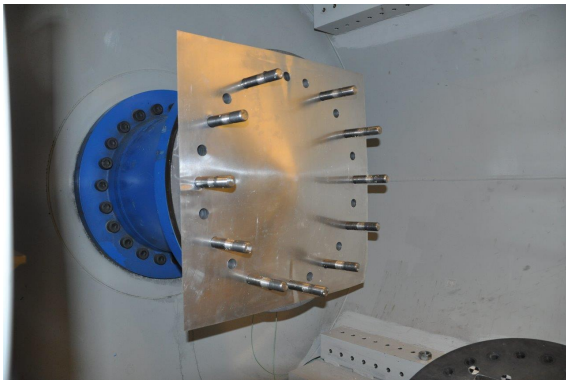


Figure B.6: Picture of front skin (top), foam (middle) and back skin (bottom left) deformation and the clamped component (bottom right) of sandwich panel with aluminum skins and XPS-400 foam core exposed to 10 *bar* firing pressure.

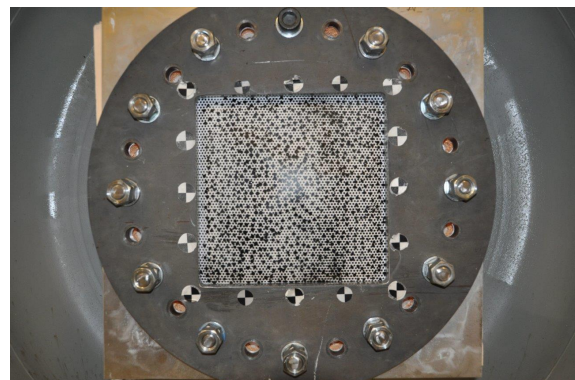
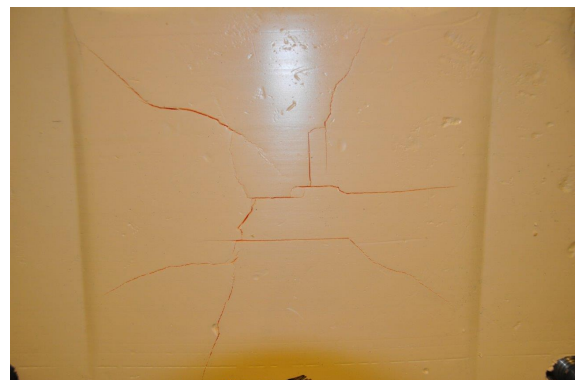
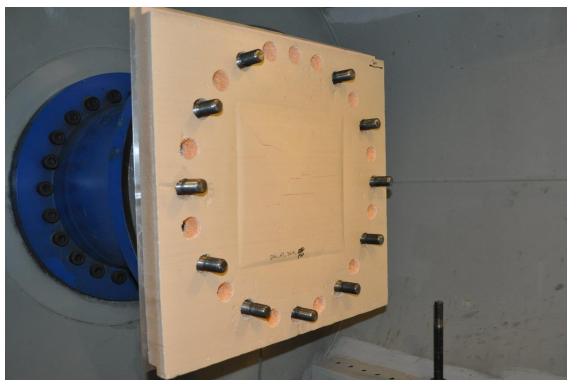


Figure B.9: Picture of front skin (top), foam (middle) and back skin (bottom left) deformation and the clamped component (bottom right) of sandwich panel with aluminum skins and XPS-700 foam core exposed to 10 *bar* firing pressure.

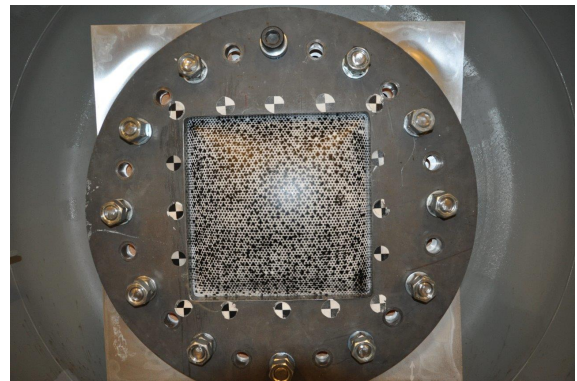
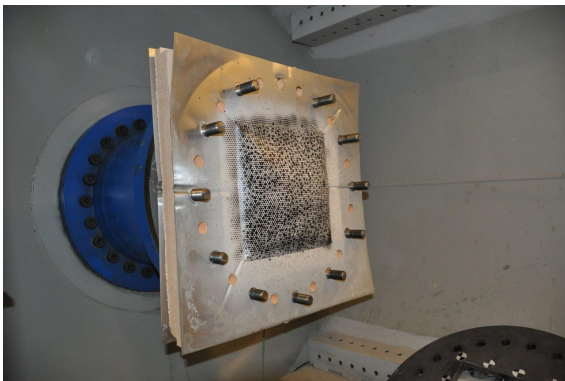
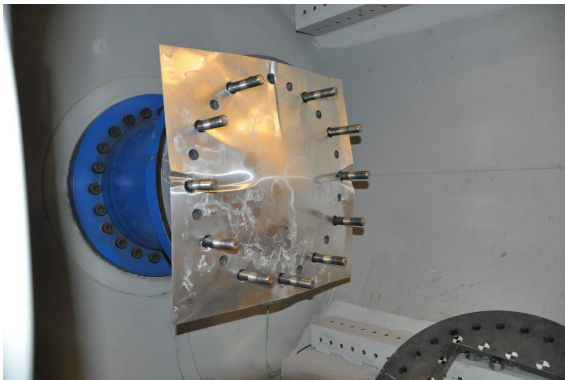


Figure B.12: Picture of front skin (top), foam (middle) and back skin (bottom left) deformation and the clamped component (bottom right) of sandwich panel with aluminum skins and XPS-250 foam core exposed to 15 *bar* firing pressure.

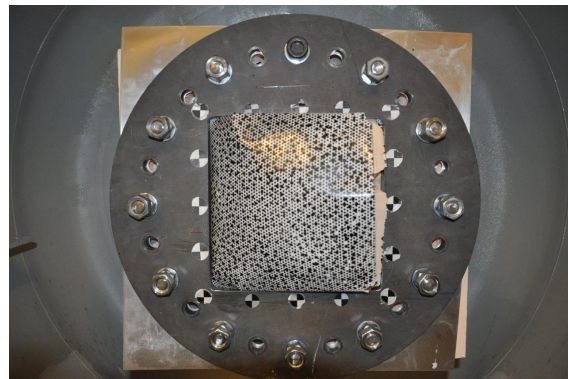
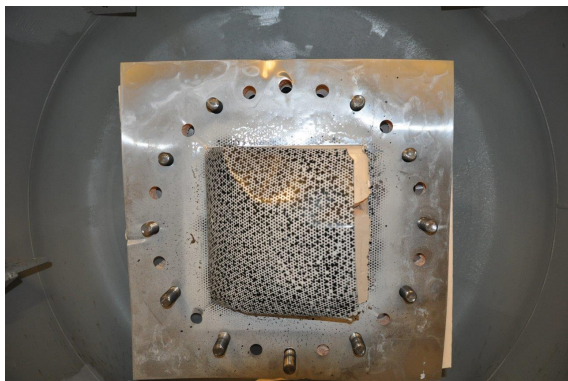
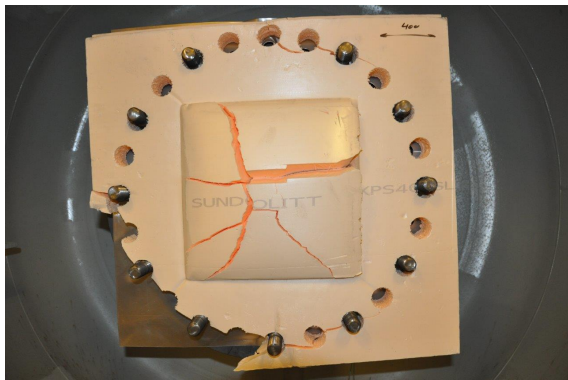
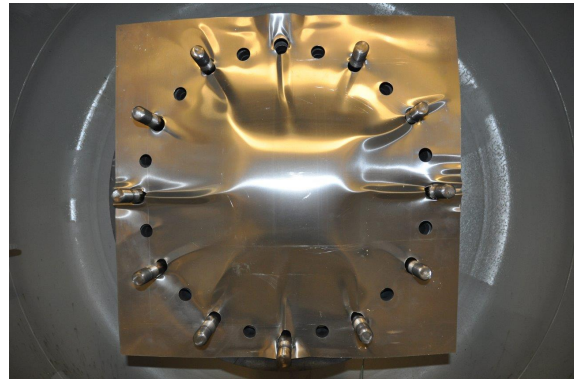
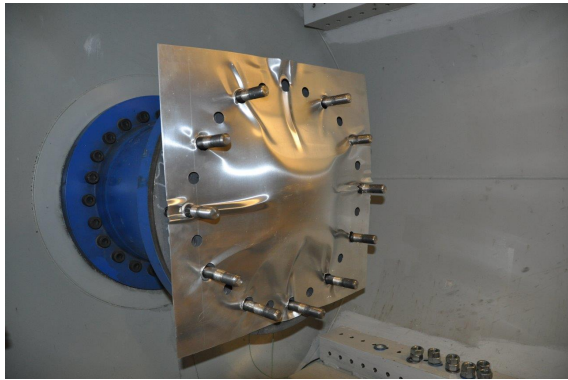


Figure B.16: Picture of front skin (top), foam (top middle) and back skin (bottom middle) deformation and the clamped component (bottom) of sandwich panel with aluminum skins and XPS-400 foam core exposed to 15 bar firing pressure.

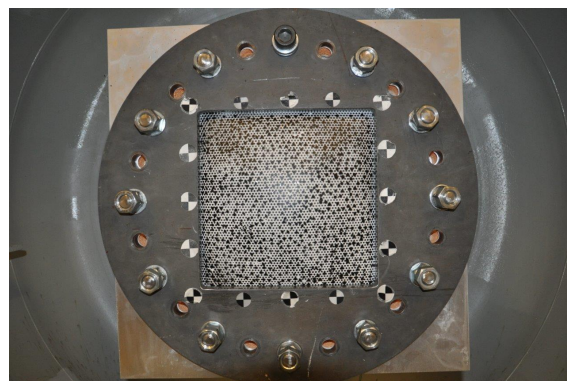
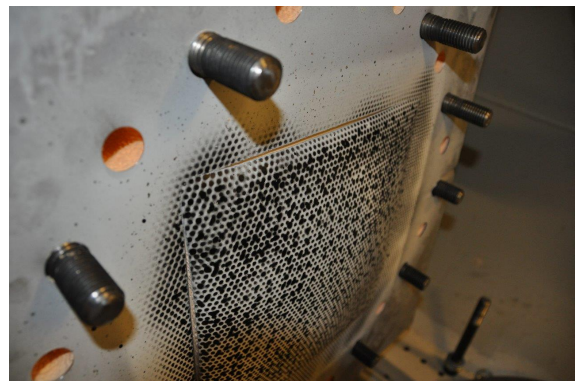
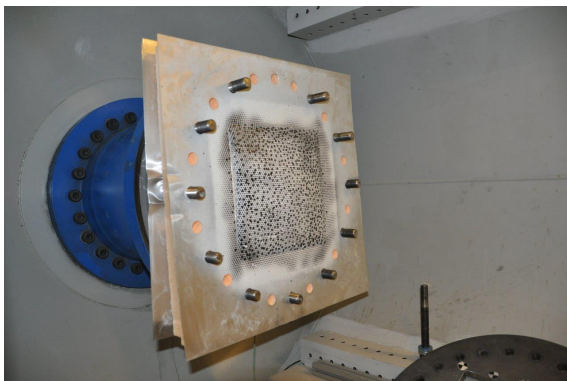
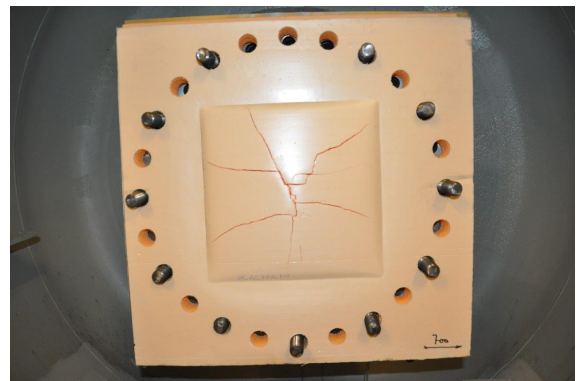
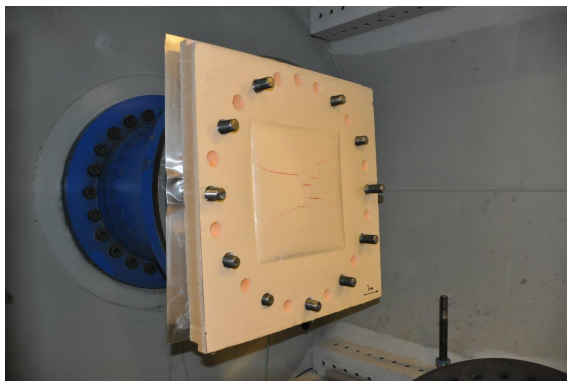
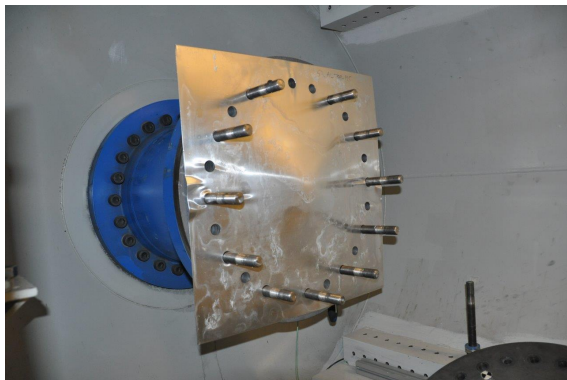


Figure B.20: Picture of front skin (top), foam (top middle) and back skin (bottom middle) deformation and the clamped component (bottom) of sandwich panel with aluminum skins and XPS-700 foam core exposed to 15 bar firing pressure.



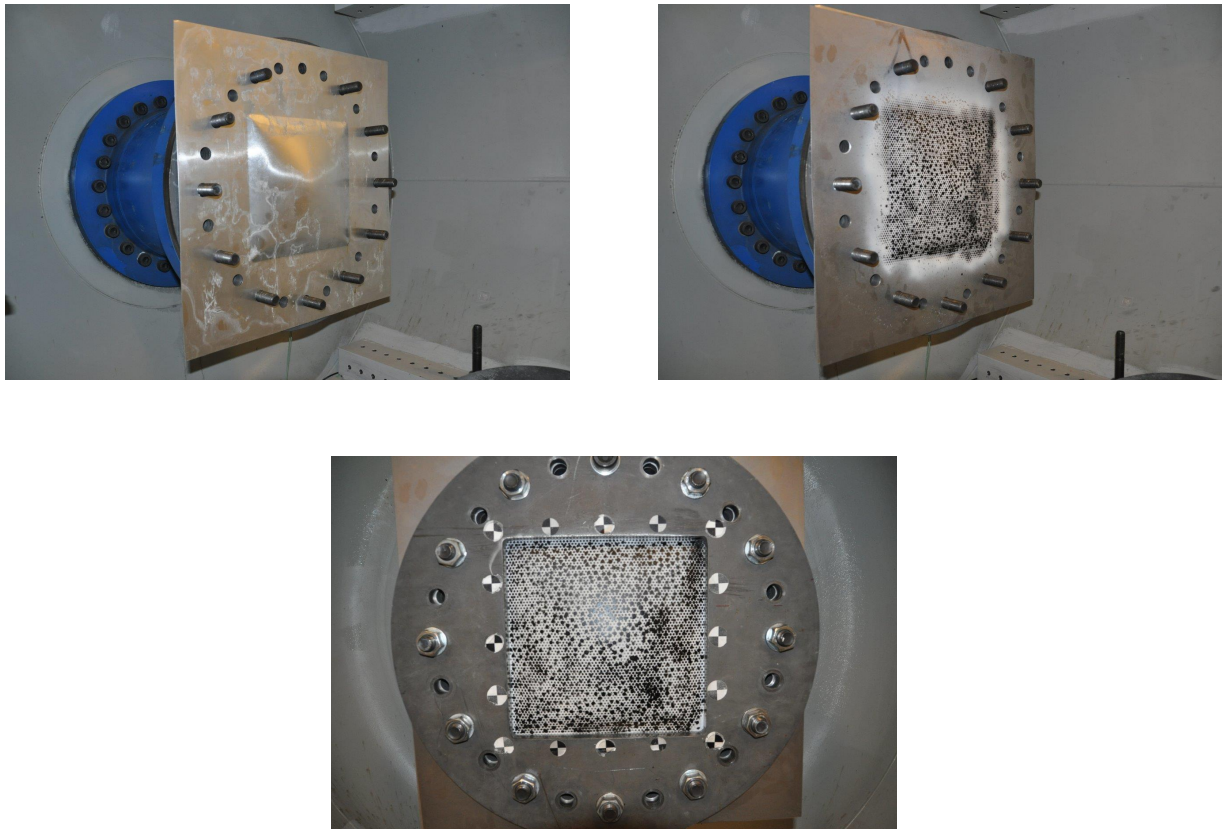


Figure B.22: Picture of front skin (top left) and back skin (top right) deformation and the clamped component (bottom) of aluminum and steel skin without foam core exposed to 25 *bar* firing pressure.

S\_AIS\_P35

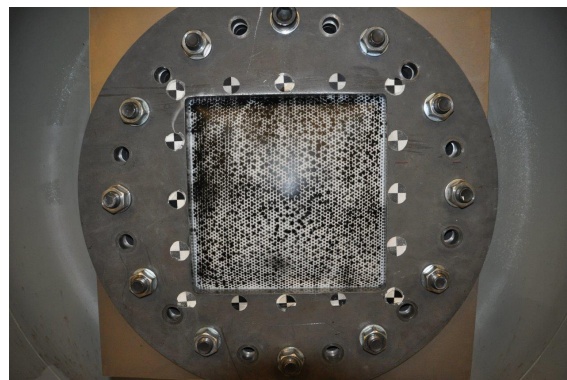
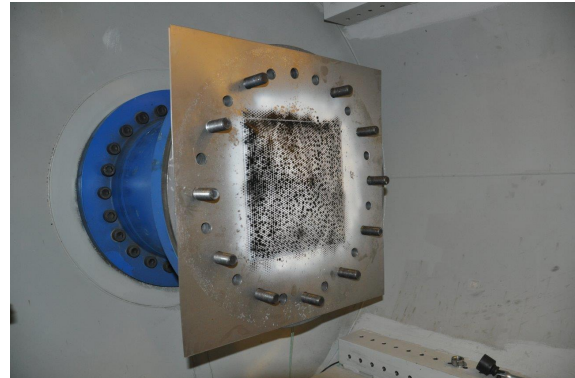
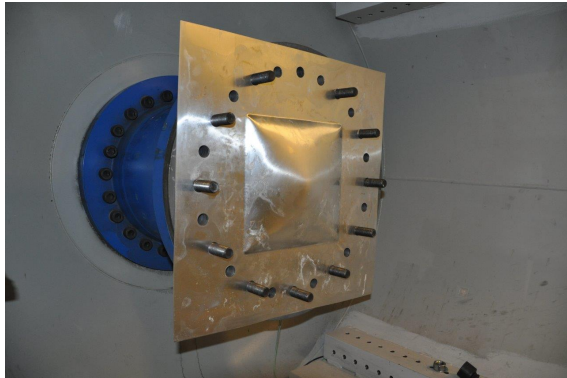


Figure B.24: Picture of front skin (top left) and back skin (top right) deformation and the clamped component (bottom) of aluminum and steel skin without foam core exposed to 35 *bar* firing pressure.

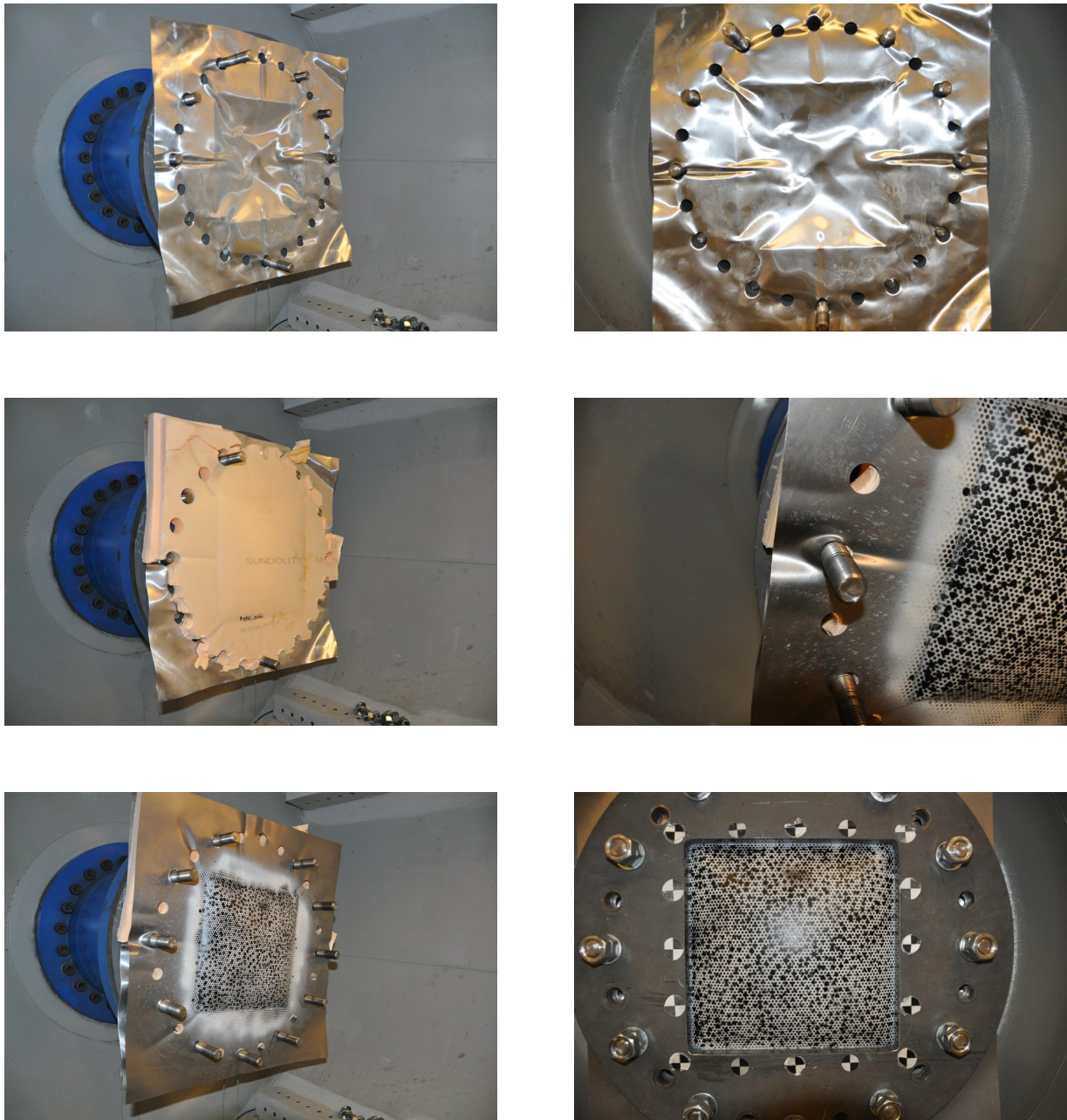


Figure B.27: Picture of front skin (top), foam (middle left) and back skin (middle right and bottom left) deformation and the clamped component (bottom right) of sandwich panel with aluminum and steel skins and XPS-250 foam core exposed to 35 *bar* firing pressure.

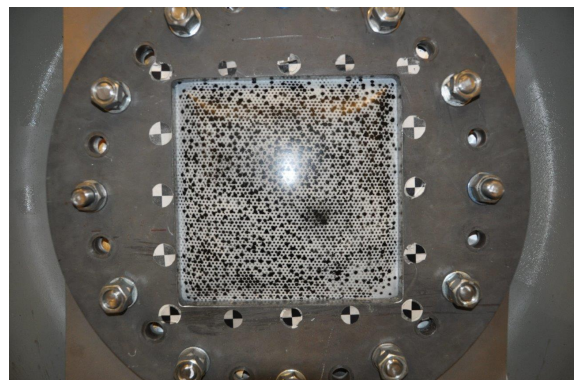
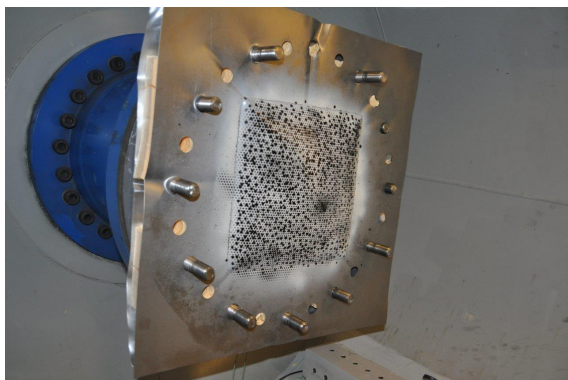
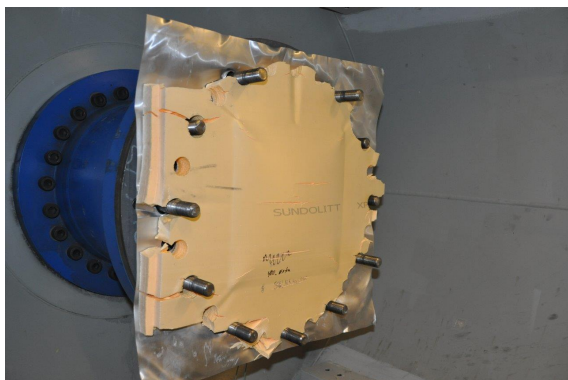
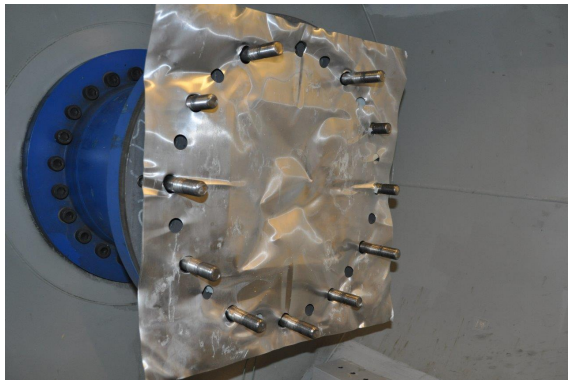


Figure B.30: Picture of front skin (top), foam (middle) and back skin (bottom left) deformation and the clamped component (bottom right) of sandwich panel with aluminum and steel skins and XPS-400 foam core exposed to 35 bar firing pressure.

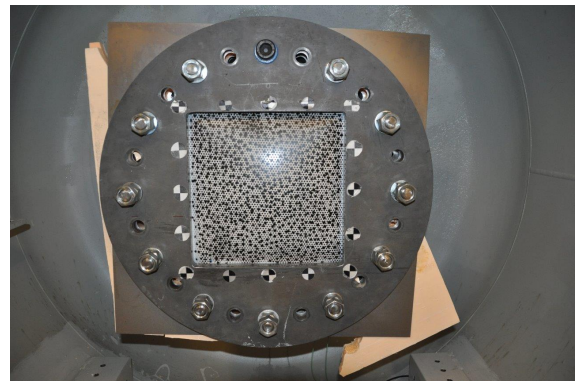
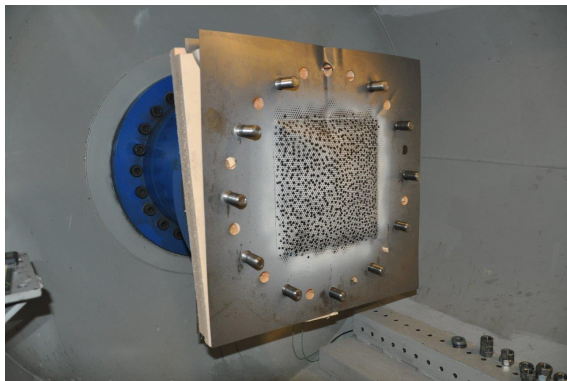
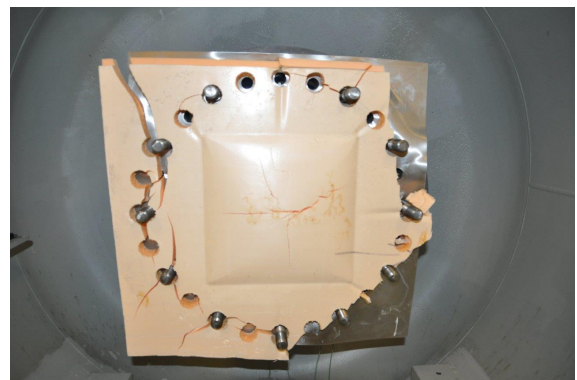
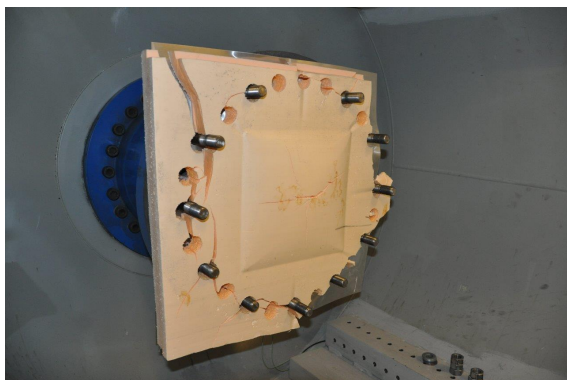


Figure B.33: Picture of front skin (top), foam (middle) and back skin (bottom left) deformation and the clamped component (bottom right) of sandwich panel with aluminum and steel skins and XPS-700 foam core exposed to 35 bar firing pressure.

# Appendix C

## Parameter Study

# C.1 Foam Density

## Aluminum skins exposed to 10 bar

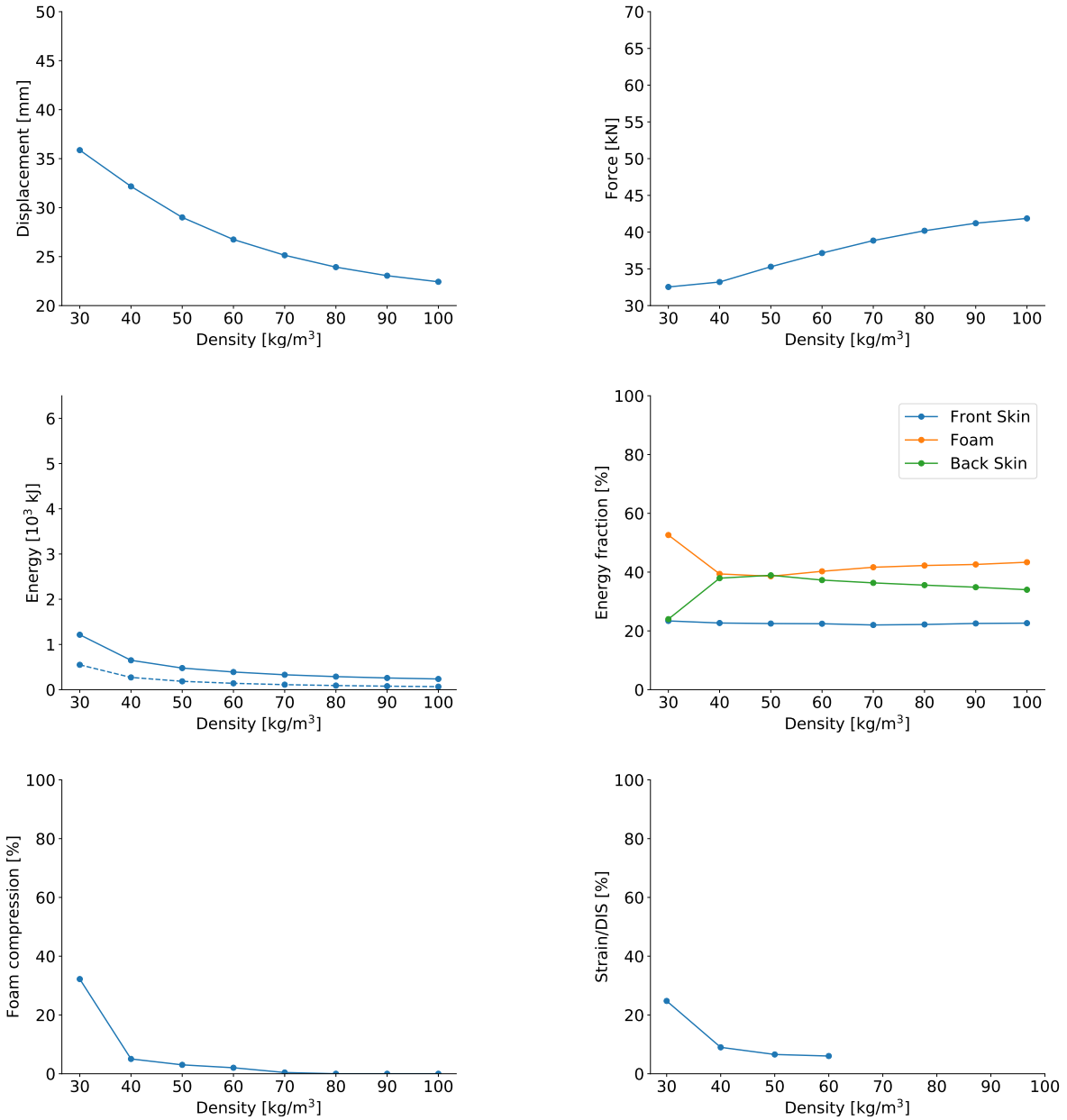


Figure C.1: Back skin displacement, reaction force between component and back clamping frame, total and total specific energy absorbed, percentage of energy absorbed in foam core, back skin and front skin, percentage of foam compression and strain percentage of density initiation strain for variation of density for sandwich components with aluminum front and back skin exposed to firing pressure of 10 bar.

## Aluminum skins exposed to 15 bar

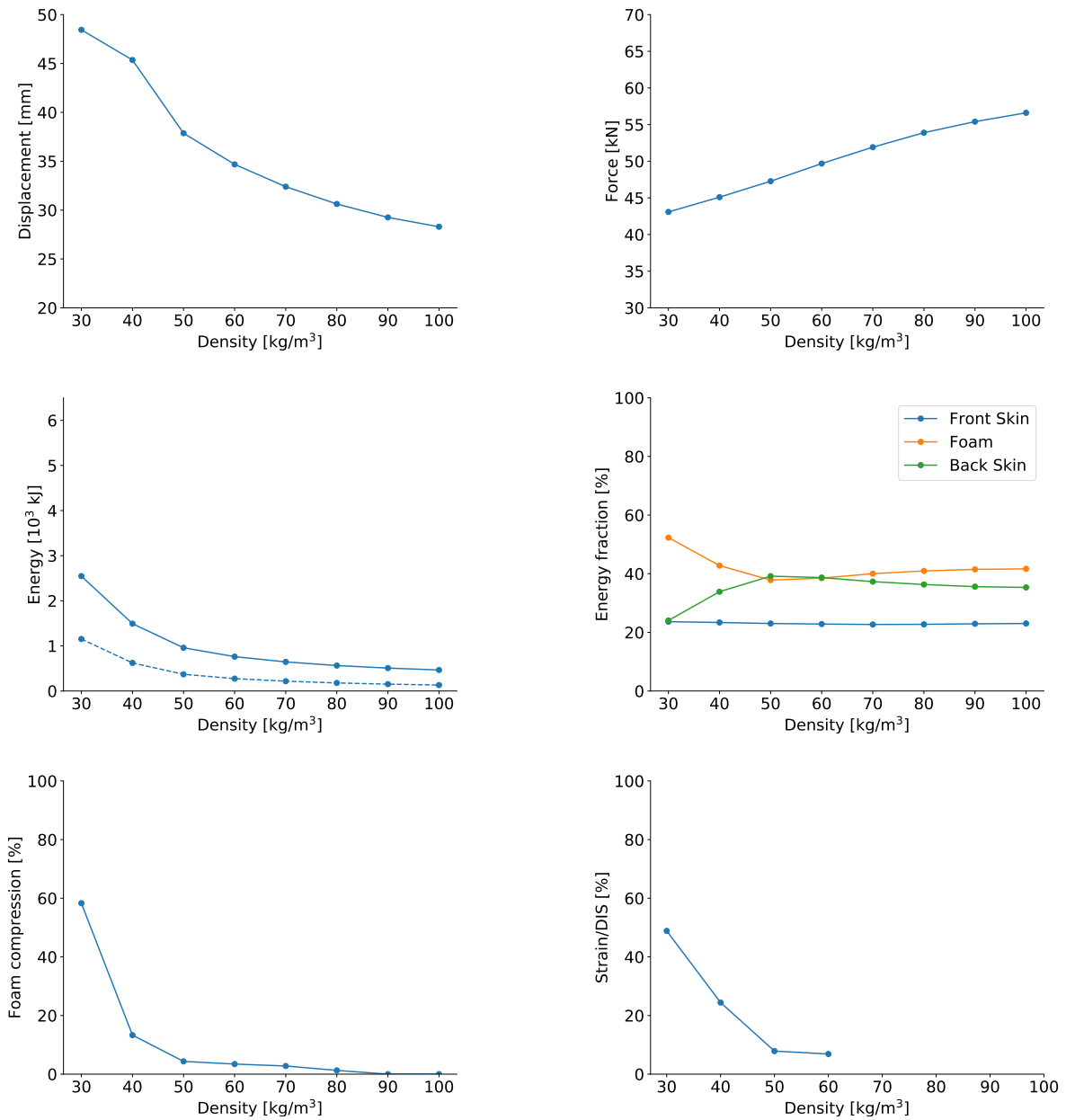


Figure C.2: Back skin displacement, reaction force between component and back clamping frame, total and total specific energy absorbed, percentage of energy absorbed in foam core, back skin and front skin, percentage of foam compression and strain percentage of density initiation strain for variation of density for sandwich components with aluminum front and back skin exposed to firing pressure of 15 bar.



## Aluminum skins exposed to 25 bar

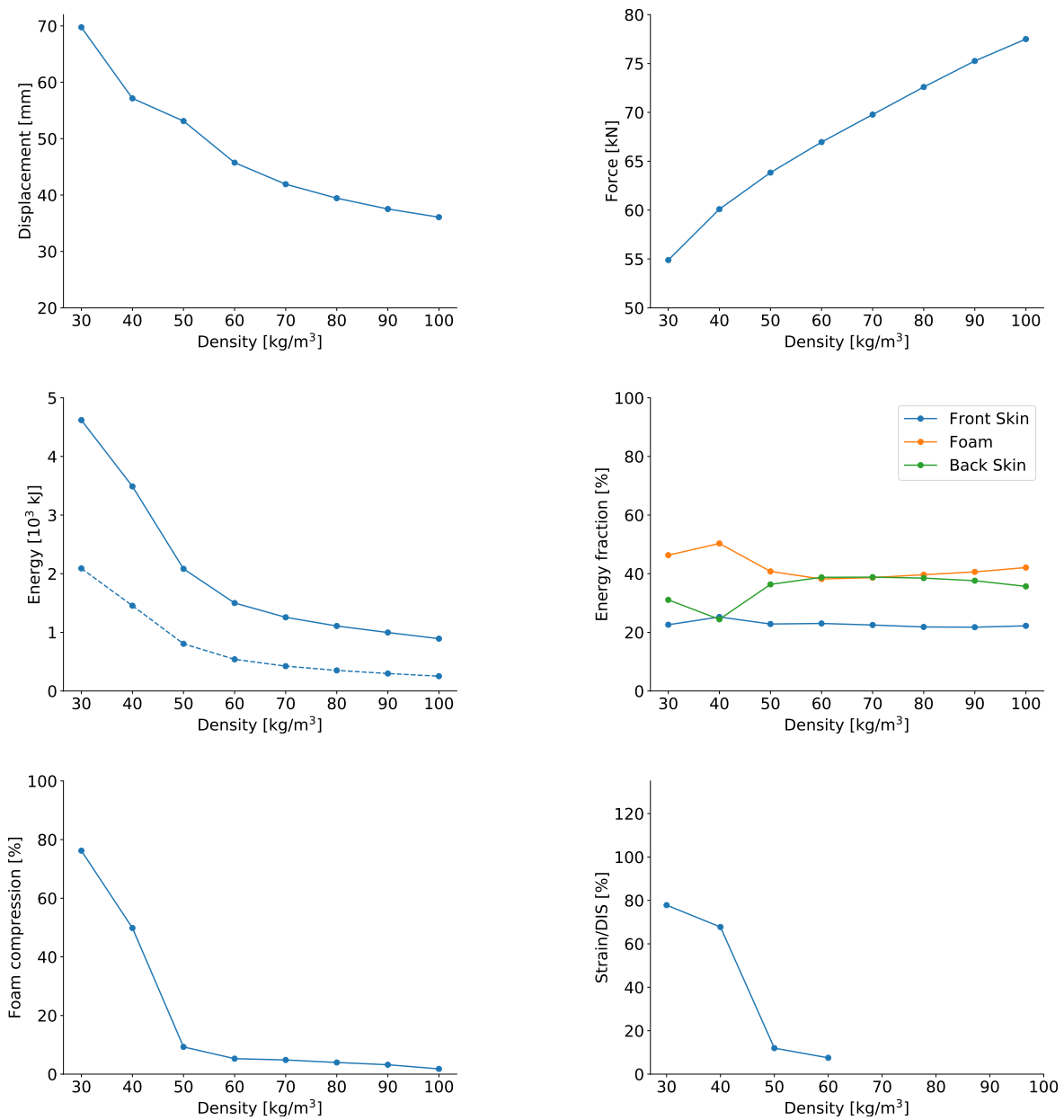


Figure C.3: Back skin displacement, reaction force between component and back clamping frame, total and total specific energy absorbed, percentage of energy absorbed in foam core, back skin and front skin, percentage of foam compression and strain percentage of density initiation strain for variation of density for sandwich components with aluminum front and back skin exposed to firing pressure of 25 bar.

## Aluminum front skin and steel back skin exposed to 25 bar

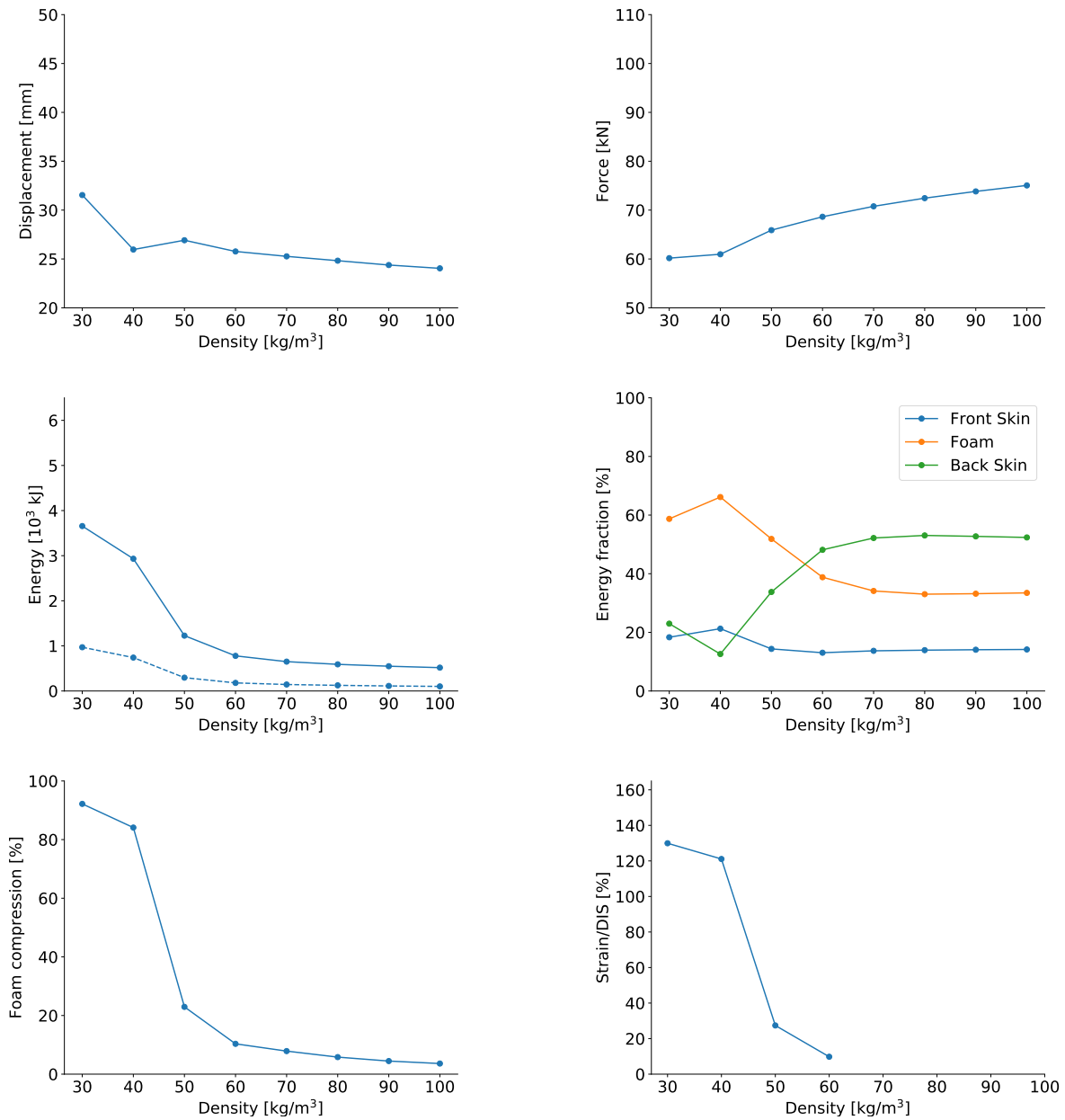


Figure C.4: Back skin displacement, reaction force between component and back clamping frame, total and total specific energy absorbed, percentage of energy absorbed in foam core, back skin and front skin, percentage of foam compression and strain percentage of density initiation strain for variation of density for sandwich components with aluminum front skin and steel back skin exposed to firing pressure of 25 bar.

## Aluminum front skin and steel back skin exposed to 35 bar

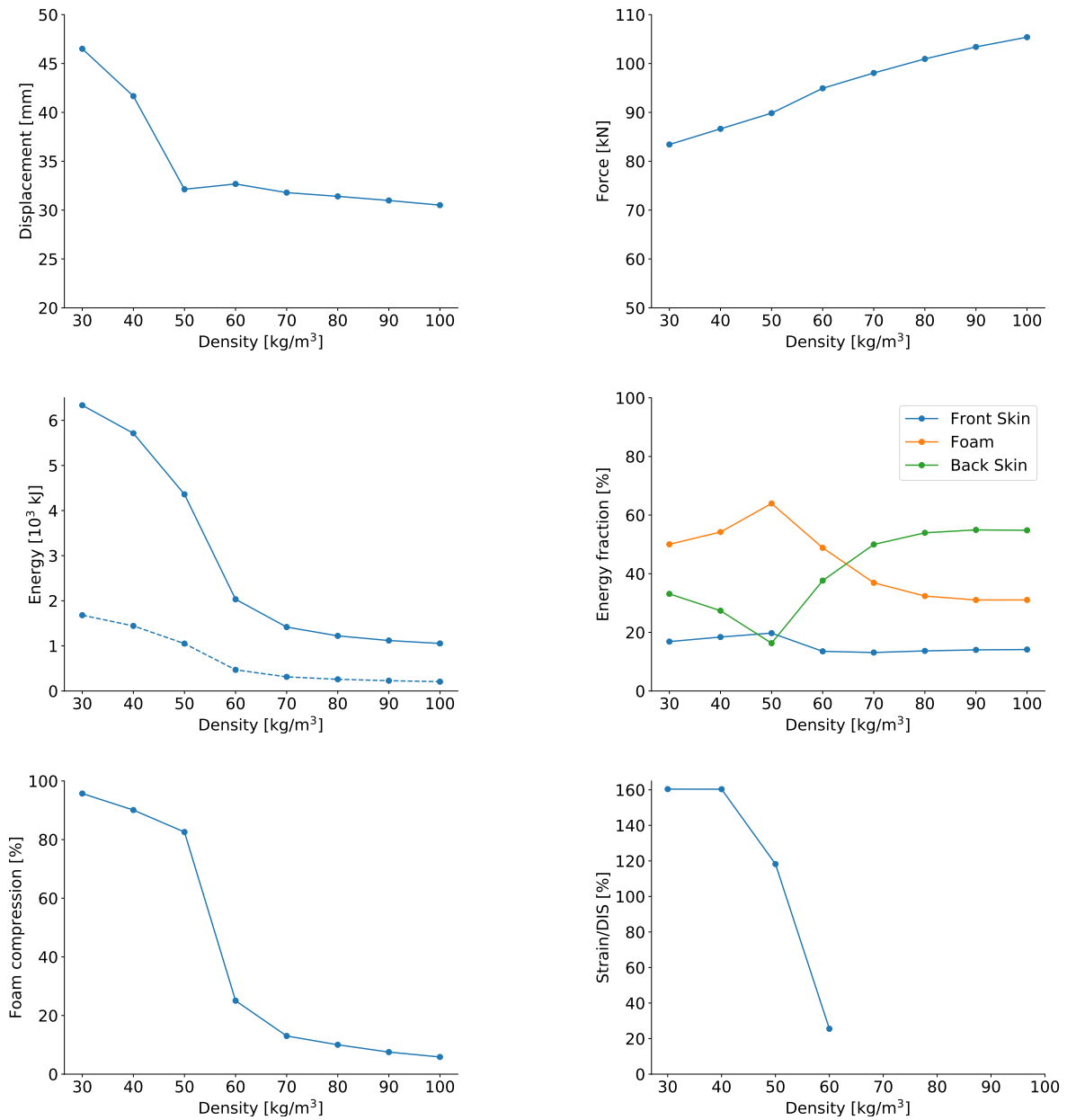


Figure C.5: Back skin displacement, reaction force between component and back clamping frame, total and total specific energy absorbed, percentage of energy absorbed in foam core, back skin and front skin, percentage of foam compression and strain percentage of density initiation strain for variation of density for sandwich components with aluminum front skin and steel back skin exposed to firing pressure of 35 bar.

## C.2 Thickness

### Aluminum skins exposed to 10 bar

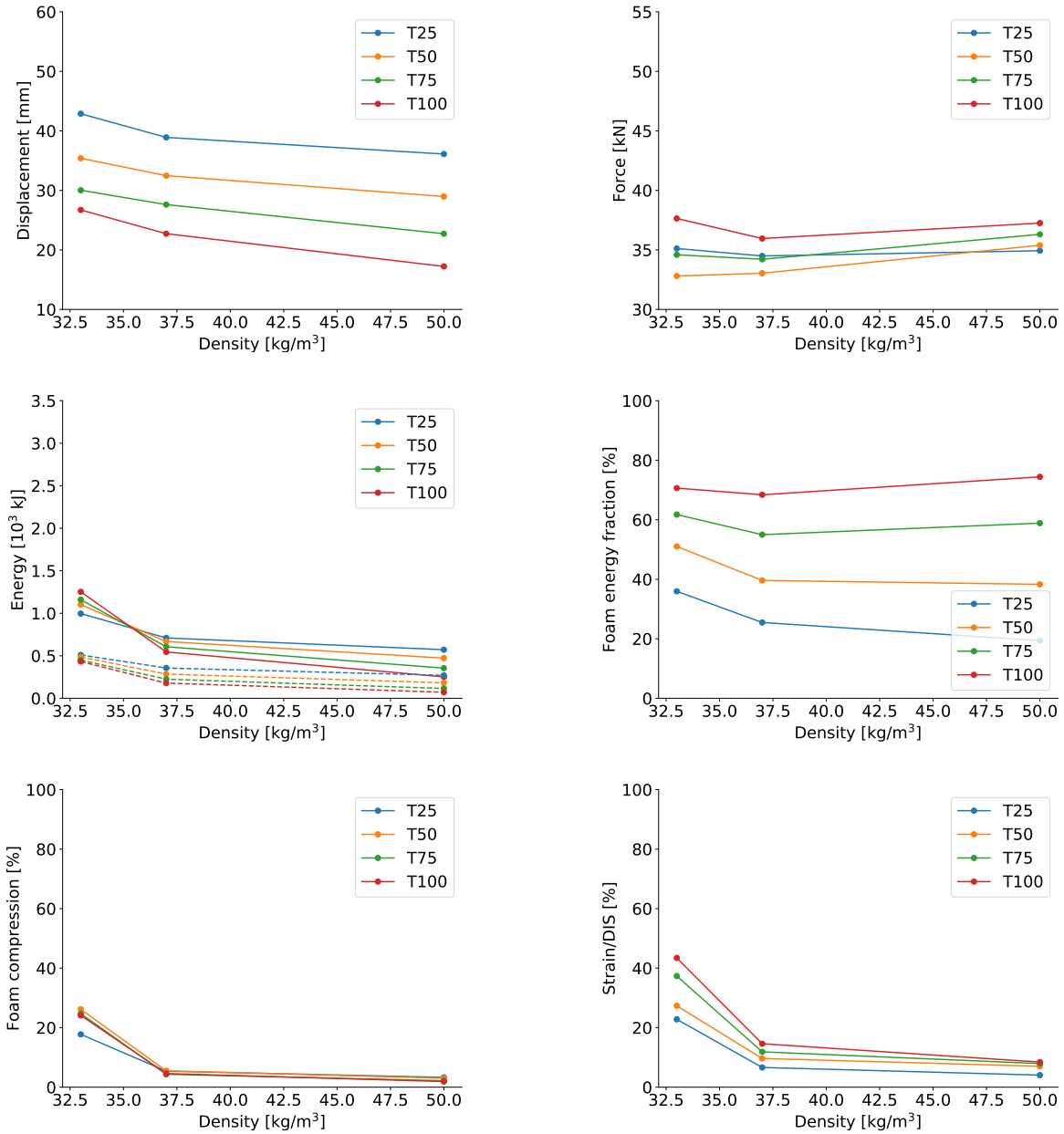


Figure C.6: Back skin displacement, reaction force between component and back clamping frame, total and total specific energy absorbed, percentage of energy absorbed in foam core, back skin and front skin, percentage of foam compression and strain percentage of density initiation strain for variation of thickness for sandwich components with aluminum front and back skin exposed to firing pressure of 10 bar.

# Aluminum skins exposed to 15 bar

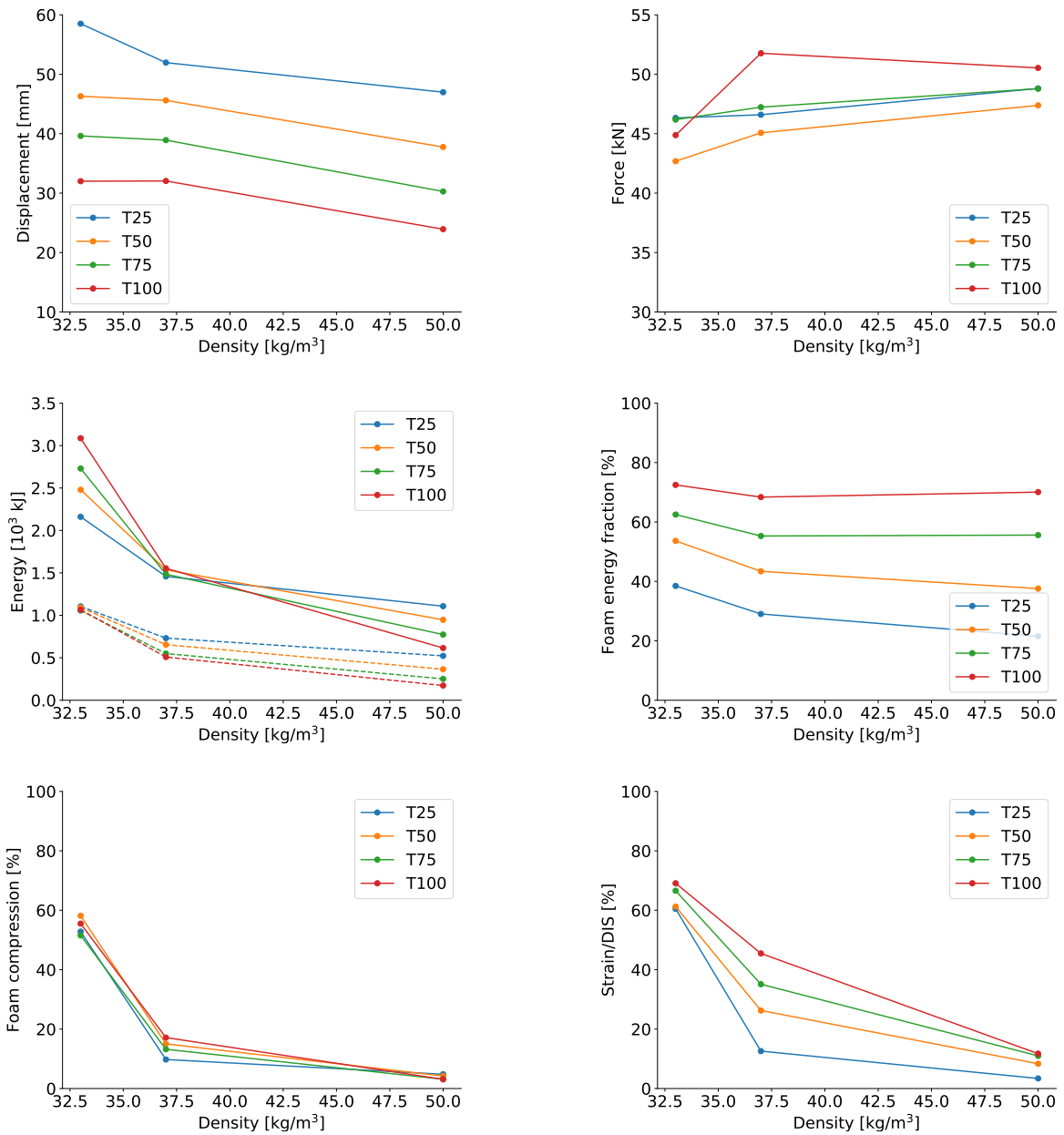


Figure C.7: Back skin displacement, reaction force between component and back clamping frame, total and total specific energy absorbed, percentage of energy absorbed in foam core, back skin and front skin, percentage of foam compression and strain percentage of density initiation strain for variation of thickness for sandwich components with aluminum front and back skin exposed to firing pressure of 15 bar.

# Aluminum skins exposed to 25 bar

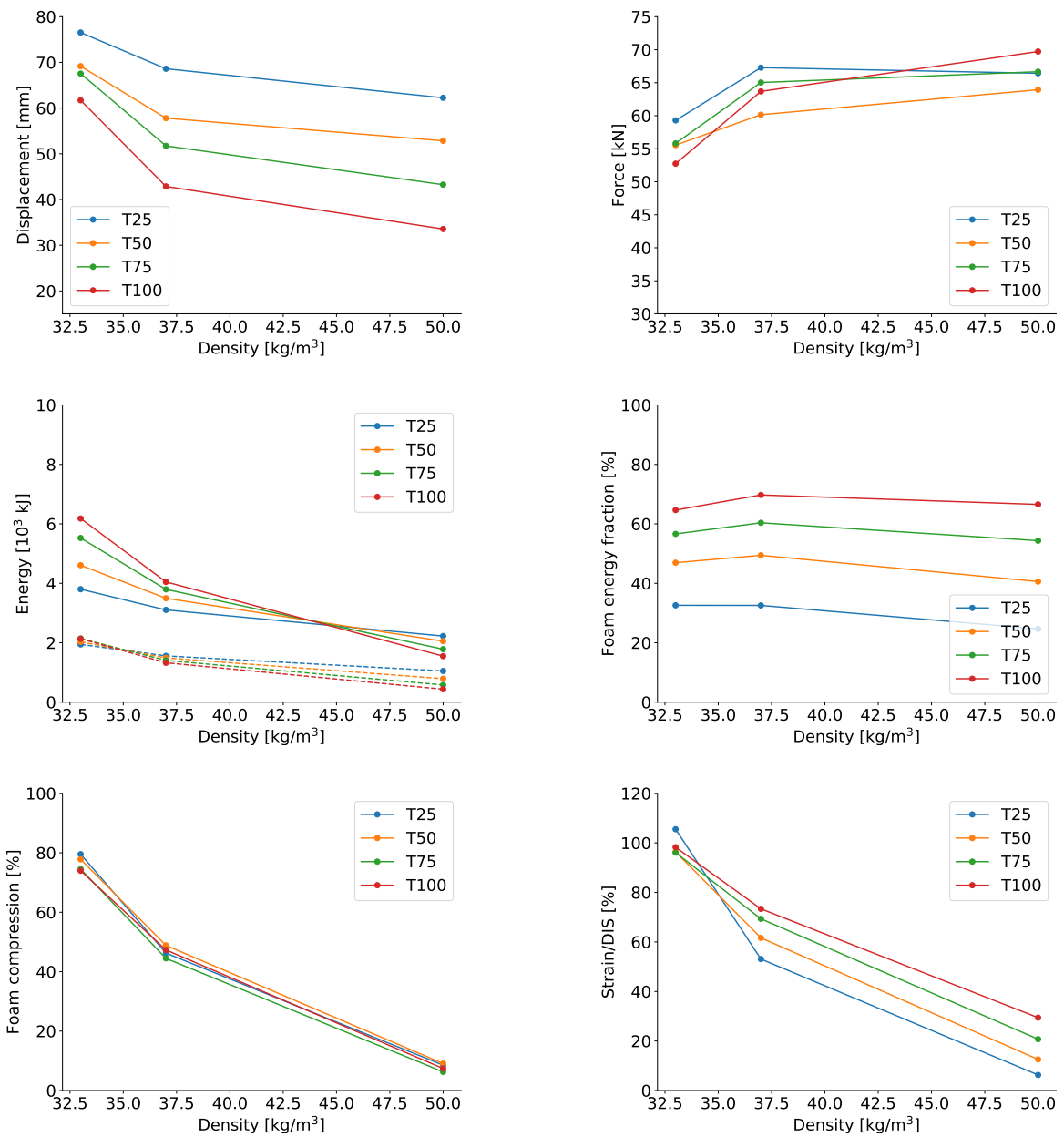


Figure C.8: Back skin displacement, reaction force between component and back clamping frame, total and total specific energy absorbed, percentage of energy absorbed in foam core, back skin and front skin, percentage of foam compression and strain percentage of density initiation strain for variation of thickness for sandwich components with aluminum front and back skin exposed to firing pressure of 25 bar.

# Aluminum front skin and steel back skin exposed to 25 bar

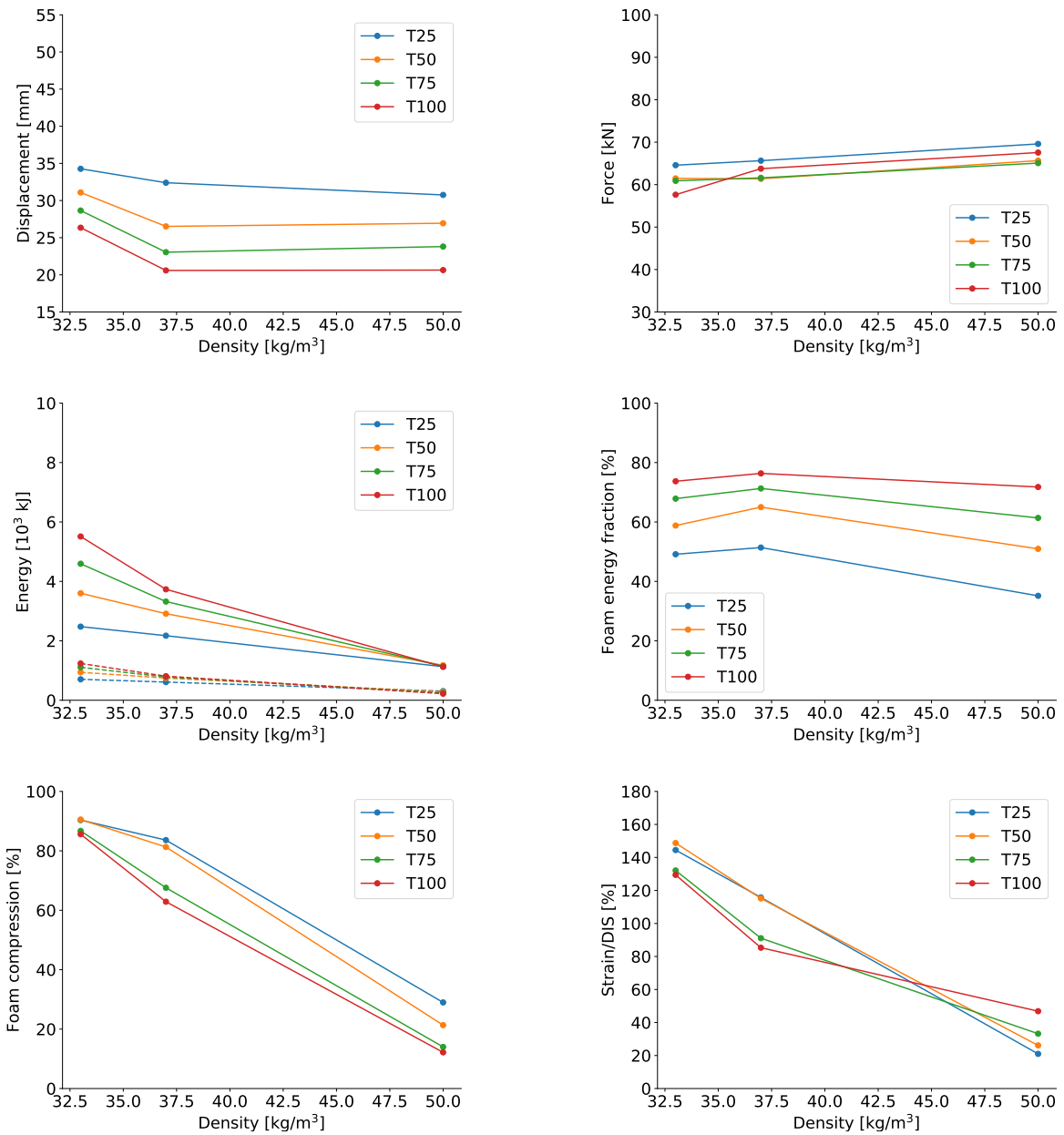


Figure C.9: Back skin displacement, reaction force between component and back clamping frame, total and total specific energy absorbed, percentage of energy absorbed in foam core, back skin and front skin, percentage of foam compression and strain percentage of density initiation strain for variation of thickness for sandwich components with aluminum front skin and steel back skin exposed to firing pressure of 25 bar.

## Aluminum front skin and steel back skin exposed to 35 bar

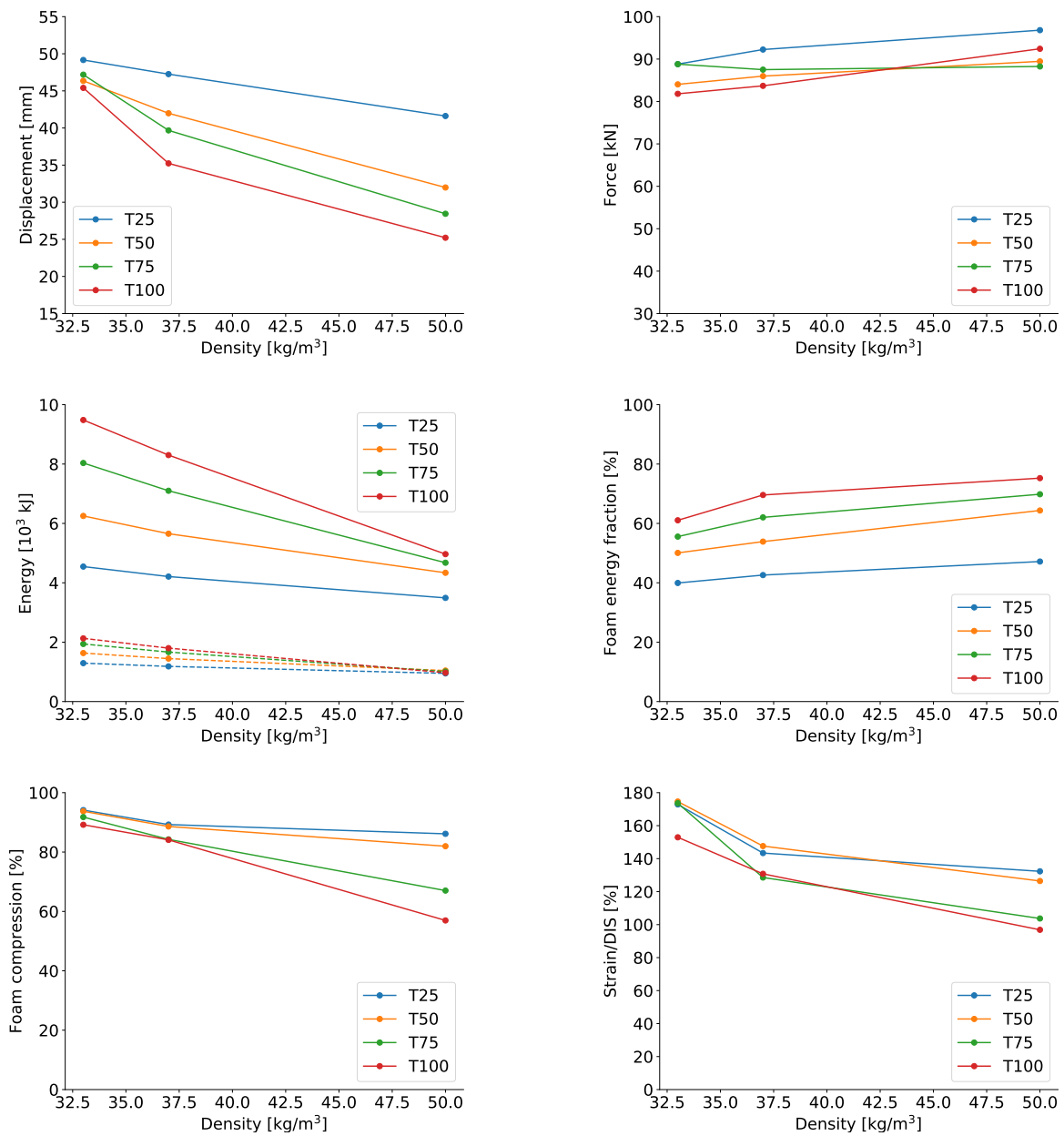


Figure C.10: Back skin displacement, reaction force between component and back clamping frame, total and total specific energy absorbed, percentage of energy absorbed in foam core, back skin and front skin, percentage of foam compression and strain percentage of density initiation strain for variation of thickness for sandwich components with aluminum front skin and steel back skin exposed to firing pressure of 35 bar.



### C.3 Thickness - Alternative Presentation

#### Aluminum skins exposed to 10 bar

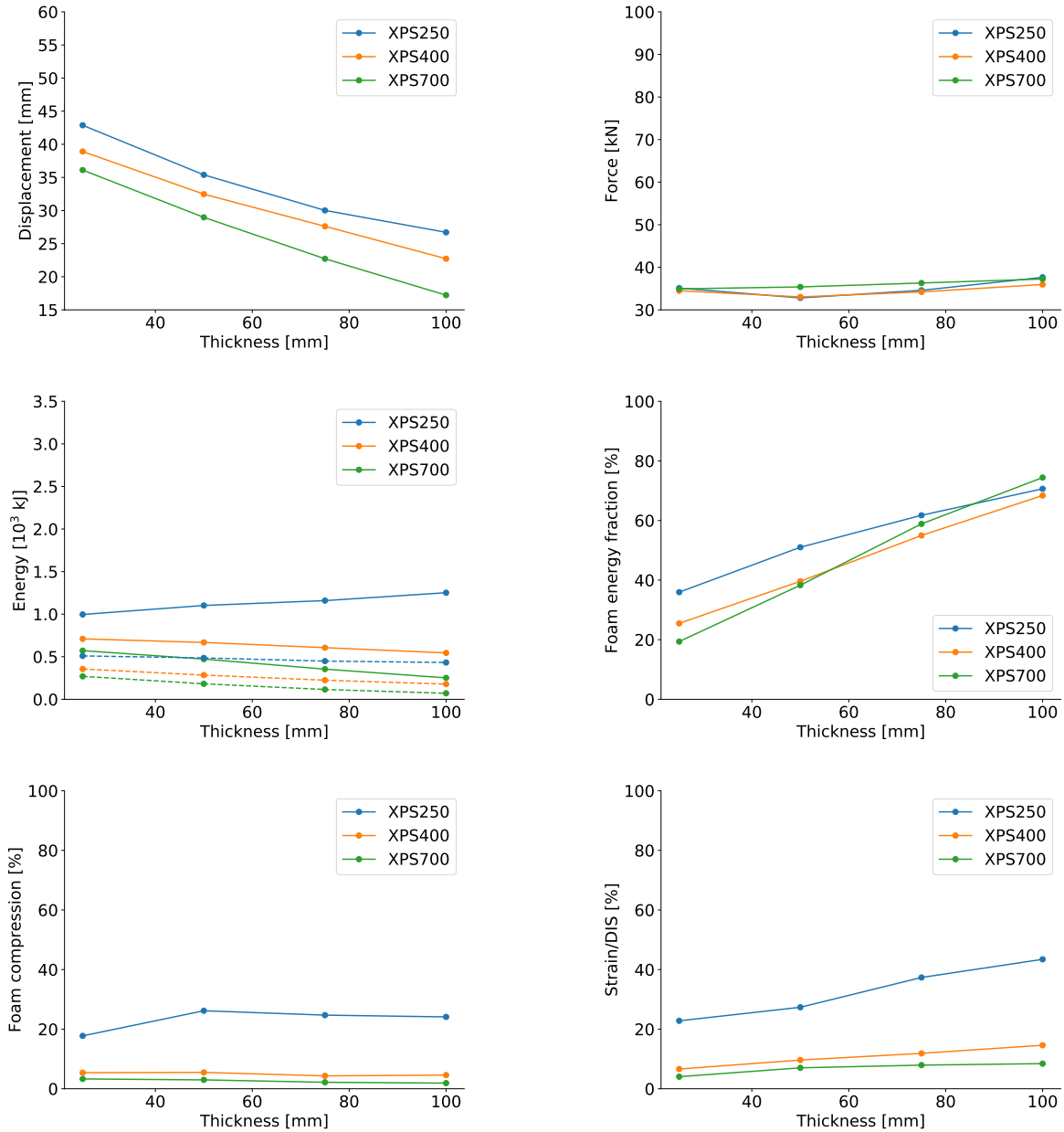


Figure C.11: Back skin displacement, reaction force between component and back clamping frame, total and total specific energy absorbed, percentage of energy absorbed in foam core, back skin and front skin, percentage of foam compression and strain percentage of density initiation strain for variation of thickness for sandwich components with aluminum front and back skin exposed to firing pressure of 10 bar.

# Aluminum skins exposed to 15 bar

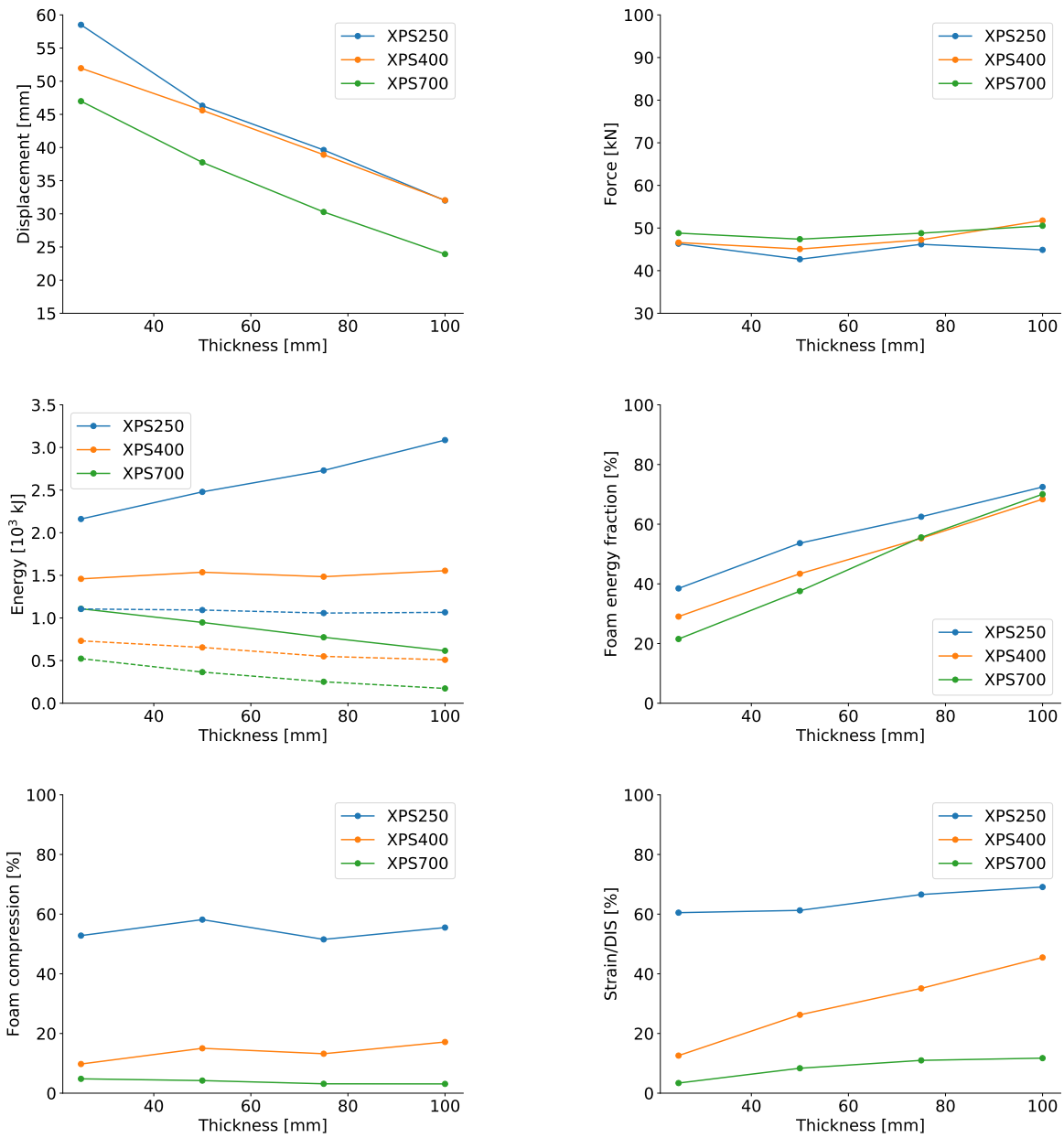


Figure C.12: Back skin displacement, reaction force between component and back clamping frame, total and total specific energy absorbed, percentage of energy absorbed in foam core, back skin and front skin, percentage of foam compression and strain percentage of density initiation strain for variation of thickness for sandwich components with aluminum front and back skin exposed to firing pressure of 15 bar.

# Aluminum skins exposed to 25 bar

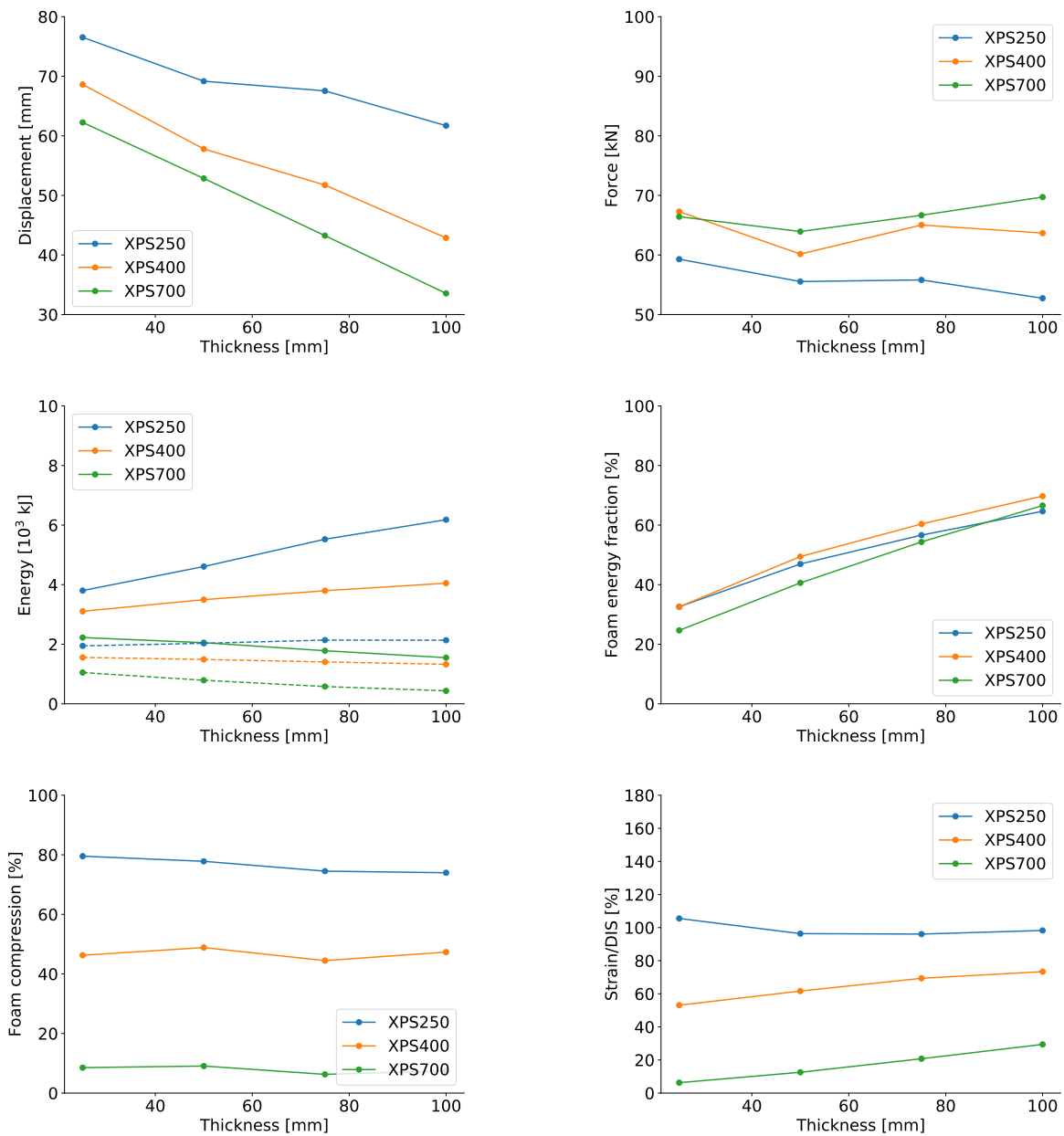


Figure C.13: Back skin displacement, reaction force between component and back clamping frame, total and total specific energy absorbed, percentage of energy absorbed in foam core, back skin and front skin, percentage of foam compression and strain percentage of density initiation strain for variation of thickness for sandwich components with aluminum front and back skin exposed to firing pressure of 25 bar.

## Aluminum front skin and steel back skin exposed to 25 bar

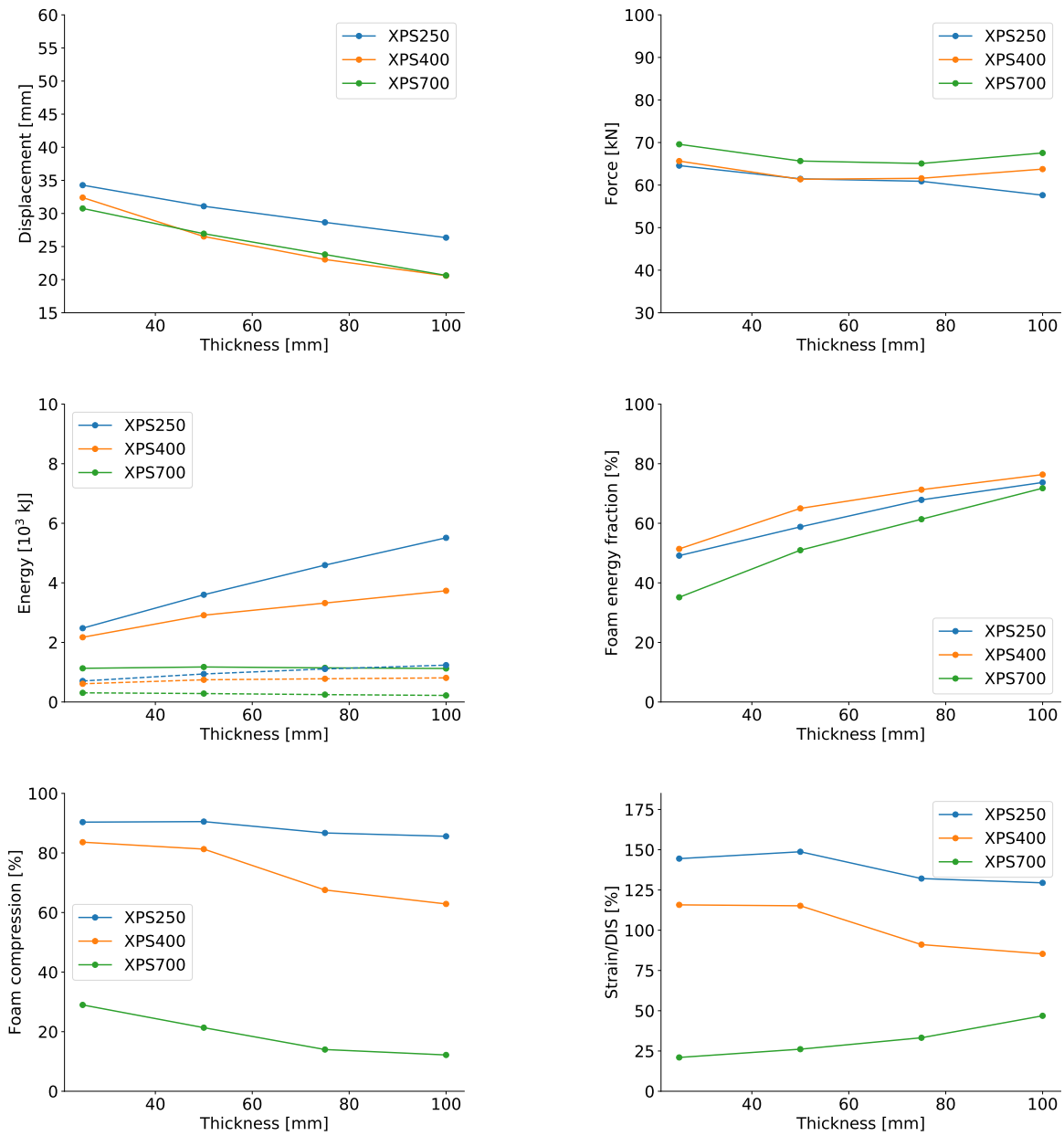


Figure C.14: Back skin displacement, reaction force between component and back clamping frame, total and total specific energy absorbed, percentage of energy absorbed in foam core, back skin and front skin, percentage of foam compression and strain percentage of density initiation strain for variation of thickness for sandwich components with aluminum front skin and steel back skin exposed to firing pressure of 25 bar.

## Aluminum front skin and steel back skin exposed to 35 bar

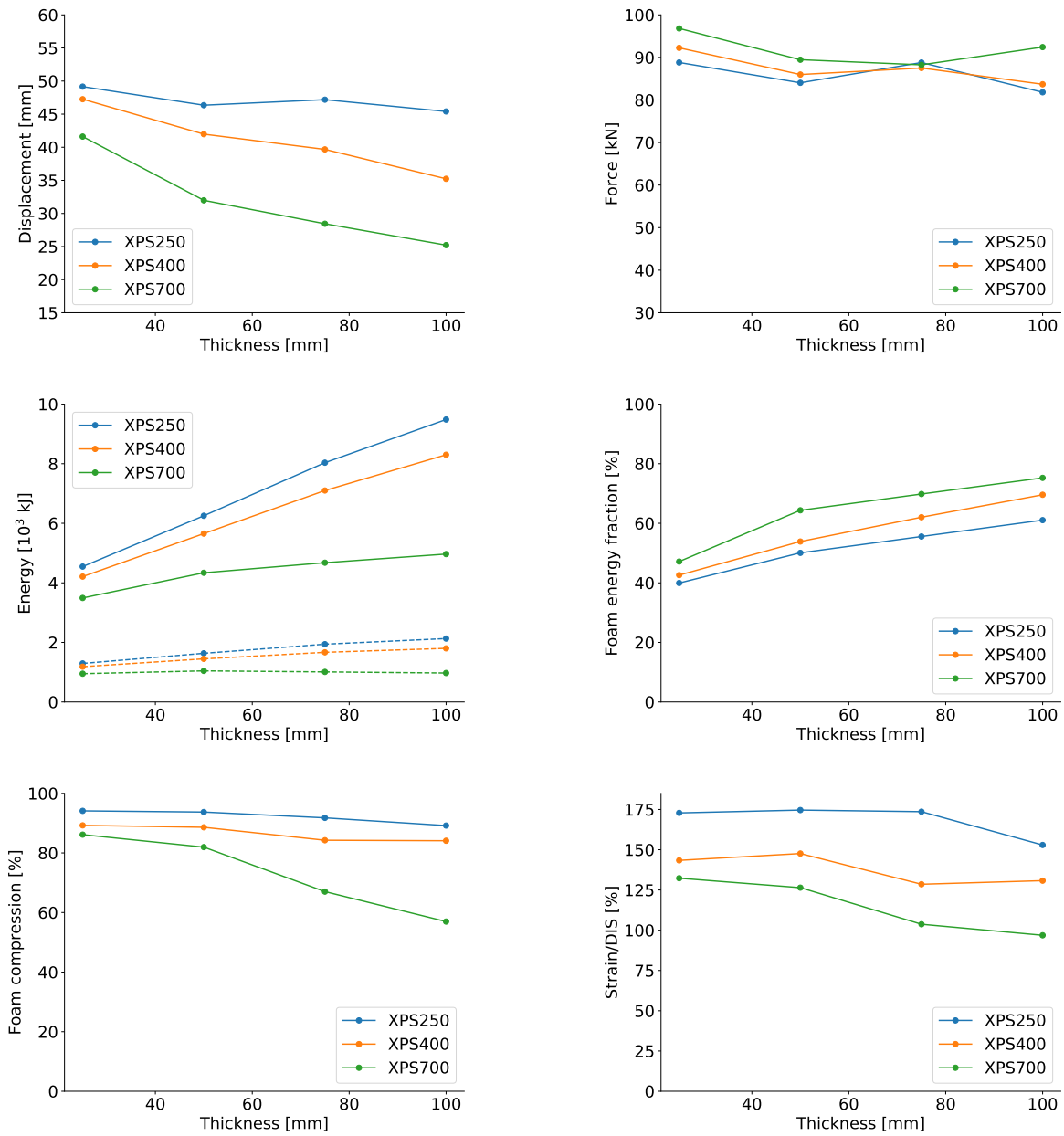


Figure C.15: Back skin displacement, reaction force between component and back clamping frame, total and total specific energy absorbed, percentage of energy absorbed in foam core, back skin and front skin, percentage of foam compression and strain percentage of density initiation strain for variation of thickness for sandwich components with aluminum front skin and steel back skin exposed to firing pressure of 35 bar.

## C.4 Constant Mass

### Aluminum skins exposed to 10 bar

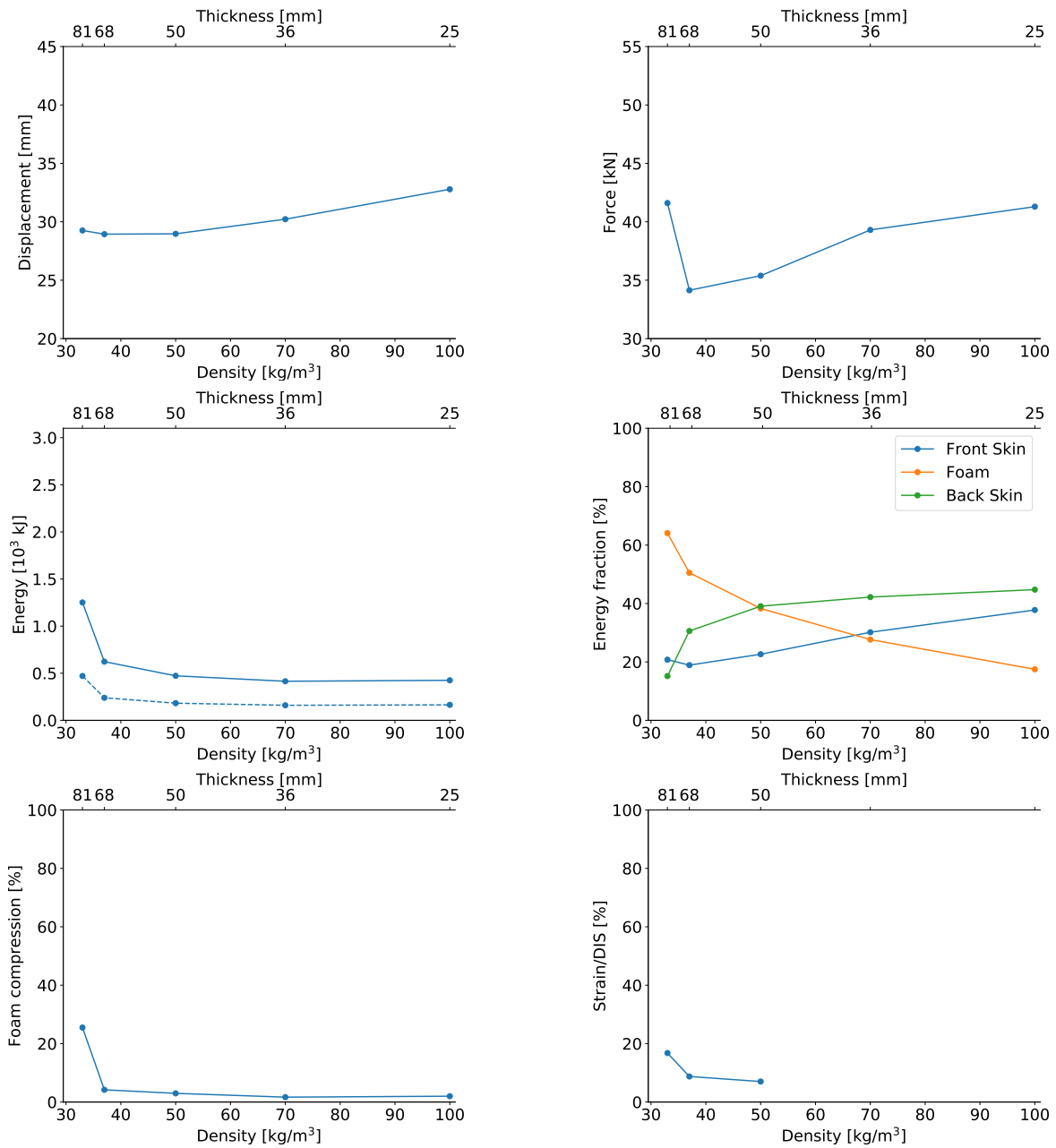


Figure C.16: Back skin displacement, reaction force between component and back clamping frame, total and total specific energy absorbed, percentage of energy absorbed in foam core, back skin and front skin, percentage of foam compression and strain percentage of density initiation strain for variation of thickness and density with constant foam mass for sandwich components with aluminum front and back skin exposed to firing pressure of 10 *bar*.

# Aluminum skins exposed to 15 bar

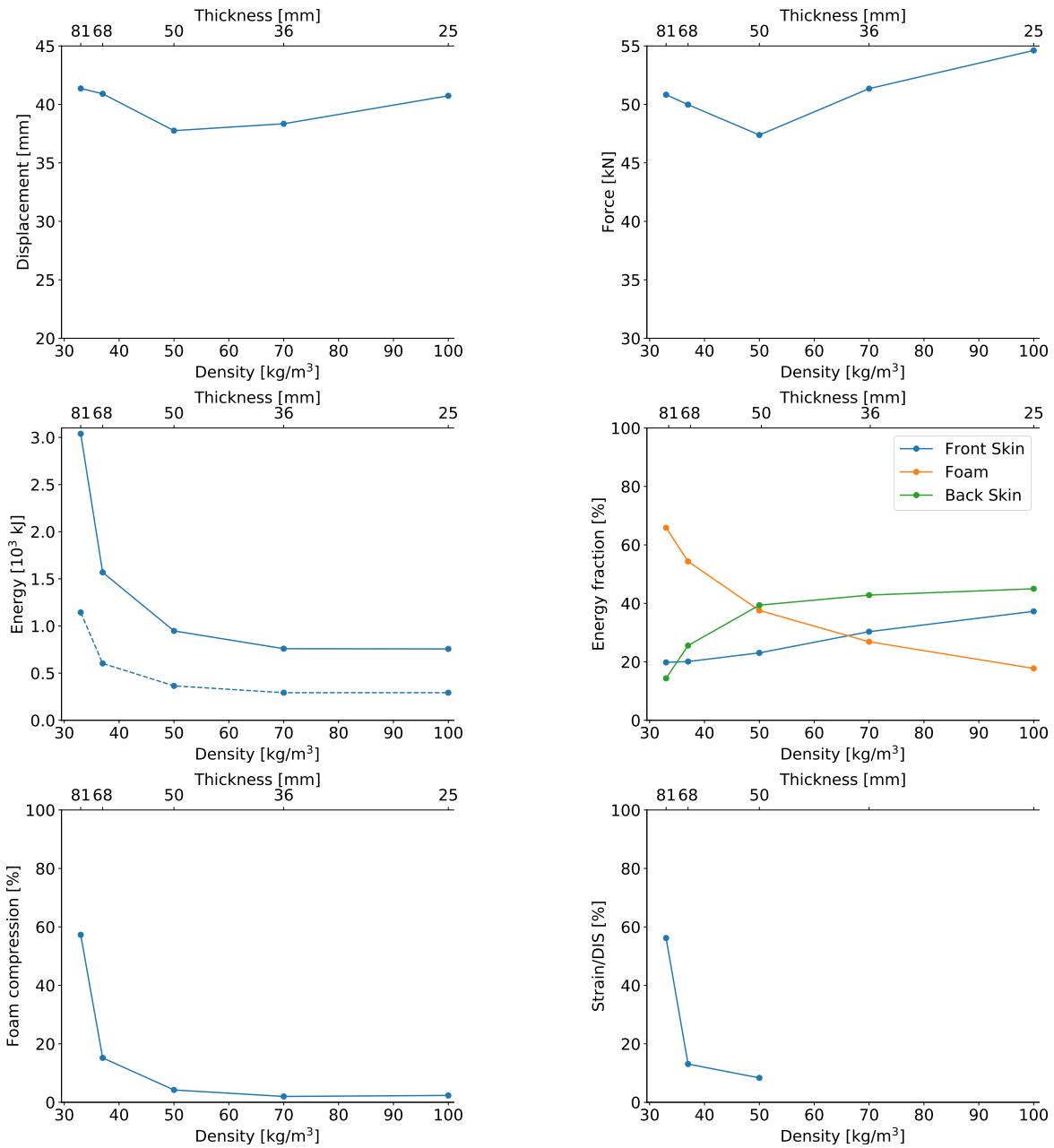


Figure C.17: Back skin displacement, reaction force between component and back clamping frame, total and total specific energy absorbed, percentage of energy absorbed in foam core, back skin and front skin, percentage of foam compression and strain percentage of density initiation strain for variation of thickness and density with constant foam mass for sandwich components with aluminum front and back skin exposed to firing pressure of 15 bar.

# Aluminum skins exposed to 25 bar

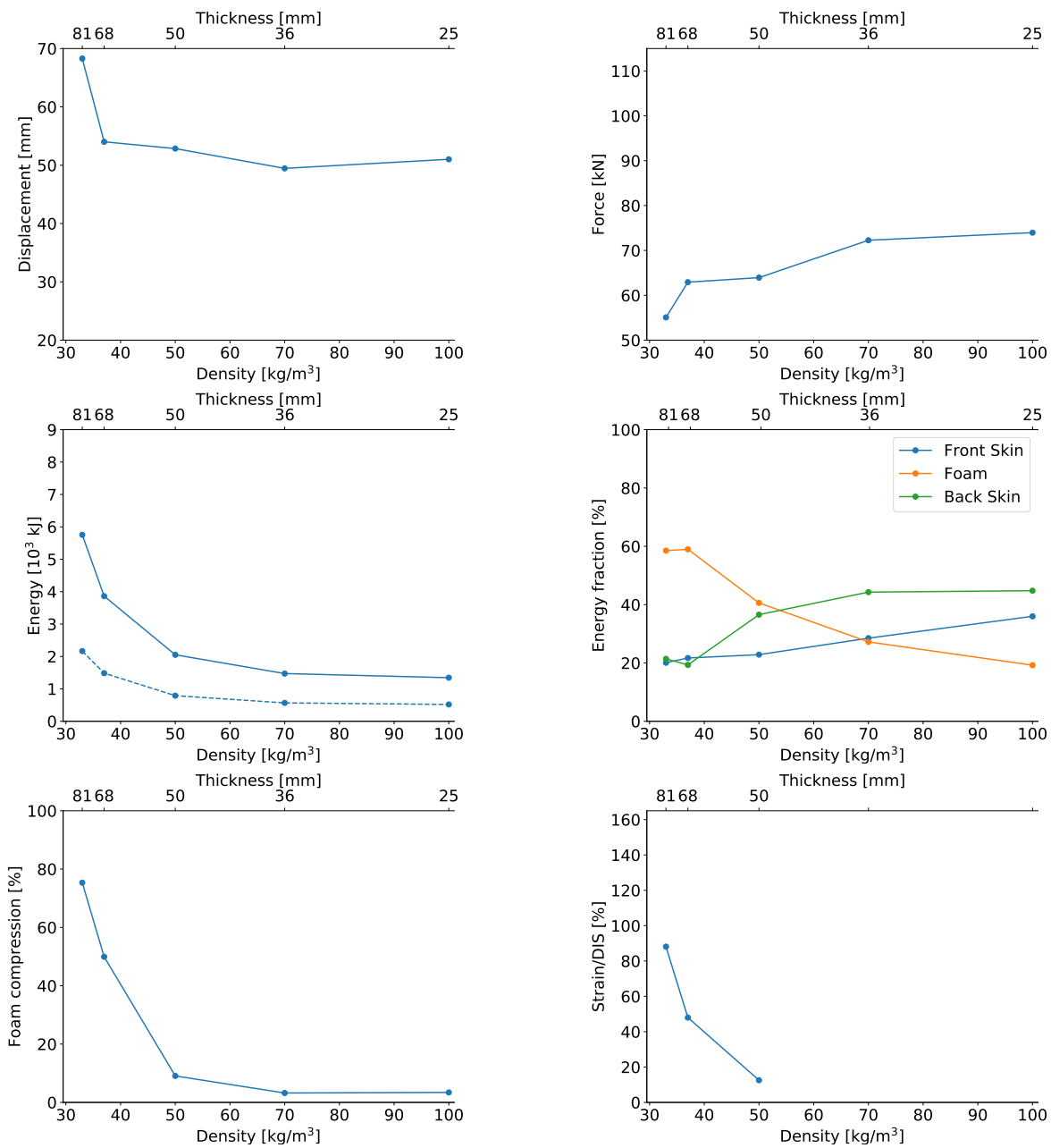


Figure C.18: Back skin displacement, reaction force between component and back clamping frame, total and total specific energy absorbed, percentage of energy absorbed in foam core, back skin and front skin, percentage of foam compression and strain percentage of density initiation strain for variation of thickness and density with constant foam mass for sandwich components with aluminum front and back skin exposed to firing pressure of 25 bar.



## Aluminum front skin and steel back skin exposed to 25 bar

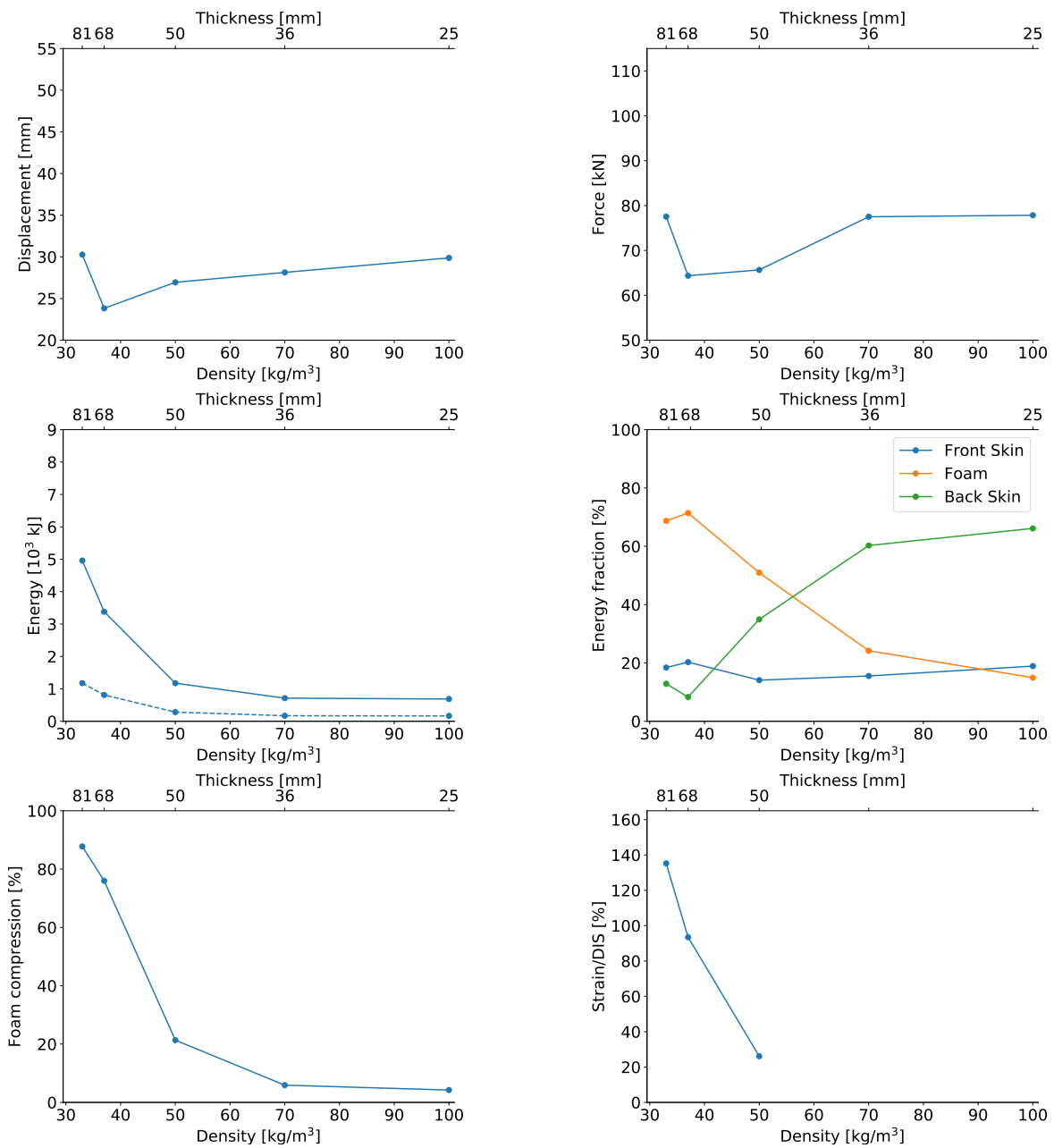


Figure C.19: Back skin displacement, reaction force between component and back clamping frame, total and total specific energy absorbed, percentage of energy absorbed in foam core, back skin and front skin, percentage of foam compression and strain percentage of density initiation strain for variation of thickness and density with a constant foam mass for sandwich components with aluminum front skin and steel back skin exposed to firing pressure of 25 bar.

## Aluminum front skin and steel back skin exposed to 35 bar

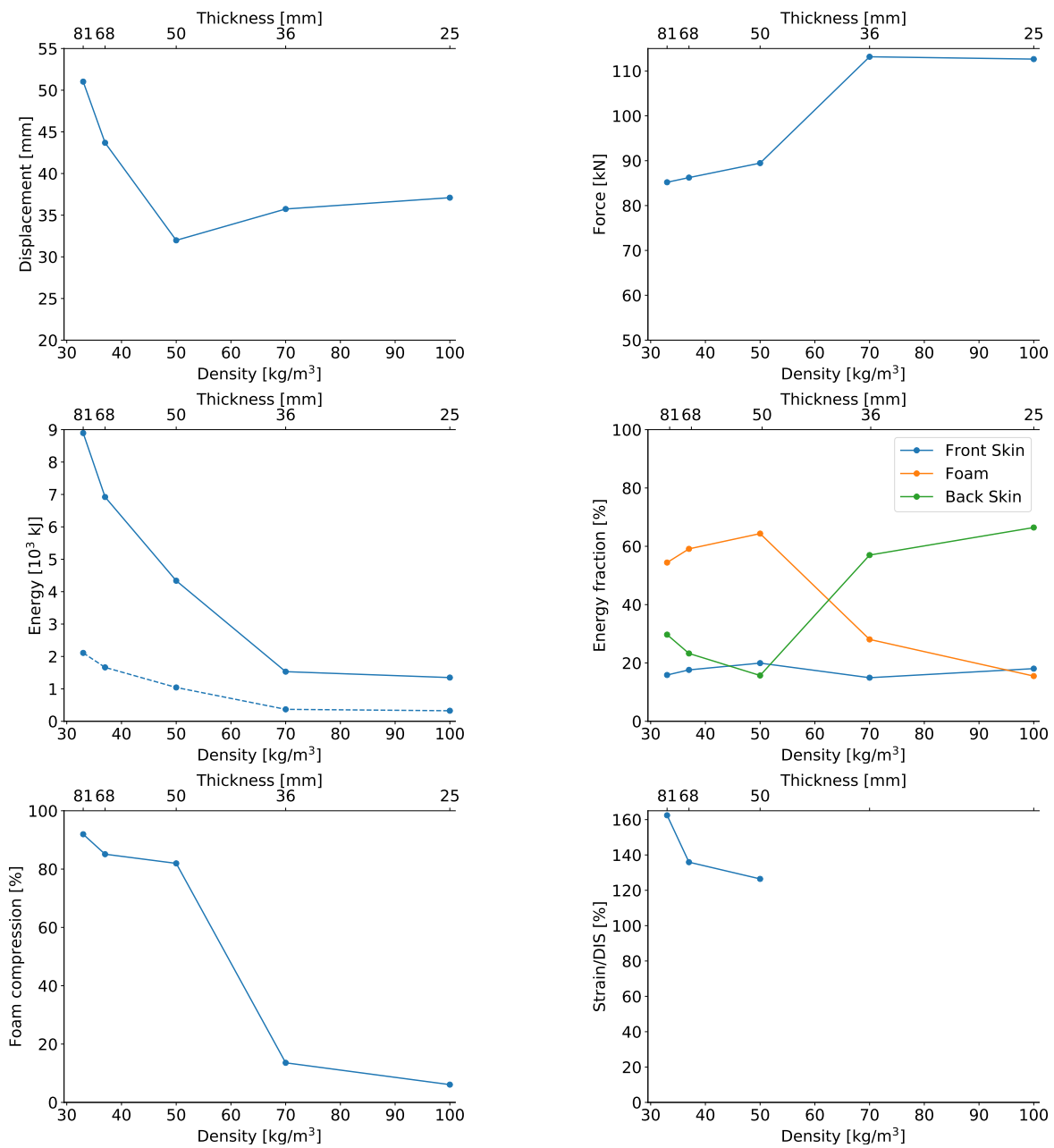


Figure C.20: Back skin displacement, reaction force between component and back clamping frame, total and total specific energy absorbed, percentage of energy absorbed in foam core, back skin and front skin, percentage of foam compression and strain percentage of density initiation strain for variation of thickness and density with a constant foam mass for sandwich components with aluminum front skin and steel back skin exposed to firing pressure of 35 bar.